A TIME - DEPENDENT QUANTUM MECHANICAL INVESTIGATION OF ION-MOLECULE REACTIONS

A Thesis Submitted

in Partial Fulfilment of the Requirements

for the Degree of

DOCTOR OF PHILOSOPHY

by

SUSANTA MAHAPATRA

to the

DEPARTMENT OF CHEMISTRY

INDIAN INSTITUTE OF TECHNOLOGY KANPUR

JANUARY, 1996

To
My Parents

STATEMENT

I hereby declare that the matter embodied in this thesis is the result of investigations carried out by me in the Department of Chemistry, Indian Institute of Technology, Kanpur, India under the supervision of Professor N. Sathyamurthy.

In keeping with the general practice of reporting scientific observations, due acknowledgement has been made wherever the work described is based on the findings of other investigators.

Kanpur

SUSANTA MAHAPATRA

DEPARTMENT OF CHEMISTRY
INDIAN INSTITUTE OF TECHNOLOGY KANPUR INDIA
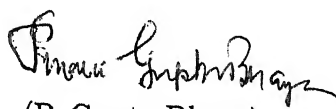### CERTIFICATE I

This is to certify that Mr. Susanta Mahapatra has satisfactorily completed all the courses required for the Ph. D. degree program. These courses include:

CHM 679   Molecular Reaction Dynamics

CHM 686   Physics and Chemistry With Ion Trap

CHM 625   Principles of Physical Chemistry

CHM 605   Principles of Organic Chemistry

CHM 645   Principles of Inorganic Chemistry

CHM 664   Modern Physical Methods in Chemistry

CHM 800   General Seminar

CHM 801   Special Seminar

CHM 900   Ph. D. Thesis

Mr. Susanta Mahapatra was admitted to the candidacy of the Ph. D. degree in February 1993, after he succesfully completed the written and oral qualifying examinations.

(S. K. Dogra) 5/1/96
Head,
Department of Chemistry
IIT Kanpur

(P. Gupta Bhaya)
Convenor,
Departmental Post Graduate Committee
Department of Chemistry
IIT Kanpur

Submitted on 3/1/96
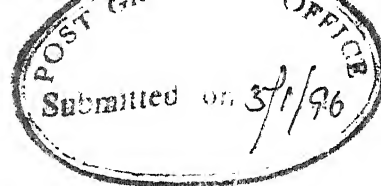
CERTIFICATE II

Certified that the work contained in this thesis entitled: "A Time-Dependent Quantum Mechanical Investigation of Ion-Molecule Reactions", has been carried out by Mr. Susanta Mahapatra under my supervision and that the same has not been submitted elsewhere for a degree.

N. Sathyamurthy

(N. Sathyamurthy)
Thesis Supervisor
Professor of Chemistry
IIT Kanpur

Kanpur

ACKNOWLEDGEMENT

atmosphere and for their delightful company on various occasions.

Finally I take immense pleasure in thanking my parents, sister, brother and brother -in-law for their constant encouragement and support.

<div align="right">(Susanta Mahapatra)</div>

Abstract

Time-dependent quantum mechanical (TDQM) wave packet (WP) methods have been applied successfully in recent years in describing a wide variety of physico-chemical processes. In the present study we have used such methods to investigate the transition state (TS) resonances and dynamics of elementary gas phase ion-molecule reactions.

In chapter 1 of the thesis, we present an overview of the chronological development of the TDQM methodology. Its application to a wide variety of problems with a special emphasis on TS spectroscopy and reactive scattering is reviewed.

In chapter 2, the general grid method of solving the time-dependent Schrödinger equation (TDSE) is presented. We describe the general set up of a grid and the commonly used numerical methods of propagation (in space as well as in time) of the initial WP represented on such a grid are reviewed. The stability of various numerical time evolution schemes in presence of a negative imaginary potential (NIP), used for damping the WP components near the grid edges, is analysed. The Fourier grid Hamiltonian (FGH) method for computing the bound state eigenvalues and eigenfunctions is presented. The spectral quantization method (SQM) is also presented in this context and its utility in quantifying the resonances is discussed. The computation of vibrational state-selected and energy resolved reaction probabilities through a time-energy mapping of the reactive flux of the WP, state-to-state reaction probabilities through a time-energy projection and state-to-state reaction probabilities from the energy resolved S-matrix elements in the Møller operator formalism is described at length.

In chapter 3, we investigate the dynamical resonances in collinear (He, H_2^+), (He, HD^-) and (He, DH^+) collisions by analysing their respective TS spectrum on the McLaughlin-Thompson-Joseph-Sathyamurthy (MTJS) potential energy surface (PES). The spectra are computed by the SQM, through Fourier transformation of the temporal autocorrelation, $C(t)$, of the initial WP. The nature of some of the resonances is examined by calculating their eigenfunctions and lifetimes. The relation to the corresponding resonant periodic orbits (RPOs) in classical mechanics at those energies for the collinear (He, H_2^+) resonances is also established. The vibrational state-selected and energy resolved reaction probabilities ($P_v^R(E)$) for collinear (He, HD^+) and (He, DH^+) collisions are also calculated on the same PES by computing the reactive flux in the product channel. The $P_v^R(E)$ values for (He, HD^-) collisions show a characteristic staircase-like structure which can be related to threshold resonances. The $P_v^R(E)$ values for (He, DH^+) on the other hand are highly oscillatory, in keeping with a densely packed TS spectrum.

In chapter 4, we examine the possibility of existence of reactive scattering resonances in collinear (H^-, H_2) collisions by computing the TS spectrum on the Stärck and Meyer (SM) PES. The nature of the H_3^- resonances is investigated by computing the corresponding eigenfunctions and their lifetimes. We also report the $P_0^R(E)$ values for the collinear reaction $H^- + H_2(v = 0) \rightarrow H_2 + H$, on the same PES to confirm the existence of the resonances. The different dynamical behaviors of H_3^- and H_3 are discussed.

In chapter 5, the TS spectrum of collinear (He, H_2^+) collisions obtained in chapter 3 is analysed to extract the signature of quantum chaos. Examination of short- and long-range correlations in the eigenvalue spectra through a study of the nearest neighbor spacing distribution (NNSD), $P(s)$, and the spectral rigidity, $\Delta_3(L)$, reveals signatures of quantum chaotic behavior. Analysis in the time domain is carried out by computing the survival probability, $<< P(t) >>$, averaged over initial states and Hamiltonian. All these indicators show behavior intermediate between regular and chaotic. A quantitative comparison of $<< P(t) >>$ with the results of random matrix theory provides an estimate of the fraction of phase space exhibiting chaotic behavior, in reasonable agreement with the classical dynamics. We also analyse the dynamical evolution of coherent Gaussian wave packets (GWP) located initially in differennt regions of phase space and compute the survival probability, power spectrum and the volume of the phase space over which the WP spreads and illustrate the different behaviors.

In chapter 6, we have presented the results of our preliminary investigation of the TS resonances in three dimensional (He,H_2^+) collisions obtained through the spectral quantization method. The computer code has been developed in mass-scaled Jacobi (R, r, γ) coordinates where the spatial evolution of the WP along (R, r) is carried out by a two dimensional FFT and the evolution along γ is carried out by a DVR constructed using the Gauss-Legendre quadrature. The temporal evolution of the WP is carried out by the SO method.

In chapter 7, a summary of our findings and the conclusions are presented.

In appendix 1, we have provided some necessary details of chapter 2.

In appendix 2, energy loss spectra of forward scattered He^+ ions in collision with HCl are reported for collision energies (E_{lab}) in the range, 20-60 eV. There is a variation of six orders of magnitude in intensity for the amount of energy transferred, up to $\Delta E \sim 2$ eV. Although there is very little difference in the extent of ΔE, for different E_{lab}, there are noticeable differences in the spetra at large ΔE, indicating propensity for large Δv transitions at high E_{lab}. Three dimensional quasiclassical trajectory (QCT) calculations treating HCl as a rigid

rotor and representing the He^+-HCl interaction as of ion-dipole(quadrupole) in the long-range and corresponding to the isoelectronic He^+-Ar in the short-range, could account for much of the energy transfer at low E_{trans}. At higher E_{trans}, the rigid rotor model is clearly inadequate and slightly better agreement between experiment and theory results when HCl is treated as a vibrating rotor.

Contents

LIST OF ABBREVIATIONS

CP	-	Chebyshev polynomial
DMBE	-	Double many body expansion
DIM	-	Diatomics in molecule
DVR	-	Discrete variable representation
FBR	-	Finite basis representation
FD	-	Finite difference
FFT	-	Fast Fourier transform
FGH	-	Fourier grid Hamiltonian
FHT	-	Fast Henkel transform
FWHM	-	Full width at half-maximum
GWP	-	Gaussian wave packet
LSTH	-	Liu-Siegbahn-Truhlar-Horowitz
MTJS	-	McLaughlin-Thompson-Joseph-Sathyamurthy
NIP	-	Negative imaginary potential
PES	-	Potential energy surface
RPO	-	Resonant periodic orbit
SIL	-	Short iterative Lanczos
SM	-	Stärck-Meyer
SO	-	Split operator
SOD	-	Second order difference
SQM	-	Spectral quantization method
TDQM	-	Time-dependent quantum mechanical
TDSE	-	Time-dependent Schrödinger equation
TDWP	-	Time-dependent wave packet propagation
TIQM	-	Time-independent quantum mechanical
TS	-	Transition state
VAP	-	Vibrational adiabatic potential
WP	-	Wave packet

Chapter 1

Introduction

Understanding the microscopic phenomena underlying physico-chemical processes is the goal of molecular dynamical research. From a theoretician's point of view such a study requires the knowledge of inter- and intramolecular interaction potentials. These are either made up by using suitable algebraic functions to model the known interaction or evaluated *ab initio* by solving the electronic Schrödinger equation for the system for fixed nuclear configurations under the conditions of Born-Oppenheimer approximation. Once the potential energy surface (PES) [1-6] is obtained the next step is the investigation of the internuclear motion on the PES by solving the corresponding equations of motion (either classical or quantum mechanical) [7-16]

Both experimental and theoretical research in molecular reaction dynamics has undergone a revolution during the past few decades. The driving force behind this is the technological developments and the emergence of new ideas. Revolution in the experimental research is largely due to two major technological developments– molecular beams and ultrashort (10^{-15} s = fs) laser pulses. Measurement of steric effect [17] in a reactive or non-reactive collision by aligning/orienting [18] the molecules either by using strong electric fields in molecular beams [19, 20] or by using lasers in a bulb experiment [21, 22] is a great achievement. Rotational cooling of polar diatomic molecules by supersonic jet expansion [23] followed by the application of electric or magnetic field perpendicular to the

beam flow has created the hybrid, *pendular states* of molecules [24-30] . Time resolution in the measurement up to many orders of magnitude less than the fastest instrumental response time has been achieved by using two synchronised laser pulses– one for excitation and another as a probe [31-34]. It has become possible to "clock" the transition state (TS) of a chemical reaction (typical lifetime of $\sim$ 10 - 100 fs) in real time and subsequently follow the nuclear motion [35-43] . The term transition state above refers to all configurations the system acquires while passing from the reactant to the product valley. This is slightly different from the traditional definition of the transition state which identifies it with the saddle point along the reaction path between the reactants and the products. Development of negative ion photodetachment spectroscopy has created an alternative route to viewing the transition state directly [44-47]. The neutral unbound transition state is obtained in this technique by photodetaching the corresponding bound negative ion. The translational energies of the emitted electrons have imprinted on them the ro-vibrational structures of the neutral transition state. This has been a long held dream of chemists to observe the transition state directly (for a recent review on transition state spectroscopy see Ref. [48]). In a recent article [49] Porter commented, "chemists are near the end of the race against time". He had initiated the "race" in 1949 through his millisecond flash photolysis experiments [50, 51].

Much of the early insights into the chemical reaction dynamics had come from quasi-classical trajectory studies [52, 53]. Subsequently, the semiclassical methods [54] were developed to incorporate quantum features in the classical framework. The time-independent quantum mechanical (TIQM) theory [8] of molecular encounters also dominated the field until recently. The last few years have seen an intense activity in a time-dependent quantum mechanical (TDQM) approach [55] to the problem.

Historically the concept of wave packet (WP) was introduced by Erwin Schrödinger (1926) [56]. The thrust behind this was to have a complementary picture of classical tra-

jectory in the quantum domain. The correspondence between the two was culminated in Ehrenfest's theorem– " in the classical limit the quantum mechanical expectation values behave classically" [57]. The classical limit of course refers to the limit of zero uncertainty. There was no real application of the WP method until Mazur and Rubin [58] solved the time-dependent Schrödinger equation (TDSE) for the first time for a model collinear exchange reaction

$$A + BC \rightarrow AB + C \tag{R1}$$

in 1959. Several years later (1967) numerical solution of the WP motion in one dimension was carried out by Goldberg et al [59] and then McCullough and Wyatt [60] studied the collinear

$$H + H_2 \rightarrow H_2 + H \tag{R2}$$

reaction. They employed an implicit (Crank-Nicholson) scheme for the time evolution of the WP and a finite difference scheme for its spatial evolution. Their method involved tedious matrix inversions and was found to be computationally intractable in higher dimension. Later on (1978), Askar and Cakmak [61] proposed an explicit time propagation scheme, which turned out [62] to be a re-discovery of the earlier work of Harmuth [63]. Their method was devoid of the tedious matrix inversion. Feit et al [64] in 1976, had introduced a Fourier based pseudo-spectral scheme to study the propagation of the laser beam through atmosphere. They proved the applicability of their method to solving the TDSE numerically on a grid to compute the energy level spectrum of the Hénon-Heiles system [65]. The Fourier method offered an accurate way to evaluate the action of kinetic energy operator on the WP by switching over to momentum space. This was the first breakthrough in the numerical technology of solving the TDSE. The accuracy of the method resulted in abandoning the finite difference scheme which was not very stable. Feit et al [65] used a split-operator scheme for the time propagation. Subsequently, Kosloff and Kosloff [66, 67] reiterated the usefulness of the fast Fourier algorithm combined with a

second order differencing scheme (explicit scheme of Harmuth) to solve the TDSE. Light et al [68] developed a general quadrature based pseudo-spectral scheme (generalised discrete variable representation (DVR)) to carry out the spatial propagation of the WP. It was found to be more promising to evaluate the angular kinetic energy part where the usual FFT method faces a singularity at $\theta=0$ and π. Tal-Ezer and Kosloff [69] developed a Chebyshev polynomial scheme for the time evolution of the WP and found it to be the most accurate. The Chebyshev scheme combined with the FFT and/or DVR method is often the method of choice for solving the TDSE, particularly, for systems exhibiting long-time dynamical behavior. Bisseling and Kosloff [70] showed the applicability of the Hankel transform in the place of the FFT and pointed out its usefulness in dealing with higher dimensions. The short iterative Lanczos scheme was introduced [71-74] as another alternative for the time evolution and found to be quite useful in dealing with the explicitly time-dependent Hamiltonians. A comparative study of different numerical time evolution schemes with respect to their accuracy and stability in solving the TDSE has been carried out by various researchers in the literature [75, 76]. A brief summary of various numerical schemes for solving TDSE is presented in chapter2.

The TDQM approach provides a realistic view of chemical reactions in a theoretical calculation. It allows one to monitor the progress of the reaction event in time by looking at the snapshots of the WP on the potential grid, for example. It has a high degree of predictive value, and it also suggests means of controlling chemical reactions [77-86]. From a practical computational point of view, the TDQM approach offers yet another advantage in that, a single wave packet propagation yields the desired result like reaction probability at a range of energy values. TIQM calculations, in contrast, pose a serious problem as a high resolution in energy requires the use of a dense grid in the energy scale, which results in a substantial increase in computational time. Finally, near the onset of the collision-induced dissociation one runs into the basis set problem in the TIQM calculations, the size

of the basis set becoming very large to take care of the contribution from the dissociation continuum, whereas, TDQM methods pose no such problem.

During the past few years the TDQM techniques have been used to solve a variety of problems, half-collisions as well as full collisions. In a half-collision study one starts from the transient and study its decay into products. The classic example of this is photodissociation and predissociation processes [87-96] In photodissociation, the molecule is prepared in the specified rovibrational state of the ground electronic state and then taken to the excited repulsive electronic state, which may be coupled with other excited electronic states, through the action of the transition dipole matrix elements and from where it fragments into products. The quantities of interest here are the photodissociation cross sections (partial and total), angular distribution of the photofragments, and the branching ratios if there is more than one product channel. In predissociation, the species is excited from a bound (ground) to a bound (excited) state and before the excited species emits light and returns back to the ground state it dissociates due to the coupling of the upper bound state with a repulsive state. Recently the idea has been extended to compute transition resonances in chemical reaction [97-102] . Resonances in a chemical reaction arises from the presence of metastable states in the transition state region of the PES. Characterization of resonances and their influence on the dynamics have played a major role in research in the area of reaction dynamics [103-106] . Some of these resonances have been identified in the photodetachment experiments of Neumark and coworkers [44-46, 107-110]. Their experiments combined with the coupled channel hyperspherical reactive scattering calculations of Schatz and others [111-116] have been utilised extensively in understanding the topology of the PES for these systems. In addition the TDQM approach has been used in several other applications, such as multiphoton dissociation processes [117-119], mode selective decay [120-131], vibrational predissociation of van der Waals complexes [132, 133], Raman scattering [134-136], computation of the cumulative reaction probabilities

[137, 138], computation of the reaction probabilities by computing the scattering matrix in the Møller operator formalism [139-143] , investigation of the nature and dynamics of the WP prepared by an ultrashort laser pulse [119, 144-153] , etc.

In a full collision study the reactants are prepared selectively in the desired internal state and then allowed to interact to lead finally to products. In addition to a study of reactive scattering processes [154-167] , inelastic [168] and gas-surface scattering [169-186] processes have also been treated by the TDQM method. The methodology has been extended to four atom systems [166, 187-190] recently. Several excellent reviews and monographs [191-199] on the TDQM approach to reaction dynamics have appeared in recent years. Some aspects of the TDQM methodology are presented in details in chapter 2. We have used the TDQM method to investigate transition state resonances in collinear (He, H_2^+), (He, HD^+) and (He, DH^+) collisions. The results are given in chapter 3. For the latter two systems, reaction probability values as a function of relative translational energy of reactants are also presented in chapter 3. Results of the investigation of TS resonances in collinear (H^-, H_2) collisions form the subject of chapter 4. Results of chapter 3 are analysed from quantum chaos point of view, in chapter 5. The methodology and preliminary results of a three dimensional investigation of (He, H_2^+) collisions are given in chapter 6. Finally a summary of our findings and conclusions are presented in chapter 7.

Chapter 2

Methodology

2.1 Introduction

In time-dependent quantum mechanics the wave function, Ψ at time, t, is evaluated by solving the time-dependent Schrödinger equation (TDSE):

$$i\hbar\frac{\partial\Psi}{\partial t} = \hat{H}\Psi \tag{2.1}$$

where $\hat{H}(=\hat{T}+\hat{V})$ is the Hamiltonian operator. In order to solve this equation numerically it is necessary to represent the initial state of the system and follow its evolution in time. The first step in this endeavour is accomplished by constructing a discrete Hilbert space in the form of a grid. This is often referred to as the *grid method* in the literature.

The molecular encounter takes place in the position-momentum and the time-energy space. The discrete grid is usually constructed in the coordinate space, with each grid point being characterized by a finite value of the interaction potential. Once this grid is set up the overall solution follows the next three steps: (i) preparation of the initial wave packet (WP) ($\Psi(t = 0)$) (depends on the system and the desired observable) and representation of this WP on the grid, (ii) its evolution in space and time and (iii) final state analysis. In this chapter we will briefly review various numerical techniques for performing steps (ii) and (iii). Step (i) will be described while dealing with a particular system.

One serious problem in the TDQM calculation is that as time progresses the WP

gradually reaches the grid edges and undergoes spurious reflections resulting in interference between the outgoing and the reflected components. One way to circumvent this problem is to use a very large grid which would delay the WP reaching the boundaries. But this results in a tremendous increase in the computer memory and time requirements particularly in higher dimensions and therefore is not feasible in most practical applications. In the late eighties Neuhauser et al [200, 201] have introduced a negative imaginary potential (NIP) of the form $-iV_0$, in addition to the real potential of the system at the last few points near the edges of the grid. The use of NIPs is well known in optics. They provide a convenient way to damp out the WP components near the grid boundary and thereby prevent the unphysical reflection. This alleviates the necessity of very large grids and minimizes the problem of computer memory and time. Although NIPs are often used in TDQM calculations, their use causes problems in some of the numerical time evolution schemes as the Hamiltonian becomes non-Hermitian in their presence. This, naturally raises questions about their use in time-dependent quantum molecular scattering. We illustrate this point at length later in the present chapter. An alternative and a better way to prevent the WP reflection at the edges by using real damping functions is also discussed in this chapter.

2.2   The Spatial Grid

Let us assume that the coordinate space is discretized into a set of N discrete points. If the spacing between two successive points is Δx, then the eigenvalue of the position operator $\hat{x}$ at each point on the grid is given by

$$x_i = (i-1)\Delta x, \qquad\qquad i = 1, ..., N \qquad\qquad (2.2)$$

The corresponding eigenvectors are denoted by $|x_i>$. The orthogonality and the completeness relations on this discrete grid are given by:

$$\sum_{i,j} \Delta x \langle x_i | x_j \rangle = \delta_{ij} \tag{2.3}$$

and

$$\hat{I}_x = \sum_{i=1}^{N} |x_i > \Delta x < x_i| \tag{2.4}$$

where $\hat{I}_x$ is the identity operator. The functions represented at the grid points are given by

$$\langle x_i | \phi \rangle = o(x_i) \tag{2.5}$$

The continuous normalization integral, $\int_{-\infty}^{\infty} \phi^*(x) o(x) dx = 1$, on this grid transforms to a discrete sum:

$$\sum_{i=1}^{N} \phi^*(x_i) \phi(x_i) \Delta x = 1 \tag{2.6}$$

The maximum length of this grid along the spatial coordinate x is, $L = N\Delta x$. This length determines the spacing between two successive points in the reciprocal k space:

$$\Delta k = \frac{2\pi}{N\Delta x} \tag{2.7}$$

In the k space the grid is centered at zero and all other points are distributed symmetrically on either side. If $p_{max}(= \hbar k_{max})$ represents the maximum momentum in the k space then the N points are distributed in the interval $\{-p_{max}, ..., 0, ..., p_{max}\}$. Hence the total length of the grid in this space is $2|p_{max}|$. Now Δx can be written as:

$$\Delta x = \frac{\pi}{|k_{max}|} \tag{2.8}$$

Therefore, the total volume represented in the phase space

$$Volume = 2L p_{max} = Nh \tag{2.9}$$

is decided by the number of grid points. The maximum energy represented on the grid through this discretization is given by:

$$
\begin{aligned}
E_{max} &= T_{max} + V_{max} \\
&= \frac{p_{max}^2}{2m} + V_{max} \\
&= \frac{\hbar^2 |k_{max}|^2}{2m} + V_{max} \\
&= \sum_{i=1}^{N} \frac{\pi^2 \hbar^2}{2m(\Delta x)^2} + V_{max}
\end{aligned}
\tag{2.10}
$$

where V_{max} is the maximum value of the potential energy represented on the grid. The minimum energy $E_{min} (= V_{min})$ is equal to the minimum value of the potential energy. Our subsequent discussion will follow upon this general set up of the discrete grid.

2.3 The Spatial Evolution of the Wave Packet

In order to evaluate the action of $\hat{H}$ on Ψ we need to evaluate separately the action of the kinetic ($\hat{T}$) and the potential ($\hat{V}$) energy operators on it. $\hat{V}$ is local in the coordinate space, so its action on Ψ is only a multiplication of its magnitude with the value of Ψ at the grid points:

$$
\hat{V}(x)\Psi(x_i) = V(x_i)\Psi(x_i)
\tag{2.11}
$$

The kinetic energy operator ($\hat{T} = \frac{p^2}{2m} = -\frac{\hbar^2}{2m}\frac{\partial^2}{\partial x^2}$) is non-local in the coordinate space and the evaluation of $\hat{T}\Psi$ constitutes a key step in quantum molecular dynamics. This is done either by a semi-local approximation in the finite difference (FD) scheme [60] or in the local representation by a suitable collocation technique [202].

In the FD scheme $\hat{T}\Psi$ is evaluated on the coordinate grid, for example, through:

$$
\begin{aligned}
\hat{T}_{FD}\Psi(x_j) &= \frac{-\hbar^2}{2m}\frac{\partial^2 \Psi(x_j)}{\partial x_j^2} \\
&= \frac{-\hbar^2}{2m}\left[\frac{\Psi(x_{j+1}) + \Psi(x_{j-1}) - 2\Psi(x_j)}{(\Delta x_j)^2}\right]
\end{aligned}
\tag{2.12}
$$

This is referred to as the 3-point FD method. Here the wave function is approximated locally by a polynomial which results in a power law convergence of the method, $(\triangle x)^4$. The semi-local description, unfortunately, does not conform to the commutation relations of quantum mechanics. The error accumulates exponentially on repetitive application of $\hat{T}$ on Ψ.

2.3.1   The Collocation Technique

The collocation technique is a global optimization technique pioneered by Gauss [203]. The basic idea underlying it utilizes the concept of discrete Hilbert space. Continuous functions are approximated at each point in this space by a discrete sum in terms of a finite functional basis set. The basis functions $(g_n(x_i))$ at various grid points x_i are connected through appropriate expansion coefficients (a_n) to approximate the continuous function at the grid points:

$$\Psi(x_i) \equiv \bar{\Psi}(x_i) = \sum_{n=0}^{N-1} a_n g_n(x_i) \tag{2.13}$$

where N is the size of the basis set. This is also known as the pseudospectral approximation. As described by Kosloff [202, 204, 198], the functional space in this method is viewed through a set of portholes, which is restricted to a local picture, and if the portholes are dense enough the full functional space is mapped on to the discrete space by interpolating the observed data by utilizing the continuous properties of the functional space. In matrix notation the above equation can be written as:

$$\Psi = \mathbf{Ga} \tag{2.14}$$

This is a set of coupled linear equations with $\Psi_i = \Psi(x_i)$ and $G_{ni} = g_n(x_i)$. The solution for the expansion coefficients for a set of linearly independent $g_n(x_i)$ becomes

$$\mathbf{a} = \mathbf{G}^{-1}\Psi \tag{2.15}$$

This is the general collocation scheme which provides a global mapping technique provided by the functional basis connected through the expansion coefficients, a_n, to the spatial grid. The scalar product of two functions on the functional space is given by

$$\langle \Psi(x)|\Phi(x)\rangle = \sum_{nm} S_{nm} a_n^* b_m \tag{2.16}$$

where S_{nm} is the overlap matrix given by

$$S_{nm} = \int_D dx\, g_n^*(x) g_m(x) \tag{2.17}$$

with

$$\Psi(x) = \sum_n a_n g_n(x) \tag{2.18}$$

and

$$\Phi(x) = \sum_m b_m g_m(x) \tag{2.19}$$

The collocation scheme (vide supra) becomes simplified when the functional basis is chosen from an orthonormal set. In this case

$$\sum_{n=0}^{N-1} g_n^*(x_i) g_n(x_j) = \delta_{ij} \tag{2.20}$$

Now left multiplying Eq. (2.13) by $g_n^*(x_i)$ and then summing over i results in:

$$a_n = \sum_i \Psi(x_i) g_n^*(x_i) \tag{2.21}$$

which shows that the coefficients a_n are the discrete functional transform of Ψ. Under this condition Eq. (2.17) becomes:

$$S_{nm} = \delta_{nm} \tag{2.22}$$

and Eq. (2.16)

$$
\begin{aligned}
\langle \Psi(x)|\Phi(x)\rangle &= \sum_n a_n^* b_n \\
&= \sum_{i=0}^{N-1} \Psi^*(x_i) \Phi(x_i)
\end{aligned}
\tag{2.23}
$$

The matrix **G** becomes unitary, and the Hilbert space becomes a discrete vector space with a unitary transformation between the discrete collocation points x_i and the discrete functional base a_n. A special case of this orthogonal collocation scheme is the Fourier method.

2.3.2 The Fourier Method

In the Fourier method the orthogonal functions $\{g_k(x)\}$ are chosen as the plane wave basis functions [64, 202, 204, 198]:

$$g_k(x) = e^{i2\pi kx/L}, \qquad k = -(N/2 - 1), ..., 0, ...N/2 \tag{2.24}$$

Expansion of a wave function in this basis is given by:

$$\Psi(x) \approx \sum_{k=-(N/2-1)}^{N/2} a_k e^{i2\pi kx/L} \tag{2.25}$$

which on inversion using the set of equidistant discrete sampling points $\{x_i\}$ gives the discrete Fourier expansion coefficients $\{a_k\}$, the amplitude of the wave function in the reciprocal k space:

$$a_k = \frac{1}{N} \sum_{i=1}^{N} \Psi(x_i) e^{-i2\pi kx_i/L} \tag{2.26}$$

The factor $\frac{1}{N}$ arises from the following orthogonality relations satisfied by the Fourier basis set:

$$\sum_{i=1}^{N} g_k(x_i) g_l^*(x_i) = \delta_{kl} N, \qquad |k - i| < N \tag{2.27}$$

Eqs. (2.25) and (2.26) constitute the discrete versions of the continuous Fourier transformation

$$\Psi(x) = \frac{1}{\sqrt{2\pi}} \int_{-\infty}^{\infty} \bar{\Psi}(k) e^{ikx} dk \tag{2.28}$$

and

$$\bar{\Psi}(k) = \frac{1}{\sqrt{2\pi}} \int_{-\infty}^{\infty} \Psi(x) e^{-ikx} dx \tag{2.29}$$

Operationally, one can switch back and forth between the two reciprocal discrete Hilbert spaces (position and momentum or the time and energy) through Fourier transformation. It has been shown [66] that in doing so the Hermitian properties of the operators and their commutation relations are preserved. The domain in which the transformation takes place has periodic boundary conditions.

The kinetic energy operator $\hat{T}$ $(=\frac{\hbar^2 k^2}{2m})$ is local in the momentum space and hence is diagonal in k. Therefore the $\hat{T}\Psi(x)$ operation is carried out by Fourier transforming (FT^+) $\Psi(x)$ to $\bar{\Psi}(k)$, followed by a multiplication by the kinetic energy spectral value at the discrete momentum grid points

$$\hat{T}\Psi(x) = \frac{\hbar^2 k^2}{2m}\bar{\Psi}(k) = \frac{\hbar^2 k^2}{2m}a_k \tag{2.30}$$

and then bringing it back to the coordinate space by an inverse Fourier transform (FT^-). The domain in which the transformation takes place requires the periodic boundary condition. The evaluation of the derivatives becomes exact for wave functions which obey this periodic boundary condition. The quantum mechanical commutation relations remain preserved for periodic potentials and functions under these potentials remain localized in the phase space box and the amplitude of the function becomes zero at the boundary of the box. For wave packets this boundary condition is met when they are band-limited functions with finite support [202]. The support of a function is defined by a set for which it has non-zero value. The wave functions are not usually band-limited with finite support since they can not be confined in both coordinate and momentum spaces. Wave packets which are semilocalised wave functions satisfy this requirement. The use of absorbing boundaries also forces wave packets to meet this requirement by reducing their amplitude to zero at the boundaries. Another important aspect which has made the Fourier transform an attractive tool in molecular dynamics is the availability of the fast Fourier transform (FFT) algorithm resulting from the work of Cooley and Tukey in the mid '60s [205] and others [206, 207] and the fact that it could be adapted to the vector and parallel computer

architectures in more recent times [208] The FFT algorithm scales with N as $O(NlogN)$.

It is shown by Kosloff [66] that the numerical dispersion in the FFT scheme is much less than that in the case of the FD scheme. The kinetic energy operator in the latter scheme, on Fourier transformation to the k-space gives [202]

$$
\begin{aligned}
T_{FD}(k) &= -\frac{\hbar^2}{2m}\frac{2(\cos(k\,\triangle\,x)-1)}{(\triangle x)^2} \\
&= \frac{\hbar^2}{2m}\left[\frac{2\sin(k\,\triangle\,x/2)}{\triangle x}\right]^2
\end{aligned}
\tag{2.31}
$$

The FD spectrum obtained from the use of the above equation deviates considerably from the Fourier spectrum as k increases. The deviation is shown [202] to be comparatively less in the case of higher order FD spectra. Kosloff [202] argues that acceptable accuracy can be obtained by using at least ten points per wave period in the FD method. This means that one has to use ten points per unit volume in phase space. Moreover, as mentioned above, the semi-local approximation in the FD scheme does not preserve the commutation relations of quantum mechanics. The FD algorithm scales as $O(N^2)$ which is inefficient for higher dimensional problems. All these factors established the superiority of the FFT scheme over the FD scheme.

2.3.3 The Hankel Transform

The fast Hankel transformation (FHT) algorithm was outlined by Siegman [209] and also by Talman [210]. Bisseling and Kosloff [70] introduced the FHT in molecular dynamics in the context of treating the radial part of the Laplacian operator in polar coordinates. The Hankel transformation of order n of a function F, from the r space to the corresponding reciprocal k space in the interval $[0, \infty]$ is defined by:

$$
F(k) = \int_0^\infty rF(r)J_n(kr)dr, \qquad k > 0
\tag{2.32}
$$

where J_n's are the nth order Bessel functions of the first kind. This is also recognised in the literature as the Fourier-Bessel transformation. Operationally, FHT is performed through

a logarithmic change of variables [209, 210], which substitutes $r = r_0 e^{-y}$ and $k = k_0 e^x$ in the above equation and results in:

$$F(k_0 e^x) = r_0^2 \int_{-\infty}^{\infty} e^{-2y} F(r_0 e^{-y}) J_n(r_0 k_0 e^{x-y}) dy \qquad (2.33)$$

In the discrete Hilbert space F is sampled at N (chosen in powers of two) uniformly spaced (Δ) discrete grid points ($x = i\Delta, y = m\Delta; i, m = 0, ..., N-1$) and the above integral is evaluated as a discrete sum:

$$F(k_0 e^{i\Delta r}) \approx r_0^2 \Delta \sum_{m=0}^{N-1} e^{-2m\Delta} F(r_0 e^{-m\Delta}) J_n(r_0 k_0 e^{(i-m)\Delta}) \qquad (2.34)$$

The right hand side of the above equation represents a convolution of two functions, which is carried out using the convolution theorem: "the Fourier transform of the convolution of two functions is equal to the product of their Fourier transforms" [211]. The evaluation of the continuous (non-circular) convolution by the discrete (circular) Fourier transformation is done by padding the values of F with N zeroes by setting:

$$b_m = \begin{cases} 0 & \text{for } m = -N, ..., -1 \\ e^{-2m\Delta} F(r_0 e^{-m\Delta}) & \text{for } m = 0, ...N-1 \end{cases} \qquad (2.35)$$

and

$$c_i = r_0^2 \, \Delta \, J_n(r_0 k_0 e^{i\Delta}) \ \ \text{for } i = -N, ..., N-1 \qquad (2.36)$$

This changes Eq. (2.34) into a $2N$- term discrete circular convolution

$$a_i = \sum_{m=0}^{N-1} b_m c_{i-m} \ \ \text{for } i = -N, ..., N-1 \qquad (2.37)$$

The $2N$-point FFTs are separately performed on b and c and the results are multiplied and an inverse FFT is performed on the product. The first N values of the result are ignored and the remaining N values of $a_i = F(k_0 e^{i\Delta})$ for $i = 0, ..., N-1$ are the approximated values of the Hankel transform of F.

Both real and complex functions can be evaluated by this method. The parameter $r_0 = r_{max}$ is the maximum value of r and $k_0 = k_{min}$ is the minimum value of k. The other

parameters are chosen such that the domains of $r(r_{min}, r_{max})$ and $k(k_{min}, k_{max})$ contain the function F. The sampling points in the discrete space are chosen such that one point falls in between two zeroes of the Bessel function J_n which occur at a separation of π. This leads to:

$$|r_0 k_0 (e^{(N-1)\Delta} - e^{(N-2)\Delta})| < \pi \qquad (2.38)$$

or approximately

$$r_0 k_0 e^{(N-1)\Delta} \Delta < \pi \qquad (2.39)$$

or

$$r_{max} k_{max} \Delta < \pi \qquad (2.40)$$

where $k_{max} = k_0(e^{(N-1)\Delta})$. The above restriction provides a criterion for choosing Δ. It is suggested by Bisseling and Kosloff [70] that the distance between two sampling points of $F(= e^{-m\Delta} - e^{-(m+1)\Delta})$ should be less than the minimum distance between two successive zeroes of $F(= \pi/k_{max})$ represented on the logarithmic grid. This ensures a sufficiently dense sampling for F.

The operator $\left[\frac{1}{r}\frac{\partial}{\partial r} r \frac{\partial}{\partial r} - \frac{n^2}{r^2}\right]$ is evaluated by performing FHT of order n followed by multiplying the result by $-k^2$ and again performing the nth order FHT. The FHT is its own inverse. An FHT of orde zero is performed for operators which do not contain terms like $\frac{n^2}{r^2}$.

The FHT method is prescribed for systems with a radially symmetric potential. For such systems the dimensionality of the problem can be reduced by switching over to the polar coordinates. The extra computation involved in the irrelevant portion of the grid (which has no value from the dynamical point of view) in Cartesian coordinates is reduced in polar coordinates. The method has been applied by Bisseling and Kosloff [70] to compute the energy eigenvalues of 2D and 3D harmonic oscillators and also for studying H + H$_2$ reactive collisions. Their estimates show that both FFT and FHT methods are of comparable accuracy. However, the CPU time is estimated to be less in case of the FFT

and it is expected that FHT will be faster for systems with a small skewing angle and where the coupling between the radial and the angular part is weak. It must be added that the FHT algorithm scales with N as $NlogN$.

2.3.4 The Discrete Variable Representation

The discrete variable representation (DVR) is another example of the orthogonal collocation method which uses specific functions and points. The method uses an orthogonal transformation between the DVR and the finite basis representation (FBR) and vice versa. In this transformation the Hermitian property of the operators is preserved. The DVR is basis localized at the discrete eigenvalues of the coordinate operator, whereas the FBR is the basis consisting of N square-integrable functions of the continuous coordinates. The latter is also known as the spectral representation. The method which utilizes a different representation of the wave function is called the pseudospectral method. Both the Fourier and the DVR are methods based on the evaluation of operators in their respective local representations. The DVR was originally developed by Harris et al [212] to evaluate the potential matrix elements in the harmonic oscillator basis (the Gauss-Hermite points) by using the DVR-FBR transformation. Subsequently, Dickinson and Certain [213] showed that classical orthogonal polynomial basis functions, (e.g. Hermite polynomials) correspond to Gaussian quadrature and an orthogonal transformation exists between the two representations; N quadrature points and N basis functions. Light and coworkers [68] developed the DVR in the context of scattering studies. Independently, Shizgal and Blackmore [214] developed DVR under the name of discrete ordinate method. Although initial interest in the DVR was to describe the internal degrees of freedom in the scattering problems, it has been extended to a wide variety of other problems now. The method is also found to be quite advantageous for multidimensional problems.

As was pointed out earlier, the DVR utilizes the idea behind the pseudospectral or

collocation method of using a mixed representation of the function $\Psi(x)$. If a grid representation of $\Psi(x)$, $\{\Psi(x_i), i = 1, ..., N\}$ is used then the action of any local operator $(\hat{A})$ on it is evaluated by multiplying its value $A(x_i)$ at the grid point with the corresponding value of the function $\Psi(x_i)$ at that point. On the other hand, the action of a non-local operator $(\hat{B})$ is evaluated in the finite basis set representation $\{\phi_n(x)\}$ where the operator $\hat{B}$ is local by switching from the grid based representation to the basis set representation. It is shown by Dickinson and Certain [213] that an isomorphic transformation exists when the transformation matrix is unitary. This is achieved by using the orthonormal (L^2) basis set of some classical polynomials for $\{\phi_n(x_\alpha)\}$ defined on a set of discrete quadrature points $(x_\alpha, \alpha = 1, ..., N)$ with the associated weights w_α. One can, in this discrete representation, write:

$$\langle \phi_n | x_\alpha \rangle = \phi_n^*(x_\alpha) \tag{2.41}$$

In pseudospectral approximation, $\Psi(x)$ can be represented as in Eq. (2.13) through [215]:

$$\Psi(x) = \sum_n c_n \phi_n(x) \tag{2.42}$$

The orthonormal property of $\phi_n(x)$ is utilized to evaluate c_n through

$$c_n = \int_D \phi_n^*(x) \Psi(x) dx \tag{2.43}$$

If the sampling points are chosen as the zeroes of the $\phi_{N+1}(x)$ polynomials then the theory of Gaussian integration enables us to write the orthonormality condition of $\phi_n(x)$ at the quadrature points as

$$\sum_\alpha w_\alpha \phi_n^*(x_\alpha) \phi_m(x_\alpha) = \delta_{nm} \tag{2.44}$$

This is used to write the inverted collocation relation at the N discrete quadrature points as

$$c_n = \sum_\alpha w_\alpha \phi_n^*(x_\alpha) \Psi(x_\alpha) \tag{2.45}$$

using which $\Psi(x)$ can be evaluated at the quadrature points through

$$
\begin{aligned}
\Psi(x) &= \sum_n \sum_\alpha w_\alpha \phi_n^*(x_\alpha) \Psi(x_\alpha) \phi_n(x) \\
&= \sum_\alpha \Psi_\alpha \delta_\alpha(x)
\end{aligned}
\tag{2.46}
$$

where

$$
\begin{aligned}
\delta_\alpha(x) &= \sqrt{w_\alpha} \sum_\alpha \phi_n^*(x_\alpha) \phi_n(x) \\
&= \sum_n T_{n\alpha}^\dagger \phi_n(x)
\end{aligned}
\tag{2.47}
$$

$T_{n\alpha}^\dagger$ is the transformation matrix from the N dimensional spectral representation (FBR) to the N dimensional quadrature representation of the discrete Hilbert space (DVR):

$$
T_{n\alpha}^\dagger = \sqrt{w_\alpha} \phi_n^*(x_\alpha)
\tag{2.48}
$$

The orthonormality condition mentioned above in Eq. (2.44) can be rearranged to show that T is column orthogonal $[(T^\dagger T)_{nm} = S_{nm} = \delta_{nm}]$. In the discrete representation the overlap matrix is given by [215]

$$
\begin{aligned}
\Delta_{\alpha\beta} &= \langle \alpha | \beta \rangle \\
&= \int_D \delta_\alpha^*(x) \delta_\beta(x) dx \\
&= \sum_n \sqrt{w_\alpha} \phi_n(x_\alpha) \sqrt{w_\beta} \phi_n^*(x_\beta) \\
&= (TT^\dagger)_{\alpha\beta}
\end{aligned}
\tag{2.49}
$$

which follows from the orthonormality of the spectral basis. Since T is column orthogonal, the above overlap matrix Δ is idempotent $[\Delta^2 = \Delta]$ and it will have elements either zero or one. Moreover, $tr(T^\dagger T) = N$, the number of basis functions and $\Delta = T^\dagger T$ will have N eigenvalues equal to one, and therefore is an identity matrix. Hence, $T_{n\alpha}^\dagger$ is orthonormal and unitary $(T^\dagger T = TT^\dagger = 1)$. Therefore T corresponds to the transformation matrix from the DVR to the FBR. $\{\delta_\alpha(x)\}$ are the spectral basis functions rotated by the unitary

transformation matrix dependent on the continuous variable x, and are the basis functions mapped onto the discrete Hilbert space. These are discrete analogs of the Dirac delta functions and hence are the eigenfunctions of the coordinate operator with eigenvalues equal to the quadrature points, x_α

$$\begin{aligned}
\langle\alpha|\hat{x}|\beta\rangle &= \int \delta_\alpha^*(x)\hat{x}\delta_\beta(x)dx \\
&= \sum_\zeta w_\zeta \delta_\alpha^*(x_\zeta)x_\zeta\delta_\beta(x_\zeta) \\
&= x_\alpha\delta_{\alpha\beta}
\end{aligned} \tag{2.50}$$

If the potential matrix is diagonal in the DVR, then its elements at the discrete points are given by

$$\langle\alpha|\hat{V}^{DVR}|\beta\rangle = V_{\alpha\beta} = V(x_\alpha)\delta_{\alpha\beta} \tag{2.51}$$

The DVR of the Hamiltonian can be constructed as

$$\begin{aligned}
\langle\alpha|\hat{H}^{DVR}|\beta\rangle &= \langle\alpha|\hat{T}^{DVR}|\beta\rangle + \langle\alpha|\hat{V}^{DVR}|\beta\rangle \\
&= \sum_{nm} \mathbf{T}_{n\alpha}^\dagger \hat{T}^{FBR}\mathbf{T}_{\beta m} + V_{\alpha\beta} \\
&= (\mathbf{T}^\dagger T^{FBR}\mathbf{T})_{\alpha\beta} + V_{\alpha\beta}
\end{aligned} \tag{2.52}$$

Whitnell et al [216, 217] constructed the DVR in manydimensions as a direct product of one dimensional DVRs by successive diagonalization, truncation and recoupling [218]. This becomes particularly simple when an orthogonal coordinate system is used, in which case the Hamiltonian does not contain mixed derivatives.

$$\begin{aligned}
\langle\alpha'\beta'\gamma'|\hat{H}^{DVR}|\alpha\beta\gamma\rangle &= K_{\alpha'\alpha}\delta_{\beta'\beta}\delta_{\gamma'\gamma} + K_{\beta'\beta}\delta_{\alpha'\alpha}\delta_{\gamma'\gamma} + K_{\gamma'\gamma}\delta_{\alpha'\alpha}\delta_{\beta'\beta} \\
&\quad + V(x_\alpha, y_\beta, z_\gamma)\delta_{\alpha'\alpha}\delta_{\beta'\beta}\delta_{\gamma'\gamma}
\end{aligned} \tag{2.53}$$

where the kinetic energy matrices all have the form

$$K = \mathbf{T}^\dagger T^{FBR}\mathbf{T} \tag{2.54}$$

In higher dimensions the matrix multiplication will have an N^2 scaling relation, where N is the dimensionality. This is to be contrasted with the $NlogN$ scaling relation found for FFT. Colbert and Miller [219] have shown the $NlogN$ scaling can be achieved in multi-dimensional DVR by using Cartesian coordinates without requiring any faster algorithm. Their argument was that in Cartesian cordinates the DVR of the kinetic energy operator is sparse, i.e, it can be written as a sum of one dimensional kinetic energy operators. Corey et al [215] have pointed out subsequently that even a non-Cartesian coordinate representation of the Hamiltonian matrix leads to an $NlogN$ scaling relation. Their argument is that the scaling relation is a result of neither the separability of the kinetic energy operator nor the sparseness of the Hamiltonian matrix, but due to the fact that any multi-dimensional Hamiltonian can be written as a sum of products of functions of the local (coordinate) operators and two derivative operators which are nonlocal only in a single coordinate. Bramley et al [220] have pointed out that any multidimensional operator is factorizable if all its off-diagonal terms couple to a single coordinate.

A wide variety of classical polynomials, viz., Jacobi, Legendre, Laguerre and Hermite polynomials are used as the finite basis set. The grid is defined by the Gaussian quadrature points and the discrete inner products in the FBR are evaluated. It has been pointed out by Light and coworkers [68] that the choice of quadrature points which are the zeroes of the $(N+1)$th term of the orthogonal polynomial eliminates the contamination of the numerical quadrature from the non-orthogonal components of the projected function which lies outside the Hilbert space. They have also defined a unitary transformation between the FBR and an arbitrary set of coordinates. There are examples of many other DVRs. For example, Muckerman [221] has constructed the DVR basis functions which satisfy the Kroenecker delta condition for a general quadrature consisting of a set of N points and weights. He has shown that by employing the Fourier basis set a periodic DVR results and leads to the equally sampled points of the Gauss-Chebyshev quadrature. Manolopoulos et

al [222] used a Lobatto shape quadrature and Lobatto shape functions. They defined a DVR basis, which satisfies the Kroenecker delta relation by

$$\Theta_i(x) = \prod_{j=0}^{N+1} (x - x_j)/(x_i - x_j), \qquad (i, j = 0, ..., N-1, j \neq i) \qquad (2.55)$$

The advantage of this DVR is that the end points of the coordinates can be included explicitly with appropriate boundary conditions. Shapiro and coworkers [223] and Clary [224] have proposed a DVR that is generated by diagonalizing the coordinate operator. However, the basis functions are not polynomials and the DVR does not correspond to a Gaussian quadrature. The DVR basis functions also do not satisfy the Kroenecker delta relation. Colbert and Miller [219] proposed a novel basis free DVR. It consists of an infinite number of equally spaced points from which one extracts the finite subset desired. The kinetic energy operator in this method is defined either in the infinite range and approximated by an infinite order finite difference approximation leading to the normal Chebyshev DVR or as the finite limit of the particle-in-a-box functions or Chebyshev polynomials. Unfortunately, the finite range definition in their scheme faces normalization problems.

The FFT scheme is numerically inefficient in solving the TDSE in the polar coordinate. This is because the kinetic energy operator in the polar angle θ contains a $(1/\sin^2\theta)$ term which leads to singularity in the discrete angle space for $\theta = 0$ and π. One can deal with this situation either by performing a discrete cosine transform or by using a DVR.

The rotational kinetic energy operator is given by [225]

$$\hat{T}_{rot} = -\frac{\hbar^2}{2I} \left[\frac{1}{\sin\theta} \frac{\partial}{\partial\theta} \sin\theta \frac{\partial}{\partial\theta} - \frac{m^2}{\sin^2\theta} \right] \qquad (2.56)$$

The discrete cosine transform was proposed by Dixon [226] in which the singularities at $\theta = 0$ and π are avoided by sampling θ at a half integral regular mesh of points between 0 and π. The Fourier amplitudes $F(j)$ in the angular momentum space are then computed by performing a discrete quarter-wave Fourier transform [227].

This situation is dealt with in the DVR by performing the kinetic energy operation in the angular momentum space (FBR). In this case the DVR points are chosen as the abscissa points in Gauss-Legendre quadrature, with associated weights w_α. The FBR is defined in terms of the normalized associated Legendre polynomials, $\Theta_{jm}(\chi_\alpha)$, of degree $|j - m|$. These functions are orthonormal in the interval $[-1, 1]$ and the orthonormality condition is given by

$$\int_{-1}^{1} \Theta_{j'm}(\chi_\alpha)\Theta_{jm}(\chi_\alpha) = \int_{-1}^{1} (1 - \chi_\alpha^2)^{|m|} P_{j'm}(\chi_\alpha) P_{jm}(\chi_\alpha) d\chi_\alpha = \delta_{j'j} \tag{2.57}$$

where $\chi_\alpha = \cos\theta_\alpha$ and $(1 - \chi_\alpha^2)^{|m|} = w_\alpha$. $\hat{T}_{rot}$, is diagonal in this basis and it results in:

$$\hat{T}_{rot}\Theta_{jm}(\chi_\alpha) = \frac{j(j+1)\hbar^2}{2I}\Theta_{jm}(\chi_\alpha) \tag{2.58}$$

The treatment of the angular coordinate in the DVR representation is described in detail by Leforestier [73, 228] and also by Corey and Lemoine [229]. These authors have formulated the scheme utilizing the generalised DVR formulation of Light and coworkers [68]. Their method has been adapted by Balint-Kurti and coworkers [230] for studying the photodissociation of HOCl and also for computing the state-to-state cross sections for 3D (Li,FH) reactive collisions [231]. The method uses the same θ grid for the different m components of the wave function. The unitary transformation matrix from the DVR to FBR is given by

$$\mathbf{T}_{j\alpha}^m = \sqrt{w_\alpha}\Theta_{jm}(\chi_\alpha) \tag{2.59}$$

The grid wave function is defined as

$$\Psi^m(\theta_\alpha) = \sqrt{w_\alpha}\psi^m(\theta_\alpha) \tag{2.60}$$

and $\hat{T}_{rot}\Psi^m(\theta_\alpha)$ is evaluated at the discrete grid point θ_α by

$$\hat{T}_{rot}\Psi^m(\theta_\alpha) = \sum_{j=|m|}^{j_{max}} \mathbf{T}_{j\alpha}^m {}^\dagger \frac{j(j+1)\hbar^2}{2I}\mathbf{T}_{j\alpha}^m \Psi^m(\theta_\alpha) \tag{2.61}$$

where $\Psi^m(\theta_\alpha)$ in the DVR is mapped onto the FBR through the transformation matrix $\mathbf{T}_{j\alpha}^m$ and multiplied by the diagonal matrix elements of $\hat{T}_{rot}$, $\frac{j(j+1)\hbar^2}{2I}$, and then transformed back to the DVR through $\mathbf{T}_{j\alpha}^m{}^\dagger$, the Hermitian conjugate of $\mathbf{T}_{j\alpha}^m$. The number of angular basis functions $j_{max} = (N_\theta - 1)$ where N_θ is the number of grid points along θ for each m is found to give good performance although different authors have used different numbers of angular basis functions.

2.4   The Time Evolution of the Wave Packet

2.4.1   The Time Evolution Operator

The solution of the TDSE is given by

$$\Psi(t) = \hat{P}\, exp\left[-i/\hbar \int_0^T \hat{H}(t')dt'\right]\Psi(0) \tag{2.62}$$

where $\Psi(0)$ is the initial wave function and $\Psi(t)$ is the wave function at time t and $\hat{P}$ is the time ordering operator [232]. For an explicitly time-independent Hamiltonian the above equation simplifies to:

$$\Psi(t) = e^{-i\hat{H}t/\hbar}\Psi(0) \tag{2.63}$$

The exponential operator in the r.h.s. of the above equation forms a continuous dynamical group where time t is a parameter, and is known as the (time) evolution operator denoted by $\hat{U}(t, t_0)$. For $t_0 = 0$,

$$\hat{U}(t, t_0) = e^{-i\hat{H}t/\hbar} \tag{2.64}$$

In actual computation, t is sliced in smaller steps of length, $\triangle t$, and the entire time evolution is accomplished through:

$$\hat{U}(t) = \prod_{n=0}^{N_t - 1} \hat{U}[(n+1)\triangle t, n\triangle t] \tag{2.65}$$

where N_t is the total number of time steps and $\triangle t = t/N_t$. $\hat{U}(t, t_0)$ is a linear operator and is unitary:

$$\hat{U}\hat{U}^\dagger = \hat{U}^\dagger\hat{U} = 1 \tag{2.66}$$

The exponential operator is approximated in various ways. For example, by the second order differencing (SOD) scheme, the split operator (SO) method, the Chebyshev polynomial (CP) scheme or the short iterative Lanczos (SIL) scheme. Each of these schemes is briefly reviewed below and special attention will be paid to the stability of these schemes in the presence of a negative imaginary potential (NIP).

2.4.2   The Second Order Differencing (SOD) Scheme

The time evolution operator and its adjoint for a time step of length $(\triangle t)$ can be written as:

$$\hat{U}(\triangle t) = e^{-i\hat{H}\triangle t/\hbar}$$
$$\hat{U}^{\dagger}(\triangle t) = e^{i\hat{H}\triangle t/\hbar} \tag{2.67}$$

Therefore,

$$\Psi(t + \triangle t) = \hat{U}(\triangle t)\Psi(t) \tag{2.68}$$

$$\Psi(t - \triangle t) = \hat{U}^{\dagger}(\triangle t)\Psi(t) \tag{2.69}$$

Using the above equations one can write

$$\Psi(t + \triangle t) - \Psi(t - \triangle t) = (e^{-i\hat{H}\triangle t/\hbar} - e^{i\hat{H}\triangle t/\hbar})\Psi(t) \tag{2.70}$$

Expanding the exponential terms in the above equation in Taylor series and keeping only the terms up to first order in $\triangle t$, the equation becomes

$$\Psi(t + \triangle t) = \Psi(t - \triangle t) - \frac{2i\hat{H}\triangle t}{\hbar}\Psi(t) \tag{2.71}$$

Thus the SOD scheme [61, 66] evaluates $\Psi(t + \triangle t)$ from its values at time t and $t - \triangle t$. Computationally, to initialize the iteration process, the value of Ψ at the first step is computed either by a fourth order Runge-Kutta scheme or by a higher order Taylor series

expansion of $\hat{U}(\Delta t)$. The above equation can also be written as:

$$
\begin{aligned}
\Psi(t + \Delta t) &= e^{i\hat{H}\Delta t/\hbar}\Psi(t) - \frac{2i\hat{H}\,\triangle t}{\hbar}\Psi(t) \\
&= Q\Psi(t)
\end{aligned}
\tag{2.72}
$$

The scheme will be unitary if $QQ^{\dagger} = Q^{\dagger}Q = 1$. From the above it follows that

$$
\begin{aligned}
QQ^{\dagger} &= \left[e^{i\hat{H}\Delta t/\hbar} - \frac{2i\hat{H}\,\triangle t}{\hbar}\right]\left[e^{-i\hat{H}\Delta t/\hbar} + \frac{2i\hat{H}\,\triangle t}{\hbar}\right] \\
&= 1 - 4\left(\frac{\Delta t\hat{H}}{\hbar}\right)\sin\left(\frac{\Delta t\hat{H}}{\hbar}\right) + 4\left(\frac{\Delta t\hat{H}}{\hbar}\right)^2 \\
&= 1 + (4/6)\frac{\Delta t^4 \hat{H}^4}{\hbar^4}
\end{aligned}
\tag{2.73}
$$

neglecting higher order terms in the expansion of the sine function. The conservation of the norm can be checked through:

$$
\begin{aligned}
<\Psi(t + \Delta t)|\Psi(t + \Delta t)> &= <Q\Psi(t)|Q\Psi(t)> \\
&= <\Psi(t)|Q^{\dagger}Q|\Psi(t)> \\
&= <\Psi(t)|\Psi(t)> + (2/3)(\Delta t)^4 <\hat{H}^2\Psi(t)|\hat{H}^2\Psi(t)>
\end{aligned}
\tag{2.74}
$$

Therefore it becomes clear that by choosing Δt sufficiently small the unitarity can be maintained throughout the time evolution. It can be shown that [66] the algorithm is stable if $\Delta t << \hbar/E_{max}$; where $E_{max}(= T_{max} + V_{max})$ is the maximum total energy represented on the grid. In practice, a choice of $\Delta t < \hbar/5E_{max}$ is found to give good results [66].

Since the Hamiltonian for the present case commutes with itself, $\left[Q, \hat{H}\right]\Psi = 0$ and energy is conserved throughout the time evolution.

If a negative imaginary potential ($\Gamma = -iV_0$) is added to the real potential of the system, the Hamiltonian becomes complex ($\hat{H}' = \hat{H} + \Gamma$) and Q' can be written as

$$
Q' = e^{i\Delta t(\hat{H} - iV_0)/\hbar} - \frac{2i\Delta t(\hat{H} - iV_0)}{\hbar}
\tag{2.75}
$$

Multiplying the above by $Q'^{\dagger}$ and expanding the exponential terms in the Taylor series and finally rearranging the equation, one obtains:

$$Q'Q'^{\dagger} = e^{2V_0\Delta t/\hbar} - 4(\frac{V_0\Delta t}{\hbar}) \tag{2.76}$$

Hence,

$$< \Psi(t+\Delta t)|\Psi(t+\Delta t) > = \left[e^{2V_0\Delta t/\hbar} - 4(\frac{\Delta t V_0}{\hbar})\right] < \Psi(t)|\Psi(t) > \tag{2.77}$$

It is clear that the error in the norm would grow exponentially. It is worth mentioning here that the use of a NIP shifts the eigenvalue spectrum to the complex plane and methods which are conditionally stable, and which depend on the eigenvalue spectrum become unstable under such conditions.

2.4.3 The Split Operator (SO) Method

In the application of the evolution operator, there is an error arising from the fact that the kinetic and potential energy operators do not commute. However, by splitting the time evolution operator symmetrically the commutator error is of third order only. Such an approach is known as the second order SO scheme [64]. It can be either potential referenced or kinetic referenced [76]. The potential referenced SO scheme is given by:

$$e^{-i\hat{H}\Delta t/\hbar} = e^{-i\hat{T}\Delta t/2\hbar}e^{-i\hat{V}\Delta t/\hbar}e^{-i\hat{T}\Delta t/2\hbar} + O(\Delta t^3) \tag{2.78}$$

In the kinetic referenced SO scheme the exponetial containing the potential energy operator is symmetrically split and that containing the kinetic energy operator is sandwiched in between. The time evolution of the wave function in the potential referenced scheme is given by

$$\begin{aligned} \Psi(t+\Delta t) &= e^{-i\hat{T}\Delta t/2\hbar}e^{-i\hat{V}\Delta t/\hbar}e^{-i\hat{T}\Delta t/2\hbar}\Psi(t) \\ &= Q\Psi(t) \end{aligned} \tag{2.79}$$

and

$$QQ^\dagger = e^{-i\hat{T}\triangle t/2\hbar}e^{-i\hat{V}\triangle t/\hbar}e^{-i\hat{T}\triangle t/2\hbar} \times e^{i\hat{T}\triangle t/2\hbar}e^{i\hat{V}\triangle t/\hbar}e^{i\hat{T}\triangle t/2\hbar}$$

$$= 1 \tag{2.80}$$

Hence the scheme is unitary, and the norm of the wave function is conserved. However, because of the non-commutability of the kinetic and the potential energy operators the scheme does not conserve energy. The scheme is unconditionally stable and it does not depend on the kinetic energy spectrum of the grid. However, the time step is selected based on the maximum value of the potential energy on the grid. Good results are obtained when

$$\triangle t < \pi/(3\triangle V_{max}) \tag{2.81}$$

where $\triangle V_{max}(= V_{max} - V_{min})$ is the maximum excursion of the potential. This step size is chosen as to accommodate the entire energy level spectrum of the system under investigation [65].

In the presence of a NIP, Q' becomes:

$$Q' = e^{-i\hat{T}\triangle t/2\hbar}e^{-i\hat{V}\triangle t/\hbar}e^{-V_0\triangle t/\hbar}e^{-i\hat{T}\triangle t/2\hbar} \tag{2.82}$$

The unitarity relation now becomes

$$Q'Q'^{\dagger} = e^{i\hat{T}\triangle t/2\hbar}e^{-2V_0\triangle t/\hbar}e^{-i\hat{T}\triangle t/2\hbar} \tag{2.83}$$

In the absence of commutation errors the last two terms can be interchanged and the norm of the wave function at time $t + \triangle t$ becomes:

$$\langle\Psi(t+\triangle t)|\Psi(t+\triangle t)\rangle = \langle\Psi(t)|Q'^{\dagger}Q'|\Psi(t)\rangle$$

$$= e^{-2V_0\triangle t/\hbar}\langle\Psi(t)|\Psi(t)\rangle \tag{2.84}$$

It is clear that the norm decreases exponentially with increase in $\triangle t$ and energy is no longer conserved.

2.4.4   The Chebyshev Polynomial (CP) Scheme

Chebyshev polynomials are found to be superior to many other polynomials and are optimal for a scalar function $F(x)$ bounded in the interval $[-1, 1]$. So, a scalar function like e^{ax} can be expressed in terms of these polynomials in the interval $-1 \leq x \leq 1$ as

$$e^{ax} = \sum_{n=0}^{\infty} (2 - \delta_{n0}) J_n(\alpha) T_n(x) \tag{2.85}$$

where δ_{n0} is the Kroenecker delta and $\alpha = \Delta E \Delta t / 2\hbar$. $J_n(\alpha)$ are the modified Bessel functions of order n. $T_n(x)$ are the Chebyshev polynomials of order n, calculated using the recursion relation [233]

$$T_{n+1}(x) = 2x T_n(x) - T_{n-1}(x) \tag{2.86}$$

with $T_0(x) = 1$ and $T_1(x) = x$.

The evolution operator is a function of an operator. It can be shown (see Appendix 1) that a function of an operator can be expressed as a function of a scalar in the *complete basis* of the operator. So, the function of the operator can be approximated in the Chebyshev series, provided the domain of the operator is confined to the interval $[-1, 1]$ in which the Chebyshev polynomials are optimal. In case of a Hamiltonian which is self-adjoint, the eigenvalues lie on a real axis, and they can be positioned from -1 to 1 by renormalizing the Hamiltonian as follows:

$$\hat{H}_{norm} = 2 \frac{\hat{H} - \hat{I}\bar{H}}{\Delta E} \tag{2.87}$$

where $\bar{H} = (E_{max} + E_{min})/2$ and $\Delta E = (E_{max} - E_{min})$. E_{max} and E_{min} have been defined earlier. In terms of this renormalized Hamiltonian, $\hat{H}_{norm}$, the evolution operator can be written as:

$$e^{-i\hat{H}\Delta t/\hbar} = e^{-i\bar{H}\Delta t/\hbar} e^{-i\alpha \hat{H}_{norm}} \tag{2.88}$$

The first term in the above expression is the phase shift due to the shift of the energy

scale. The second term is approximated by the Chebyshev series as [69, 191, 196]

$$e^{-i\alpha\hat{H}_{norm}} = \sum_{n=0}^{\infty}(2 - \delta_{n0})J_n(\alpha)\Phi_n(-i\hat{H}_{norm})$$
(2.89)

where $\Phi_n(-i\hat{H}_{norm})$ are the complex Chebyshev polynomials of order n satisfying the recursion relation:

$$\Phi_{n+1} = -2i\hat{H}_{norm}\Phi_n + \Phi_{n-1}$$
(2.90)

where $\Phi_0 = 1$ and $\Phi_1 = -iH_{norm}$. Therefore, the evolution of $\Psi(t)$ in this scheme on a discrete grid is given by:

$$\Psi(t + \Delta t) = e^{-i\bar{H}\Delta t/\hbar}\sum_{n=0}^{N}(2 - \delta_{n0})J_n(\alpha)\Phi_n(-i\hat{H}_{norm})\Psi(t)$$
(2.91)

The number of terms to be used in the above expansion is estimated from the time - energy phase space volume α. In practice the number of terms used is slightly larger than this estimate for a good convergence. Since the evolution operator is expanded in a series of polynomials in the Chebyshev method by definition the scheme is not unitary. The deviation from the unitarity corresponds to the remainder term in the expansion. This deviation is used as an accuracy check of the scheme. The errors are uniformly distributed in the bounded interval [191, 196]. Since Bessel functions show exponential convergence for $n > \alpha$, the error is usually very small.

The instability of the CP scheme in presence of a NIP was first noticed by Mowrey [234, 185]. It has been realised subsequently [235, 196, 236, 237] that the instability of the scheme is caused by the NIP. The main point to note here is that the Hamiltonian ceases to be Hermitian once the NIP is introduced. The eigenvalue spectrum of the Hamiltonian shifts to the complex energy plane and the renormalization of the Hamiltonian introduced above becomes invalid.

Kosloff and coworkers [238, 196] have proposed the Newton interpolating polynomials in which the interpolation points are predetermined on a boundary curve which encloses

the spectrum of the Hamiltonian. This is done by conformal mapping. For a Hermitian Hamiltonian the interpolation points become the zeroes of the Chebyshev polynomial, which is not the case for a non-Hermitian Hamiltonian. Huang et al [235] proposed the use of generalized Faber polynomials of which Chebyshev polynomials constitute a special case. The latter are generated by a one-to-one conformal mapping of the exterior of a disk to the exterior of a simple closed curve, L_γ. In case of the Chebyshev polynomials, L_γ becomes an ellipse. The renormalization of the Hamiltonian is done in a way as to account for the shift of its eigenvalue spectrum to the complex plane in the non-Hermitian case. These authors used the renormalization

$$\hat{H}_{norm} = 2\frac{\hat{H} - \hat{I}\bar{H}}{2\gamma} \tag{2.92}$$

where $2\gamma \geq \triangle E$. The eigenvalues of $\hat{H}_{norm}$ are no longer bounded by one but are mapped conformally from a unit disk. 2γ equals the sum of the major and the minor axis. $\bar{H}$ in Eq. (2.92) is given by

$$\bar{H} = 1/2\left[E_{max} + E_{min}\right] - iV_0 \tag{2.93}$$

The evolution operator becomes

$$e^{-i\hat{H}t/\hbar} = e^{-i\bar{H}t/\hbar}\sum_{n=0}^{N}(-i)^n(2 - \delta_{n0})J_n(\triangle Et/\hbar)T_n(\hat{H}_{norm}) \tag{2.94}$$

Mandelstham et al [236] have made a simple analytic continuation of the Chebyshev polynomials while keeping their properties unaltered. Their method preserves the renormalization step as in the case of the Hermitian Hamiltonian in presence of the NIP. They have derived an expression for the time evolution operator as:

$$\hat{U}(t) = \sum_{n=0}^{N} a_n(t)Q_n(\hat{H}_{norm}; \hat{\gamma}) \tag{2.95}$$

where $a_n(t) = \left[(2 - \delta_{n0})e^{-i\bar{H}t/\hbar}(-1)^n J_n(\triangle Et/\hbar)\right]$ and $Q_n(\hat{H}_{norm}, \hat{\gamma})$ are the analytic continuation of the Chebyshev polynomials satisfying the following recursion relation:

$$e^{-\hat{\gamma}}Q_{n-1}(\hat{H}_{norm}; \hat{\gamma}) + e^{\hat{\gamma}}Q_{n+1}(\hat{H}_{norm}; \hat{\gamma}) = 2\hat{H}_{norm}Q_n(\hat{H}_{norm}; \hat{\gamma}) \tag{2.96}$$

with $Q_0(\hat{H}_{norm}; \hat{\gamma}) = \hat{I}$ and $Q_1(\hat{H}_{norm}; \hat{\gamma}) = e^{-\hat{\gamma}}\hat{H}_{norm}$. The operator $\hat{\gamma}$ is dimensionless and it defines the damping factor. This is connected to the NIP $[\Gamma]$ in the expansion of the Green's function by:

$$\Gamma = \Delta E\left[\cos\phi(1 - \cosh\gamma) - i\sin\phi\sinh\gamma\right] \tag{2.97}$$

where $\phi\left[= \cos^{-1}\left(\frac{E-\hat{H}}{\Delta E}\right)\right]$ is the phase. γ is set to zero in the strong interaction region and it rises slowly as the asymptotic regions are approached. In this prescription, the NIPs are used externally as a damping function. Therefore, their complex nature does not interfere with the eigenvalue spectrum of the Hamiltonian. Another important point to be mentioned here is that the CP expansion method is conditionally stable because the scheme will be unstable if the energy range of the Hamiltonian ΔE is underestimated. The scheme does not conserve norm and energy and the resulting deviation is used as measure of the error [191, 196].

Very recently Neuhauser [237] has investigated the applicability of the NIPs in TIQM scattering. He proposes an anomaly-free very short range imaginary potentials which cover only 1-2 grid points. His method involves the computation of the full S–matrix by diagonalization/inversion of the complex Hamiltonian.

2.4.5 The Short Iterative Lanczos (SIL) Method

The short iterative Lanczos (SIL) scheme, originally developed by Park and Light [72] computes the action of time evolution operator by forming a reduced subspace (Krylov space) of the Hamiltonian matrix. The orthonormal basis set, $q_j(j = 0, ..., N - 1)$ (Krylov basis set) which is spatially and temporally tailored, is generated from the initial vector $q_0 = \psi(0)$ as follows [72, 239, 240]:

$$\hat{H}q_0 = \alpha_0 q_0 + \beta_0 q_1 \tag{2.98}$$

$$\hat{H}q_j = \beta_{j-1}q_{j-1} + \alpha_j q_j + \beta_j q_{j+1}, \quad j \geq 1 \tag{2.99}$$

with

$$\alpha_j = \langle q_j | \hat{H} | q_j \rangle \tag{2.100}$$

and

$$\beta_{j-1} = \langle q_{j-1} | \hat{H} | q_j \rangle \tag{2.101}$$

The Hamiltonian matrix becomes tridiagonal [71] in this reduced subspace:

$$\hat{H}_{N_L} = \begin{pmatrix} \alpha_0 & \beta_0 & 0 & \cdots & \cdots & 0 \\ \beta_0 & \alpha_1 & \beta_1 & 0 & \cdots & 0 \\ 0 & \beta_1 & \alpha_2 & \beta_2 & \cdots & 0 \\ \vdots & \vdots & \vdots & \ddots & \vdots & \vdots \\ 0 & 0 & 0 & \cdots & \alpha_{N_L-2} & \beta_{N_L-2} \\ 0 & 0 & 0 & \cdots & \beta_{N_L-2} & \alpha_{N_L-1} \end{pmatrix} \tag{2.102}$$

It is of size $N_L \times N_L$ compared to $N \times N$ (where N is the total number of grid points, of the order of several hundred thousands for multidimensional scattering problems) of the original Hamiltonian. The Hermiticity of $\hat{H}$ is retained in $\hat{H}_{N_L}$. $\hat{H}_{N_L}$ is diagonalized by the unitary transformation matrix $\mathbf{Z}$, the column of which contains its eigenvectors:

$$\hat{H}_{N_L} = \mathbf{Z}^\dagger D_{N_L} \mathbf{Z} \tag{2.103}$$

where D_{N_L} is the diagonal matrix of eigenvalues and $\mathbf{Z}^\dagger$ is the conjugate transpose of $\mathbf{Z}$. The evolution operator can now be written as [75]

$$\begin{aligned} \hat{U}(\Delta t) &= e^{-i\Delta t \hat{H}_{N_L}/\hbar} \\ &= \mathbf{Z}^\dagger e^{-i\Delta t D_{N_L}/\hbar} \mathbf{Z} \end{aligned} \tag{2.104}$$

The time-evolved wave function then becomes

$$\begin{aligned} \Psi(t + \Delta t) &= \mathbf{Z}^\dagger e^{-i\Delta t D_{N_L}/\hbar} \mathbf{Z} \Psi(t) \\ &= \sum_{n=0}^{N-1} \hat{U}(\Delta t) q_n \end{aligned} \tag{2.105}$$

The summation here arises because the first basis function in the Krylov spacs, q_0 is identical to $\Psi(t)$. The above procedure is repeated iteratively N times. For small Δt ($\approx 0.1fs$) typically 5-10 basis functions are sufficient to construct the tridiagonal matrix. This method is particularly useful for small Δt and since the scheme involves the exponential operation in the reduced subspace, it conserves norm as in the case of the SO scheme. It conserves energy also as the exponential operator commutes with the Hamiltonian unlike in the case of the SO scheme where it involves a splitting into kinetic and potential energy parts. The scheme is unconditionally stable.

In the presence of a NIP the SIL scheme is stable. But the basis vectors become nonorthogonal and one needs to resort to Gram-Schmidt orthogonalization at regular intervals.

For large grid computations the method has additional disadvantage in terms of storage requirement. This is because the recursion vectors of size ($N_L \times N$) need to be stored to evaluate the final time-evolved wave function. This problem can be circumvented if the recursion vectors are computed twice, once for constructing the tridiagonal matrix and then for use in the final equation to obtain the time-evolved wave function. In that case, the method becomes CPU intensive. With an increase in the number of iterations the recursion vectors loose the orthogonality readily because of the truncation error introduced at each time step. Error starts building up when the recursion vectors span outside the reduced space. Park and Light [72] estimated this error by multiplying together the off-diagonal elements of the tridiagonal matrix:

$$|q_{N_L}(\Delta t)| \approx \frac{(-i\Delta t)^{N_L-1}}{(N_L-1)!} \prod_{n=0}^{N_L-1} \beta_n \tag{2.106}$$

where $|q_{N_L}(\Delta t)|$ is the magnitude of the first vector lying outside the Krylov space.

A comparison of the various time evolution schemes in terms of their stability has been made by Leforestier et al [75]. We summarise our findings, with special emphasis on the

influence of the NIP on the various schemes.

The SOD scheme is conditionally stable. It requires the Hamiltonian to be strictly Hermitian. It conserves norm of the wave function and energy. The error accumulates in the phase of the wave function. The scheme is unstable in presence of a NIP. The SO scheme is unconditionally stable. It conserves norm but the non-commutability of $\hat{T}$ and $\hat{V}$ leads to non-conservation of energy. The exponential operation gives rise to a damping factor in presence of a NIP and it can be used successfully for damping of WP near the grid edges. Since the method does not depend upon the spectral range of the Hamiltonian it is stable in presence of a NIP. The CP scheme is conditionally stable, and it does not conserve either norm or energy. The deviations are used as a check on the accuracy of the method. The stability of the scheme depends strongly on the energy range of the Hamiltonian. The scheme becomes unstable in presence of a NIP. This can be made stable by accounting for the shift of the eigenvalue spectrum of the Hamiltonian to the complex plane in presence of the NIP. The SIL scheme also involves an exponential operation and is also unconditionally stable like the SO scheme. It conserves norm as well as energy. This also results in the same damping factor as the SO, in presence of a NIP. The accuracy of the scheme depends on the length of the time step. The additional complication of the non-orthogonality of the basis vectors in presence of a NIP can be taken care of by using the Gram-Schmidt orthogonalization scheme. The last point to be mentioned here is that the Hamiltonian becoming complex does not preserve the time-reversal symmetry (see Appendix 1) of the TDSE. This raises a fundamental question on the use of NIPs in solving the TDSE. We will show some numerical results to highlight this aspect in chapter 3.

2.5   The Fourier Grid Hamiltonian Method

The Fourier Grid Hamiltonian (FGH) method was proposed by Marston and Balint-Kurti [241] for computing bound state eigenvalues and eigenvectors using the variational principle. In this approach the Hamiltonian matrix is discretized on a set of uniformly sampled points on the discrete Hilbert space and the forward and the reverse Fourier transforms are reduced to a sum over cosine functions. The diagonalization of the kinetic energy operator in the FGH method, as can be seen below, is a special case of the DVR method.

For a one dimensional system, we can write

$$
\begin{aligned}
\langle x|\hat{H}|x'\rangle &= \langle x|\frac{\hat{p}^2}{2m}|x'\rangle + \langle x|\hat{V}(x)|x'\rangle \\
&= \langle x|\frac{\hat{p}^2}{2m}\left\{\int_{-\infty}^{\infty}|k\rangle\langle k|\right\}|x'\rangle dk + V(x)\delta(x-x') \\
&= \int_{-\infty}^{\infty}\langle x|k\rangle\frac{\hbar^2 k^2}{2m}\langle k|x'\rangle dk + V(x)\delta(x-x') \\
&= \frac{1}{2\pi}\int_{-\infty}^{\infty}e^{ik(x-x')}\frac{\hbar^2 k^2}{2m}dk + V(x)\delta(x-x')
\end{aligned}
\tag{2.107}
$$

The last equality is obtained by using

$$
\langle k|x\rangle = \frac{1}{2\pi}e^{-ikx}
\tag{2.108}
$$

In finite space, the above equation can be written as

$$
\begin{aligned}
\langle x_i|\hat{H}|x_j\rangle &= \frac{1}{2\pi}\sum_{l=-n}^{n}e^{il\Delta k(x_i-x_j)}\left\{\frac{\hbar^2(l\Delta k)^2}{2m}\right\}\Delta k + \frac{V(x_i)\delta_{ij}}{\Delta x} \\
&= \frac{1}{\Delta x}\left\{\frac{1}{N}\sum_{l=-n}^{n}e^{il2\pi(i-j)/N}\{T_l\} + V(x_i)\delta_{ij}\right\}
\end{aligned}
\tag{2.109}
$$

where $T_l = \frac{\hbar^2(l\Delta k)^2}{2m}$. Combining the negative and positive values of l one obtains

$$
H_{ij} = \frac{1}{\Delta x}\left\{\frac{2}{N}\sum_{l=1}^{n}\cos(l2\pi(i-j)/N)T_l + V(x_i)\delta_{ij}\right\}
\tag{2.110}
$$

since $T_0 = 0$ by definition. Any arbitrary state vector $|\phi>$ can be written as a linear combination of the eigenvectors $|x_i>$ for the discrete grid points:

$$
|\phi> = \sum_i |x_i> \Delta x <x_i|\phi>
$$

$$= \sum_i |x_i > \Delta x \phi(x_i) \tag{2.111}$$

where $\phi(x_i)$ are the values of the wave function at the grid points and are the unknown coefficients to be evaluated by the variational method:

$$
\begin{aligned}
E &= \frac{< \phi|\hat{H}|\phi >}{< \phi|\phi >} \\
&= \frac{\sum_{ij} \phi(x_i)^* \Delta x H_{ij} \Delta x \phi(x_j)}{\Delta x \sum_i |\phi(x_i)|^2} \\
&= \frac{\sum_{ij} \phi(x_i)^* H_{ij}^0 \phi(x_j)}{\sum_i |\phi(x_i)|^2}
\end{aligned}
\tag{2.112}
$$

where $H_{ij}^0 = H_{ij}\Delta x$. Minimization of this energy with respect to the variational parameters $\phi(x_i)$ yields the set of secular equations:

$$\sum_j \left[H_{ij}^0 - E_\lambda \delta_{ij} \right] \phi(x_j)^\lambda = 0 \tag{2.113}$$

The nontrivial solution for the $\phi(x_j)$s are obtained if

$$det(H_{ij}^0 - E\delta_{ij}) = 0 \tag{2.114}$$

This is the characteristic equation having λ roots for E.

In the numerical calculation we have started by defining an eigenvector matrix for ϕ containing λ columns. The matrix is composed entirely of zeroes except for a single element of unity which occurs at the λth row. The matrix H_{ij}^0 is computed using these eigenvector matrices in which a forward and a reverse FFT are performed for computing the action of the kinetic energy operator on ϕ. This Hamiltonian matrix H_{ij}^0 is then diagonalized using the standard matrix diagonalization routine. The diagonal elements of the resulting Hamiltonian matrix are the λ eigenvalues and the columns of ϕ are the corresponding orthonormal eigenvectors of H_{ij}^0. The resulting eigenvectors are renormalised using a standard integration procedure.

2.6   The Spectral Quantization Method

The spectral quantization method (SQM) was proposed by Feit et al [65, 242] for computing the bound state eigenvalues and eigenfunctions by solving the TDSE. In this method a WP (usually a stationary Gaussian wave packet (GWP)), $\Psi(0)$, is located initially in the interaction region of the PES. The WP at time t, $\Psi(t)$, is obtained by evolving $\Psi(0)$ in space (by the FFT method) and in time (by the SO method). The temporal autocorrelation function

$$C(t) = \langle \Psi(0)|\Psi(t) \rangle \tag{2.115}$$

is computed at various time intervals and Fourier transformed to generate the power spectrum:

$$I(E) = \left| \int_0^\infty C(t) e^{iEt/\hbar} dt \right|^2 \tag{2.116}$$

$I(E)$ is known as the spectral intensity. The peaks in the power spectrum arise from the bound and/or quasibound states of the system and the energy values corresponding to the peak maxima are their eigenvalues. The energy resolution of the spectrum is decided by:

$$\Delta E = \frac{2\pi\hbar}{T} \tag{2.117}$$

where $T(= N_t \times \Delta t)$ is the total time up to which the WP is evolved. Fourier transform of $C(t)$ leads to a superposition of δ-functions [65]:

$$I(E) = \sum_{n,j} |A_{nj}|^2 \delta(E - E_n) \tag{2.118}$$

where $\sum_j |A_{nj}|^2 = W_n$, are the relative weights of the states. This δ-function behavior implies an infinite record of the autocorrelation function data. In order to correct for the finite time computations, the autocorrelation function is multiplied at each time step by the normalized Hanning window function $w(t)/T$ where

$$
\begin{aligned}
w(t) &= 1 - cos\left(\frac{2\pi t}{T}\right) && if \ 0 \le t \le T \\
&= 0 && if \ t > T
\end{aligned}
\tag{2.119}
$$

before Fourier transformation. The use of the window function improves the resolution of the spectral peaks. In the absence of the window function, the spectral peaks resemble the function [65], $\frac{\sin\left[\frac{1}{2}(E-E_n)T\right]}{(E-E_n)}$, and their soulders overlap with the nearby peaks. The accuracy of the eigenvalues is improved by fitting $I(E)$ to a lineshape function $L_1(E-E_n)$ assuming a single-line fit:

$$I(E) = W_n L_1(E-E_n) \tag{2.120}$$

where $L_1(E-E_n)$ is given by [65]:

$$
\begin{aligned}
L_1(E - E_n) &= \frac{1}{T}\int_0^T exp[i(E-E_n)t]w(t)dt \\
&= \frac{exp[i(E-E_n)T]-1}{i(E-E_n)T} \\
&\quad -\frac{1}{2}\left[\frac{exp\{[i(E-E_n)T+2\pi]\}-1}{i[(E-E_n)T+2\pi]}\right] \\
&\quad +\frac{1}{2}\left[\frac{exp\{[i(E-E_n)T-2\pi]\}-1}{i[(E-E_n)T-2\pi]}\right]
\end{aligned} \tag{2.121}
$$

This single line fit is described in detail by Feit et al [243].

Once the eigenvalues are computed, the eigenfunctions can be obtained by projecting the time evolved wave packet at the desired eigenstate E_n:

$$\Psi(E_n) \approx \frac{1}{T}\int_0^T \Psi(t)w(t)exp(iE_nt)dt \tag{2.122}$$

The eigenfunctions obtained in this way are renormalised by using either the Simpson's rule or by some other quadrature scheme. It is worth mentioning at this point that the eigenfunctions obtained by this method may have an error in their phase, arising from the use of the second order SO scheme. Our experience shows that these eigenfunctions lead to inaccuracies in the reaction probability calculation. The phase error vanishes when the probability density of the eigenfunction is computed and there is no problem in characterizing the states based on the nodal pattern. We have verified this by computing the bound state eigenfunctions for H_2^+ using an extended Rydberg potential, both by the

FGH [241] method and the SQM [65]. We find that the eigenfunctions obtained by the two methods do not differ in terms of their probability density patterns but do show the difference when they are used in reactive scattering calculations. The eigenfunctions obtained by the FGH method are found to be quantitatively accurate. Bandrauk and Shen [244] proposed the exponential SO method which is accurate up to third order:

$$e^{-i(\hat{T}+\hat{V})t/\hbar} = e^{\gamma\lambda\hat{T}/2}e^{\gamma\lambda\hat{V}}e^{(1-\gamma)\lambda\hat{T}/2}e^{(1-2\gamma)\lambda\hat{V}}e^{(1-\gamma)\lambda\hat{T}/2}e^{\gamma\lambda\hat{V}}e^{\gamma\lambda\hat{T}/2} \tag{2.123}$$

where $\gamma = \frac{1}{(2-2^{1/3})}$ and $\lambda = \frac{-i\Delta t}{\hbar}$. Their analysis shows that use of this exponential SO in place of the second order SO removes the phase error in the eigenfunctions. The SQM is used to compute the resonances in the present thesis and the relevant computational details are given in chapter 3.

2.7 Scattering Analysis

2.7.1 Time-Energy Mapping of the Wave Packet Flux

In scattering studies the reactants are initially represented in terms of an appropriate wave packet located far out in the asymptotic reagent channel where the the interaction potential is almost zero. The configuration space is divided into reagent, interaction and product regions and the vibrational state-selected energy resolved reaction probabilities ($P_v^R(E)$) are calculated by computing the energy resolved flux of the WP across a dividing line in the product channel. This strategy was developed initially by Neuhauser and Baer [155, 156, 164] and later on was adapted by others [166, 167, 245, 246]. In collinear (A,BC) type collisions the initial WP ($\Phi(R, r, t = 0)$ in mass-scaled Jacobi coordinates R (A, BC translation) and r (BC vibration) consists of a product of a minimum uncertainty Gaussian wave packet (GWP), $F(R)$, corresponding to (A,BC) translation and the vibrational eigenfunction, $\phi_v(r)$, corresponding to the vibrational state v of the BC molecule:

$$\Phi(R, r, t = 0) = F(R)\phi_v(r) \tag{2.124}$$

where

$$F(R) = (2\pi\delta^2)^{1/4} exp\left[-\frac{(R-R_0)^2}{4\delta^2} - ik_0R\right] \tag{2.125}$$

Here δ is the width parameter, R_0 and k_0 denote the location of the maximum in the coordinate and the momentum space respectively. The vibrational eigenfunctions, $\phi_v(r)$, of BC are numerically computed using the FGH method [241]. The reaction probability, $P_v^R(E)$, is computed from

$$P_v{}^R(E) = \frac{\hbar}{\mu} Im\left[\left\langle \Psi(R, r_I, E)\left|\frac{\partial\Psi(R, r_I, E)}{\partial r}\right\rangle\right] \tag{2.126}$$

where $\mu = [m_A m_B m_C/(m_A + m_B + m_C)]^{1/2}$, is the three body reduced mass and the quantity within the angular bracket is the energy-resolved flux of the WP (computed along the dividing line at $r = r_I$ in the product channel), which is integrated over the entire range of R. $\Psi(R, r_I, E)$ is the energy-resolved wave function normalized with respect to the initial translational energy distribution of the WP, i.e.,

$$\Psi(R, r_I, E) = \Phi(R, r_I, E)/a_E \tag{2.127}$$

$\Phi(R, r_I, E)$ is obtained by Fourier transforming the time evolved WP, $\Phi(R, r, t)$, along the dividing line at $r = r_I$:

$$\Phi(R, r_I, E) = \frac{1}{\sqrt{2\pi}}\int_{-\infty}^{\infty} \Phi(R, r, t)\exp\left(iEt/\hbar\right)dt\big|_{r=r_I} \tag{2.128}$$

a_E in Eq. (2.127) is the weight of the energy component, E, contained in the initial translational WP and is evaluated by

$$a_E = \left(\frac{\mu}{\hbar k}\right)^{1/2}\frac{1}{\sqrt{2\pi}}\int_{-\infty}^{\infty} F(R)\exp\left(ikR\right)dR \tag{2.129}$$

$$= \left(\frac{\mu}{\hbar k}\right)^{1/2} F(k) \tag{2.130}$$

where

$$F(k) = (2\delta^2/\pi)^{1/4} exp\left[-\delta^2(k-k_0)^2 + i(k-k_0)R_0\right] \tag{2.131}$$

The factor $(\mu/\hbar k)^{1/2}$ in Eq. (2.130) accounts for the energy normalization of $\Psi(R, r_I, E)$. Incorporating the result of Eqs. (2.127) - (2.131) in Eq. (2.126), we obtain

$$P_v^R(E) = \left(\frac{\hbar^2 k}{\mu^2 |F(k)|^2}\right) Im\left[\left\langle \Phi(R, r_I, E) \left| \frac{\partial \Phi(R, r_I, E)}{\partial r} \right\rangle\right]\right] \quad (2.132)$$

with $k = \sqrt{2\mu(E - E_v)}/\hbar$, and E_v the initial vibrational energy of the BC molecule.

In actual computation, $\Phi(R, r_I, E)$ and its derivative with respect to r are computed at each time step along $r = r_I$ by evaluating the continuous Fourier transform (Eq. (2.128)) as a discrete sum as follows:

$$\Phi(R, r_I, E) = \frac{\Delta t}{\sqrt{2\pi}} \sum_{n=0}^{\infty} \Phi(R, r, n\,\Delta t) e^{iEn\Delta t/\hbar}|_{r=r_I} \quad (2.133)$$

$$\frac{\partial \Phi(R, r_I, E)}{\partial r}\bigg|_{r=r_I} = \frac{\Delta t}{\sqrt{2\pi}} \sum_{n=0}^{\infty} \frac{\partial \Phi(R, r, n\,\Delta t)}{\partial r} e^{iEn\Delta t/\hbar}|_{r=r_I} \quad (2.134)$$

Such an approach reduces the storage requirement of the computer to the size of the R grid times the number of energy values at which $P_v^R(E)$ is sought. Once the contributions from each time step are added coherently to the values from the previous step in Eq. (2.133) and (2.134), the WP is damped out with the help of either a NIP or a masking function.

2.7.2   Time-Energy Projection

In this method the energy resolved state-to-state reaction probabilities ($P_{v,v'}(E)$) are computed from the energy resolved $S_{v,v'}$ matrix elements for the transition from a specified initial reactant level (v) to a specific product level (v'). The $S_{v,v'}$ matrix elements in this method are computed by solving the TDSE. The method was proposed by Balint-Kurti and coworkers [162, 227]. These authors have applied the method initially for F + H$_2$ [162] and later for Li + FH [247, 231] reactive scattering. For the collinear (A,BC) type of collisions the $\Psi(R, r, t = 0)$ is prepared in the same way as mentioned in the previous subsection. This WP is time evolved and the resulting $\Psi(R, r, t)$ is converted to Ψ in product coordinates (R', r'). One may use a Fourier type of interpolation scheme [164] in

which $\Psi(R, r, t)$ is first transformed to the momentum domain $\Psi(p_R, p_r, t)$ through an FFT route and then projected on to the product coordinates through an inverse FFT :

$$\Psi(R', r', t) = \sum_{p_R, p_r} e^{i(p_R R' + p_r r')} \Psi(p_R, p_r, t) \tag{2.135}$$

where

$$\Psi(p_R, p_r, t) = \frac{1}{N_R N_r} \sum_{R, r} e^{-i(p_R R + p_r r)} \Psi(R, r, t) \tag{2.136}$$

N_R and N_r are the number of grid points along R and r respectively. This interpolated WP at a fixed value of the product scattering coordinate R'_I, $\Psi(R'_I, r', t)$, is projected onto the specific vibrational state (v') of the product molecule to extract the contribution of that particular state in $\Psi(R'_I, r', t)$. This yields a time-dependent coefficient at each time:

$$C_{v'}(t) = \int_{r'_{min}}^{r'_{max}} \phi_{v'}(r') \Psi(R'_I, r', t) dr \tag{2.137}$$

where $\phi_{v'}(r')$ are generated in the same way as $\phi_v(r)$ by the FGH method [241]. The Fourier transform of $C_{v'}(t)$ results in energy dependent amplitude

$$A_{v'}(E) = \frac{1}{2\pi} \int_0^T e^{iEt/\hbar} C_{v'}(t) dt \tag{2.138}$$

from which the $P_{v,v'}(E)$ values are calculated:

$$P_{v,v'}(E) = |S_{v,v'}(E)|^2 = \frac{\hbar^2}{\mu^2} k_v k_{v'} \left| \frac{A_{v'}(E)}{F(k_v)} \right|^2 \tag{2.139}$$

In this method the interpolation of the WP takes much of the CPU time but, storage is no longer a problem. The CPU requirement can be reduced if the WP is interpolated only once when it reaches the interaction region and then the dynamics is monitored in the product grid. This also reduces the error arising from interpolation, as the entire process requires only one interpolation and that too in a compact form of the WP.

2.7.3   The Møller Wave Operator Formalism

Viswanathan et al [139] have described computation of the S-matrix elements through a time-dependent wave packet (TDWP) calculation employing Møller wave operators.

Weeks and Tannor have [140, 141, 142] adapted their technique to compute the scattering attributes. The Møller operators are defined as:

$$\Omega_{\pm}^{\gamma} = lim_{t \to \mp \infty} e^{i\hat{H}t/\hbar} e^{-i\hat{H}_0^{\gamma}t/\hbar} \qquad (2.140)$$

where γ refers to the channel index. $\hat{H}_0^{\gamma}(= \hat{T}(R) + \hat{h}^{\gamma}(r))$ and $\hat{H}(= \hat{H}_0^{\gamma} + V^{\gamma})$ are the asymptotic and the full interaction Hamiltonians, $\hat{h}^{\gamma}(r)$ is the diatomic Hamiltonian in the γth channel and V^{γ} is the interaction potential. These Møller operators are used to prepare the appropriate scattering states of reactants (products). For the reactant packet one initially starts with $\Psi(R, r, t = 0)$ centered at the interaction region of the PES $(t = 0)$ and operates with Ω_{+}^{α} on it to prepare the appropriate reactant channel (α) WP, Ψ_{+}^{α}. The action of Ω_{+}^{α} on $\Psi(R, r, t = 0)$ is to propagate it backward in time under the action of the asymptotic Hamiltonian $(\hat{H}_0^{\alpha})$ and then to propagate it forward in time again to the interaction region under the action of the full interaction Hamiltonian $(\hat{H})$. In actual computation, the reactant packet is back propagated for a length of time $t = -\tau_1$ which takes it far out in the asymptotic reagent channel and then propagated forward in time to the interaction region. This forward propagation is stopped before the WP starts bifurcating. This whole process is called the reactant channel dynamics. A similar exercise is undertaken to prepare the appropriate product channel (β) WP, Ψ_{-}^{β}, and this is called the product channel dynamics. In this case the initial WP is written in terms of the product Jacobi coordinates, $\Psi(R', r', t = 0)$ and located in the interaction region of the PES and Ω_{-}^{β} is acted on it to obtain Ψ_{-}^{β}. The initial propagation under the action of the appropriate asymptotic product channel Hamiltonian $(\hat{H}_0^{\beta})$ is carried out forward in time $(t = \tau_1)$ on the product grid and brought back to the interaction region by propagating backward in time and the propagation is stopped before the WP starts bifurcating. Once these Møller states are obtained the dynamics is followed on a common grid.

The common grid can be obtained either by interpolating the reactant channel packet to the product grid and product channel packet to the reactant grid or by interpolating

both the channel packets to a common grid. A Fourier type of interpolation [164] as mentioned earlier can be used for this purpose. The reactant packet is then propagated forward in time from $t = 0$ to $t = \tau$ and its correlation function with the product channel packet (frozen at t=0) is computed:

$$C_{\beta\alpha}(t) = \langle \Psi_-^\beta | e^{-i\hat{H}t/\hbar} | \Psi_+^\alpha \rangle \tag{2.141}$$

Similarly, the product channel packet is propagated backward in time from $t = 0$ to $t = -\tau$ and its correlation function with the reactant channel packet (frozen at t=0) is computed:

$$C_{\alpha\beta}(t) = \langle \Psi_+^\alpha | e^{-i\hat{H}t/\hbar} | \Psi_-^\beta \rangle \tag{2.142}$$

When these two parts are combined together it results in the correlation function between the reactant and product channel packets over the entire time range from $-\tau$ to τ. The symmetric partitioning is possible because of the symmetric form of the correlation function $C_{\beta\alpha} = C_{\alpha\beta}$ [140]. The time τ corresponds to the value of time when the correlation function becomes zero. The components of the WP which reach the grid edges during the correlation function computation are absorbed using a NIP. The correlation function is Fourier transformed to compute the energy resolved S-matrix elements:

$$S_{\beta\alpha}(E) = \frac{\hbar(|k_-^\beta||k_+^\alpha|)^{1/2}}{2\pi\mu F_-^*(\pm k_-^\beta) F_+(\pm k_+^\alpha)} \int_{-\infty}^{+\infty} e^{iEt/\hbar} C_{\beta\alpha}(t) dt \tag{2.143}$$

where the F terms are computed using the Eq (2.125) and $k_\pm^\gamma = \left(\frac{2\mu}{\hbar^2}(E - E_\gamma)\right)^{1/2}$. The state-to-state reaction probabilities are computed from the S-matrix elements as:

$$P_{\beta\alpha}(E) = |S_{\beta\alpha}(E)|^2 \tag{2.144}$$

An alternative way is to start initially with a rectangular bond coordinate grid (r_{AB}, r_{BC}). The reactant and product cannel WPs are then prepared by switching over to the respective grid through interpolation and then the channel WPs are transformed back to the bond

coordinate grid where the rest of the dynamics is followed in the same way as mentioned above with the kinetically coupled Hamiltonian [248]:

$$\hat{H} = -\frac{\hbar^2}{2\mu_{AB}}\frac{\partial^2}{\partial r_{AB}^2} - \frac{\hbar^2}{2\mu_{BC}}\frac{\partial^2}{\partial r_{BC}^2} + \frac{\hbar^2}{2\mu_B}\frac{\partial}{\partial r_{AB}}\frac{\partial}{\partial r_{BC}} + V(r_{AB}, r_{BC}) \qquad (2.145)$$

This approach exploits the collinear constraint on the dynamics and is better because the grid spacings remain uniform. Jäckle and Meyer [143] have recently applied this correlation function approach of computing the S-matrix elements in the bond coordinates to the collinear $H + H_2$ reactive collision in the frame work of multi-configuration time-dependent Hartree approach and obtained results which are in excellent agreement with the time-independent results. We have developed a code to compute the state-to-state reaction probabilities for the collinear $He + H_2^+$ collisions using the Møller operator formalism and we are in the process of debugging it.

Chapter 3

Transition State Resonances and Collinear He, H_2^+ (HD^+/DH^+) Dynamics

3.1   Introduction

Resonances in (He,H_2^+) collisions have received considerable attention from several research groups during the past two decades. Quantum mechanical studies of the collinear reaction

$$He + H_2^+(v) \rightarrow HeH^+(v') + H \tag{R1}$$
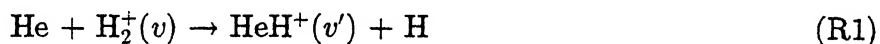
by Kouri and Baer [249] revealed several oscillations in the reaction probability, P_v^R, versus energy (E) plots in the range 0.93-1.4 eV on a diatomics-in-molecules (DIM) potential-energy surface [250]. Subsequent calculations by Adams [251] using the integral equation approach on the same PES, on a finer mesh of E, in addition to reproducing the results of Kouri and Baer, revealed additional resonances. Chapman and Hayes [252] discovered several oscillations in the vibrationally inelastic transition probability versus energy plot in the energy range 0.4-0.65 eV, well below the reaction threshold. They characterized one of the oscillations to be a shape (open) resonance and the others as of Feshbach (compound) type. Joseph and Sathyamurthy [253] carried out R-matrix calculations for the system in collinear geometry on an accurate *ab initio* PES due to McLaughlin and Thompson [254]. Their results also revealed several oscillations in the $P_v^R(E)$ curves and

most of them were interpreted in terms of quasi-bound states supported by vibrational adiabatic potentials [255]. Kress et al [256] adopted the adiabatically adjusted principal axis, hyperspherical formulation of Pack et al [257] for quantum reactive scattering in three dimensions (3D) and reported the results for total angular momentum, $J = 0$, collision on the McLaughlin-Thompson-Joseph-Sathyamurthy [258] (MTJS) PES. Their results revealed numerous resonances with life-times of ~ 1 ps or more. Similar calculations were carried out by Lepetit and Launay [259] on the same PES and they reported some of the resonances having life-times ~ 3 ps. Results of Zhang et al [260] for 3D, $J = 0$ collisions on the DIM PES also showed several resonances.

Stroud et al [261] had carried out a time-dependent quantum mechanical (TDQM) investigation of the collinear reaction on a spline-fitted *ab initio* PES. Balakrishnan and Sathyamurthy [262] carried out a TDQM calculation for the collinear collision on the MTJS PES and they also obtained several resonances. These were related to chaotic dynamics in classical calculations [263, 264] and turbulence in the flux patterns obtained in the quantal calculation. They also reported [265] the preliminary results of a 3D, $J = 0$ quantal investigation of the reaction (R1). Although they did not report energy resolved P_v^R values, the probability density plots obtained by them were highly structured, suggesting the existence of dynamical resonances for the system. Mandelshtam et al [266] have, traced the connection between the quantum mechanical resonances and the classical chaotic scattering in three dimensions. Marston [267] have interpreted the resonances in the chaotic region in terms of periodic orbits of the collinear HeH_2^+ system. More recently, we have extracted the signature of quantum chaos in collinear (He, H_2^+) collisions [268].

Recently Sakimoto and Onda [269] obtained the resonances in the system for the collinear geometry on MTJS and DIM PESs using a time independent quantal calculation. While the positions of resonances computed by them were in agreement with those of Sathyamurthy et al [255] the magnitudes of P_v^R were at variance. More recent calcula-

tions through [167] time-energy mapping of the reactive flux of the WP yield $P_v^R(E)$ values which are in quantitative agreement with those of Sakimoto and Onda.

In the present chapter, we analyse the dynamical resonances in collinear (He,H$_2^+$) collisions and its isotopic variants when either one of the two H atoms is replaced by D, in terms of their transition state spectrum. Recently, Sadeghi and Skodje [97, 98] showed that they could obtain thirteen high energy resonances for collinear (H,H$_2$) system by a correlation function approach. They solved the TDSE for the system by the spectral quantization method [64, 65, 242] to generate the transition state spectrum for the dynamics on the double-many-body-expansion (DMBE) potential-energy surface. We have extended their approach to a study of collinear (He,H$_2^+$) dynamics and its isotopic variants. We have also calculated the vibrational (v) state-selected energy resolved reaction probabilities ($P_v^R(E)$) for collinear (He, HD$^+$) and (He, DH$^+$) collisions by the time-energy mapping of the reactive flux [155, 156, 164, 167] of the WP as described in Sec.2.7.1.

3.2   Computational Details

3.2.1   Computation of the Transition Spectrum

We have used the SQM outlined in sec. 2.6 for the computation of the transition state spectrum. The interaction Hamiltonian for the collinear A + BC system in mass-scaled Jacobi coordinates (R,r) is given by

$$\hat{H} = \frac{-\hbar^2}{2\mu}\left[\frac{\partial^2}{\partial R^2} + \frac{\partial^2}{\partial r^2}\right] + V(R,r) \tag{3.1}$$

where μ is the three-particle reduced mass. The MTJS potential-energy surface, used for $V(R,r)$, has a well of depth 0.32 eV in the interaction region. The TDSE is solved on a 256×256 grid in (R,r) space with the origin at (2.2,0.4) a.u. and $\triangle R = \triangle r = 0.05$ a.u.

The initial wave function, $\Psi(R, r, t = 0)$ was taken as an even parity Gaussian wave packet (GWP) in terms of A-B and B-C bond coordinates:

$$\Psi(R, r, t = 0) = N \, exp \left[-\frac{(r_{AB} - r_{AB}^0)^2}{2\delta^2} - \frac{(r_{BC} - r_{BC}^0)^2}{2\delta^2} \right] \qquad (3.2)$$

where N is the normalisation constant and (r_{AB}^0, r_{BC}^0) specifies the initial location of the WP. R and r are related to r_{AB} and r_{BC} through:

$$
\begin{aligned}
r_{AB} &= d\,R - \frac{r_{BC}}{2} \\
r_{BC} &= d^{-1}\,r
\end{aligned}
\qquad (3.3)
$$

where d is the scaling parameter, given by the square root of the ratio of the reduced mass of BC to the three body reduced mass μ and δ is the width parameter. The average energy of the WP, dependent on its location and its width, is obtained from

$$\langle E \rangle = \frac{\langle \Psi(R, r, t = 0) | \hat{H} | \Psi(R, r, t = 0) \rangle}{\langle \Psi(R, r, t = 0) | \Psi(R, r, t = 0) \rangle} \qquad (3.4)$$

The value of $\triangle t$ used in the SO method for time evolution was selected on the basis of the desired width of the energy spectrum. The maximum width in energy that could be obtained is given by

$$\triangle E_{max} = \frac{\pi \hbar}{\triangle t} \qquad (3.5)$$

We have carried out six sets of calculations for the HeH_2^+ and three sets each for the $HeHD^+$ and $HeDH^+$ by varying the position of the initial WP in the interaction region. We have used $\triangle t = 0.161625$ fs for each set except for the sixth set of the first system, in which $\triangle t$ was taken to be 0.10775 fs. The lengths of the time step are selected in accordance with the Eq. (2.81). The grid parameters for the different calculations are given in Table 3.1.

We have used the NIP of Neuhauser et al [200, 201] in both reactant and product channels in the asymptotic region to suppress the reflection of the WP from the grid edges

at a later time. The form of the potential used in the calculation is the linear ramp:

$$V_I(X) = \begin{cases} -iV_0 \frac{X-X_{1I}}{X_{2I}-X_{1I}} & \text{if } X_{1I} \leq X \leq X_{2I} \\ 0 & otherwise \end{cases} \tag{3.6}$$

where $V_I(X)$ is the absorbing potential applied at the channel coordinate X, V_0 is a real constant specifying the height of the potential, X_{1I} is the point where the absorbing boundary starts and X_{2I} is the end of the boundary. $X_{2I} - X_{1I} = \triangle X_I$ is thus the width of the boundary. The height and the width of the absorbing boundary were chosen to satisfy the inequality condition [200, 201, 270, 271]:

$$\frac{\hbar E_t^{\frac{1}{2}}}{\triangle X_I \sqrt{8\mu}} \leq V_{I0} \leq \frac{\triangle X_I \sqrt{8\mu} E_t^{\frac{3}{2}}}{\hbar} \tag{3.7}$$

The left-hand inequality in the above equation guarantees complete absorption of the flux and the right-hand inequality guarantees that no reflection takes place due to interaction of the wave function with the imaginary potential. Choice of $V_0 = 0.25$ eV and $\triangle X_I = 2.75$ a.u. was found to give 99% absorption. We have also used a quadratic NIP used by Seideman and Miller [137]:

$$V_I(X) = \begin{cases} -iV_0 \left[\frac{X-X_{1I}}{\triangle X_I}\right]^2 & \text{if } X_{1I} \leq X \leq X_{2I} \\ 0 & otherwise \end{cases} \tag{3.8}$$

In this case values of $V_0 = 0.25$ eV and $\triangle X_I = 2.25$ a.u. were found to damp the WP more smoothly than the linear potential.

The autocorrelation function for each initial choice of the WP was computed at each time step, multiplied by the normalized Hanning window function and Fourier transformed to the energy domain to generate the transition state spectrum as described in sec. 2.6.

We have time evolved for a total of 32768 time-steps in each set of our calculations. That corresponds to a total time of 5.29 ps. This gives an energy resolution of the order of 7.8×10^{-4} eV (Eq. (2.117)). This duration of time evolution was found to be sufficient to get most of the wave function out of the interaction zone, thus bringing the autocorrelation

No.	r^0_{AB}(a.u.)	r^0_{BC}(a.u.)	$<E>$ (eV)		
			HeH_2^+	$HeHD^+$	$HeDH^+$
1	2.133	3.399	0.6928	0.6632	0.6332
2	2.462	3.567	0.9924	0.9628	0.9332
3	2.533	3.860	1.2159	-	-
4	2.874	4.529	1.7693	-	-
5	3.345	5.283	2.2816	2.2520	2.2224
6	3.846	6.414	2.6834	-	-

Table 3.1: Parameters for different choices of initial wave functions used in time evolution.

function down nearly to zero. The transition state spectrum, I(E), exhibits several sharp maxima, positions of which give the eigenvalues of the resonance states. Since the system possesses a large number of closely spaced scattering resonances, some overlapping contribution remains even after multiplication by the window function. To make an accurate estimate of the eigenvalues, we have fitted I(E) to the lineshape function (Eq. (2.121)).

The eigenfunction at any given eigenenergy was computed through Eq. (2.122). The life-time of some of the well resolved states are computed by a stable nonlinear least-squares fitting of the spectral peaks to a Lorentzian function:

$$\sigma(E) = \frac{\sigma_{max} \left(\frac{\Gamma_n}{2}\right)^2}{(E - E_n)^2 + \left(\frac{\Gamma_n}{2}\right)^2} \qquad (3.9)$$

where Γ_n gives the width of the nth resonance state, and the life-time for the nth state is related to its width by

$$\tau_n = \frac{\hbar}{\Gamma_n} \qquad (3.10)$$

3.2.2 Computation of Reaction Probabilities

The $P_v^R(E)$ values are computed by the time-energy mapping of the reactive flux of the WP (Sec. 2.7.1) for the collinear (He,HD$^+$) and (He,DH$^+$) collisions. The vibrational

eigenfunctions $\phi_v(r)$ of HD$^+$ are numerically computed by the FGH method (Sec. 2.5) using the diatomic Hamiltonian:

$$\hat{h} = -\frac{\hbar^2}{2\mu_{HD^+}} \left[\frac{\partial^2}{\partial r^2} \right] + V(r) \tag{3.11}$$

where $V(r)$ is the extended Rydberg potential used in the MTJS PES [258]:

$$V(r) = -D_e \left[1 + a_1\rho + a_2\rho^2 + a_3\rho^3 \right] \times e^{-a_1\rho}, \quad \rho = r - r_e \tag{3.12}$$

Here D_e is the equilibrium bond dissociation energy of H$_2^+$ and a_1, a_2, a_3 are the parameters reported elsewhere [272]. We have used the FFT algorithm for the spatial evolution of the WP and the SO method for the temporal evolution. We have used a masking function activated outside the dividing line in the product channel and in the asymptotic reactant channel in order to damp out the WP from grid edges:

$$f(x_i) = \sin \left[\frac{\pi}{2} \frac{(x_{max} - x_i)}{\Delta x} \right] \tag{3.13}$$

where x_{max} is the maximum length of the grid along the coordinate x, x_i is the point at which the function has the maximum value (=1) and Δx is the width over which the function decays from 1 to 0. $f(x_i)$ values are multiplied with the final time evolved WP in each channel which results in a sin^2 masking. The WP is time evolved for a total of 773 fs which is found to be sufficient to obtain converged $P_v^R(E)$ values. The grid parameters used in this calculation are given in Table 3.2.

3.3 Results and Discussion

3.3.1 Bound states and Resonances in HeH$_2^+$

An initial WP, (No.2) with $\langle E \rangle$= 0.9924 eV, was located at $(r_{HeH}^0, r_{HH^+}^0) = (2.462, 3.568)$ a.u. and time evolved as described in section 3.2. Snapshots of the time-evolved wave function, at different time intervals are shown in Fig.3.1(a-l), in the form of probability density contours, superimposed on the potential-energy contours. In about 8 fs, the WP

N_R	256
N_r	256
$(R_{min}, R_{max}, \triangle R)$(a.u.)	(2.2, 14.95, 0.05)
$(r_{min}, r_{max}, \triangle r)$(a.u.)	(0.4, 13.15, 0.05)
R_0 (a.u.)	10.0
δ(a.u.)	0.25
$\triangle t$(fs)	0.19
r_I (a.u.)	8.4
R_{mask}(a.u.)	12.95
r_{mask}(a.u.)	11.15

Table 3.2: Grid parameters used in the scattering calculation.

spreads along the asymmetric stretch direction and in another 8 fs, it develops interesting structures. These structures are amplified with further time evolution and part of the wave function spreads in the (He,H_2^+) channel and part in the (HeH$^+$,H) channel. Since we have used NIPs (eq. (3.6)) in both channels we do not see any back reflection of these outgoing waves from the grid edges. As discussed by Balakrishnan and Sathyamurthy [262] substantial portion of the WP lingers on in the interaction region, revealing characteristic nodal structures which indicate high vibrational excitation of H_2^+ and also vibrational excitation of the HeH$_2^+$ complex. Even after 5.296 ps, there is 0.05% of the WP remaining in the interaction region indicating that some portion of the WP has a lifetime greater than 5.3 ps.

We have computed the autocorrelation function (Eq. (2.115)) during the entire time evolution and it is clear from Fig. 3.2 that a sharp decline in the first few fs of evolution is followed by a large number of recurrences over a long time (5 ps). The inset in Fig. 3.2 shows clearly the magnitude of recurrences in the ps time scale. These recurrences can be interpreted in terms of a number of symmetric and asymmetric stretch orbits for the
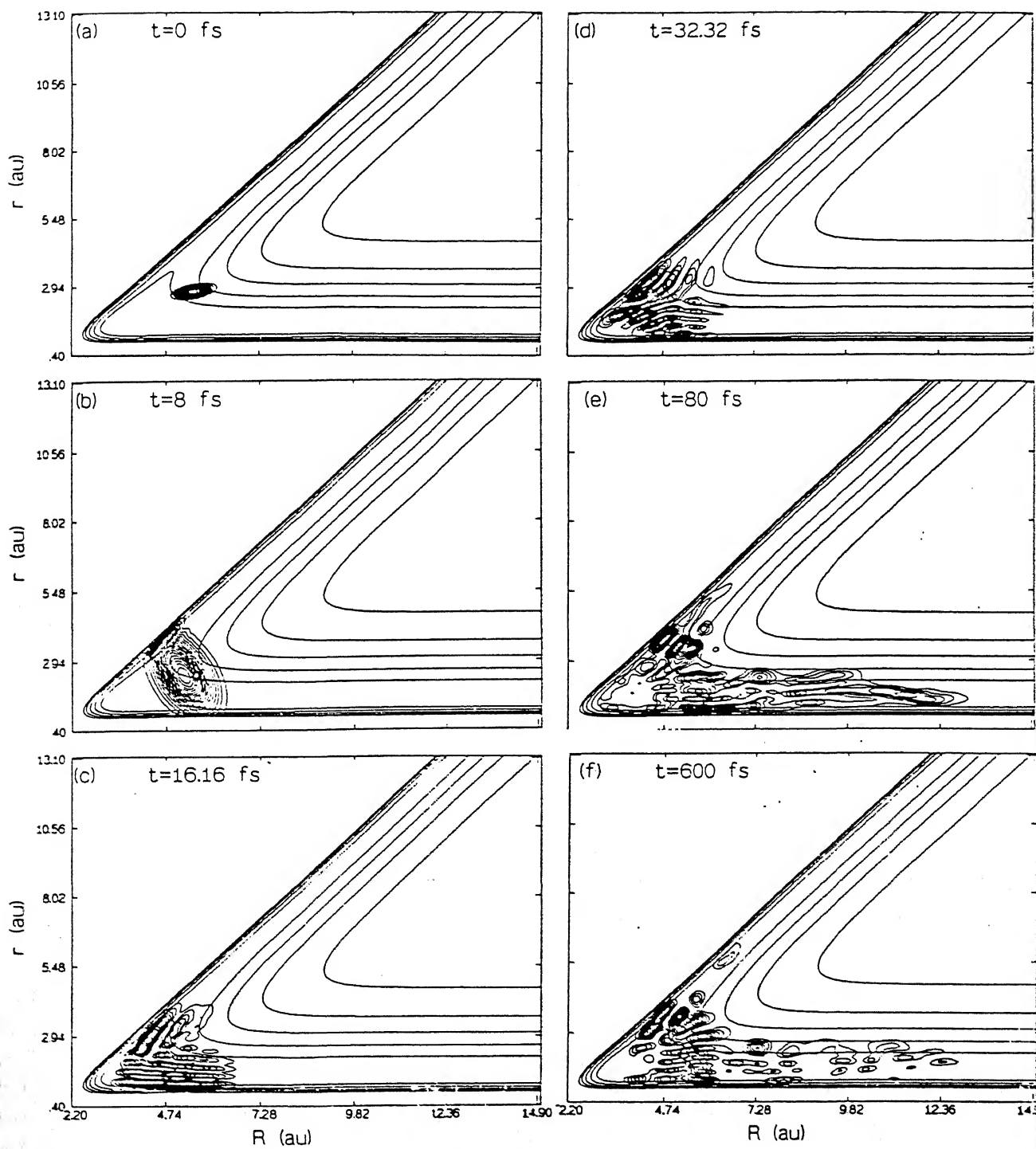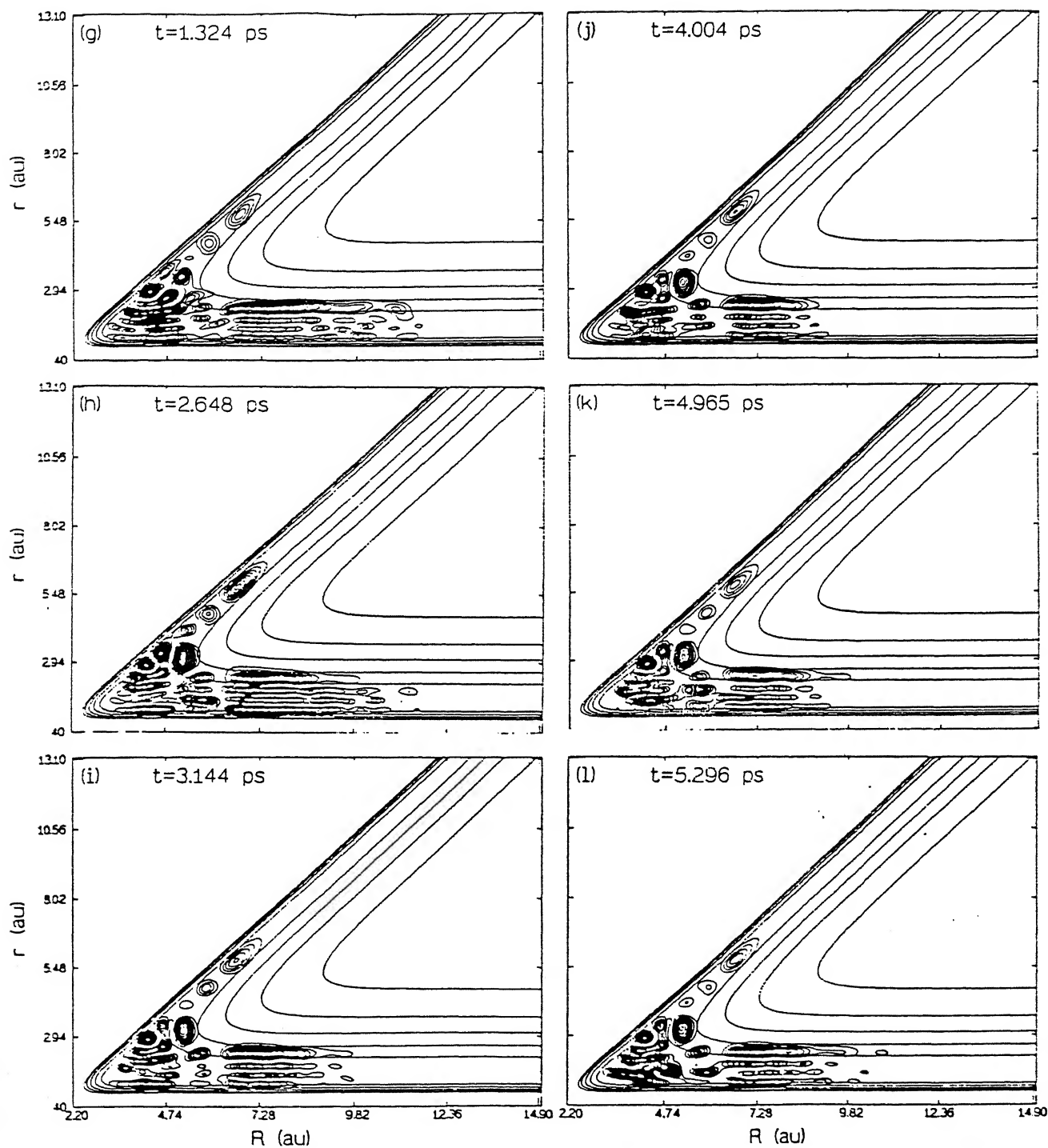
Figure 3.1: Probability density contours of the initial Gaussian wave packet (No.2) with <E> = 0.9924 eV and width, δ = 0.25 a.u. at different times t (indicated inside each box) showing its evolution on the (256×256) potential grid. The total probability density of the WP retained on the grid at different times are: 1, 1, 0.99, 0.99, 0.77, 0.035, 0.01, 6.5×10⁻⁴ and 5.3×10⁻⁴ in a, b, c, d, e, f, g, k and l respectively.

system and the time interval between the recurrences can be connected to the periods of such classical orbits [273]. The natural oscillation of, $|C(t)|$, persists up to 4.85 ps.

The spectral intensity, I(E), (Eq. (2.116)) obtained by a half-Fourier transform of the above autocorrelation data, in the negative energy range is shown in Fig. 3.3. There are two sharp intense peaks corresponding to the two bound states (-0.1281 eV and -0.0328 eV). These values are in agreement with those computed by Sathyamurthy et al [255].

The spectrum in the energy range 0-3 eV is shown in Fig. 3.4 in the form of a $\log_{10} I(E)$ plot. The intense peaks therein would correspond to quasi-bound states and hence to resonances. The spectrum shows a decaying pattern in the energy range beyond 2.4 eV, presumably due to increased noise arising from the fact that we have used a cut-off value of 3 eV for the potential on the grid. Such spectra are expected to be reliable up to 80% of the cut-off potential. The spectrum shows a complicated pattern due to the existence of a large number of closely spaced quasibound states for HeH_2^+. Overlapping contributions to the spectral lines from the neighbouring states persist even after filtering, as indicated by the presence of shoulders on some of the spectral peaks.

We have superimposed, in Fig. 3.5, the I(E) values in the range, E=0.90-1.30 eV on the reaction probability $(P_v^R(E))$ values for the ground vibrational state of H_2^+, reproduced from Ref. [255]. It is clear that some of the peaks in the $P_0^R(E)$ results must be actually made up of several narrower peaks. Alternatively, R-matrix calculations on a finer mesh of E-values would have revealed additional resonances.

It is important to point out that the intensities of the different spectral peaks are dependent on the choice of location of the initial wave function. The latter decides the $\langle E \rangle$ and hence the contributions from different quasibound states. A comparison of the power spectrum obtained from the different sets of calculations reveals the commonality in the resulting spectra. It is also clear from these spectra that there is a sharp resonance near the threshold for each v and v' state of H_2^+ and HeH^+ respectively. They are all
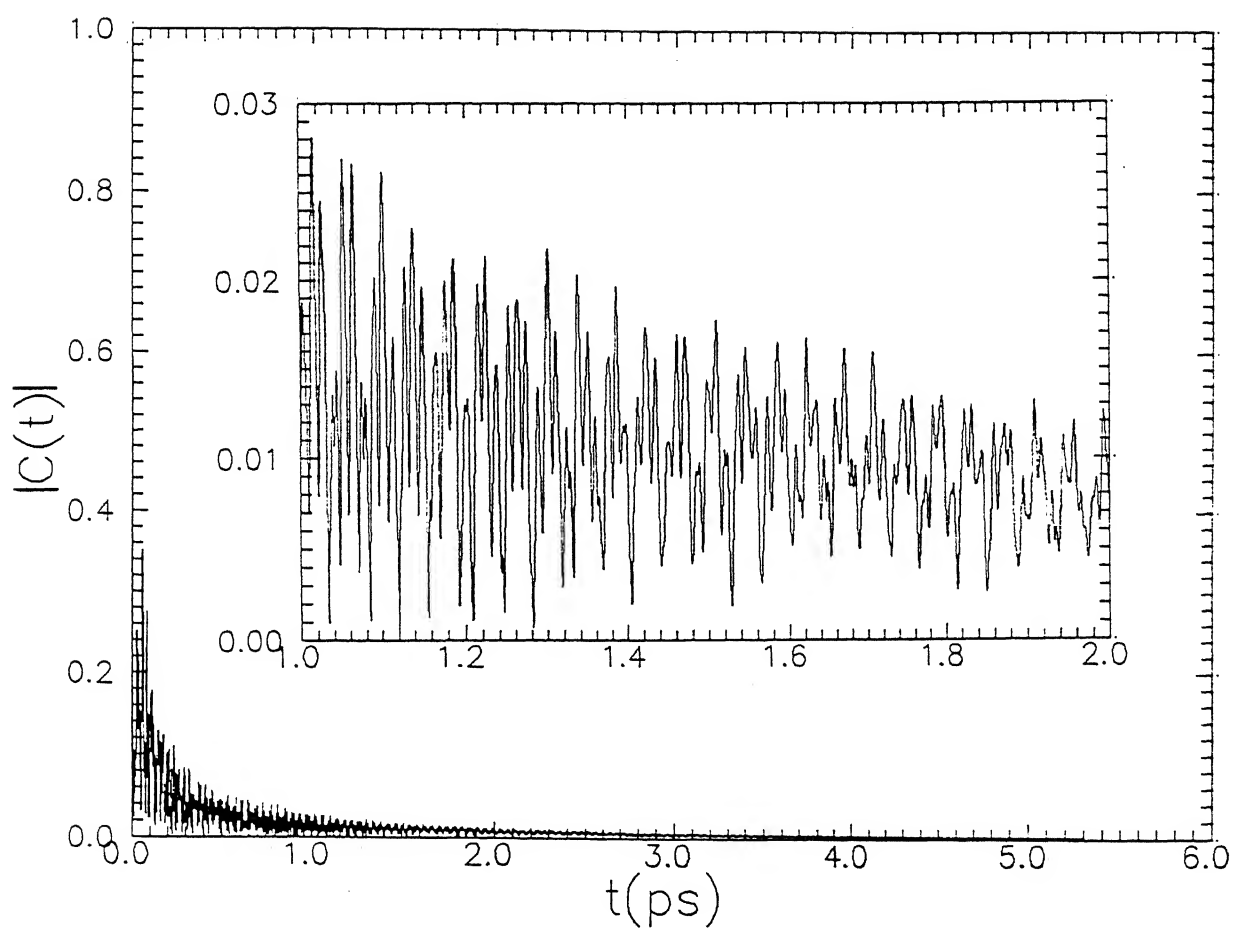
Figure 3.2: Decay of the absolute value of the autocorrelation function, $|C(t)|$ for the WP No.2. The portion of the curve over $t = 1 - 2$ ps is magnified and shown in the inset.
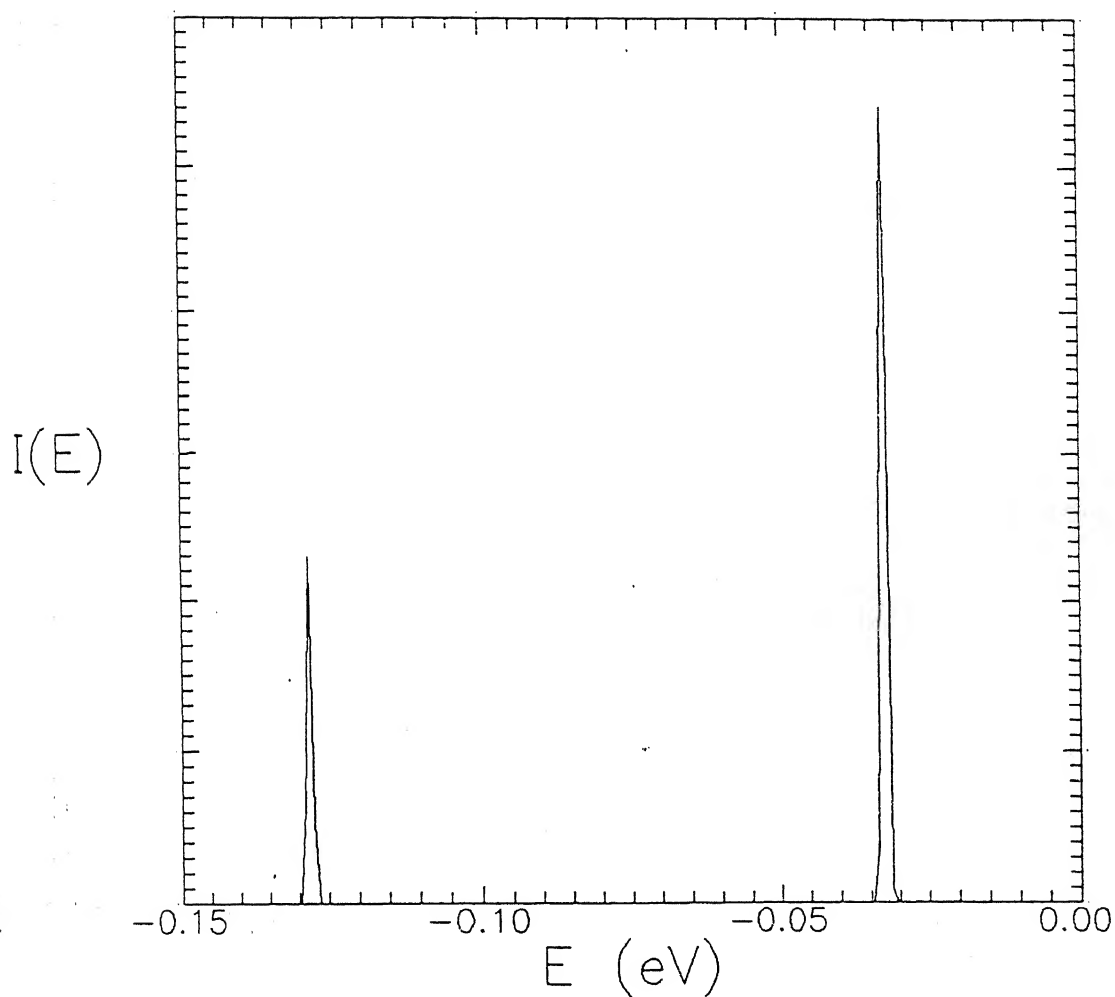
Figure 3.3: Transition state spectrum in the energy range -0.15-0.0 eV computed with the initial Gaussian WP No.2. Two distinct peaks in the spectrum correspond to the two true bound states of the HeH_2^+ complex. Intensity, I(E) is plotted in arbitrary units.
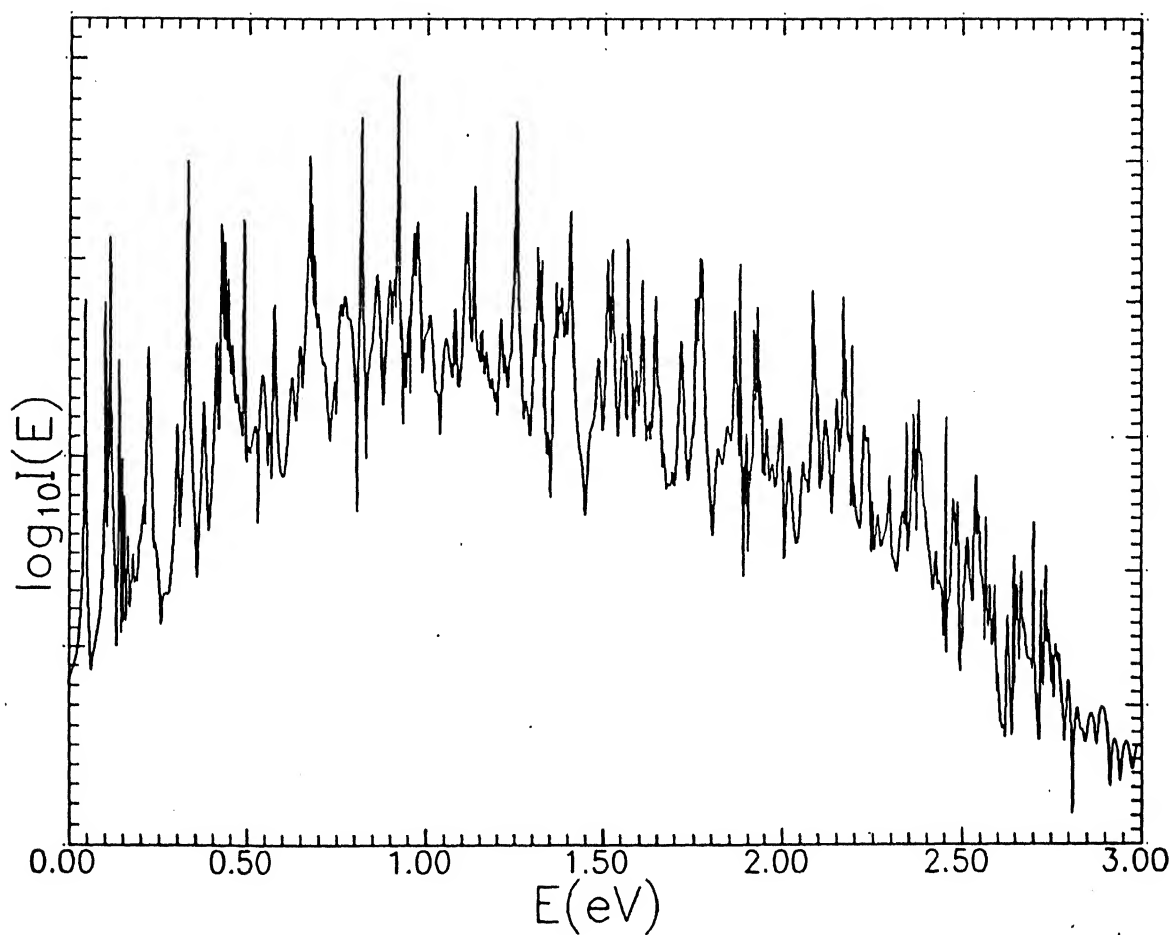
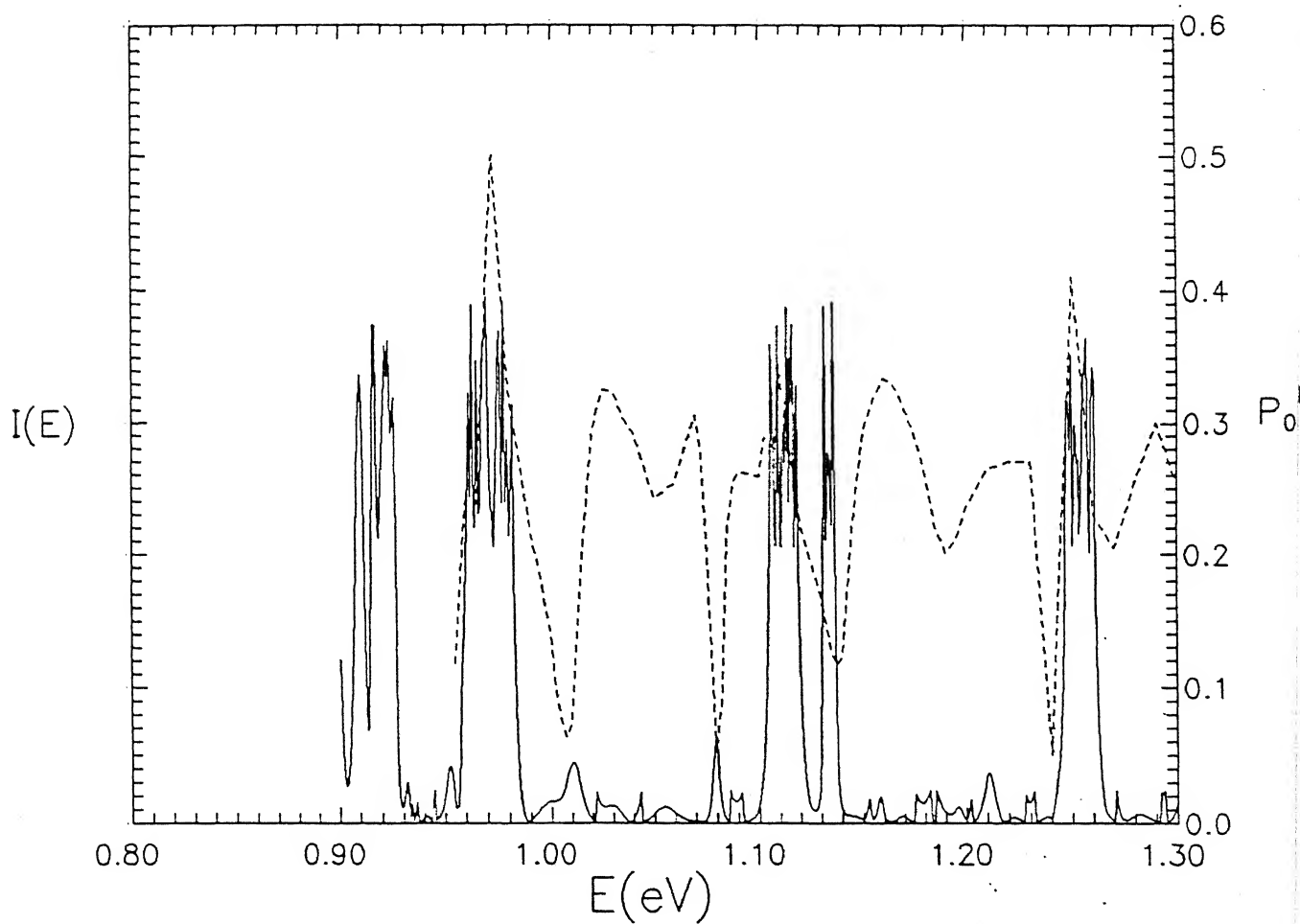Figure 3.4: Power spectrum in the energy range 0.0-3.0 eV computed with the initial Gaussian WP No.2.

Figure 3.5: The reaction probability, P_0^R versus E (dashed line) plot obtained from the results of Ref. [255] superimposed on the I(E)(in arbitrary unit) versus E plot (solid line) obtained with the initial Gaussian WP No.2 in the energy range 0.80-1.30 eV.

listed along with the vibrational eigenvalues for H_2^+ and HeH^+, in Table 3.3. It is worth re-iterating that we also observe a number of resonances which do not correspond to the thresholds.

Results obtained using the WP with $\langle E \rangle$=2.6834 eV is particularly interesting. As can be seen from Fig. 3.6, the decay of the autocorrelation function and the spectral pattern, shown as an inset are much simpler than in Fig. 3.2 and 3.3 respectively. The power spectrum stops abruptly around 2.78 eV (the dissociation threshold, E_{th}^{dis}) and decays smoothly thereafter. It is also clear from Fig. 3.6 that there is a large number of resonances, just below E_{th}^{dis}. This is to be contrasted with the lack of resonances at higher energies reported by Sakimoto and Onda [269]. This could be partly due to the fact that the correlation function predicts the resonances but it does not give any indication of the magnitude of the oscillations in the $P_v^R(E)$ curve.

Since our calculations reveal a large number of resonances corresponding to the quasi-bound states of the HeH_2^+ transient we have analysed some of the eigenfunctions. First we show the probability density contours for the two true bound states in Fig. 3.7(a) and 3.7(b). Then we show the contour plots of $|\Psi_n(E)|^2$ for the two low-lying quasi-bound states in Fig. 3.7(c) and Fig. 3.7(d). The former is dominated by motion along R while the latter is dominated by motion along r. Such states can be characterized by a set of two quantum numbers: $(\nu_{HeH^+}, \nu_{H_2^+})$. Thus the eigenfunctions depicted in Fig. 3.7(a-d) would correspond to (0,0), (1,0), (2,0) and (0,1) in that order.

The wave functions plotted in Fig. 3.7(e-h) show an interesting behavior that is to be expected of those for quasibound states. With increase in R, the nodal structure along r decreases. For example, in Fig. 3.7(e), at small R, the wave function has one node in r direction but with increase in R the node along r ceases to exist. Similarly in Fig. 3.7(f), the wave function exhibits one node along r at short R values and no node along r at large R. In Fig. 3.7(g) and 3.7(h) the number of nodes along r decreases from 2 to

E_n(eV)	E_v^{th}(eV)*	E_n(eV)	$E_{v'}^{th}$(eV)*
0.1458	0.1433	0.9522	0.9543
0.4147	0.4182	1.3138	1.3153
0.6751	0.6751	1.6369	1.6362
0.9140	0.9161	1.9193	1.9181
1.1456	1.1422	2.1634	2.1616
1.3540	1.3540	2.3661	2.3668
1.5525	1.5520		
1.7494	1.7364		
1.9074	1.9074		
2.0647	2.0648		
2.1933	2.2086		
2.3386	2.3385		

Table 3.3: Eigenvalues (E_n) of the resonances near the threshold of various vibrational channels for He+H_2^+(v) $\rightarrow$ HeH$^+$(v')+H reaction. * Results of Ref. [255].

1 to 0 with increase in R. Therefore, it becomes difficult to assign clear-cut quantum numbers based on local modes for those eigenfunctions. With further increase in energy, the motion can no longer be characterised in terms of R or r only. It acquires the characteristics of hyperspherical modes [274], as can be seen from Fig. 3.8(a) for the quasibound state at E_n=0.9661 eV, slightly above the reaction threshold. An attempt to compute the resonant periodic orbit (RPO) [275] at that energy led to locating one at E_{RPO}=0.8861 eV, the difference arising presumably due to lack of zero-point-energy in the classical orbit [276].

The resonance eigenfunction shown in Fig. 3.8(b) corresponds to the threshold of v'=1 and v=4 and therefore shows clearly one node in the HeH$^+$ channel and 4 nodes in the H_2^+ channel indicating that it is indeed a predissociative state of v'=1 and v=4.

As is expected of quantum states, increase in energy is accompanied by increase in the number of nodes in the eigenfunction, as illustrated in Fig. 3.8(b-d). In order to fully characterise them we need to assign two quantum numbers associated with them: (ν_1, ν_3)
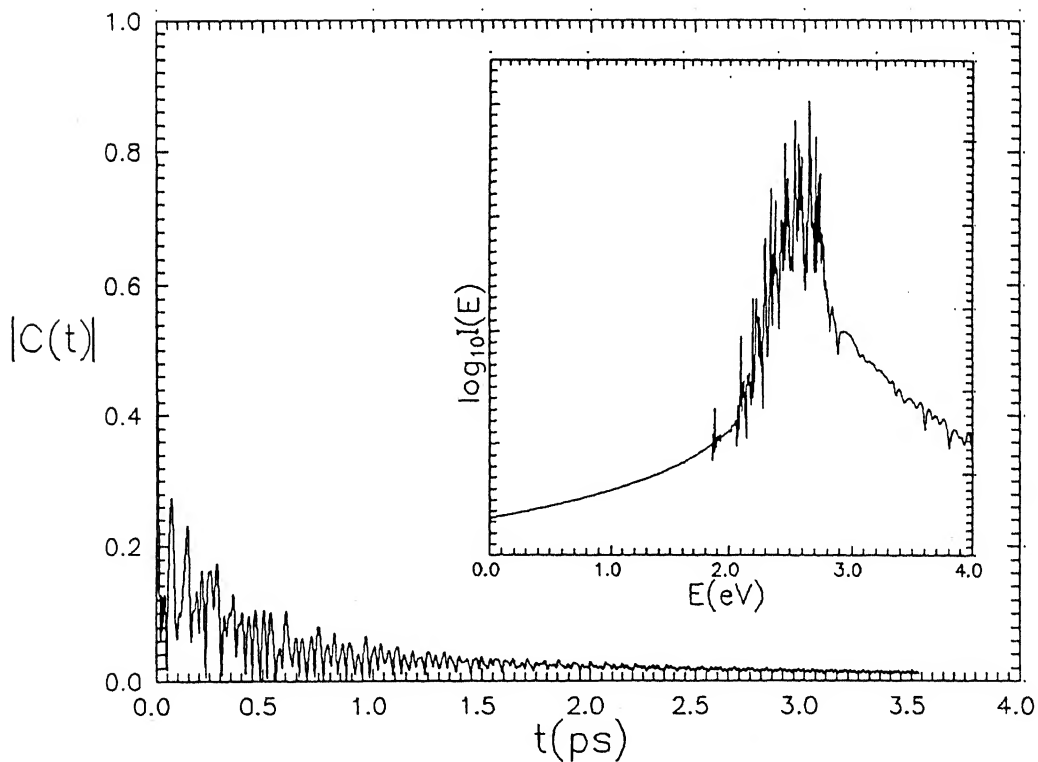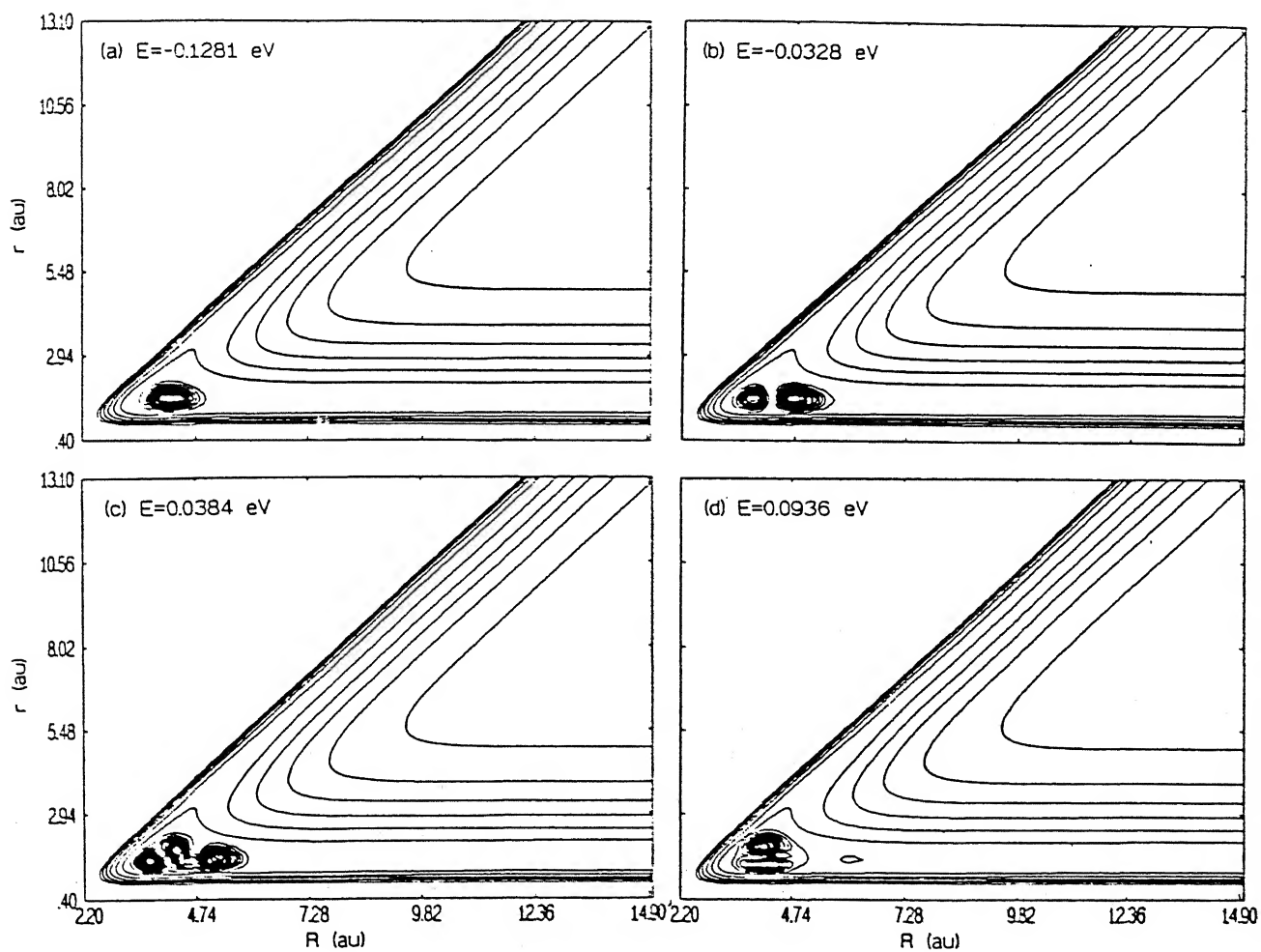
ure 3.6: Decay of the absolute value of autocorrelation function, $|C(t)|$ for an initial ussian WP (No.6) with $\langle E \rangle$=2.6834 eV and $\delta = 0.25$ a.u. The inset shows the corre- nding power spectrum.
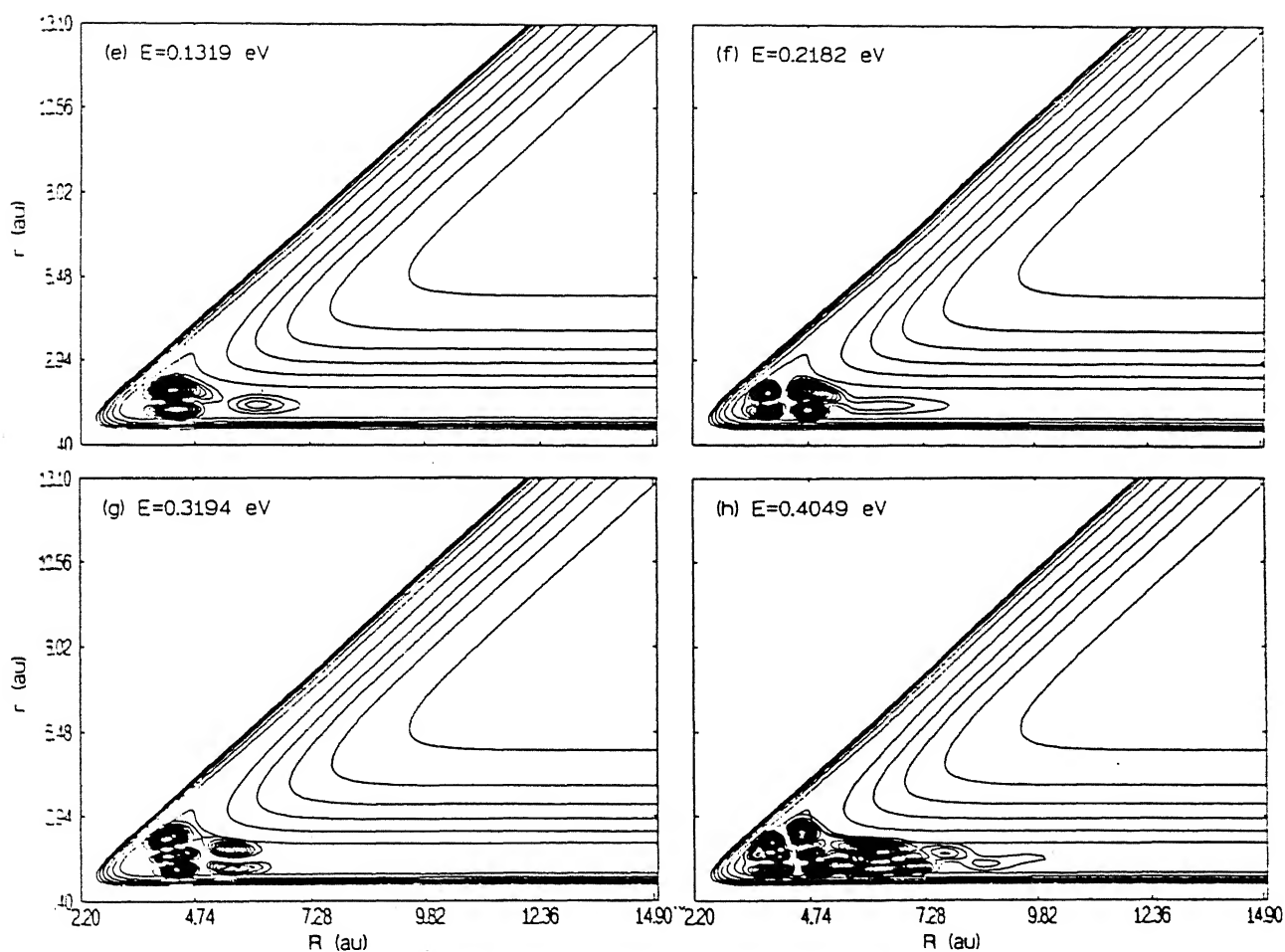
Figure showing four contour plots labeled (a) E=-0.1281 eV, (b) E=-0.0328 eV, (c) E=0.0384 eV, and (d) E=0.0936 eV, with axes R (au) and r (au).

Figure 3.7: Probability density contours superimposed on the potential grid for eight resonance wave functions (a-h) at energies below E_{th}. The eigenenergies, E_n, are indicated in the box as E.
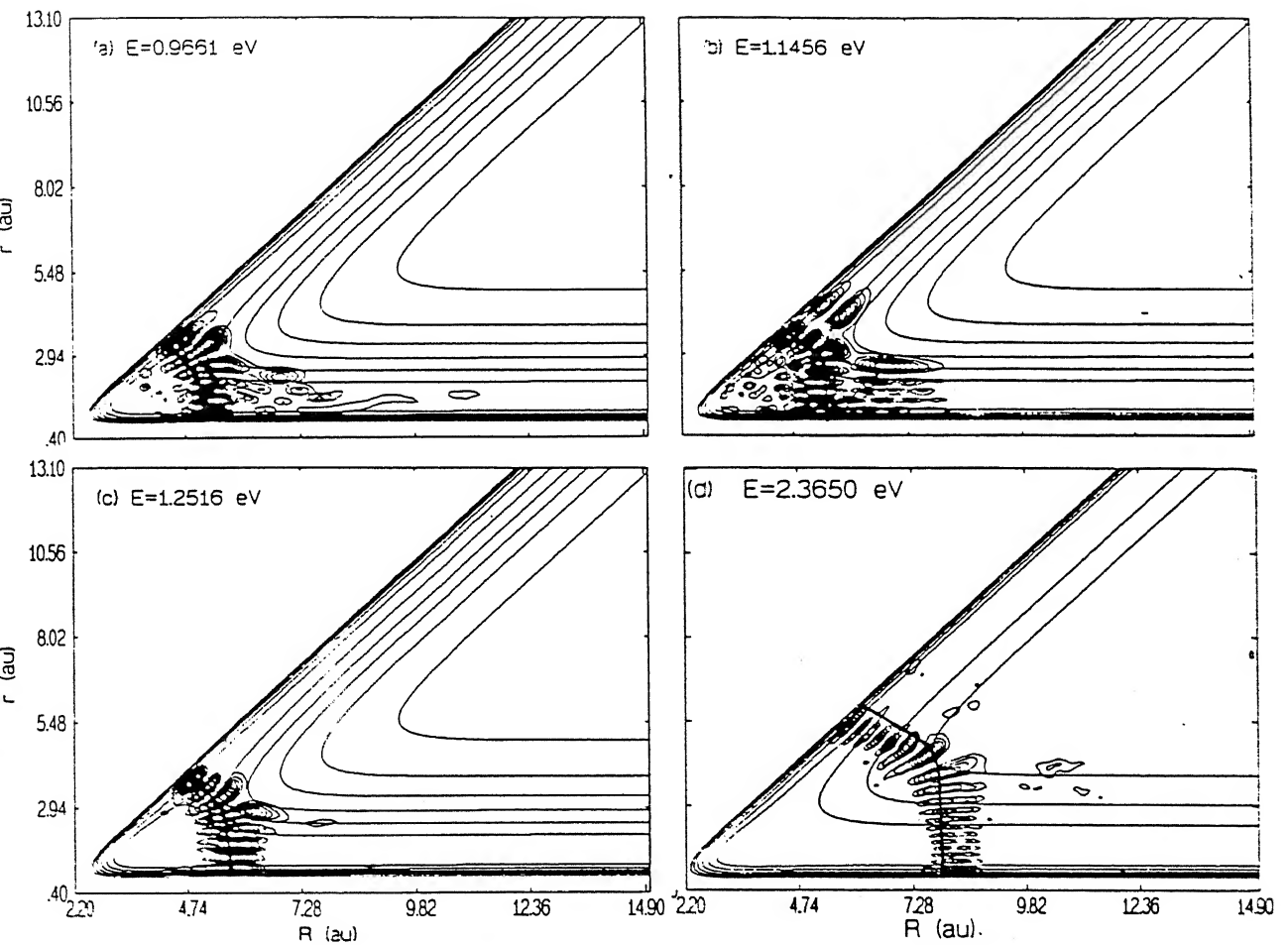
Figure 3.8: Probability density contours superimposed on the potential grid for four resonance wave functions (a-d) at energies above E_{th}. The eigenenergies, E_n, are indicated in the box by E. The number of nodes along the hyperspherical angle are: 6, 7, 8 and 18 for a, b, c and d respectively. The closely lying resonant periodic orbits at 0.8861, 1.0649, 1.2216 and 2.3470 eV are superimposed on the corresponding resonance eigenfunctions to illustrate the classical-quantal correspondence.

where ν_1 corresponds to the hyperspherical radial (ρ) motion and ν_3 to the angular (ϕ) motion. None of Fig. 3.8(a-d) corresponds to an excited state along ρ. Therefore we assign states (0,6), (0,7), (0,8), and (0,18) to the eigenfunctions plotted in Fig. 3.8(a)-3.8(d) in that order. It is worth pointing out that with increase in energy the hyperspherical modes are centered at successively larger ρ values and they also exhibit degeneracy. Understandably the lack of symmetry in the HeH$_2^+$ system prevents us from assigning parity to these eigenstates.

One thing that became clear from the examination of these eigenfunctions is that some of them show a tendency to decay into the (He+H$_2^+$) channel, some into the (HeH$^+$+H) channel and some into neither of the two. Fig. 3.9 shows a function which reveals oscillations characteristic of classical trajectories for large R values and Fig. 3.10 reveals a hyperspherical mode which lives for a long time.

The break-up of the hyperspherical mode into motion that is dominantly in the R or r channel is illustrated in Fig. 3.11(a) for an energy slightly below E$_{th}^{dis}$ and into motion along the dissociative channel as well in Fig. 3.11(b) for an energy slightly greater than the E$_{th}^{dis}$.

Except for the two true bound states shown in Fig. 3.7(a) and 3.7(b) all other eigenstates discussed in this chapter are of quasibound nature and they have finite lifetimes. The lifetime varies with the state. For example, Fig. 3.12 shows a spectral peak fitted to a Lorentzian (Eq. (3.9)) lineshape function for the resonance eigenstate with $E_n = 0.9661$ eV which gives a τ_n value (Eq. (3.10)) of 215 fs. Other resonances at 0.9600, 1.2516, 1.3540 and 2.5336 eV were found to have $\tau_n = 140$, 445, 55 and 366 fs respectively. The one at $E_n = 2.4442$ eV (Fig. 3.10) has a particularly long lifetime of 1.91 ps. Unfortunately there are no other quantal estimates of lifetimes available for collinear (He,H$_2^+$) collisions for us to compare our results with.
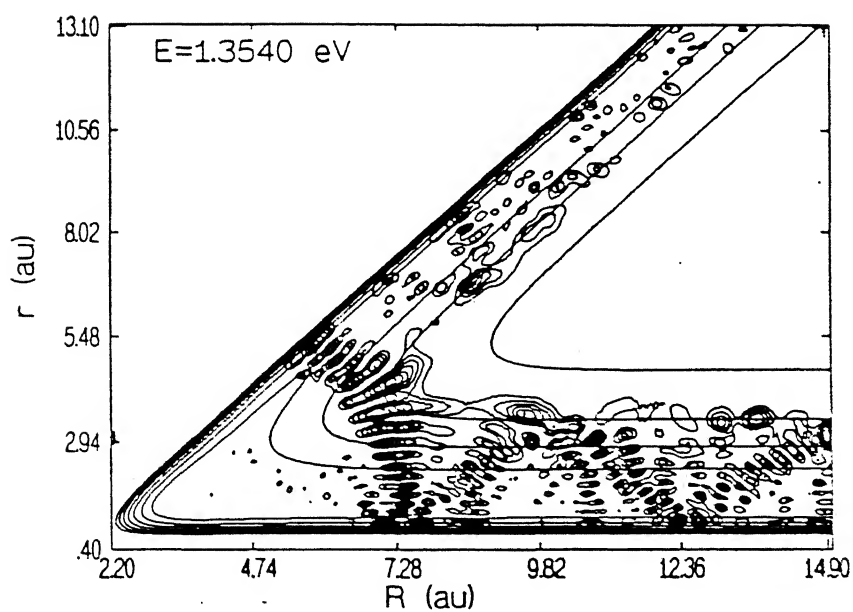
Figure 3.9: Probability density contours superimposed on the potential grid for the resonance eigenfunction corresponding to the eigenenergy = 1.3540 eV showing the oscillation, characteristic of classical trajectories.
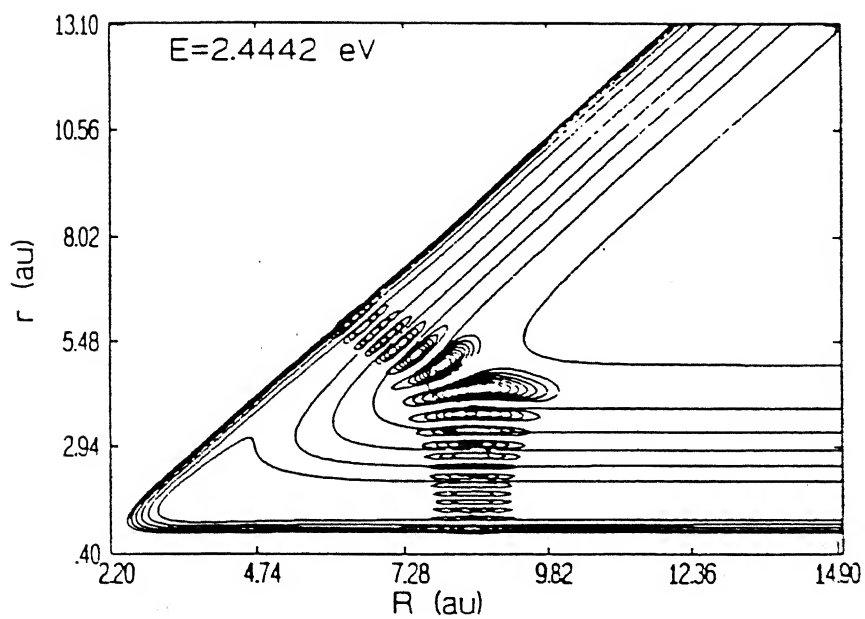
Figure 3.10: Probability density contours for a resonance eigenfunction at E_n=2.4442 eV. It is a hyperspherical mode with 19 nodes and it has a life-time $\sim$ 1.91 ps.
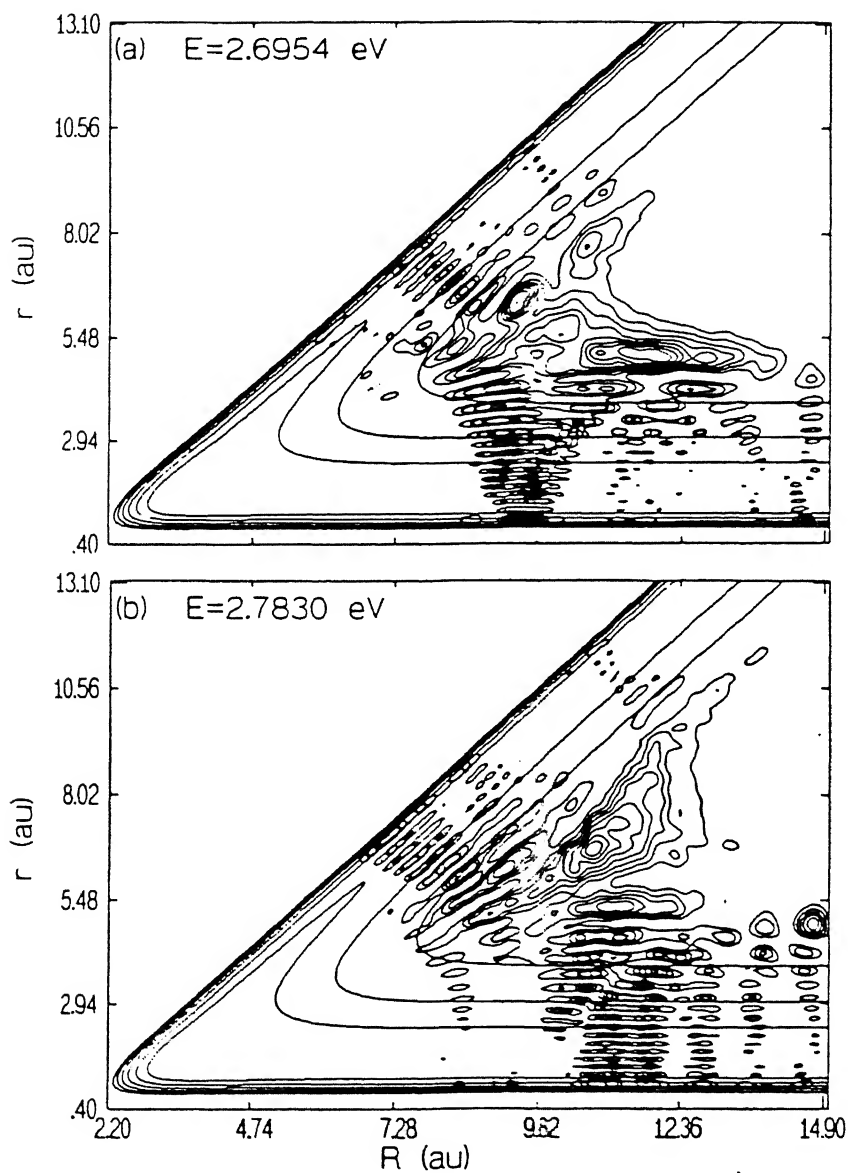
Figure 3.11: Probability density contours of resonance eigenfunctions superimposed on the potential grid at energies (a) slightly below and (b) slightly above E_{th}^{dis}. Eigenenergies are indicated in the box by E.
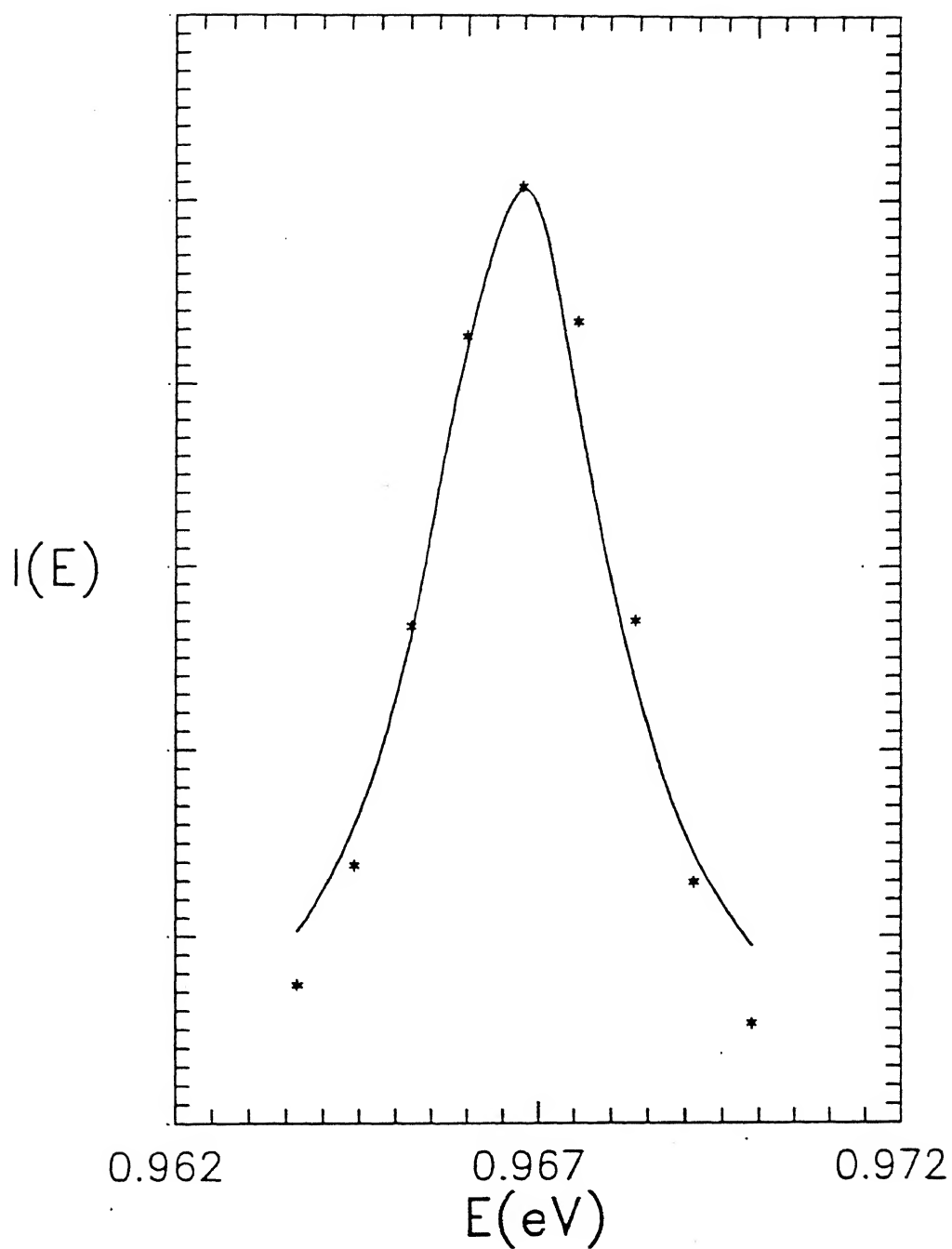
Figure 3.12: Lorentzian lineshape fitting for a typical spectral peak. The dots are the intensity in arbitrary units, I(E) resulting from the transition state spectrum and the solid line is the best fit Lorentzian.

3.3.2 Bound States and Resonances in Collinear HeHD$^+$ and HeDH$^+$

The power spectrum, as obtained from time evolution of WP No.2 (Table 3.1) for collinear HeHD$^+$ is shown in Fig. 3.13 along with the autocorrelation function $|C(t)|$ as an inset. The recurrences in $|C(t)|$ persist until about 3–4 ps. This is reinforced by the probability density plots (not shown) on the potential grid during time evolution, carried out for a total of 5.29 ps. As mentioned earlier, the wave function is absorbed by the NIP (Eq. (3.8)) applied at the grid edges, bringing the norm $< \Psi|\Psi >$ down to $\leq 10^{-3}$ at the end of the time evolution. The peaks in the spectrum correspond to quasibound states and hence to the resonances of the system. Although some of the peaks appear broad due to the overlap with the neighbouring peaks, many others have well resolved structure. This is to be contrasted with the finding on the HeH$_2^+$ system, for which the the spectrum was much more complicated. For HeHD$^+$ the resonances are less in number and are farther spaced.

The transition state spectrum, obtained from time evolving WP No.2 (Table 3.1) along with the $|C(t)|$ as an inset for HeDH$^+$ is plotted in Fig. 3.14. The recurrences in $|C(t)|$ persist till the end of time evolution (5.29 ps), by which time the norm of the wave function has come down to 0.027 . This implies that the lifetime of the HeDH$^+$ complex is more than that of HeHD$^+$ and HeH$_2^+$. It is worth pointing out that the spectrum in Fig. 3.14 is more complicated than that in Fig. 3.13 and that the number of quasibound states is larger and more closely spaced for HeDH$^+$ than for HeHD$^+$ and HeH$_2{}^+$ (cf. Fig. 3.4). Interestingly, the spectra in Fig. 3.13 and Fig. 3.14 share some common peaks, particularly in the low energy region. This is due to the fact that those peaks correspond to the reagent diatomic vibrational thresholds which are the same for both systems.

The spectra obtained from the time evolution of WP No. 1 (Table 3.1) for HeHD$^+$ and HeDH$^+$ are shown in Fig. 3.15(a) and 3.15(b) respectively. Clearly, there are two bound
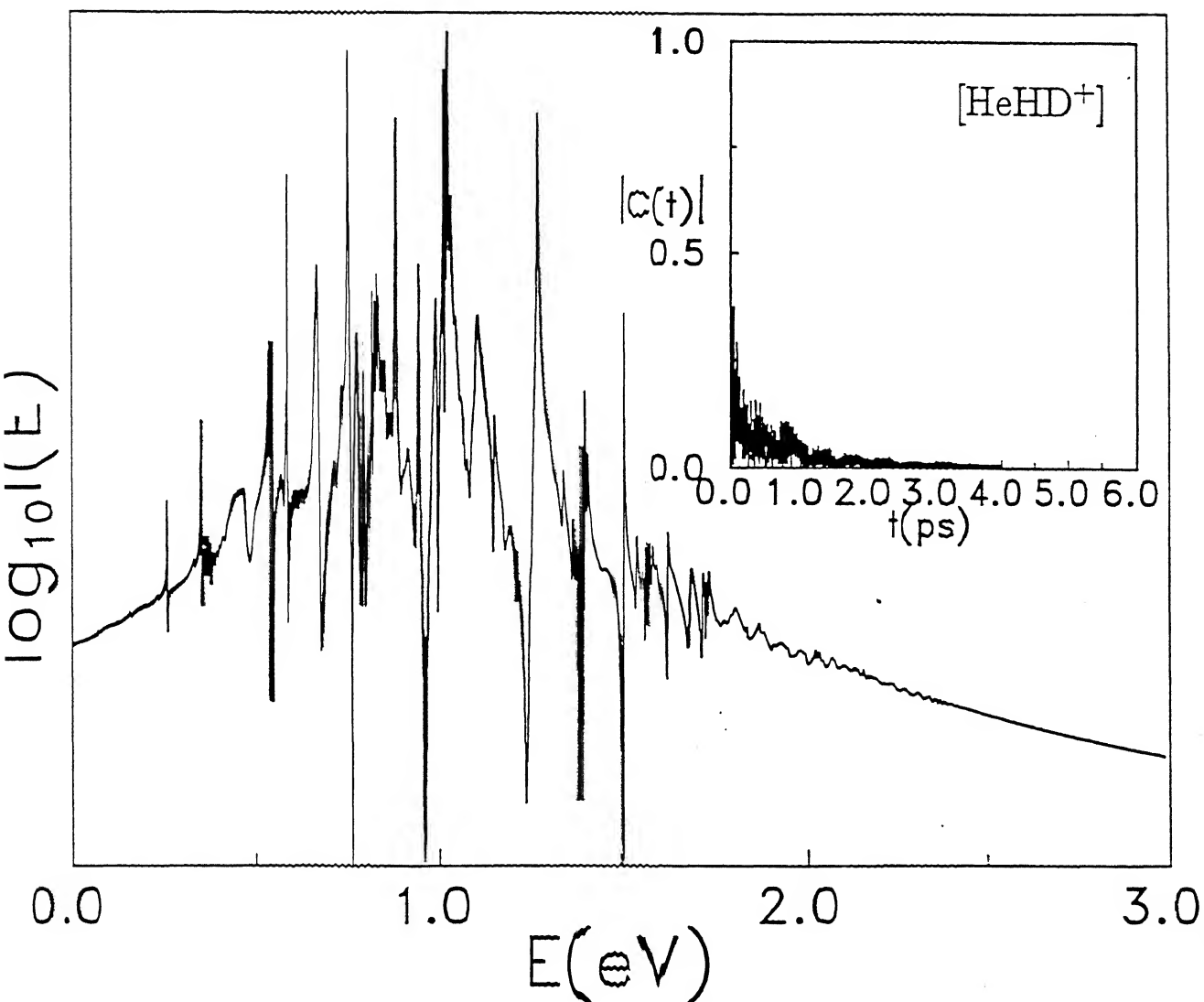
Figure 3.13: Transition state spectrum in the energy range 0-3 eV for collinear HeHD$^+$ computed using the initial Gaussian wave packet No. 2. Corresponding autocorrelation function is shown in the insert.

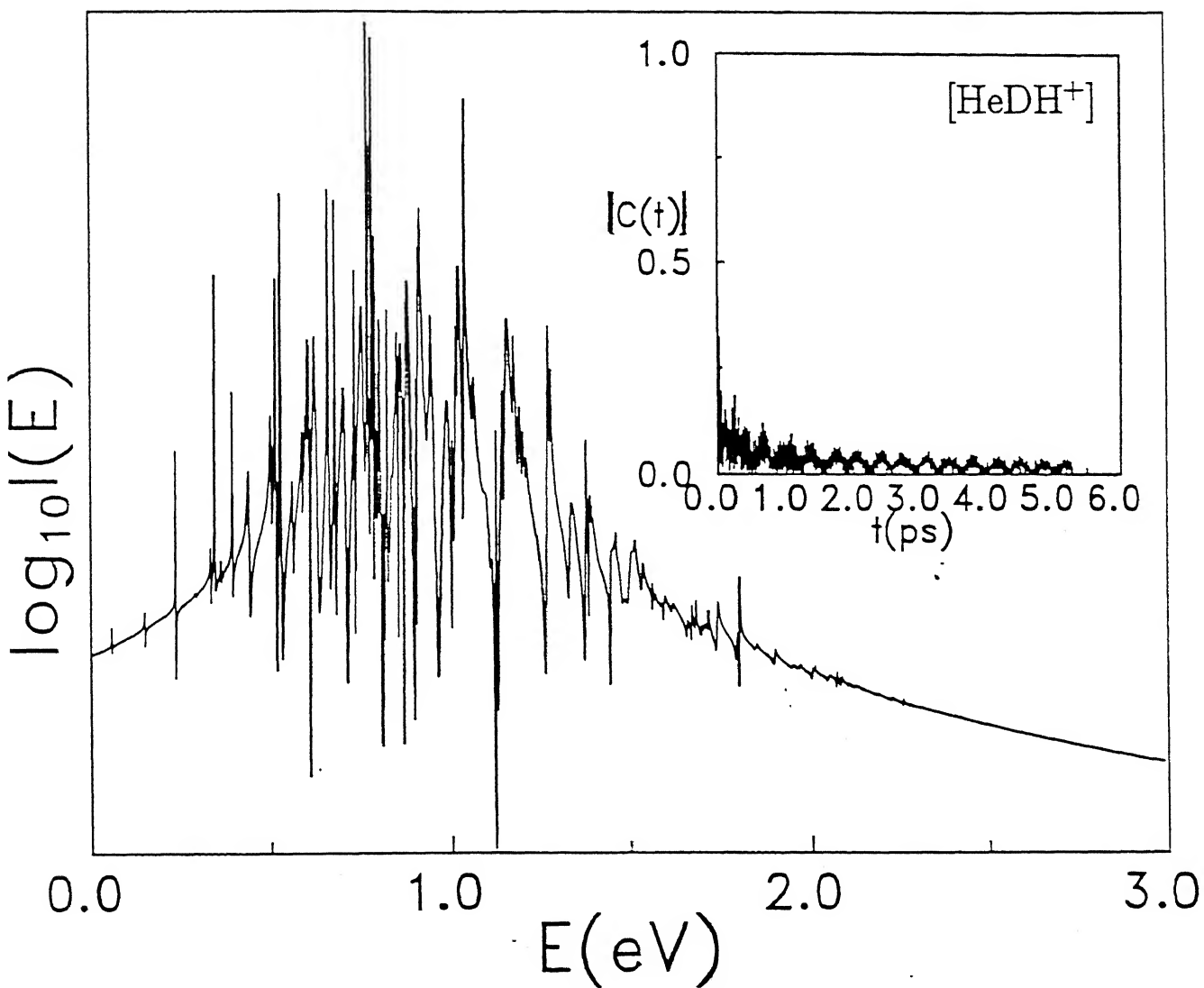Figure 3.14: Same as in Fig. 3.13 for collinear HeDH$^+$, computed using the initial Gaussian wave packet No. 2.
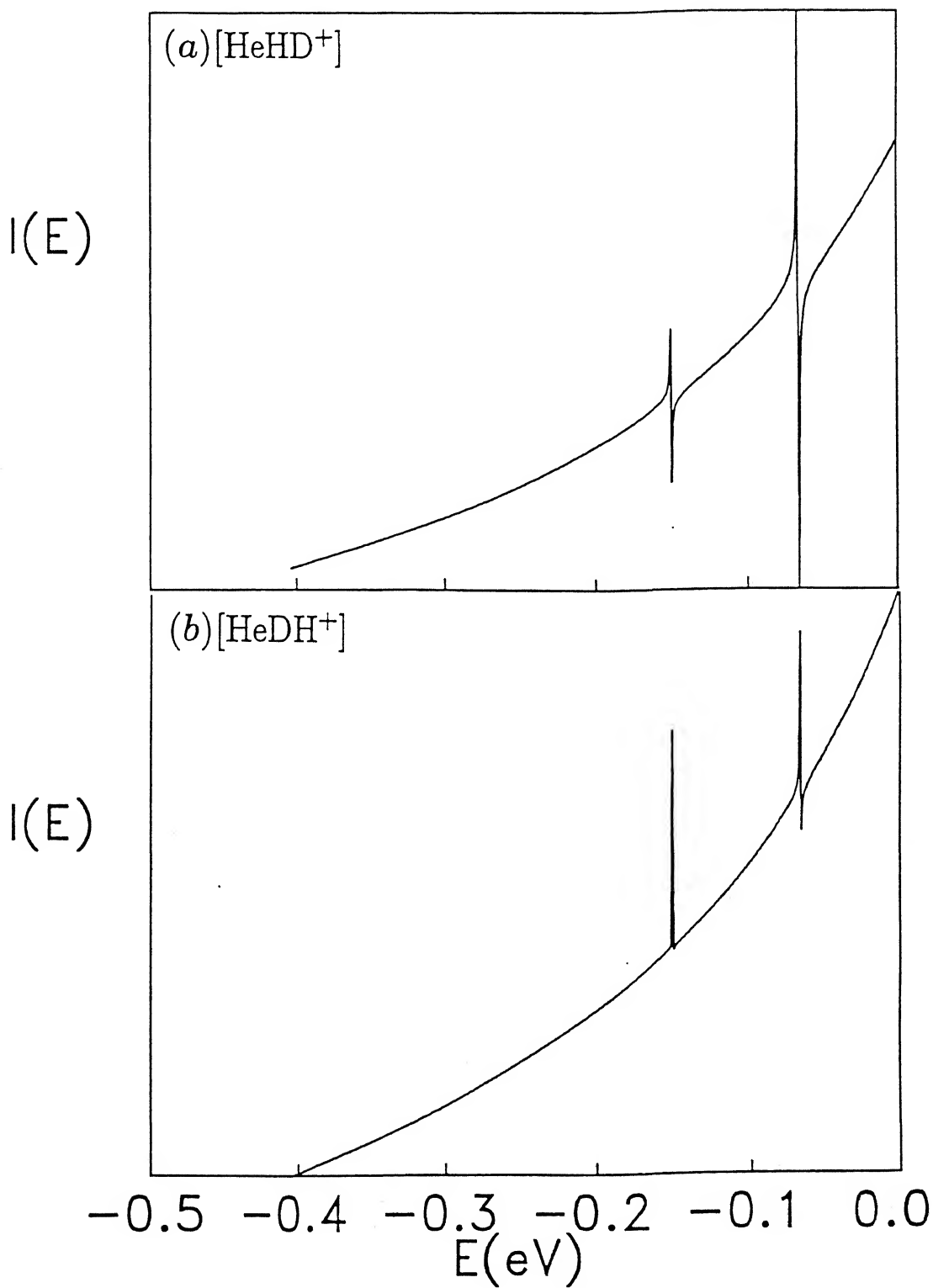
Figure 3.15: Transition state spectrum in the energy range -0.5 - 0.0 computed with the initial Gaussian wave packet No. 1 for HeHD$^+$ (panel a) and for HeDH$^+$ (panel b). The intensity I(E) is plotted in arbitrary units.

states for both systems at E = -0.1507 and -0.0664 eV. The spectra differ only in terms of the intensity of the peaks. It is worth adding that our investigation on collinear HeH_2^+ had also revealed only two eigensates at energy below zero, but at -0.1281 and -0.0328 eV.

Probability density contours of twelve resonance eigenfunctions ($|\Psi_n(E)|^2$) of $HeHD^+$ are shown in Fig. 3.16(a-l). The eigenfunctions in Fig. 3.16(a) and 3.16(b) correspond to the two eigenstates having energy below zero. They correspond to the ground vibrational ($v = 0$) state having no nodes and the first excited vibrational ($v = 1$) state having one node of the complex. The wave function in Fig. 3.16(c) having two nodes corresponds to the $v = 2$ state of the complex of energy 0.2616 eV implying that there are no other bound states for collinear $HeHD^+$. It corresponds to $\nu_P = \nu_R$ (ν_P corresponds to the number of nodes along the product channel ($HeH^+ + D$) and ν_R corresponds to the number of nodes along the reactant channel($He + HD^+$)) progression. The wave functions in Fig. 3.16(d-f), correspond to $\nu_P = \nu_R - 3$ progression. In terms of (ν_R, ν_P) assignment (the spectroscopic ν_3 assigned to the HeH_2^+ resonances corresponds to $\nu_R + \nu_P$ and ν_1 is zereo for these resonances), these are (3,1), (5,2) and (6,3) respectively. This is in contrast to the findings of Skodje et al [100], who obtained the $\nu_P = \nu_R - 1$ and $\nu_P = \nu_R - 2$ progressions for the $D+H_2$ resonances. They did not find any $\nu_P = \nu_R$ progression of the resonances. The two wave functions in Fig. 3.16(g) and 3.16(i) correspond to $\nu_P = \nu_R - 4$ progression and their assignments are (7,3) and (8,4) respectively. The eigenfunction in Fig. 3.16(h), in contrast, has a slightly distorted structure and can be assigned (7,4). The resonances in Fig. 3.16(j) and 3.16(k) are (12,6) and (14,7) respectively which belong to $\nu_P = \nu_R/2$ progression, as is the case with the resonance in Fig. 3.16(i). Finally, the resonance in Fig. 3.16(l) corresponds to the (15,8) assignment and is more reactant channel specific. Therefore it becomes clear from the above discussion that resonances in $HeHD^+$ do not follow any unique progression. There are many other resonances for the system, but they could not be given any clear assignment owing to their complicated structure. We must

(a) E=-0.1507 eV

(b) E=-0.0664 eV

(c) E=0.2616 eV

(d) E=0.8074 eV

(e) E=1.0142 eV

(f) E=1.3443 eV
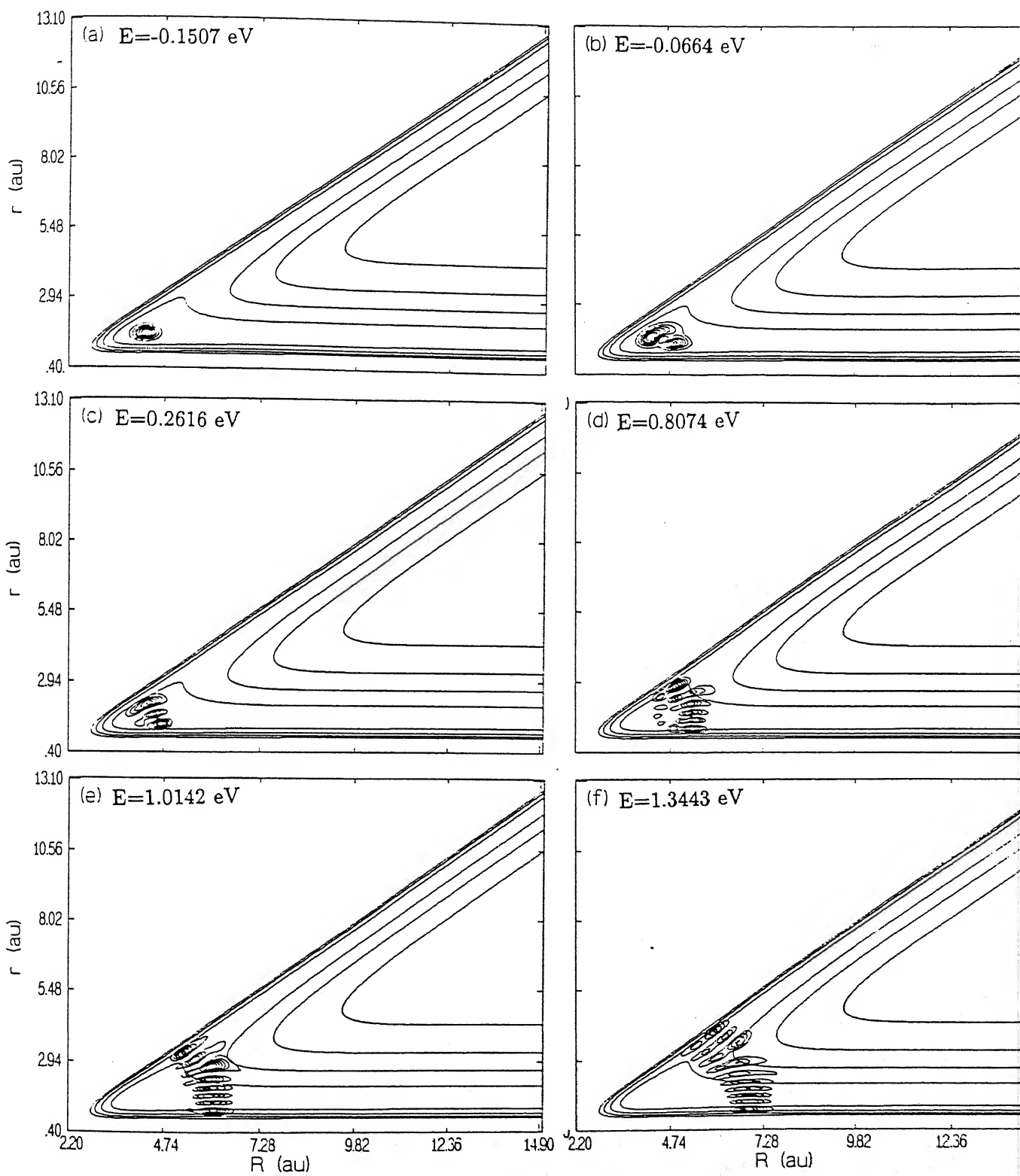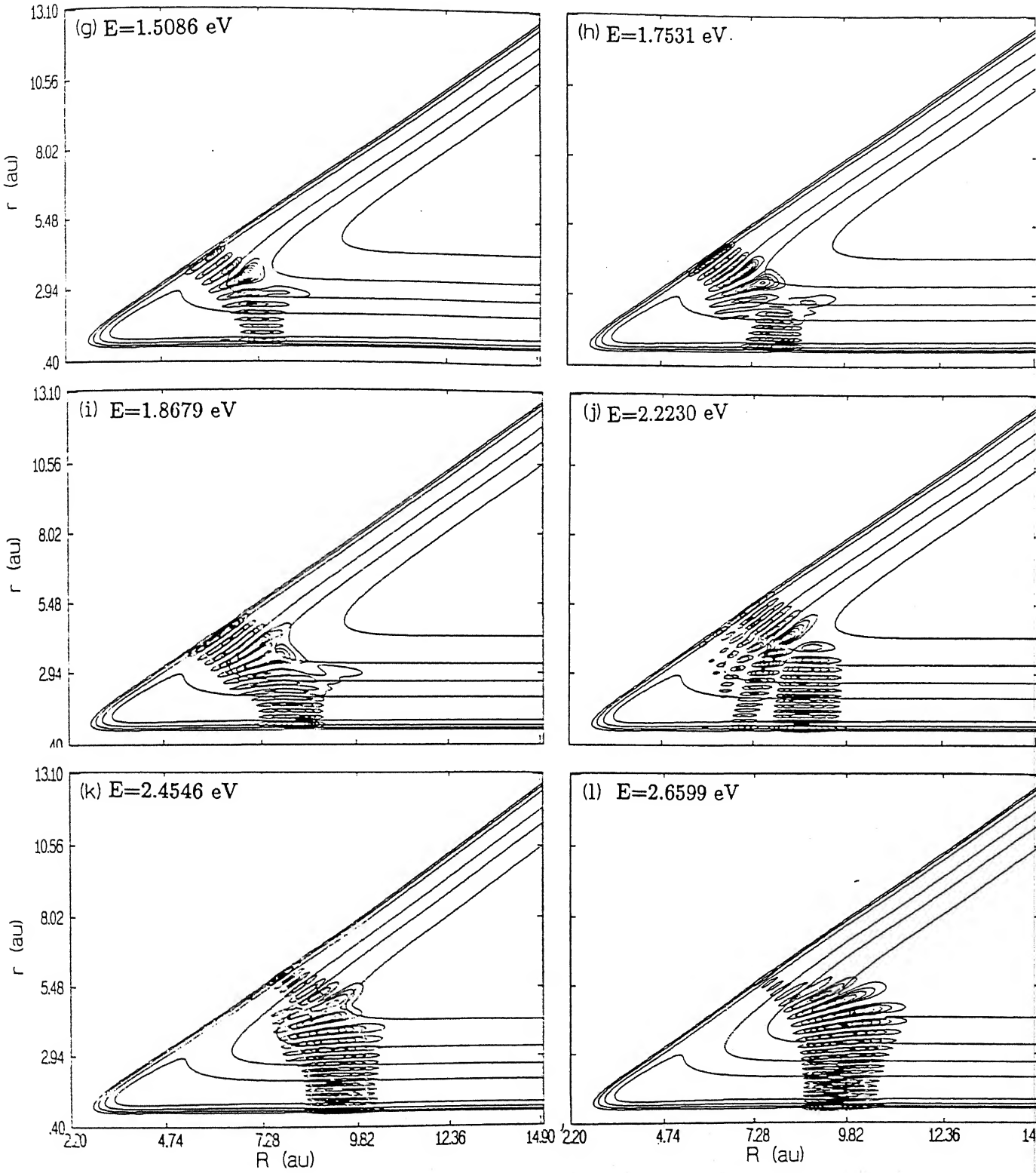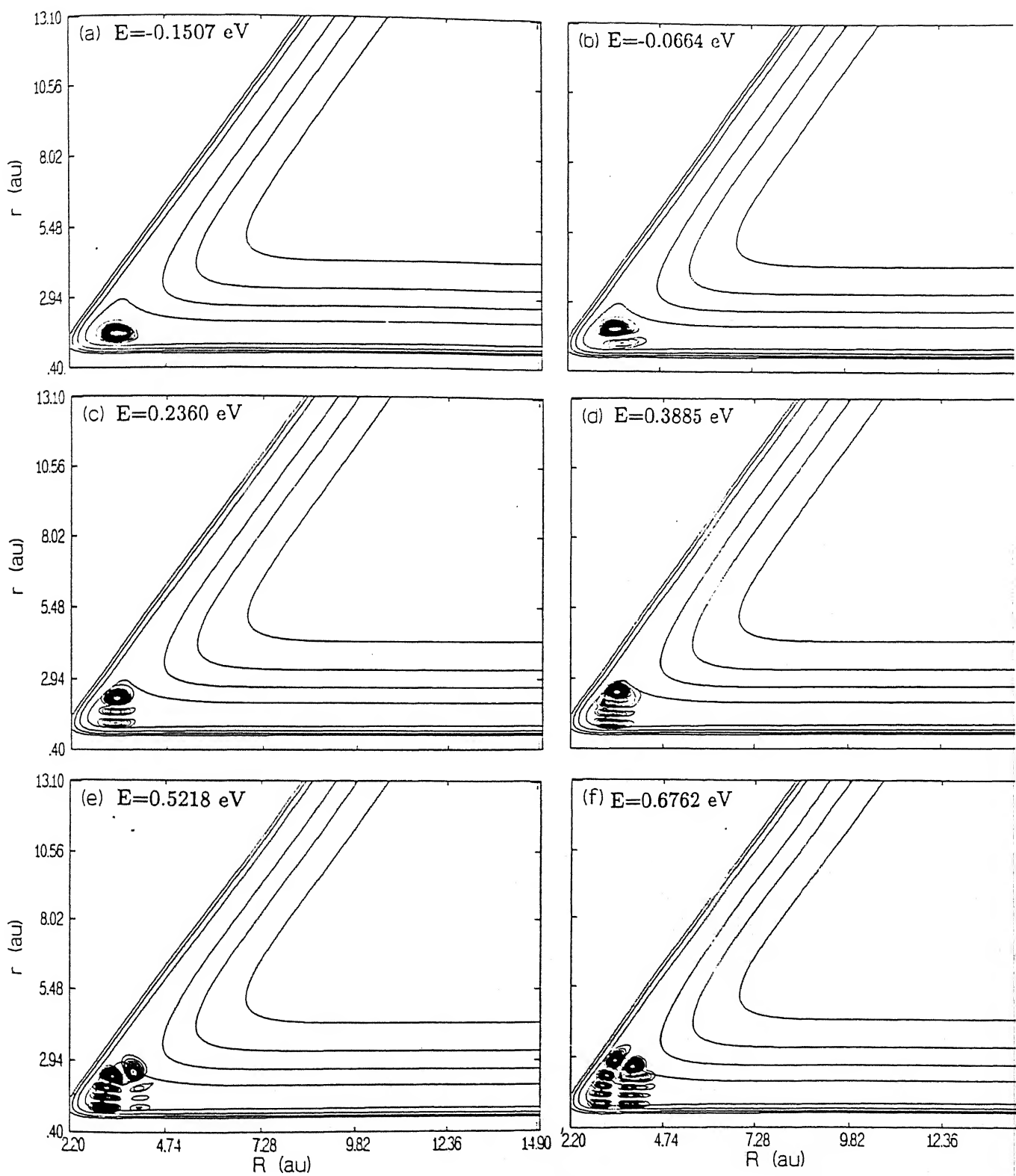
Figure 3.16: Probability density $(|\Psi_n(E)|^2)$ contours of the HeHD$^+$ resonance eigenfunctions superimposed on the potential grid for various eigenenergies indicated in panels (a) to (l).

add here that all the resonances discussed above exhibit the characteristics of hyperspherical modes.

In Fig. 3.17(a-l) the probability density contours of twelve resonance eigenfunctions of $HeDH^+$ are presented. Fig. 3.17(a) and 3.17(b) are the eigenfunctions of two bound states having the same energy as those of $HeHD^+$. Fig. 3.17(a) represents the ground vibrational state ($v = 0$) and 3.17(b) the first excited vibrational state ($v = 1$) of the $HeDH^+$ complex. Interestingly the eigenfunctions for $HeDH^+$ reveal a local mode character. These can be labelled in terms of quantum numbers representing He-D stretching (ν_{He-D}) and H-D^+ stretching (ν_{H-D^+}) respectively. In terms of the above specification, Fig. 3.17(a) and 3.17(b) correspond to (0,0) and (0,1) states respectively. Similarly, 3.17(c) and 3.17(d) represent the (0,2) and (0,4) states, in that order. With increasing energy the nature of the eigenfunctions becomes more complicated and any clear assignment becomes difficult. For example, the eigenfunctions in Fig. 3.17(e) and 3.17(f) exhibit an inverted 'U' shaped structure and the one in Fig. 3.17(g) shows a similar 'U' shaped structure and also the characteristics of a hyperspherical mode. The latter suggests a $\nu_P = \nu_R - 3$ progression and can be labelled as (5,2) in terms of (ν_R, ν_P) as was done for $HeHD^+$. The eigenfunction in Fig. 3.17(h) also can be assigned (5,2). The one in Fig. 3.17(i) has a large probability density build up in the product channel ($HeD^+ + H$), and is difficult to assign. The wave functions in Fig. 3.17(j) and 3.17(k) have a matted structure. We have noticed a similar behavior in the case of H_3^- resonances[102] which are discussed in chapter 4. However, the nodal pattern along the hyperspherical radius (ρ) is nonuniform, particularly in the case of Fig. 3.17(k). If we consider only the nodes along the hyperspherical angle (ϕ) these two states can be assigned (11,7) and (13,8) respectively, in terms of (ν_R, ν_P) nomenclature. The eigenfunction in Fig. 3.17(l) seems to be quantized almost exclusively along the ϕ direction and it contains a total of 25 nodes and can be assigned as (15,10). Many more resonances are found to have complicated eigenfunctions and are not shown here. Actually

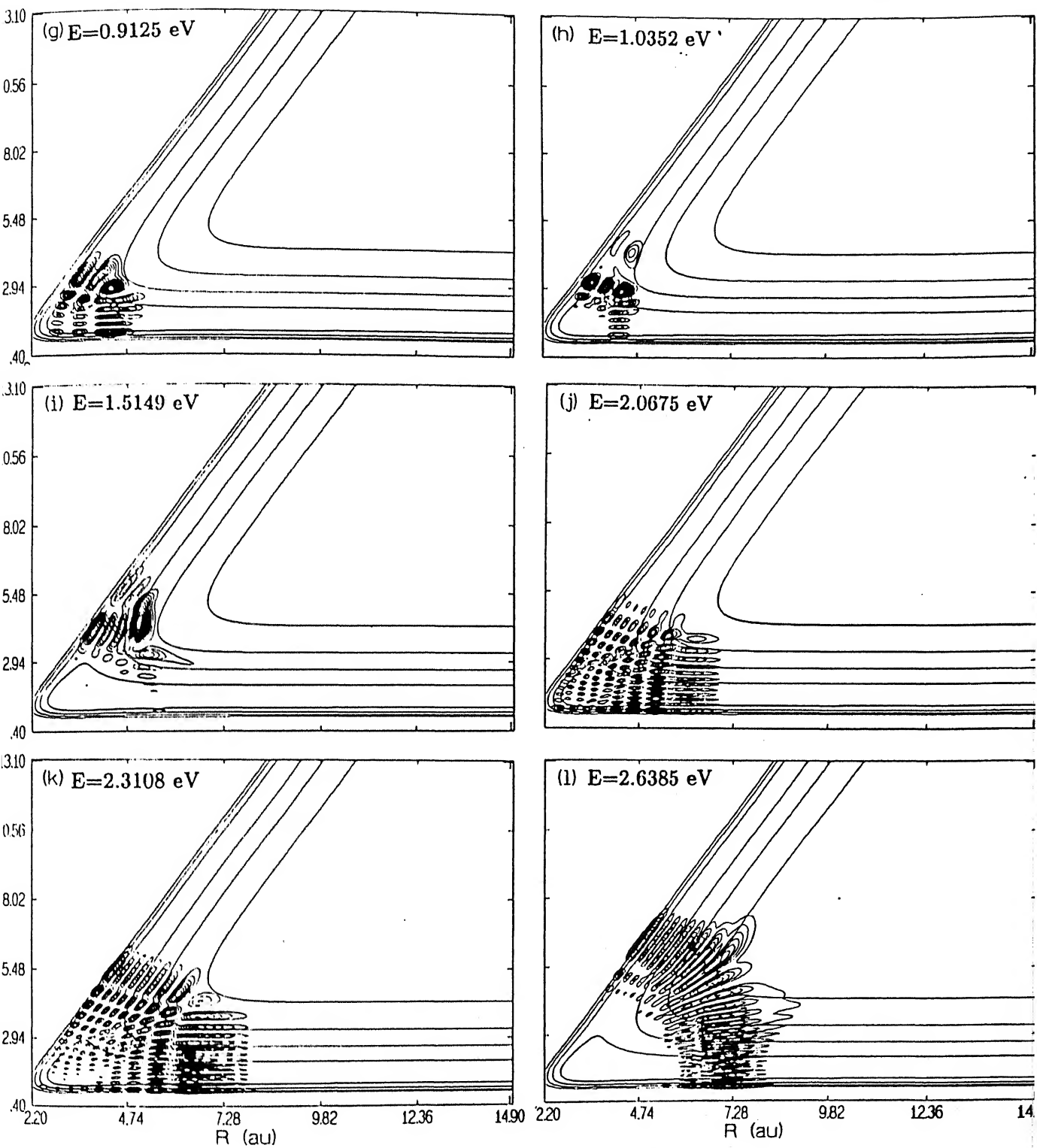Figure with six panels (a)–(f):
- (a) E=-0.1507 eV
- (b) E=-0.0664 eV
- (c) E=0.2360 eV
- (d) E=0.3885 eV
- (e) E=0.5218 eV
- (f) E=0.6762 eV

Axes: R (au) on horizontal, r (au) on vertical.

Figure 3.17: Same as in Fig. 4, for HeDH$^+$ resonances.

| HeHD$^+$		HeDH$^+$	
E_n (eV)	τ_n (fs)	E_n (eV)	τ_n (fs)
0.2616	383	0.9149	510
0.8074	208	1.0352	645
1.0142	647	1.5149	136
1.3443	52	2.0675	480
1.5086	380	2.3108	454
1.8679	22	2.6385	378
2.2230	256		
2.4546	514		
2.6599	60		

Table 3.4: Eigenenergy (E_n) and line-width lifetime (τ_n) of some of the HeHD$^+$ and HeDH$^+$ resonances.

the large density of states makes it nearly impossible to identify all the resonances systematically. As was found for collinear HeH$_2^+$ [268] this could be an indication of the underlying classical chaos.

The lifetimes, of many of the resonances have been estimated from the width of the spectral peaks fitted to the Lorentzian (Eq. (3.9)) and they are listed in Table 3.4. Some of the peaks could not be fitted to a Lorentzian because either they have a δ- function shape or they are not true resonances (but a superposition).

3.3.3 Vibrational State-Selected Reaction Probabilities

The reaction probabilities over a wide range of energies extending up to the three body dissociation threshold (2.78 eV) for the reaction

$$\text{He} + \text{HD}^+(v) \rightarrow \text{HeH}^+(v') + \text{D} \tag{R2}$$
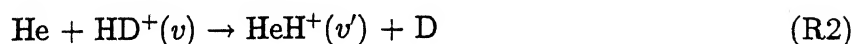
for the initial vibrational states $v = 0 - 3$ of HD$^+$ are plotted in Fig. 3.18(a-d). In all cases, the dynamical threshold coincides with the energetic threshold. The reaction probability increases sharply with energy and then levels off; it rises again and levels off once again.

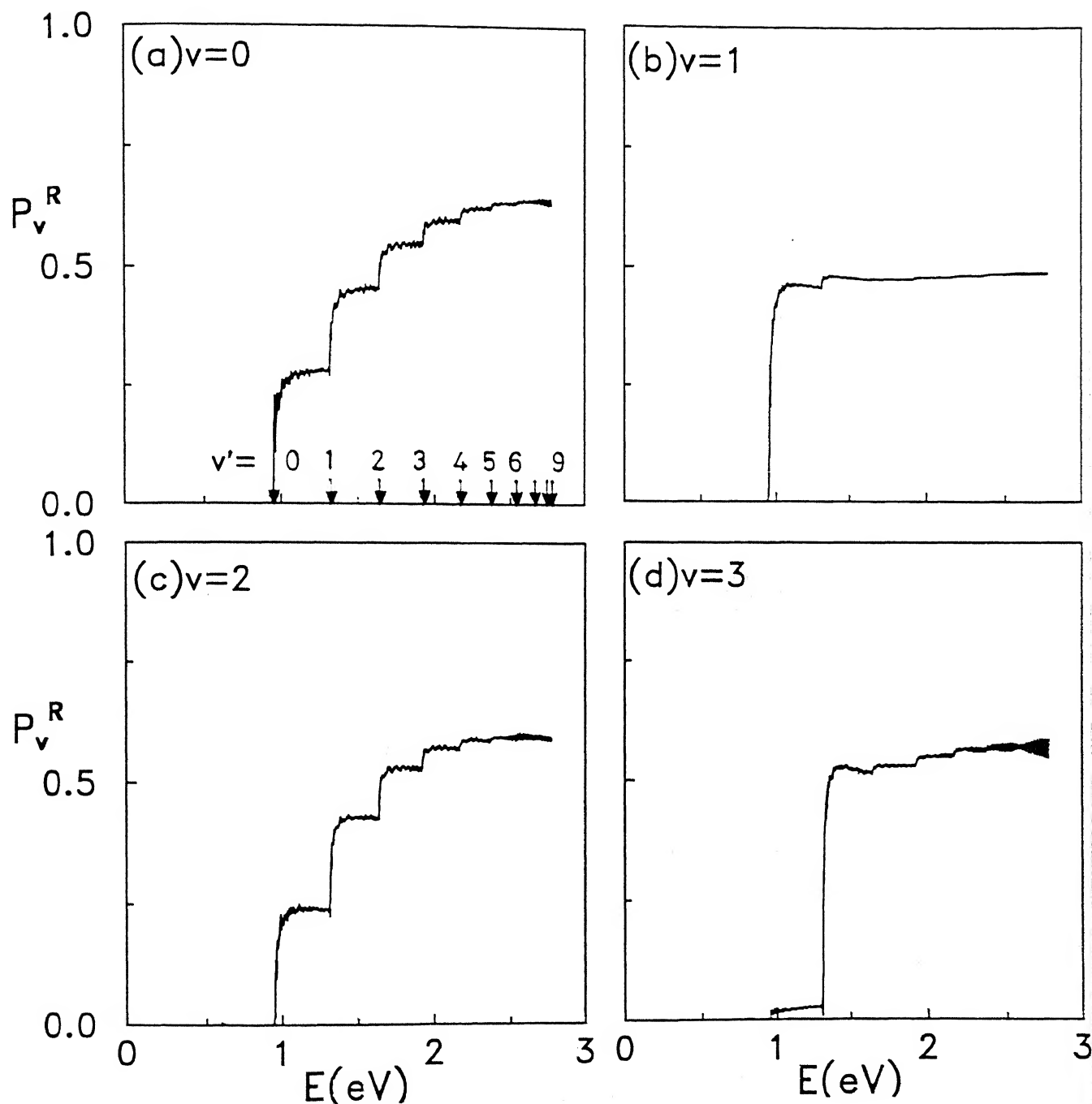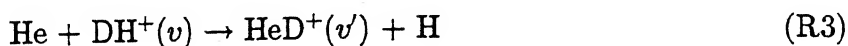Figure 3.18: State-selected reaction probabilities obtained by time-energy mapping of the reactive flux of the wave packet for different initial vibrational states (v) of HD^+ for the reaction $He + HD^+(v) \rightarrow HeH^+ + D$. The threshold energies of various v' channels are marked in the lower abscissa of panel a to illustrate the occurrence of sharp variations in P_v^R near each channel threshold.

This process is repeated until $P_v^R(E)$ approaches a limiting value. This results in an ascending staircase like structure for the $P_v^R(E)$ curve, particularly for $v = 0$ and 2 (Fig. 3.18(a) and 3.18(c)). Each step in the staircase occurs near the onset of a vibrational (v') threshold of HeH$^+$ as can be seen from the threshold values marked on the lower abscissa of the Fig. 3.18(a). The steps in $P_v^R(E)$ in Fig. 3.18(a) clearly show that the prominent resonances for reaction (R2) are of threshold origin [277]. In addition to these threshold resonances, there are other resonances in the transition state spectrum (Fig. 3.13) and they can be correlated with the undulations of smaller amplitude in the plateau regions of the probability curve. The $P_v^R(E)$ curve for $v = 1$ (Fig. 3.18(b)) gives no indication of resonances except one near the $v' = 1$ threshold. The magnitude of the probability for $v = 1$ remains nearly constant over a wide energy range. A similar behavior is seen in Fig. 3.18(d) for $v = 3$. It may be added that the $P_2^R(E)$ values are slightly lower than the $P_0^R(E)$ indicating a slight vibrational inhibition. There is a marked drop in $P_3^R(E)$ when compared to $P_1^R(E)$ near the reaction threshold but at higher energies, $P_3^R(E)$ is clearly larger than $P_1^R(E)$.

Dynamics of heavy-light-heavy reactions has received considerable attention over the years [278]. Oscillatory behavior of $P_v^R(E)$ and the reactive scattering resonances for such reactions in collinear geometries have been well documented in the literature. An explanation for a step-wise behavior in cumulative reaction probability for the reaction in three dimensions in terms of quantized transition state energy levels has been proposed by Chatfield et al [279]. To the best of our knowledge, this is the first time that a clear cut staircase like structure for $P_v^R(E)$ is being reported and identified with threshold resonances.

The reaction probability curves for the reaction

$$\mathrm{He} + \mathrm{DH}^+(v) \rightarrow \mathrm{HeD}^+(v') + \mathrm{H} \tag{R3}$$

are reported in Fig. 3.19(a-d) for $v = 0-3$. The $P_v^R(E)$ curve in each panel exhibits a dense oscillation, suggesting the existence of a large number of very closely spaced quasibound
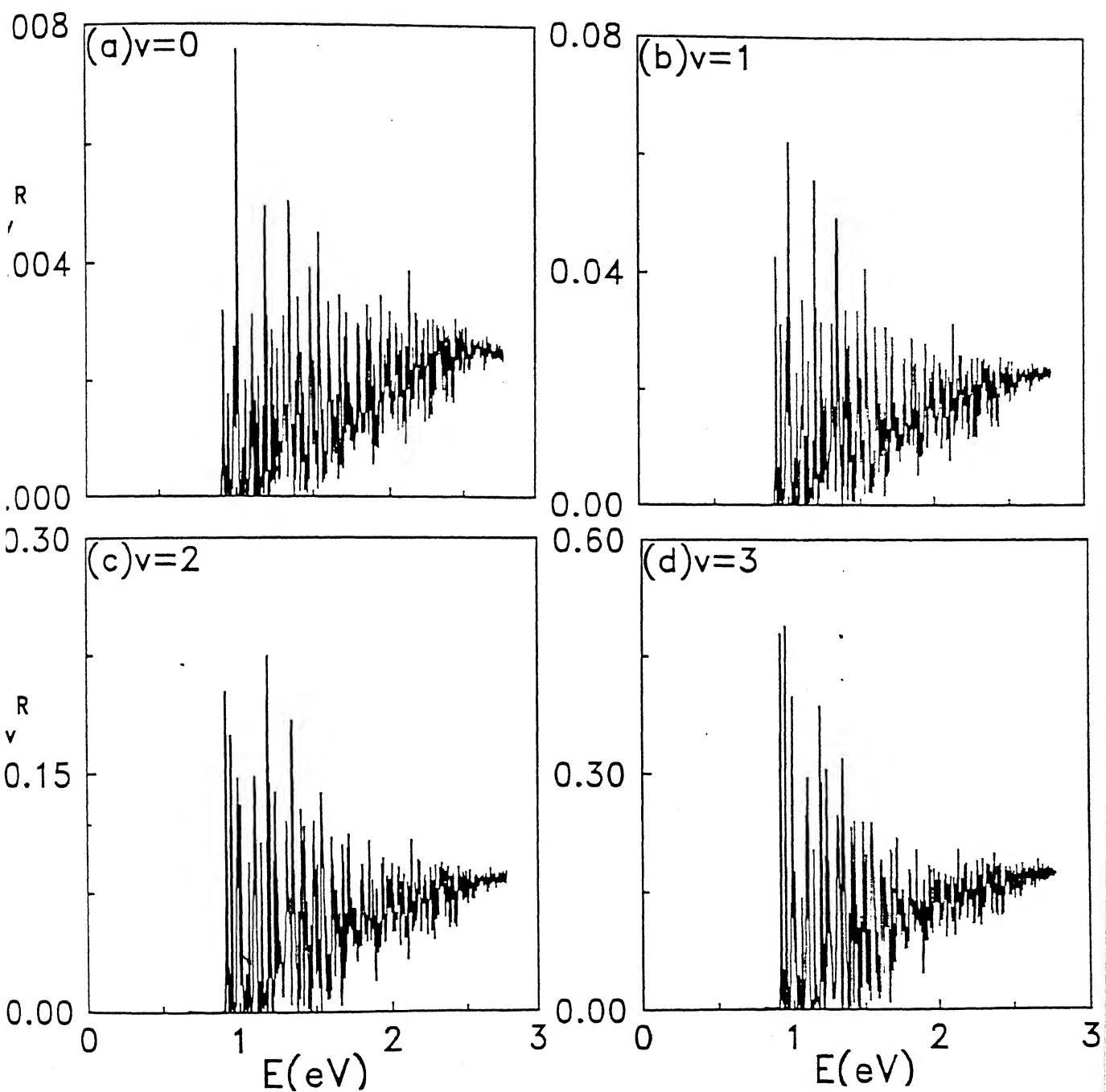
Figure 3.19: State-selected reaction probabilities for different initial vibrational states (v) of DH$^+$ for the reaction He + DH$^+$(v) $\rightarrow$ HeD$^+$ + H.

states at the transition state. This is in agreement with the densely packed structure of the transition state spectrum reported in Fig. 3.14. Although the oscillations in $P_v^R(E)$ are similar for all the v states, their magnitude differs considerably. The probability values for $v = 0$ of DH$^+$ (Fig. 3.14(a)) are close to zero. Snapshots of the WP during time evolution reveal that much of the input translational energy gets converted into the vibrational energy of the inelastically scattered DH$^+$. The reaction probabilities for $v = 1$ (Fig. 3.19(b)) are about 10 times larger than those for the $v = 0$, $P_2^R(E)$ values are about 4 times larger than $P_1^R(E)$ and $P_3^R(E)$ values, in turn, are about a factor of 2 larger than $P_2^R(E)$. Therefore it is clear that there is an overall vibrational enhancement of reaction (R3) in contrast to the vibrational inhibition noted earlier for (R2).

Perhaps the most striking feature of the $P_v^R(E)$ values for reaction (R3) is the large number of oscillations, suggesting "chaotic" behavior in dynamics. While the term "chaos" seems to be well understood in classical mechanics, its meaning and implication in quantum mechanics continues to be the subject of debate. Sathyamurthy and coworkers have reported [263] on the chaos and fractals and their possible relation to quantal reactive scattering resonances for the collinear reaction (R1). More recently we have tried to characterize the quantal chaos in this system by analysing the transition state (TS) spectra and the results are documented in chapter 5. While many of the peaks in the TS spectrum (Fig. 3.13) for collinear HeHD$^+$ could be interpreted in terms of threshold resonances for the reaction (R1) no such explanation is readily available for the TS spectrum of collinear HeDH$^+$. There seems to be a direct link between the oscillations in $P_v^R(E)$ and the large number of oscillation in the TS spectrum in Fig. 3.14.

3.4   The Negative Imaginary Potential Anomaly

In section 2.3 we have discussed the applicability of NIPs when used in conjunction with the numerical time evolution schemes. In this section we compute the $P_v^R(E)$ values for
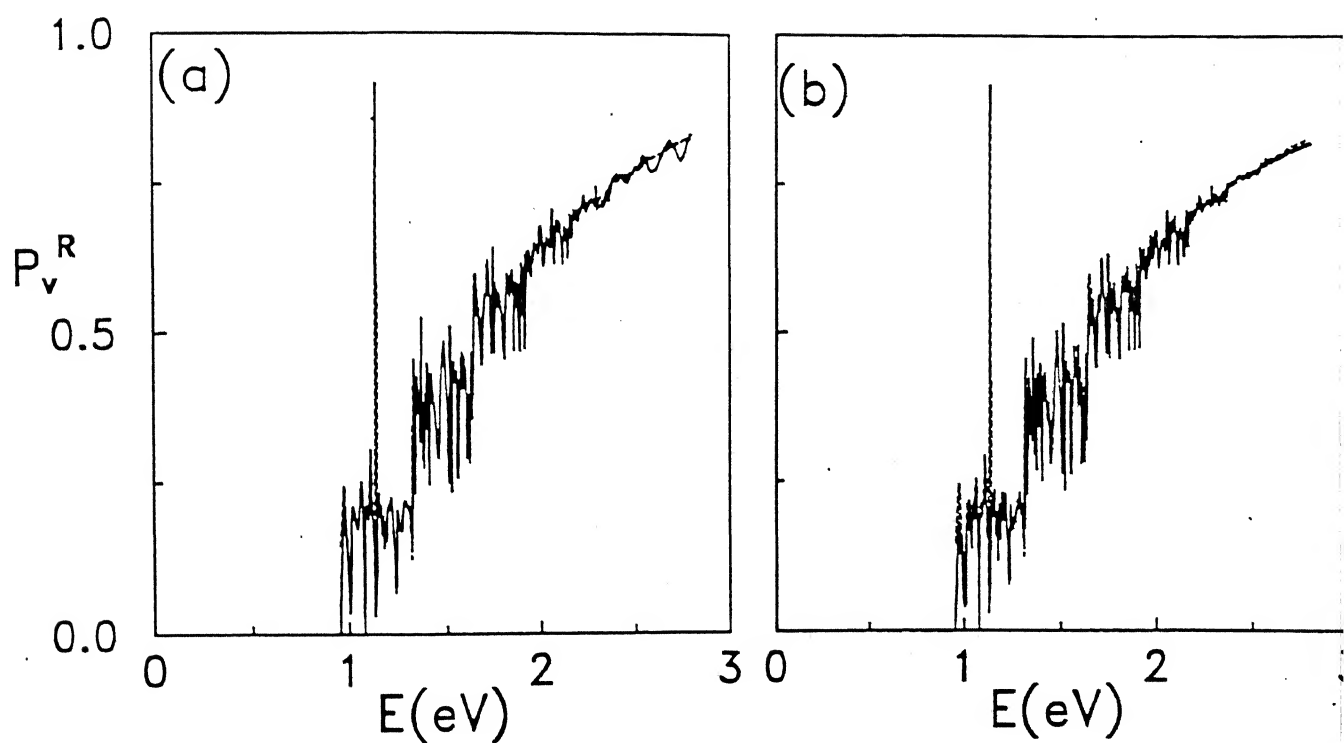
Figure 3.20: State-selected reaction probabilities for the reaction He + H$_2^+(v = 0) \rightarrow$ HeH$^+$ + H, (a) computed by adding NIPs to the real potential (solid curve) and (b) computed by using a masking function (solid curve). The TIQM results for the same (Ref. [269]) are plotted as dashed curves.

the reaction (R1) both in presence as well as in absence of NIPs. We have used the FFT method for the spatial evolution of the WP and the SO method for its time evolution. The SO method revealed an exponential damping of the WP in presence of the NIP in section 2.3. However the Hamiltonian, becoming complex in presence of a NIP, does not preserve the time reversal symmetry of the TDSE and possibly results in an anomaly.

In Fig. 3.20(a) we show the $P_0^R(E)$ values for the reaction (R1) (solid curve) computed in presence of the NIP (eq. (3.8)) superimposed with the time-independent quantal values of the same reported by Sakimoto and Onda [269]. We have used the $\phi_0(r)$ corresponding to the extended Rydberg potentials of H_2^+, computed by the FGH method [241], in the initial wave function (Eq. (2.124)). The same calculation was repeated several times by varying the height and width of the NIP. The $P_0^R(E)$ values show the artificial oscillation at higher energies near the onset of collision induced dissociation. The $P_v^R(E)$ values computed by using the masking function (Eq. (3.13)) for damping do not reveal such oscillations and are presented in Fig. 3.20(b) (solid curve). The latter $P_0^R(E)$ values are also in agreement with those obtained by Sakimoto and Onda (dashed curve). The $P_0^R(E)$ values obtained by Balakrishnan and Sathyamurthy [167] using a FFT-SIL propagator also do not reveal any oscillation and are in excellent agreement with the latter calculation. Balakrishnan and Sathyamurthy have used a damping function derived from the Neuhauser and Baer's linear absorbing potential (Eq. (3.6)) and multiplied it with the time evolved WP at the end of each time step without adding it directly to the real potentials at the grid points. The damping function derived in this way is real and exponential and preserves the Hermitian property of the Hamiltonian.

The implication of the above results is that the artefact in the numerical calculations result, particularly at higher energies, when NIPs are added to the real potentials at the grid points. The artefact disappears when an exponential damping function resulting from NIPs ($e^{-i\Gamma\Delta t/\hbar}$, $\Gamma = -iV_0$) or any other real damping function (e.g. the one in Eq. (3.13))

is used. This way of damping can be achieved more easily than the use of NIPs. The prescription outlined by Taylor and coworkers [236] on the use of the NIPs in conjunction with the CP scheme follows the latter idea and is free from anomaly since the Hamiltonian never becomes complex.

3.5 Summary and Conclusion

We have computed the transition state spectrum of all three transients, HeH_2^+, $HeHD^+$ and $HeDH^+$ by the spectral quantization method and the reaction probabilities ($P_v^R(E)$) for (He,HD^+) and (He,DH^+) collisions through a time–energy mapping of the reactive flux of the WP. We have found that the spectra for HeH_2^+ and $HeDH^+$ are dominated by a large number of TS resonances compared to that for $HeHD^+$, for which the threshold resonances seem to dominate. There are two bound states found for all three transients. The analysis of resonance eigenfunctions from their nodal progression reveals the local mode behavior at lower energies and the hyperspherical mode behavior at higer energies. A comparison of the transition state spectrum of the three transients reveals that the density of state is largest for $HeDH^+$. The recurrences in the $|C(t)|$ persists till the end of the time evolution for $HeDH^+$ implying the existence of long lived resonances for this system when compared with the other two. The classical resonance periodic orbits are superimposed with the quantal resonances of HeH_2^+ to establish the classical-quantal correspondence. The energy resolved reaction probabilities for reaction (R2) reveal a characteristic staircase like structure which can be related to the threshold resonances, particularly for $v = 0$ and 2. In contrast, the $P_v^R(E)$ for reactions (R1) (computed by Balakrishnan and Sathyamurthy [167]) and (R3) are highly oscillatory in keeping with their densely packed transition state spectra. This also suggests the possible chaotic dynamical behavior of (R3) for which the classical trajectory dynamics would be worth investigating.

Chapter 4

Transition state Resonances and Dynamics of Collinear (H^-, H_2) Collisions

4.1 Introduction

Reactions involving hydrogen atom and hydrogen molecule and their ionic counterparts are of fundamental interest to the molecular dynamicists as they represent some of the simplest prototype exchange reactions. Two of them, viz., $H + H_2$ and $H^+ + H_2$ have been studied extensively both experimentally and theoretically [106, 279, 280]. However, much less is known about the reaction involving H^-:

$$H^- + H_2 \rightarrow H_2 + H^- \tag{R4}$$

The available experimental results on the system [281-283] provide an impetus to theoretical studies, particularly in view of the competing electron detachment channel (with a threshold energy E_{th}^{ed} of ~ 1.45 eV) which becomes dominant over the charge transfer rearrangement channel for which the cross section becomes appreciable at ~ 0.45 eV. In contrast to the (H^+, H_2) system which shows large vibrational inelasticity the (H^-, H_2) collisions are only weakly inelastic [284]. Therefore, a comparative quantum mechanical study of the vibrational inelasticity in (H^+, H_2) and (H^-, H_2) collisions have been undertaken on the available ground state *ab initio* PESs for both the systems [285].

Earlier calculation of the potential-energy surface (PES) [281] for the H_3^- system showed a qualitative similarity with the neutral H_3. This was reinforced by a more recent *ab initio* calculation of the ground state PES [286], which revealed a saddle point at $r_{H^--H}^{\neq} = r_{H-H}^{\neq} = 1.997$ a.u. with a barrier height of 0.4648 eV, relative to asymptotically separated reactants. The PES exhibits a van der waals minimum in the collinear geometry which has been reported [286] to be capable of supporting four bound vibrational levels. Belyaev et al [287] computed the state-resolved reaction probabilities for the collinear $H^- + H_2(D_2)$ rearrangement reaction by S matrix Kohn variational method on a diatomics-in-molecules (DIM) PES and they did not reveal the existence of any resonance although a number of transition state resonances (TSRs) have been predicted for H_3 [288, 97, 98].

Therefore we have undertaken a study of the possible existence of TSRs in collinear (H^-, H_2) collisions, by following the temporal evolution of wave packets chosen in the transition state region on the recently published *ab initio* PES [286]. We find that there exist a number of TSRs, at energies above the reaction threshold. While some of them could be related to the onset of higher vibrational channels for the product H_2, some others could not be. By computing the corresponding eigenfunctions we have obtained an insight into the nature of these resonances.

We have also computed $P_v^R(E)$ values for the collinear reaction (R4) to further check the existence of TSRs. The $P_v^R(E)$ values for the collinear reaction

$$H + H_2(v) \rightarrow H_2(v') + H \tag{R5}$$

are also computed on the Liu-Siegbahn-Truhlar-Horowitz (LSTH) PES [289] in order to compare the dynamical behaviors of the two system.

4.2   Computational Details

4.2.1   Transition State Spectrum

Since the detailed methodology has been described in previous two chapters we present only the essential details here. We have used mass-scaled Jacobi coordinates (R, r) to solve the TDSE on a 256×256 grid with the origin at $(1.5, 0.5)$ a.u. in (R, r) with $\Delta R = 0.02$ a.u. and $\Delta r = 0.016$ a.u.

An even parity GWP (Eq. (3.2)) in H^--H and H-H stretching coordinates, is placed initially in the interaction region of the PES and time evolved like for a half–collision. The spatial propagation is carried out by the FFT technique and the temporal evolution is carried out by the SO method. The time autocorrelation function is computed at each time step and half-Fourier transformed after filtering through the normalized Hanning window function to generate the transition state spectrum. The energy values corresponding to the maximum of the intense peaks in the spectrum are identified as the eigenvalues of the quasibound states that lead to resonances. The eigenvalues are accurately estimated by fitting the spectral peaks to a line shape function assuming a single line fit. The eigenfunction (Ψ_n) at any given eigenenergy (E_n) is computed by Fourier transforming the time evolved wave function at that particular energy. Lifetimes (τ_n) of some of the quasi-bound states corresponding to the resonances are calculated by estimating the full width at half maximum (FWHM) (Γ_n) of the spectral peaks fitted to a Lorentzian function (Eq. (3.9)).

The reflection of the WP from the grid edges at longer times is prevented by absorbing it near the edges with the use of NIPs (Eq. (3.6)). The height and the width of the NIP is appropriately chosen using the inequality condition (Eq. (3.7)) so as to obtain 99% absorption of the WP.

We have carried out seven sets of WP calculations for the system by varying the location and the width of the GWP in the interaction region of the PES. The grid parameters for

those are listed in Table 4.1. The first four sets of those calculations were performed on a finer grid with $\Delta R = 0.02$ a.u. and $\Delta r = 0.016$ a.u. and the remaining three were performed on a relatively coarse grid with $\Delta R = \Delta r = 0.05$ a.u. We set the width parameter (δ) of the GWP 0.25 a.u. except for the second set for which δ was taken to be 0.20 a.u. The upper limit of the potential V_{lim} set on the grid is indicated in Table 4.1. We have time evolved the WP for a total of 32768 steps with Δt for each step indicated in Table 4.1 in order to bring the autocorrelation function down to zero.

4.2.2 Computation of Reaction Probabilities

The energy resolved reaction probabilities $P_v^R(E)$ are computed for the collinear reactions (R4) and (R5) on a 256×256 grid with the origin at (1.5,0.5) a.u. in (R,r) and $\Delta R = \Delta r = 0.05$ a.u. The Stärck-Meyer (SM) PES [286] is used for (R4) whereas the LSTH PES [289] is used for (R5). The width parameter of the GWP is chosen (between 0.25 - 0.15 a.u.) sufficiently narrow in coordinate space so that in momentum space it is broad enough to contain most of the energy components in it. This also exploits the power of the time-dependent wave packet approach in that a single WP propagation gives rise to reaction probabilities at various energies. The Morse oscillator wave function is used for $\phi_v(r)$ corresponding to the vibrational state of H_2 with vibrational quantum number v. The GWP is initially centered at $R_0 = 10.0$ a.u. which is sufficiently far away from the interaction region so that initially the separation of variable condition (Eq. (2.124)) is met. The dividing line in the product channel is taken at $r_I = 8.5$ a.u. The upper potential on the grid is fixed at 4 eV which allows $\Delta t = 0.1616$ fs for a stable propagation of WP by the SO scheme. The WP is time evolved for 662 fs which is found to be sufficient to remove essentially all the WP from the interaction region. The components of the WP reaching grid edges are absorbed by using NIPs (Eq. (3.6)).

WP No.	$r^0_{H-_-H}$(a.u.)	r^0_{H-H}(a.u.)	$<E>$(eV)	Δt	V_{lim}
1	1.907	2.247	0.7142	0.1077	5.0
2	2.220	2.526	1.0909	0.1347	4.0
3	2.825	3.209	2.0017	0.1077	5.0
4	3.111	3.461	2.4910	0.1077	5.0
5	4.000	4.000	3.6482	0.1077	5.0
6	4.300	4.300	4.0204	0.1347	5.5
7	5.000	5.000	4.6093	0.1077	5.5

Table 4.1: Parameters for different choices of initial wave packets used in time evolution in the spectral quantization technique

4.3 Results and Discussion

4.3.1 Transition State Resonances

We illustrate the temporal evolution of the wave packet on the PES by plotting the probability density contours, superimposed on the potential grid at various time intervals in Fig. 4.1. The initial location of the WP corresponding to WP no. 2 is shown in Fig. 4.1a. In 2.69 fs the WP spreads along the asymmetric stretch coordinate of H_3^- (Fig. 4.1(b)) and in 4.04 and 5.39 fs it acquires a highly stretched configuration along the asymmetric stretch coordinate as can be seen from Fig. 4.1(c) and 4.1(d) respectively. The WP starts developing structures in 8.02 fs (which in turn shows recurrences in the $|C(t)|$ plot) and shows progression along the symmetric stretch line (Fig. 4.1(e)). At 410 fs all of the WP is found to be removed from the transition state region and this time is sufficient to lead to a converged spectrum. However we have time evolved the WP further for considerably longer time (2.2 ps) to ensure a finer resolution in E.

The transition state spectra along with the autocorrelation functions as insets, corresponding to WP No. 2 and 3 are shown in Fig. 4.2. It is clear from the insets of the figures that the $|C(t)|$ at the higher energy decays at a much faster rate than that at a lower energy and the number of resonances are far more in the higher energy region (Fig. 4.2(b)). The amplitude of the oscillation in the autocorrelation function decays to zero

within 0.4

ps in Fig. 4.2(a) and 0.2 ps in Fig. 4.2(b) which indicates the short-time nature of the (H^-, H_2) collision dynamics. The intensity of the spectral peak at a particular energy is a strong reflection of the amplitude of that state in the initial basis set, which can be altered by varying the location and the width of the initial WP. Due to this reason some lower intensity peaks at one $< E >$ of the WP become the most intense peaks at some other $< E >$.

The decay of the $|C(t)|$ along with the transition state spectrum in the form of a $log_{10} I(E)$ plot as inset, resulting from the time evolution of WP No. 5 is presented in Fig. 4.3. This WP is initially centered along the symmetric stretch line ($r_{H^--H} = r_{H-H} = 4.0$ a.u.) of the H_3^- transient and has the average energy 3.6482 eV. The most striking feature of the spectrum in Fig. 4.3 is that it reveals the existence of a large number of resonances for the system in the higher energy (2 - 4.74 eV) range.

A list of computed resonance energies is given in Table 4.2. We see that near each threshold of $H_2(v)$ there is one resonance [277] and besides that, there are other resonances too. These eigenvalues are quite different from those computed by Sadeghi and Skodje [97, 98] for collinear H_3 which made us conclude that the resonances in collinear H_3^- are significantly different from those of the neutral analog.

Our conclusion is supported by the analysis of some of the eigenfunctions and their lifetimes. Eigenfunctions of four such resonances, shown in Fig. 4.4(a-d) in the form of probability density contours reveal a progression of nodes along hyperspherical radius (ρ) as well as hyperspherical angle (ϕ) with increase in energy. We have tried to classify these states in terms of ν_1 (radial) and ν_3 (angular) quantum numbers as was done in the previous chapter. In addition we also label the states in terms of local mode quantum numbers $(n, m\pm)$ by utilising its connection with (ν_1, ν_3) [274, 290, 291].

The eigenfunction at 0.7767 eV (Fig. 4.4(a)) has essentially the local mode character.
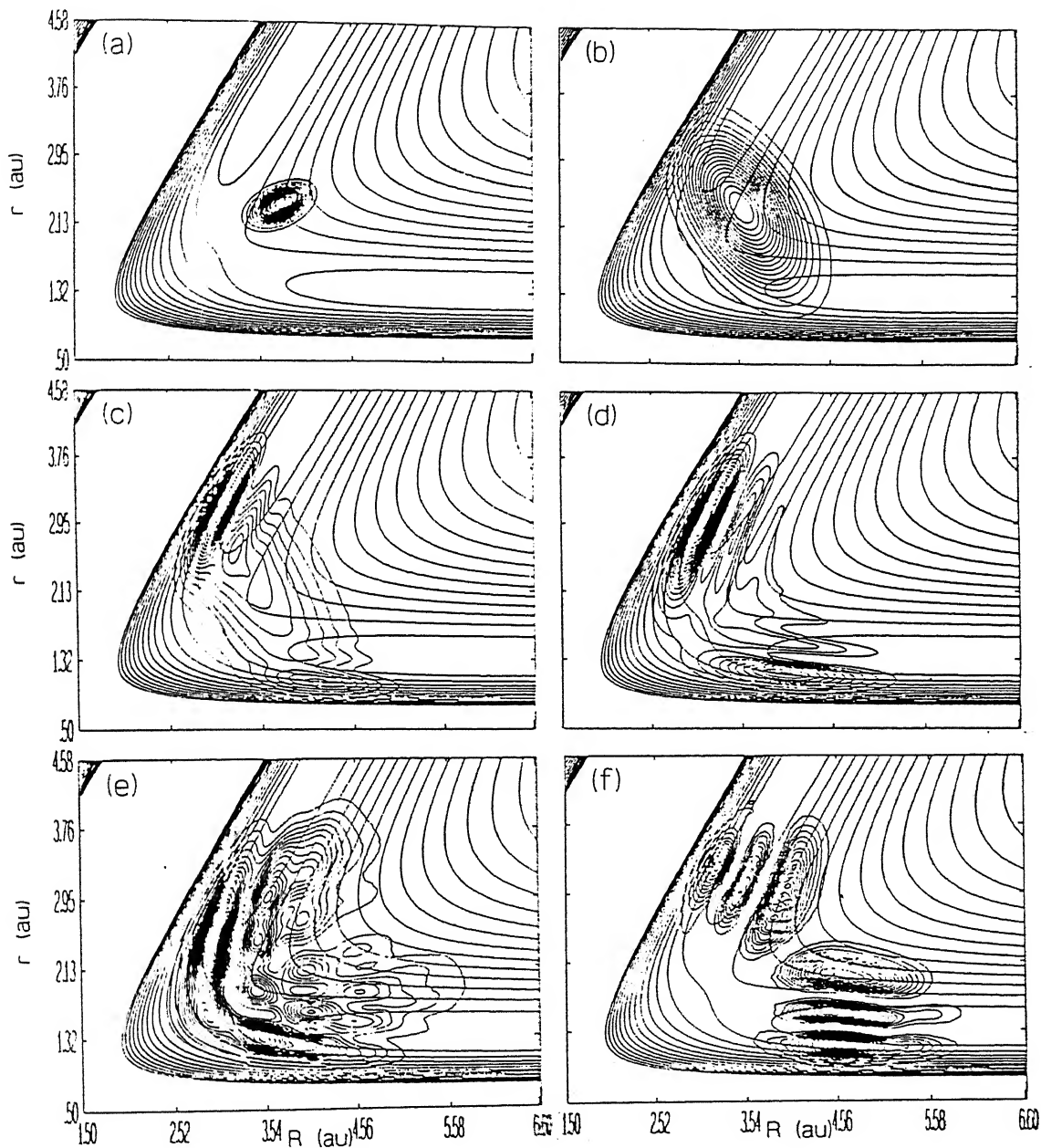
Figure 4.1: Time evolution of the (initial) Gaussian wave packet ($<E> = 1.0909$ eV and δ = 0.2 a.u.) in the form of contours of $|\Psi|^2$, superimposed on the potential grid at various times (0, 2.69, 4.04, 5.38, 8.08 fs and 2.2 ps) are shown in a, b, c, d, e and f respectively. The norm ($< \Psi|\Psi >$) of the WP retained on the grid are: 1.0, 0.999, 0.995, 0.981, 0.942, and $\sim 10^{-9}$ in panels (a)-(f), in that order.
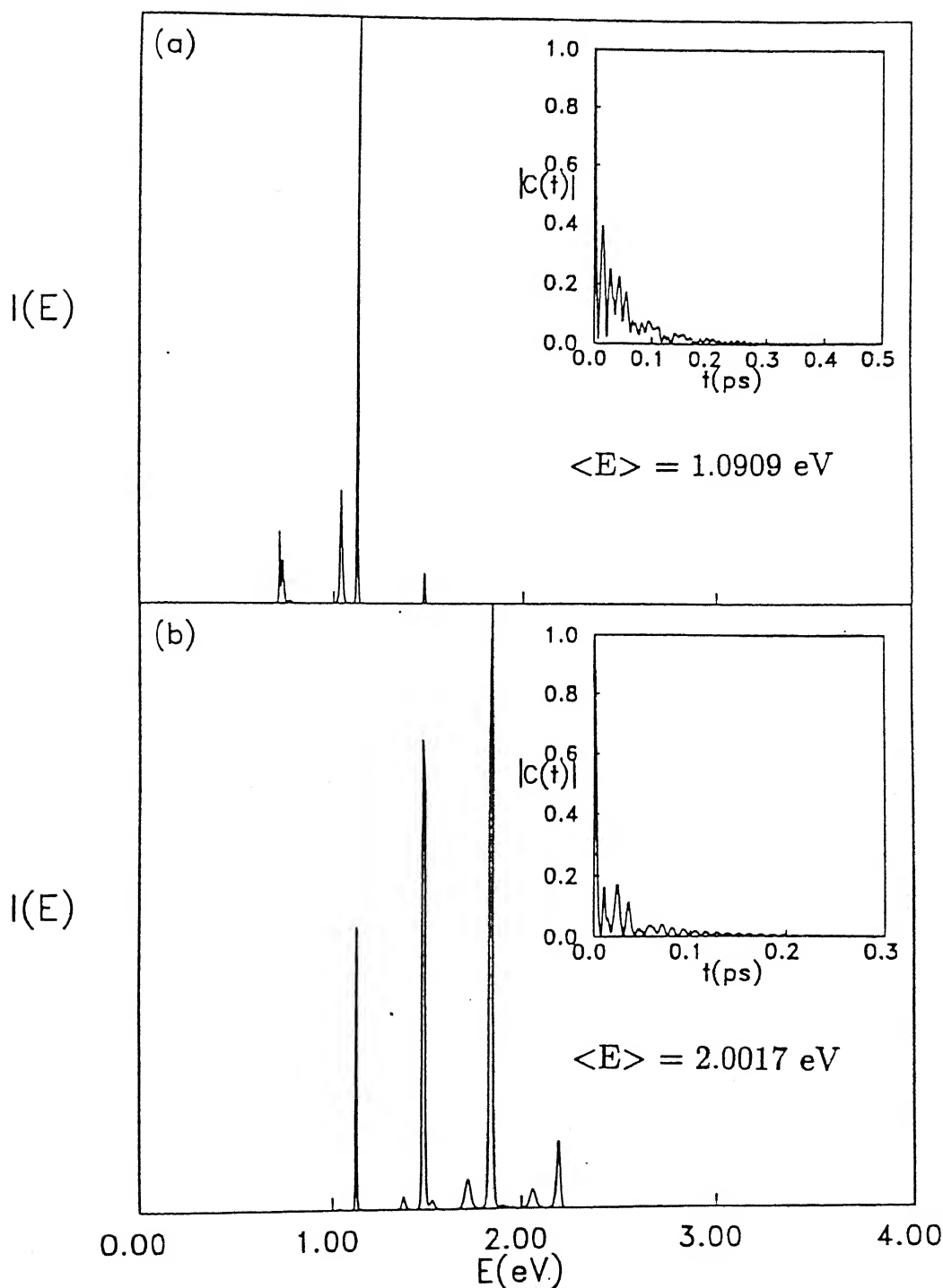
Figure 4.2: Transition state spectrum in the energy range 0-3 eV obtained from two different initial locations of the WP. The average energy of the WP is indicated inside each box. Intensity, I(E) is plotted in arbitrary units. Insets show the decay of the corresponding autocorrelation functions.

This is a (0,2) state in terms of (ν_1, ν_3) specification and (1,1+) in terms of $(n, m\pm)$ specification. The + sign indicates that this is an even parity state. The other states in Fig. 4.4(b-d) are dominantly hyperspherical modes. The state at 1.3796 eV (Fig. 4.4(b)) is a (3,6) state in terms of the former and a (3,6+) state in terms of the latter specification. Accordingly the 1.7160 eV state (Fig. 4.4(c)) is (4,8) (and (4,8+)) and 2.8664 eV state (Fig. 4.4(d)) is (7,14) (and (7,14+)) respectively. In terms of the $(\nu_1, \nu p)$ specification, where $\nu = \nu_3/2$, and p=parity, the states in Fig. 4.4(b),(c) and (d) are (3,3g), (4,4g) and (7,7g) respectively. The PES of collinear H_3^- is symmetric so that, we have parity choices. Since the states reported in this study have originated from even parity WPs, they all end up having even parity. However, the apparent asymmetry in the eigenfunctions in Fig. 4.4 arises from the asymmetry of the (R, r) coordinates.

The lifetimes of the states in Fig. 4.4(a-d) as estimated from the widths of the spectral peaks fitted to Lorentzians are 38, 30, 18 and 6 fs respectively, reiterating the short time nature of the dynamics.

Probability density contours of twelve high energy resonance eigenfunctions of the collinear H_3^- on the extended grid are shown in Fig. 4.5(a-j). It is obvious from the nature of these eigenfunctions that with increasing energy the corresponding quasibound states becomes excited along the asymmetric stretch coordinate. This is indicated by the disappearance of the nodal progression along the symmetric stretch (ρ) coordinate and increasing number of nodes along the asymmetric stretch (ϕ) coordinate. The eigenfunction in Fig. 4.5(a) is a (8,6) state in terms of (ν_1, ν_3) assignment and the other eigenfunctions in Fig. 4.5(b) - 4.5(j) are (9,18), (7,18), (7,20), (3,22), (2,22), (3,24), (1,24), (1,26), and (0,28) respectively. Interestingly, the nodal progression of the H_3^- resonance eigenfunctions resembles that of the H_3 resonance eigenfunctions at higher energies.
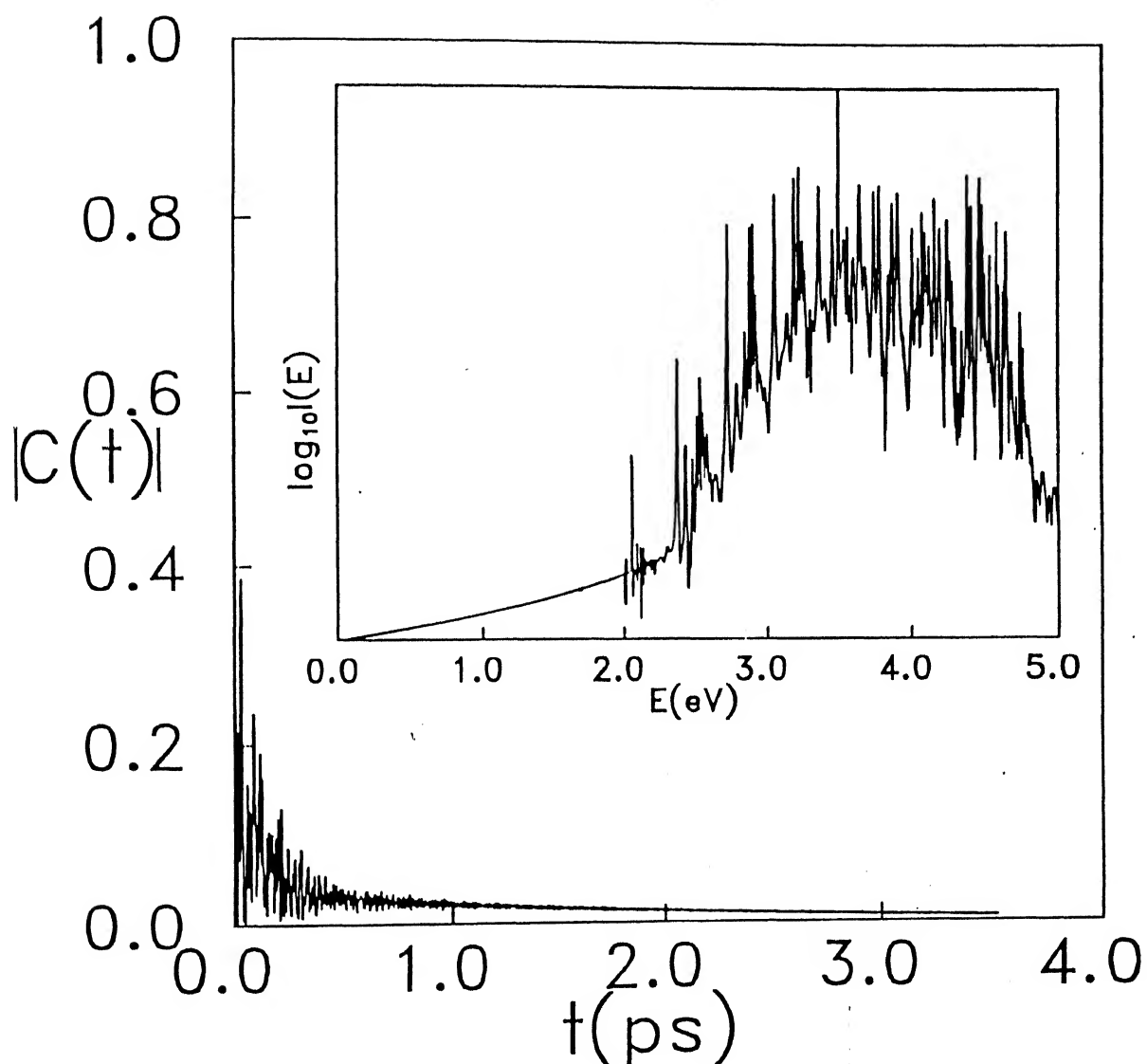
Figure 4.3: Decay of the autocorrelation function along with the corresponding transition state spectrum in the form of a log plot shown in the inset for the WP No. 5.

v	E_n(eV)	E_v^{th}(eV)	$E_n(H_3)(eV)^a$
	0.7238		
	0.7397		
1	0.7767	0.782	0.886
	1.0409		
	1.1212		
2	1.3796	1.269	1.300
	1.4832		
	1.5118		
3	1.7160	1.728	1.713
	1.7771		
	1.8384		
	1.8987		
4	2.0591	2.159	2.108
	2.1916		
	2.4013		
	2.5348		
5	2.5981	2.563	2.496
	2.6255		
	2.7094		
6	2.8664	2.938	2.868
	3.0457		
	3.0526		
	3.1762		
	3.2077		
7	3.2424	3.283	3.214
	3.3533		
	3.4048		
	3.5509		
8	3.6417	3.598	3.532
	3.7757		
9	3.9079	3.880	3.829
	4.0172		
10	4.1542	4.129	4.085
	4.2450		
11	4.3834	4.341	4.310
	4.4145		
12	4.4654	4.514	4.492
13	4.7432	4.643	4.633
Dissociation		4.747	

Table 4.2: Eigenvalues (E_n) of the collinear H_3^- resonances on the Stärck-Meyer potential-energy surface [286]. E_v^{th} values are the energetic thresholds for the various H^- + $H_2(v)$ channels. $E_n(H_3)$ values are the collinear H_3 resonance energies, for comparison.
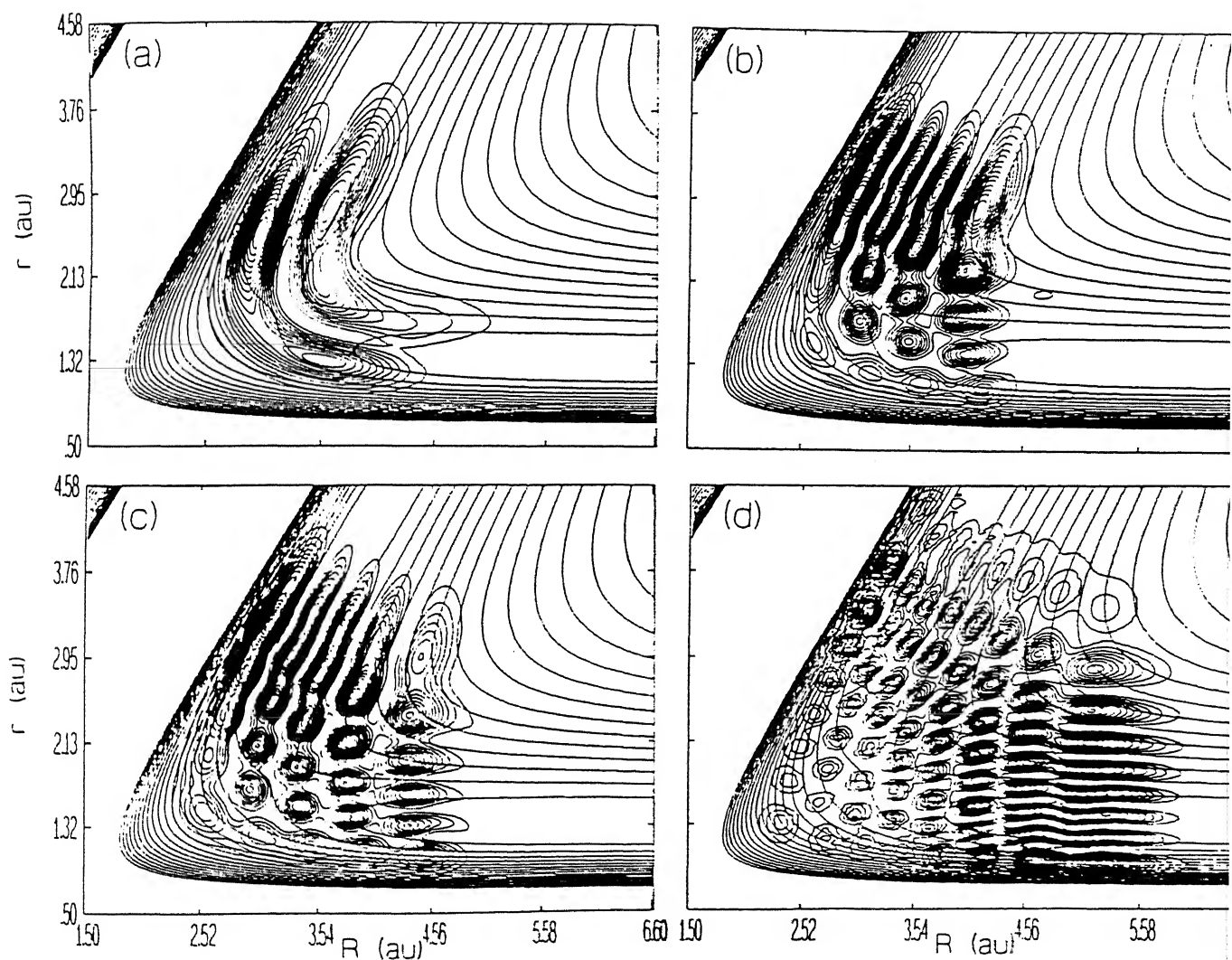^{a}Reproduced from Ref. [98].

Figure 4.4: Probability density ($|\Psi|^2$) contours of the resonance eigenfunctions superimposed on the potential grid for eigenenergies (E_n) 0.7767, 1.3796, 1.7160 and 2.8664 eV in a, b, c, and d respectively.
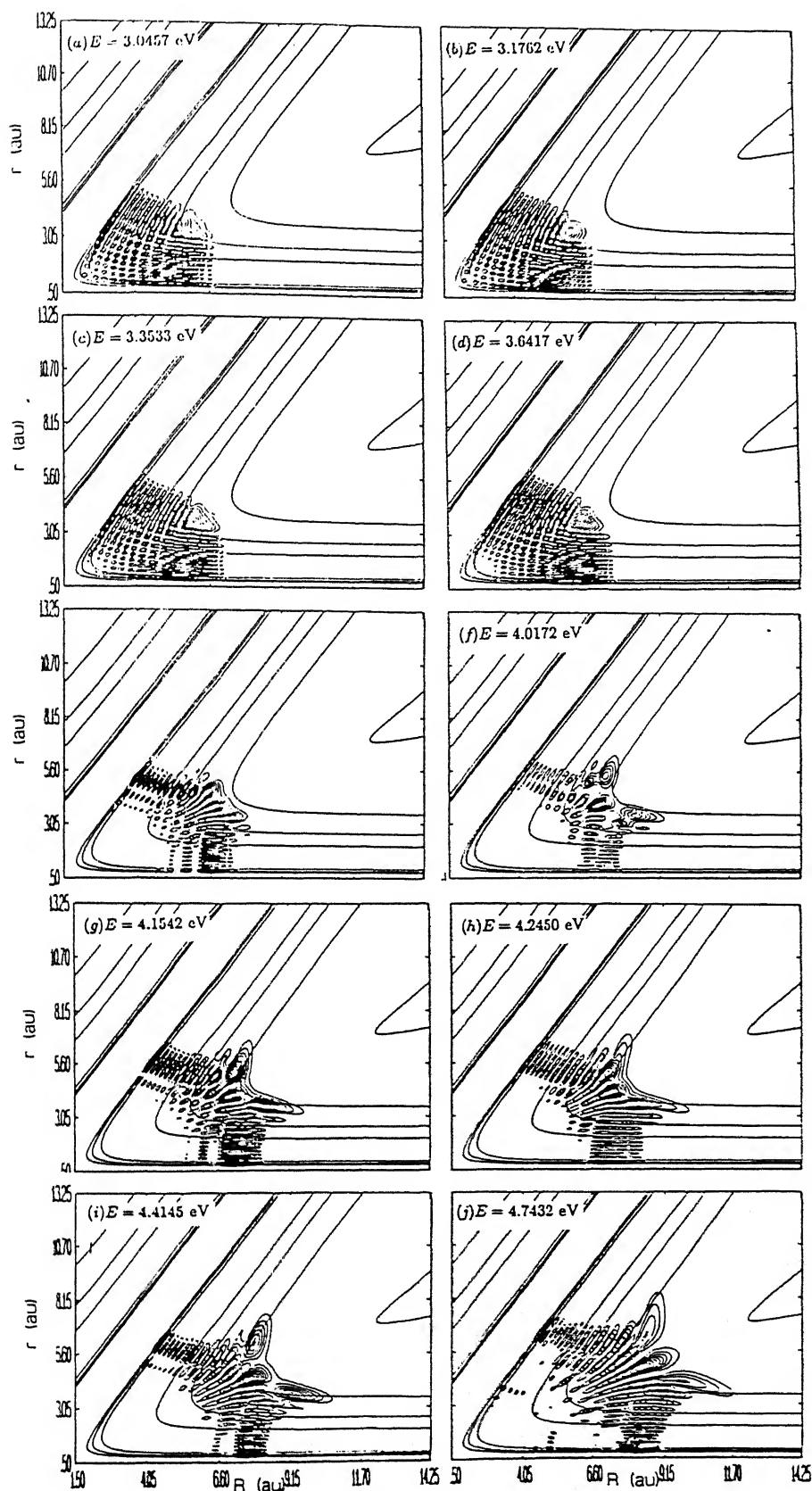
Figure 4.5: Same as Fig. 4.4. The eigenenergies are indicated in each panel.

4.3.2 Vibrational State-Selected Reaction Probabilities

The $P_v^R(E)$ values for (R4) for $v = 0$ state of H_2 thus obtained are plotted in Fig. 4.6 (as a solid line). Clearly, there is a large number of oscillations in $P_0^R(E)$, far in excess of what one would have expected, based on the results of Belyaev et al [287] on a DIM PES and also based on the well known results [155, 292] for collinear reaction (R5) in the same energy range. In order to ensure that we have not obtained any spurious results because of the choice of (R, r) grid or the computational scheme, we computed the $P_0^R(E)$ values for reaction (R5) under identical conditions on the LSTH PES [289] and found them (included as dashed lines in Fig. 4.6) to be in agreement with the values published in the literature [155, 292]. Thus it becomes clear that indeed there is a large number of reactive scattering resonances for collinear (H^-, H_2) in contrast to a much smaller number for (H, H_2) despite comparable E_b values for the two reactions. We must add that for both reactions $P_v^R(E)$ becomes appreciable at ~ 0.45 eV, rises to near unity and eventually becomes nearly zero around 3.0 eV.

The most prominent resonance observed for (R5) is at 0.882 eV, near the threshold of the $v' = 1$ channel of H_2 (0.782 eV). The first substantial dip in $P_0^R(E)$ occurs at a higher energy (1.1 eV) in case of (R5) and is less sharp. Our calculations [102] using the autocorrelation function approach had predicted the resonance at 1.12 eV. Preliminary investigations indicate that this is a Feshbach (compound state) resonance arising from a quasibound state supported by the vibrationally adiabatic potential (VAP) for $v = 2$ in hyperspherical coordinates [293, 274, 255]. Fig. 4.6 also reveals that at higher energies, near each (vibrational) channel threshold, there is a resonance as anticipated by Friedman and Truhlar [277]. Some of the congestion near each such threshold resonance could be attributed to the Feshbach resonances arising from quasibound states supported by the higher VAPs. Still, there are some more oscillations in $P_0^R(E)$ remaining to be accounted for and their origin is presently under investigation.

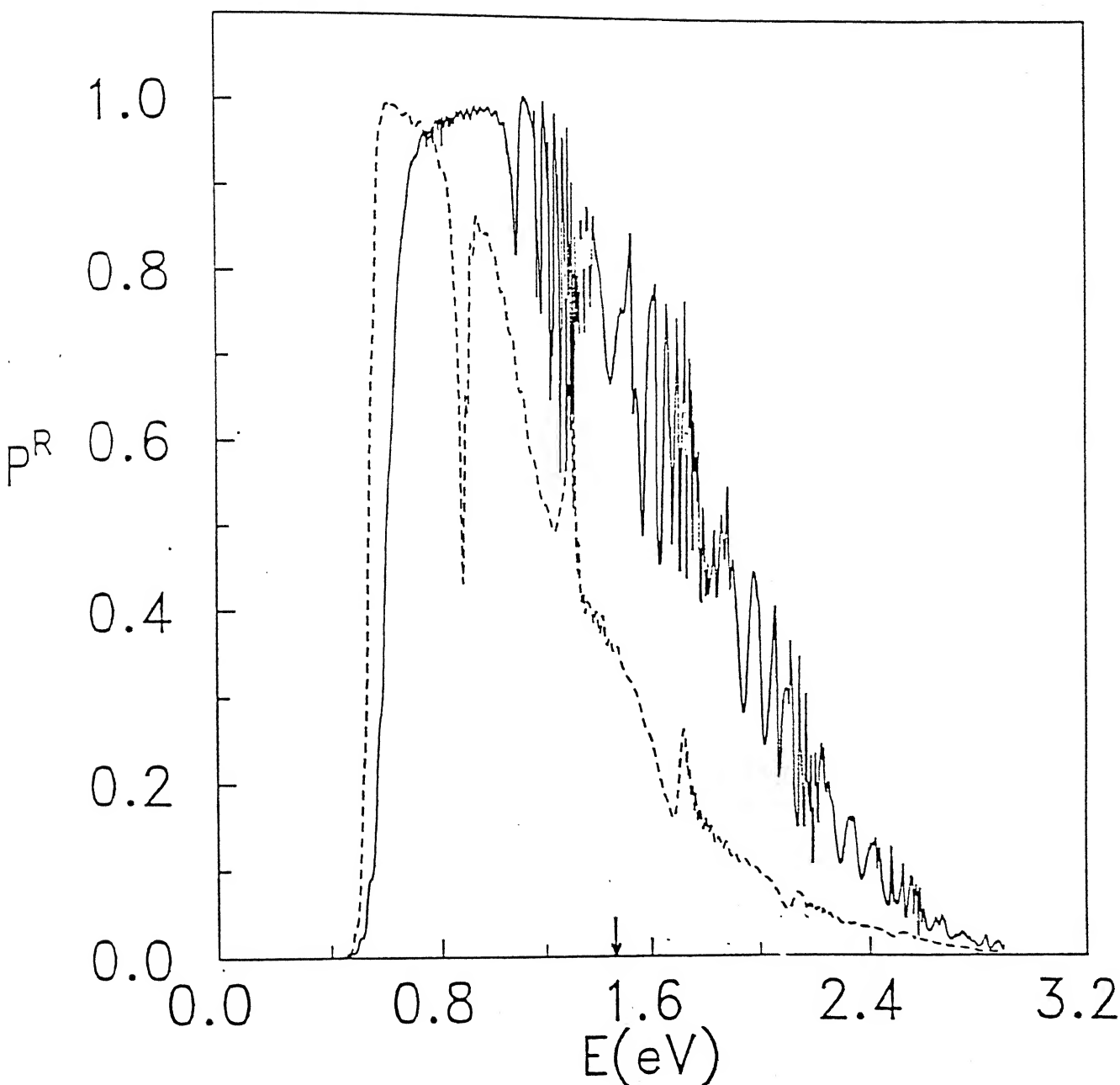Figure 4.6: Energy resolved reaction probability, P^R, as a function of energy, E, for collinear $H^- + H_2(v=0)$ reaction on SM PES (solid line). The $P^R(E)$ values of collinear $H + H_2(v=0)$ reaction on LSTH PES are shown by a dashed line to highlight the dynamical differences between the two systems. The arrow along the abscissa indicates the threshold for the electron detachment channel.

The SM PES [286] has a shallow well of depth ~ 0.05 eV at $(R, r) = (5.75, 1.52)$ a.u.. But, this is unlikely to be the source of the large number of resonances found for (R4). As mentioned earlier, there is an electron detachment channel opening up at ~ 1.45 eV and one can anticipate that some of the rearrangement channel resonances would be quenched at higher energies. We have tried to include the detachment channel by using a NIP along the detachment seam in the PES. The magnitude of $P_0^R(E)$ is highly sensitive to the choice of NIP and a more careful investigation is necessary.

We must add here that we have checked for convergence in $P_0^R(E)$ by varying the height and the width of the NIP and the results have been further verified by obtaining them using the masking function (Eq. (3.13)) in place of the NIP.

4.4   Discussion and Summary

We have shown the existence of a large number of resonances for collinear reaction (R4) on SM PES [286] in contrast to their absence on the DIM PES [287] and for reaction (R5) on the LSTH PES [289].

Qualitatively the *ab initio* PES for collinear H_3^- looks very similar to that of H_3. Quantitatively, there are slight differences in the barrier height ($E_b(H_3) = 0.418$ eV on the DMBE PES [294] and 0.4249 eV on the LSTH PES [289]; $E_b(H_3^-) = 0.465$ eV [286] and in the barrier location ($r_{H-H}^{\neq} = r_{H-H}^{\neq} = 1.76$ a.u. for H_3 [294] and $r_{H--H}^{\neq} = r_{H-H}^{\neq} = 1.99$ a.u. for H_3^- [286]). The transition state for H_3^- being slightly more extended than for H_3 is understandable from the lower stability of the former, arising from the added electron in the antibonding orbital. This would also explain the tendency for electron detachment in H_3^-. The autocorrelation function for H_3^- decays faster than that of the neutral analog presumably due to the slightly increased barrier at an extended configuration for the former. As was pointed out earlier in the text all the resonances in collinear H_3 could be identified as of (vibrational) threshold origin [277] but for H_3^-, there are also resonances of

different origin. In addition, it should be pointed out that all the resonances in H_3 are of the asymmetric stretch type [97, 98] while no such generalization can be made in the case of H_3^-. However, the asymmetric stretch type resonances dominate for the latter at higher energies. A classical mechanical study might lead to a clear understanding of the origin of some of the congestion in the $P_v^R(E)$ curve as well as in the transition spectrum of the collinear (H^-,H_2) collisions. Such a study will be undertaken in future.

The barrier for the exchange reaction is the lowest for the collinear approach in (H^-,H_2) as well as (H,H_2). Therefore, the resonances reported herein could be considered representative of (H^-,H_2) dynamics in three dimensions and the dynamical differences found here for the collinear geometry could be indicative of the differences in the dynamics in three dimensions for reaction (R4). Although E_b for exchange becomes larger for lateral (C_{2v}) approach, the threshold for electron detachment is the lowest in that geometry ($E_{th}^{ed} =$ 1.2, 1.32 eV for the C_{2v} and the collinear approach respectively). Therefore collisions along non-collinear geometries can be expected to show a larger tendency to electron detachment in (H^-,H_2). A three dimensional study of reaction (R1) is presently in progress.

Chapter 5

Quantum Chaos in Collinear (He,H_2^+) Collisions

5.1 Introduction

Quantum chaotic behavior – the distinctive quantal feature of systems that show dynamical chaos in the classical limit – has been shown to be significant in a variety of systems of chemical interest [295, 296]. The usual methods of analysis are statistical, wherein the eigenvalue spectra of systems are examined for short- and long- range correlations, following similar analytical tools derived from random matrix theory (RMT) [297-303] .

Satisfactory and reliable application of these techniques typically requires a large set of data (energy levels), which is often not accessible experimentally. Apart from numerous applications to model Hamiltonian systems with two or more degrees of freedom, such analysis has been applied to a number of systems of practical interest, including nuclear spectra, [297-299] the complicated electronic spectra of polyatomic molecules [304, 305] and vibrational spectra of rare gas clusters [306].

Irregular behavior in scattering systems is well known from both classical and quantum points of view [307]. However, the application of quantum chaotic analysis to realistic scattering systems, as for example chemical reactions, have been few, primarily since such analysis becomes possible only if the underlying PES can support a large enough number

of bound or quasibound states. The ion-molecule reaction R1 satisfies this requirement to a great extent: it is well known that there is a large number of narrow resonances [249, 251-253,255,256,259-262,167,266] corresponding to a large number of closely spaced quasibound states in its vibrationally adiabatic PES. In chapter 3, we have analysed the nature of some of these resonances by computing the transition state spectrum of the system (R1) through time-dependent wave packet calculations although a complete and detailed analysis of all the resonances proves to be both laborious and complicated, owing to the large density of states.

The present work re-examines the transition state spectrum of the above reaction using the methods of analysis of quantum chaos.

Short-range correlations in quantum spectra can be studied through the nearest neighbor spacing distribution (NNSD). For systems which are integrable in the classical limit, the spacings have a Poisson distribution, while for systems which are classically completely chaotic, the spacings follow the Wigner distribution [297, 298]. Long-range correlations are examined through the spectral rigidity, $\Delta_3(L)$, or the two-point variance, $\Sigma^2(L)$, which again, are characteristically distinctive for regular and chaotic systems.

The classical dynamics of the He,H$_2^+$ system is known to show chaotic behavior at sufficiently low energies [263]. A careful analysis [264] of the Poincaré surface of section of the system reveals that chaotic regions of the phase space are surrounded by regular regions and vice versa. The quasibound spectrum originating from such a mixed phase space consists of energy levels from both regular and chaotic regions intertwined with the result that measures such as NNSD or $\Delta_3(L)$ or $\Sigma^2(L)$ reveal neither a completely regular nor a completely irregular behavior, but an intermediate between the two. Systems that are intermediate– neither completely chaotic nor completely regular– pose a problem inasmuch as interpolation between the two limits of behavior (of the NNSD or $\Delta_3(L)$ or $\Sigma^2(L)$) is necessary. Since many systems of practical interest fall in this category, [308]

this is a problem of considerable importance, and several suggestions on characterising their behavior have been made. These include a straightforward interpolation based on the relative fractions of regular and chaotic parts of the classical phase space, as well as phenomenological forms [299, 308].

There is a further source of difficulty in these analyses. Although the HeH_2^+ scattering system has a fairly high density of resonances, the number is still far from ideal (or sufficient), and the sparse data set results in large fluctuations in the NNSD, $\triangle_3(L)$ and $\Sigma^2(L)$. This problem can be overcome partially by examining other indicators of chaotic quantum behavior. The time domain characteristics of regular and irregular spectra are analysed by computing

$$P(t) = |\langle \Phi(0)|\Phi(t)\rangle|^2 \qquad (5.1)$$

which is the survival probability of a given initial wave function $\Phi(0)$. $\Phi(t)$ is defined as

$$|\Phi(t)> = \sum_{i=1}^{N} a_i e^{-\frac{iE_i t}{\hbar}} |E_i > . \qquad (5.2)$$

Following Pechukas, [309] Wilkie and Brumer [310] showed that there is a distinct difference in $\langle\langle P(t)\rangle\rangle$, the survival probability *averaged over initial states and Hamiltonian*, for regular and irregular spectra. Irregular spectra give rise to a 'correlation hole' in $\langle\langle P(t)\rangle\rangle$, which is a graphic evidence of spectral rigidity or level repulsion. This is absent in $\langle\langle P(t)\rangle\rangle$ for regular spectra. For systems that are intermediate in behavior Alhassid and Whelan [311] derived expressions for $\langle\langle P(t)\rangle\rangle$. These methods have been seen to be of considerable utility in a quantitative analysis [312] of experiments on wave chaos in microwave cavities, where the number of states is insufficient for a clear diagnosis based on the NNSD or $\triangle_3(L)$ alone.

In the present work, we also explore the correspondence between classical trajectory dynamics and quantum dynamics of wave packets. Feit and Fleck [276] have studied the evolution of coherent Gaussian wave packets (GWPs) with a variety of mean positions

and momenta under the influence of Hénon-Heiles potential and have shown the transition from regular to chaotic behavior with increasing energy (a similar kind of observation was made earlier by Hutchinson and Wyatt [313]). They have investigated the phase space trajectories obtained from the expectation values of coordinates and momenta, behavior of the survival probability, nature of the power spectrum and the volume of the phase space covered by the wave packet during its evolution. All these diagnoses were found to lead to a reasonable interpretation of the system behavior.

We perform similar analysis for the reaction R1. Three initial points in the phase space are chosen from the Poincaré surface of section, [264] corresponding to the initial conditions of quasiperiodic, periodic and chaotic trajectories. The evolution of coherent GWPs corresponding to these initial conditions shows poor correspondence with the classical dynamics, in contrast with the results of Feit and Fleck [276] for bound states. The difficulty in the present case, we feel, is that this is a scattering situation with a relatively high density of states. The finite width of the wave packet extends over both chaotic and regular regions and thus gives rise to mixed or intermediate behavior. As may be expected, though, the correspondence improves significantly in the $\hbar \to 0$ limit.

The spectral analysis of the transition state quasibound levels for He, H_2^+ are described in detail in Section 5.2. The dynamical evolution of wave packets with different initial locations in the classical phase space is studied in Section 5.3. The results are discussed and summarized in Section 5.4.

5.2   Analysis of Eigenvalue Spectra

The generation of the eigenvalue spectrum for collinear He, H_2^+ system by time-dependent wave packet calculations has been described in detail in chapter 3. A typical spectrum, obtained from the time evolution of an initial Gaussian wave packet with an average energy, $\langle E \rangle = 0.9924$ eV, placed in the interaction region of the MTJS PES [254, 258] is

shown in Fig. 3.4. The spectrum contains approximately 170 quasibound states up to the limit of the three body HeH_2^+ dissociation threshold (2.78 eV). The complex nature of the spectrum is due to the mixing of different frequency components of a large number of classical orbits of the system, which is an indication of the chaotic nature of the underlying dynamics.

Prior to statistical analysis it is essential to "unfold" the spectrum, *i.e.* make the average density of energy levels uniform over the entire energy range. A new set of energy levels $\left\{ \bar{E}_1, \bar{E}_2, ..., \bar{E}_n \right\}$ is calculated from the old set $\{E_1, E_2, ..., E_n\}$ by dividing all the level spacings by the local average spacing [314, 315]

$$\bar{E}_{i+1} = \bar{E}_i + (2k+1)\frac{E_{i+1} - E_i}{E_{j_2+1} - E_{j_1}};\ j_1 = i - k, (i - k > 0); j_2 = i + k, (i + k < n) \quad (5.3)$$

where k is the number of consecutive spacings used to calculate the local average spacing.

The short-range correlation between the levels is estimated from the NNSD $P(s)$, where s is the spacing between two consecutive levels normalised with respect to average level spacing which is, after unfolding, 1. That is, $P(s)ds =$ probability of finding two consecutive energy levels at a distance s apart from each other, in which the lower one is at x and the upper one is in the interval $x + s \leq \bar{E} \leq x + s + ds$ with the condition

$$\int P(s)ds \quad = 1 \quad = \int sP(s)ds. \quad (5.4)$$

For a system known to be classically chaotic, the spacing distribution shows 'level repulsion' with $P(s) \rightarrow 0$ as $s \rightarrow 0$ whereas, for a classically integrable system there is 'level clustering', $P(s) \rightarrow 1$ as $s \rightarrow 0$. For the former, the distribution curve, in the semiclassical limit, is given by the Wigner surmise [298, 316]:

$$P(s) = \frac{\pi s}{2}exp\left(-\frac{\pi}{4}s^2\right) \quad (5.5)$$

while for the latter, the Poisson distribution [298, 317]

$$P(s) = exp(-s) \quad (5.6)$$

is applicable. The spectral rigidity, $\Delta_3(L)$, and the two - point variance, $\Sigma^2(L)$, calculated from the unfolded spectrum, are used to diagnose long-range correlations [298] between the eigenstates in an interval of energy, L. $\Delta_3(L)$ actually measures the least-square deviation of the staircase function $N(E)$, the number of energy levels below energy E from the best straight line at any interval. Following Dyson and Mehta [318], $\Delta_3(2L)$ can be written as

$$\Delta_3(2L) = \left\langle \frac{1}{2L} Min(A,B) \int_{x-L}^{x+L} \left[N(\bar{E}) - A\bar{E} - B \right]^2 d\bar{E} \right\rangle \quad (5.7)$$

where $A\bar{E}+B$ represents the best straight line fit of the staircase in the interval $[x-L, x+L]$. In terms of unfolded eigenvalues $\left\{ \bar{E}_1, \bar{E}_2, \bar{E}_3, ..., \bar{E}_n \right\}$ lying in the interval $[-L, L]$ $\Delta_3(2L)$ is given by [319]

$$\Delta_3(2L) =$$

$$\left\langle \left(\frac{n^2}{16} \right) - \frac{1}{4L} \left(\sum_{i=1}^{n} \bar{E}_i \right)^2 + \frac{3}{8L^2} \left(\sum_{i=1}^{n} \bar{E}_i \right)^2 - \frac{3}{16L^4} \left(\sum_{i=1}^{n} \bar{E}_i^2 \right)^2 + \frac{1}{2L} \left(\sum_{i=1}^{n} (n - 2i + 1)\bar{E}_i \right) \right\rangle$$

$$(5.8)$$

where n is the actual number of levels within each ensemble of the unfolded spectrum. It is well established [296, 298, 320] that the Gaussian orthogonal ensemble (GOE) limit of Hamiltonian matrices provides a suitable standard to measure chaos.

The chaotic limit of $\Delta_3(L)$ is identical to the GOE value of RMT:

$$\Delta_3^{GOE}(L) = \frac{1}{\pi^2} log L - 0.00695 \quad (5.9)$$

On the other hand, $\Delta_3(L)$ for an integrable system follows the Poisson value

$$\Delta_3^{Poisson}(L) = \frac{L}{15} \quad (5.10)$$

We have also computed $\Sigma^2(L)$ [298, 299, 301, 321] of the number, n, of levels in the interval x to $x + L$:

$$\Sigma^2(L) = \left\langle [n(x,L) - <n(x,L)>]^2 \right\rangle \quad (5.11)$$

$\Sigma^2(L)$ measures the two-point fluctuation in the spectrum and it gives the same long-range correlation as $\triangle_3(L)$. The GOE value of $\Sigma^2(L)$ is given by

$$\Sigma^2_{GOE}(L) = 2\Sigma^2_2(L) + \frac{1}{\pi^2}\left[Si(\pi L)\right]^2 - \frac{1}{\pi}Si(\pi L) \qquad (5.12)$$

with

$$\Sigma^2_2(L) = \frac{1}{\pi^2}\left[log(2\pi L) + \gamma + 1 - cos(2\pi L) - Ci(2\pi L)\right] + L\left[1 - \frac{2}{\pi}Si(2\pi L)\right] \qquad (5.13)$$

Quantal fluctuation patterns in the time domain are analysed by computing the survival probability using Eq. 5.1. In case of regular spectra the survival probability, averaged over initial states and Hamiltonian, $\langle\!\langle P(t)\rangle\!\rangle$, starts from an initial value 1.0 and approaches the asymptotic value monotonically. In case of an irregular spectrum, however, $\langle\!\langle P(t)\rangle\!\rangle$ falls *below* the asymptotic value at short times (t $= 2\pi\hbar/ < \triangle E >$) and then approaches the asymptotic limit at a later time, thus giving rise to a 'correlation hole'. To compute $\langle\!\langle P(t)\rangle\!\rangle$, the averaging over the initial states is done through [322]

$$\langle P(t)\rangle = \frac{3}{N+2}\left\{1 + \frac{2}{3N}\sum_{n,m;n>m}\cos\left[2\pi(E_n - E_m)\frac{t}{<\triangle E>}\right]\right\} \qquad (5.14)$$

and the averaging over the Hamiltonian is done by averaging over n levels which are divided into several segments, each containing N levels.

The NNSD, $P(s)$, for four different transition state spectra are shown in Fig. 5.1(a-d). Each spectrum originates from different parts of the interaction region of the MTJS PES, and therefore differs in detail, in terms of some of the eigenenergies and intensities of the common peaks. In all cases, the distribution is neither Poisson nor Wigner, but is intermediate in behavior.

In Fig. 5.2(a-d) the spectral rigidity, $\triangle_3(L)$, is plotted as a function of L. Again, the behavior is intermediate between the GOE and Poisson limits, although the fluctuations are large, resulting from the relatively small number of energy levels in the system. The two-point variance, $\Sigma^2(L)$ (which is not shown here), varies in a similar manner.
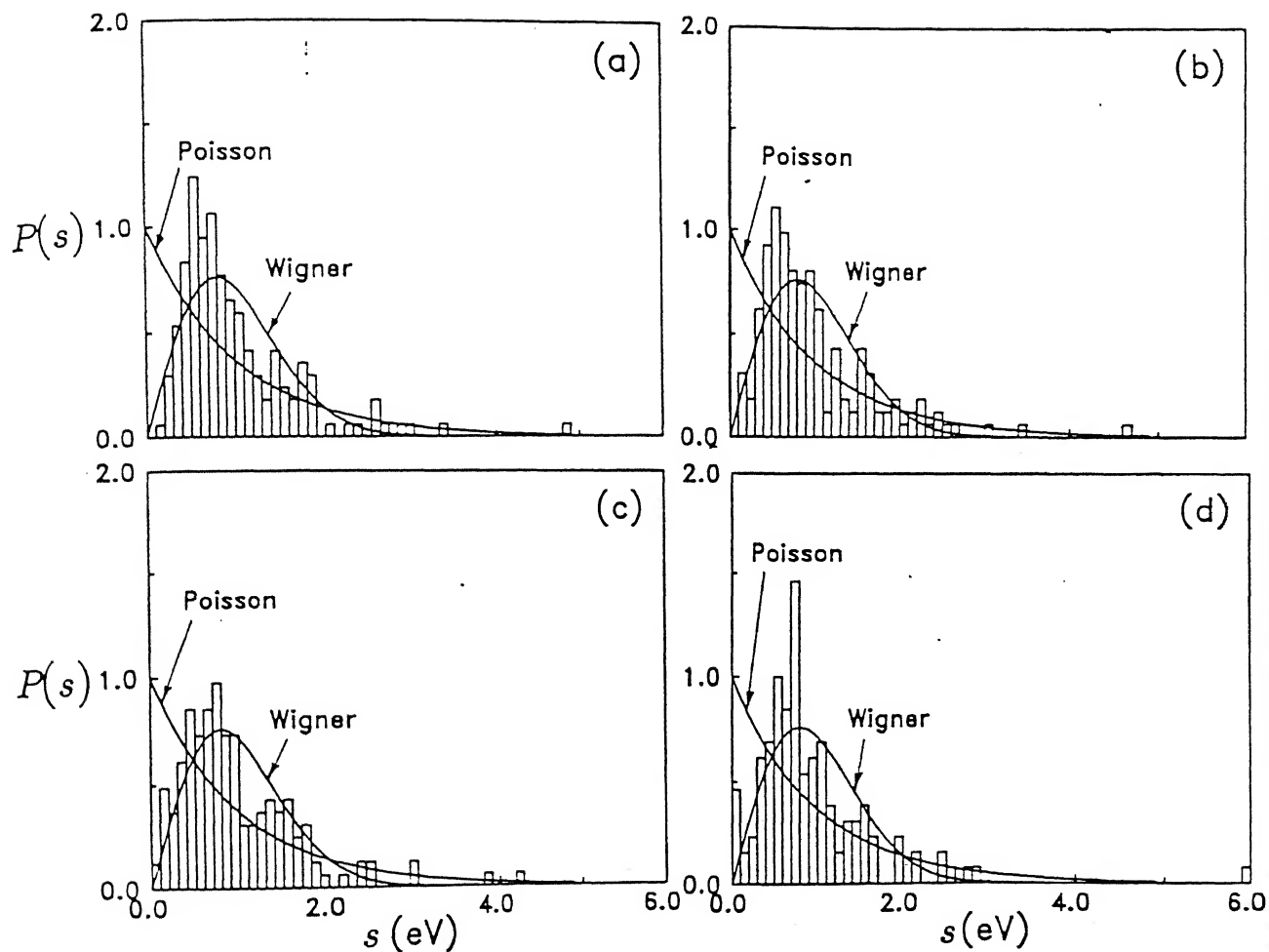
Figure 5.1: The nearest neighbor spacing distribution, $P(s)$, as a function of the spacing between energy levels, s, showing short - range correlation. (a), (b), (c) and (d) are for 170, 163, 165 and 131 quasibound states obtained from four initial Gaussian wave packets with $\langle E \rangle = 0.9924$, 1.2159, 1.7694 and 2.2816 eV respectively. Poisson and Wigner indicate the distributions in the regular and the irregular limits respectively.
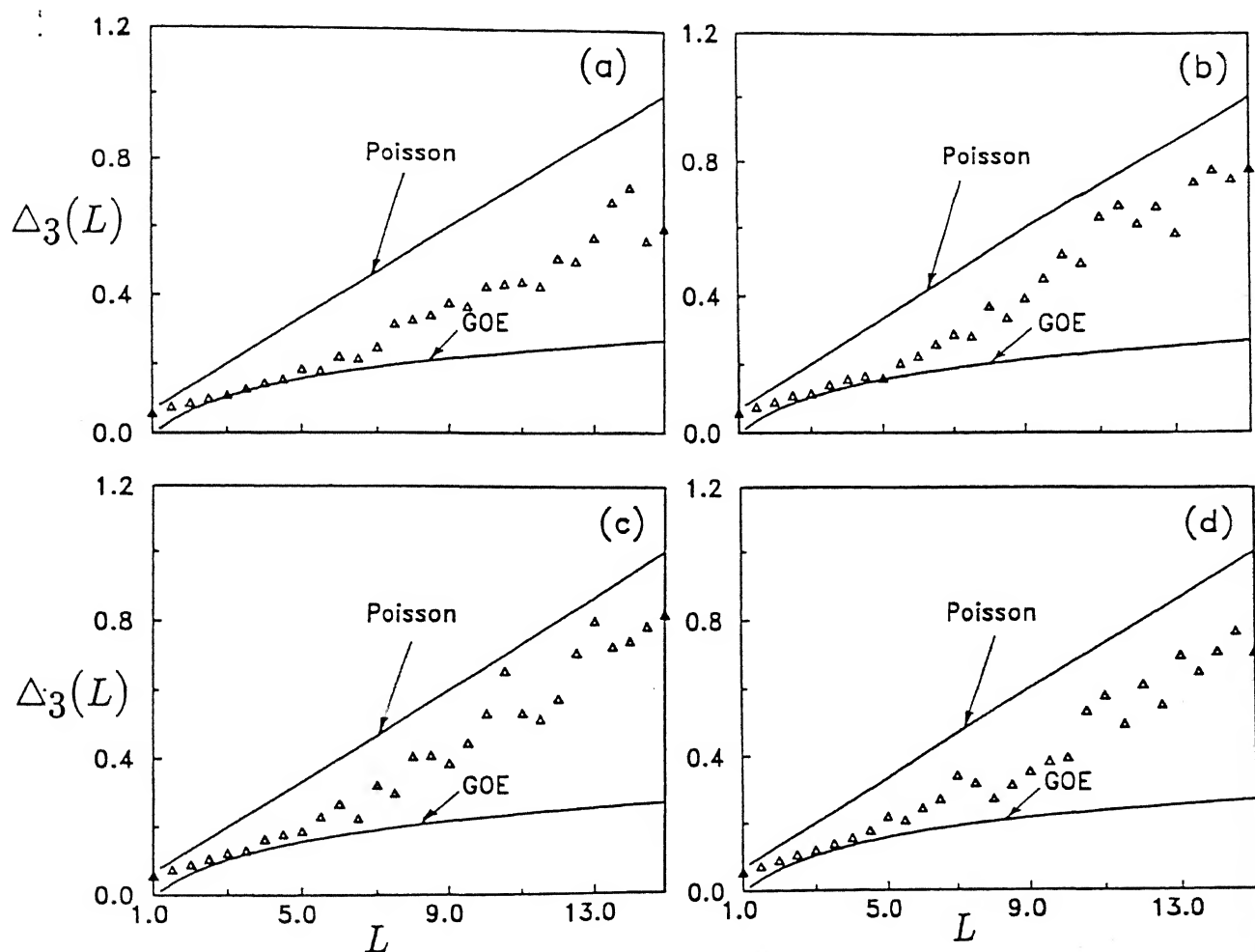
Figure 5.2: The spectral rigidity, $\Delta_3(L)$, as a function of the segment length, L, showing the long - range correlation. (a), (b), (c) and (d) correspond to the WPs referred to in Fig. 5.1. Poisson and GOE indicate the regular and the irregular limit respectively.

The behavior of the average survival probability for the four sets of energy levels is more revealing, and is shown in Fig. 5.3(a-d). In our calculation we use $N = 10$, which gives an asymptotic value of $\langle\langle P(t)\rangle\rangle = 0.25$. As can be seen from Fig. 5.3, at short times $\langle\langle P(t)\rangle\rangle$ falls below the asymptotic value and then only it approaches the asymptotic limit. Again, the somewhat large fluctuations of $\langle\langle P(t)\rangle\rangle$ at long times around the asymptotic value is due to the inadequate number of energy levels in the system. However, the signature of level repulsion is distinctly present in all the four sets of resonances. Due to the mixed (partly integrable and partly non-integrable) nature of the phase space the $\langle\langle P(t)\rangle\rangle$ curves show a behavior that is intermediate between the regular and chaotic limits. (For illustration, the behavior of $\langle\langle P(t)\rangle\rangle$ in the regular limit, estimated from a set of 8000 random numbers, is included in Fig. 5.3(a), as shown in dots.)

Since all the measures discussed above indicate that the system has mixed dynamics, we can estimate the fraction of the regular and the chaotic regions in the phase space by fitting the experimental (*i.e.* derived from the present data) $\langle\langle P(t)\rangle\rangle$ curve to that predicted from an RMT analysis. For mixed systems, $\langle\langle P(t)\rangle\rangle$ can be written as [311]

$$\langle\langle P(t)\rangle\rangle = \frac{3}{N+2}\left\{1 + \frac{1}{3}\triangle_N * [\delta(\tau) - b_{2\beta}(\tau)]\right\} \tag{5.15}$$

where $\tau = t/2\pi <\rho>$ ($<\rho>$ is the average level density) and $\beta = 1, 2$ and 4 for Gaussian orthogonal, unitary and symplectic ensembles respectively. $b_{2\beta}(t)$ is the two-level form factor [298] obtained by Fourier transform of the two-point cluster function, $Y_{2\beta}(\omega)$. The asterisk signifies the convolution

$$\triangle_N * f(t) \equiv \int dt'\, \triangle_N(t') f(t - t') \tag{5.16}$$

and

$$\triangle_N(t) = N^{-1}\left[\frac{\sin(\pi N t)}{\pi t}\right]^2 \tag{5.17}$$

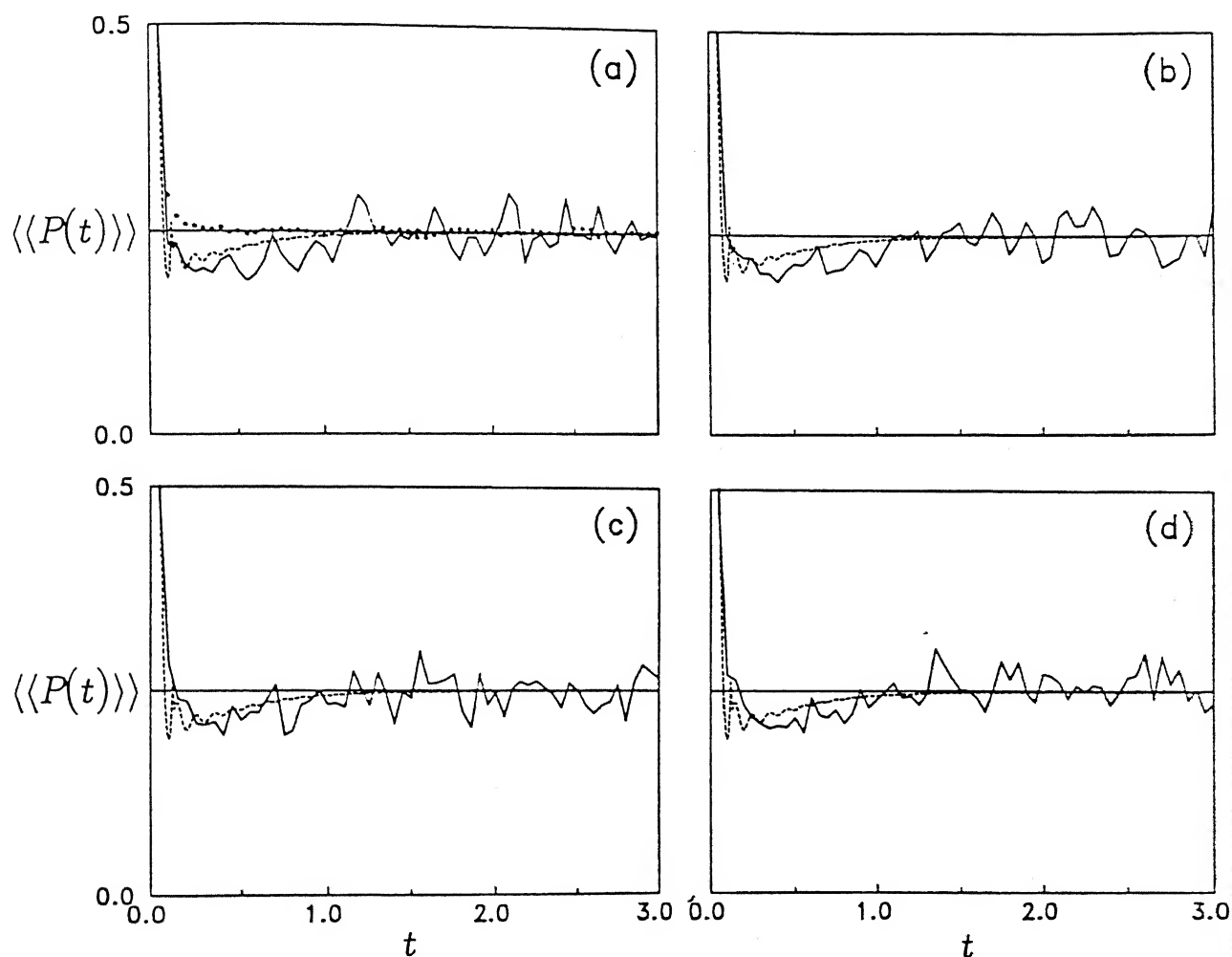The convolution with $\triangle_N$ results from the use of finite subspace, N. If a fraction, β,

Figure 5.3: Variation of survival probability, $\langle\langle P(t)\rangle\rangle$ with time t. (a), (b), (c) and (d) have the same meaning as in Fig. 5.1. $\langle\langle P(t)\rangle\rangle$ for a regular spectrum (generated from 8000 uniformly distributed random numbers) is shown by a dotted line in Fig. 5.3(a). The RMT $\langle\langle P(t)\rangle\rangle$ values for intermediate β are included in each panel by a dashed line.

of the levels obey GOE statistics and 1-β obey Poisson statistics, $b_{2\beta}(t)$ ($0 \leq \beta \leq 1$) is given by

$$b_{2\beta}(t) = \beta b_2(t/\beta) + [(1-\beta)/N]\,\delta(t) \tag{5.18}$$

where b_2 indicates the exact GOE value which is given from the two-level cluster function [297, 298] as

$$
\begin{aligned}
b_2(t) &= 1 - 2|t| + |t|\log(1+2|t|) & |t| \leq 1, \\
&= -1 + |t|\log((2|t|+1)/(2|t|-1)) & |t| \geq 1
\end{aligned} \tag{5.19}
$$

Eqs. 5.17, 5.18 and 5.19, when substituted in Eq. 5.15 give the desired expression for $\langle\langle P(t)\rangle\rangle$ for the mixed case, which is superimposed in Figs. 5.3(a-d), as a dashed line. The agreement is reasonable for a value of $\beta \approx 0.9$, indicating that the effective chaotic region is large at these energies. We return to this point in Section 5.4.

5.3   Wave Packet Dynamics

The dynamical behavior of a wave packet in coordinate space is studied by solving the TDSE in mass-scaled Jacobi coordinates (R, r). The Hamiltonian for collinear He,H_2^+ is given by Eq. (3.1) The initial wave function is taken as a coherent state GWP,

$$\Phi(R,r,t=0) = N exp\left[-\frac{(R-R_0)^2}{2\sigma^2} + \frac{iP_R^0 R}{\hbar}\right] exp\left[-\frac{(r-r_0)^2}{2\sigma^2} + \frac{iP_r^0 r}{\hbar}\right] \tag{5.20}$$

where N is the normalization constant and σ is the width parameter of the wave packet. The initial conditions are specified in terms of the average quantities

$$< R >= R_0; \; < P_R >= P_R^0$$

$$< r >= r_0; \; < P_r >= P_r^0 \tag{5.21}$$

As has been described in chapter 3, the spatial propagation of the wave packet is carried out by the FFT method [66] and the temporal evolution is carried out by the SO

| Wave packet	Initial Conditions				$\langle E \rangle$ (eV)	Behaviour (eV)
	$< R >$	$< r >$	$< P_R >$	$< P_r >$		
(a)	3.5780	1.5623	-0.2191	0.7902	0.2148	Regular
(b)	4.3360	1.1865	0.0	0.0	0.7091	Regular
(c)	4.2170	1.5623	-0.0626	2.0106	1.2263	Chaotic

Table 5.1: Parameters for different choices of initial wave functions used in wave packet dynamics.

method [64]. The parameters chosen for the initial wave function are listed in Table 5.1. All calculations were done on a 256 × 256 spatial grid with the origin at (2.2,0.4) a.u. in (R, r) space. The grid spacings are 0.05 a.u. in both R and r. The upper limit of the potential on the grid is set at 3 eV which allowed a time step of 0.19 fs in the propagation scheme. The width parameter of the GWP is taken as 0.25 a.u.. The survival probability (Eq. (5.1)) is computed at each time step and the power spectrum is generated through Eq. (2.116). The volume occupied by the wave packet in phase space during its evolution is computed from the uncertainty product as [276]

$$V(t) = \left\{ < (P_R - < P_R >)^2 > < (P_r - < P_r >)^2 > < (R - < R >)^2 > < (r - < r >)^2 > \right\} \tag{5.22}$$

The time evolution of three wave packets in (R, r) space is shown in Figs. 5.4(a-c). Initial conditions are chosen from the Poincaré surface of section [264] of the system R1. Although the behavior of the classical trajectories originating from the initial conditions corresponding to WP (a) and (b) has been found to be regular, the wave packets, because of their non-zero width, extend to nearby nonintegrable regions of the phase space and spread. The spreading of a coherent GWP is dependent on the extent of anharmonicity of the region of the PES it is located initially. The energy of the wave packet in Fig. 5.4(c) is large compared to that in Fig. 5.4(a) and 5.4(b) and since it is located initially at a position corresponding to a chaotic trajectory, there is a large degree of spreading.
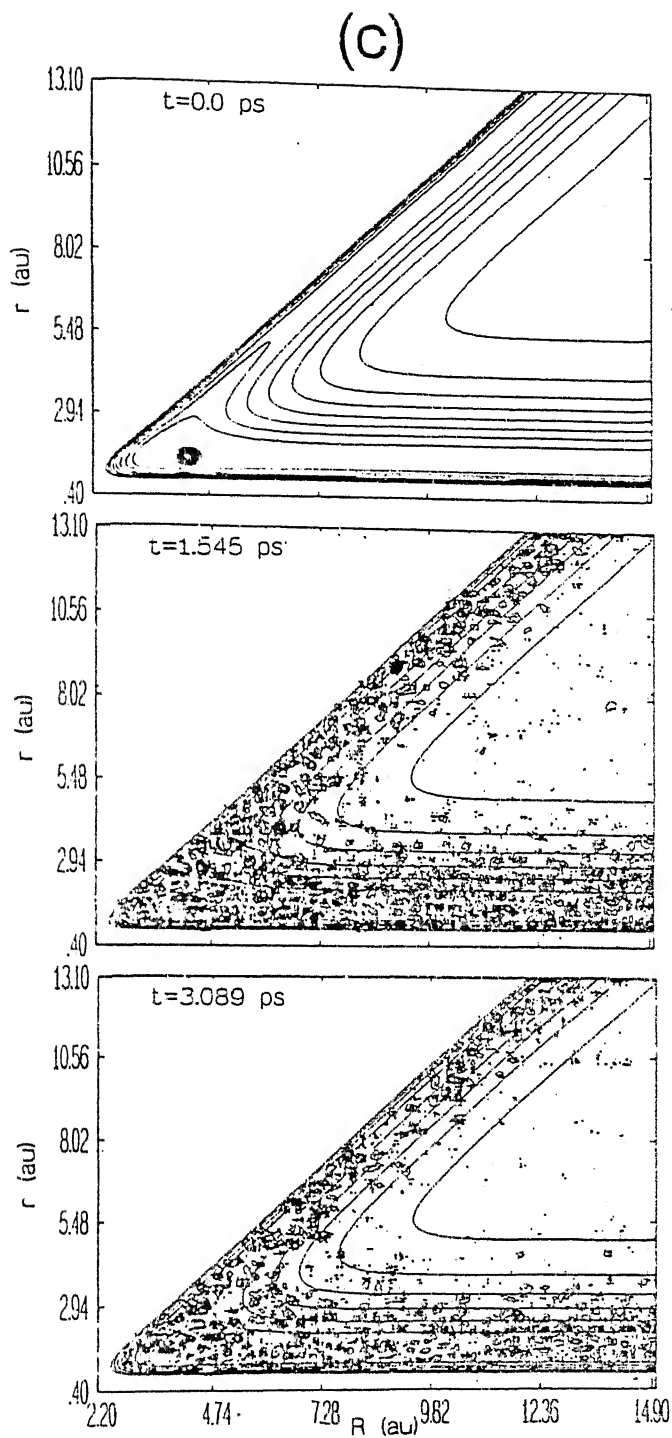
(a)

(b)

(a) t=0.0 ps

t=1.545 ps

(d) t=3.089 ps
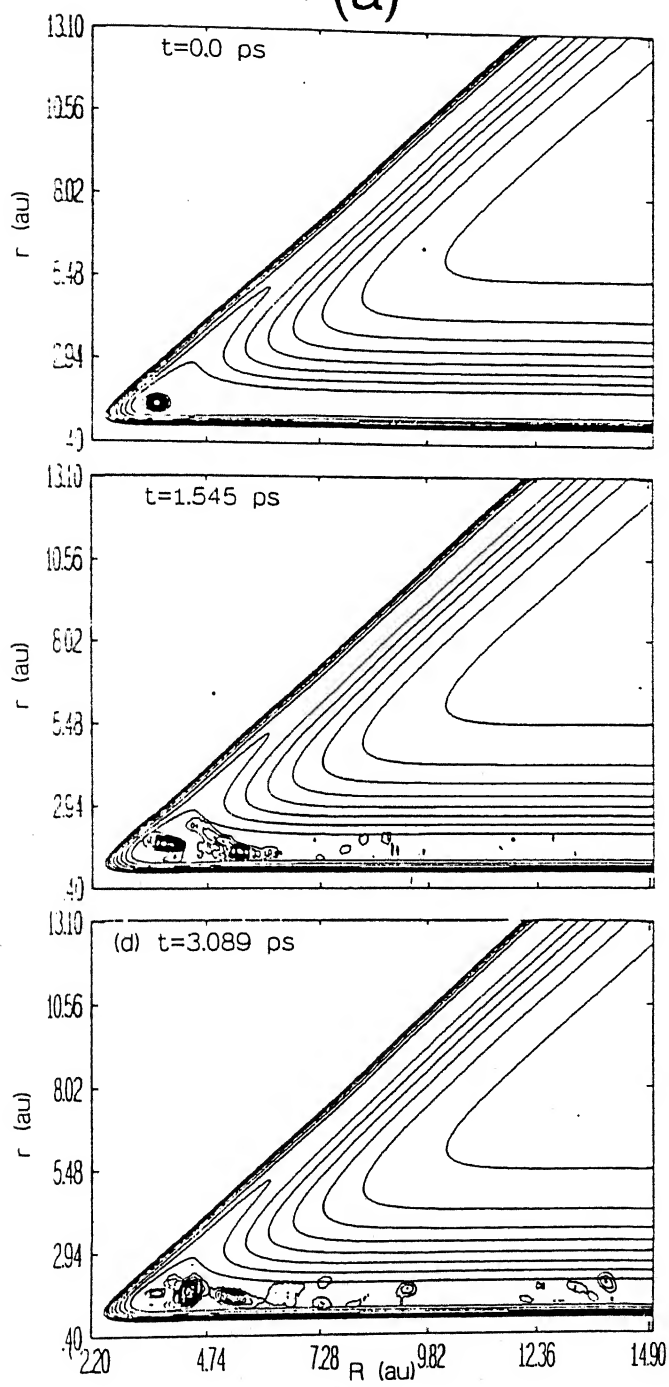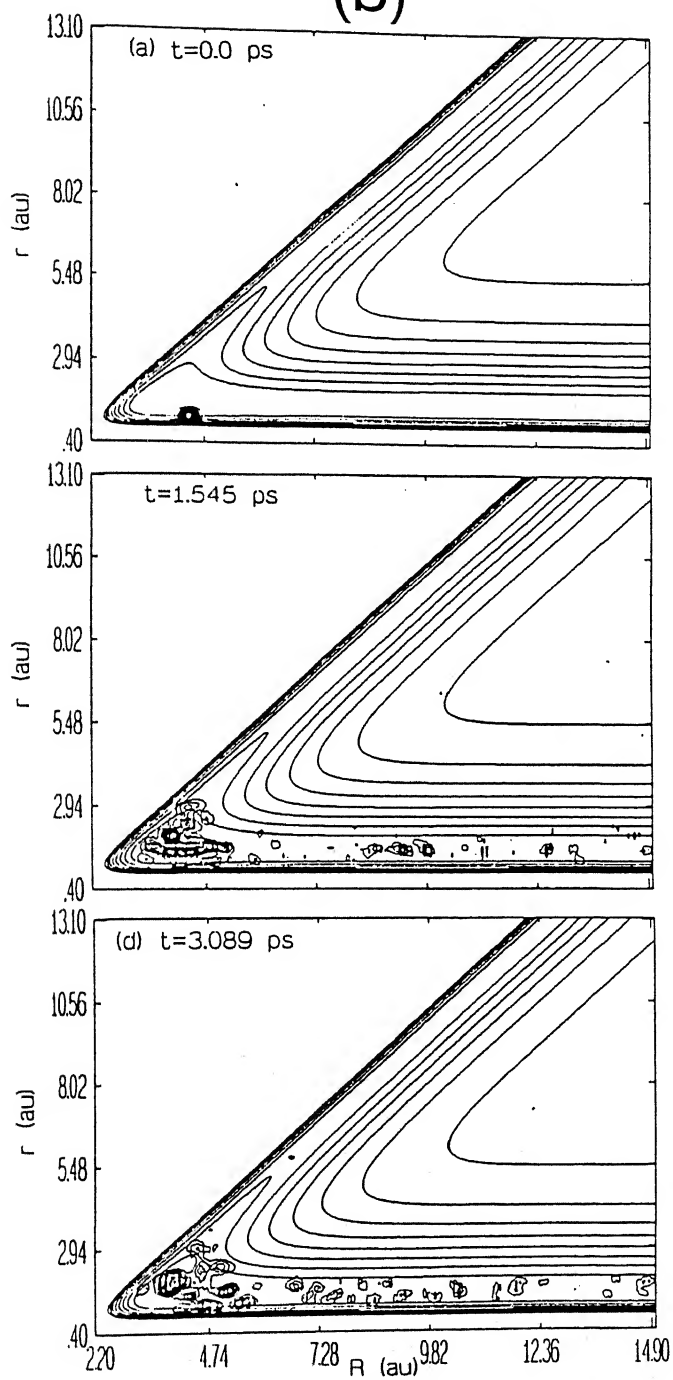
Figure 5.4: Probability density contours ($|\Phi|^2$) of the initial coherent Gaussian wave packet superimposed on the potential energy surface showing spreading of the wave packet with time. (a), (b) and (c) are for the different initial conditions given in Table 5.1.
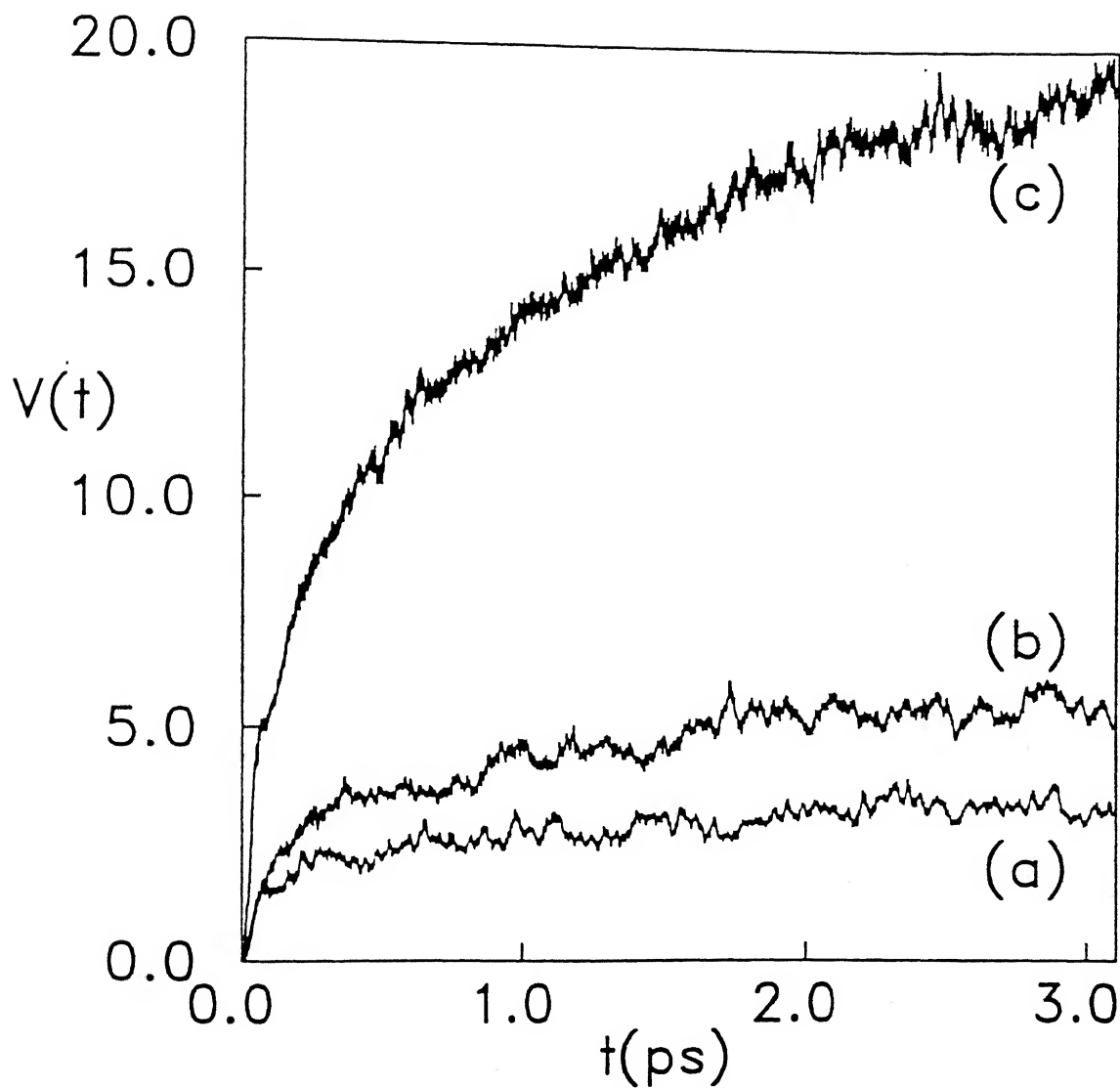
Figure 5.5: The volume of the phase space, $V(t)$, over which the wave packet spreads in time, t. (a), (b) and (c) have the same meaning as in Fig. 5.4.

The volume $V(t)$ of the phase space occupied (calculated through Eq. (5.22)) by the wave packets during their time evolution is shown in Figs. 5.5(a-c). A large increase in $V(t)$ for the wave packet (c) compared to (a) and (b) is in agreement with its high degree of spreading in phase space.

The shape of $P(t)$ for the three wave packets is shown in Figs. 5.6(a-c) respectively. An exponential decay at very short times is observed due to the dephasing of the initial wave packet. This phenomenon is well known in quantum mechanics and the dephasing time is given by $\tau_d = \hbar/\Gamma$, where Γ is the energy spread of the wave packet. Classically this is the time needed for the wave packet to move a distance equal to its width ($\tau_d = \sigma/v$, where v is the wave packet velocity). For time $t > \tau_d$, P(t) exhibits a large number of recurrences of different amplitudes which is composed of a large number of independent frequencies, and hence accounts for the spreading of wave packets. The wave packets (a) and (b) exhibit a moderate correlation till the end of the time evolution and hence reveal intermediate kind of behavior with a high degree of regularity. The wave packet (c) on the other hand does not show any correlation which is an indication of the chaotic behavior.

We have examined the power spectrum and found that the wave packets (a) and (b) show a moderate degree of correlation between the successive peaks and there is a high degree of regularity hidden inside the overall irregularity. On the other hand the spectrum of (c) is purely uncorrelated and shows the contribution of a large number of states with a high degree of anharmonicity.

We have also studied the behavior of the wave packet (b) in the classical limit ($\hbar \to 0$). Classically the initial conditions of wave packet (b) correspond to a periodic orbit. This wave packet does not show any spreading as $\hbar \to 0$. The behavior of $P(t)$ also shows a high degree of correlation and the corresponding power spectrum is regular with constant spacings between successive peaks.
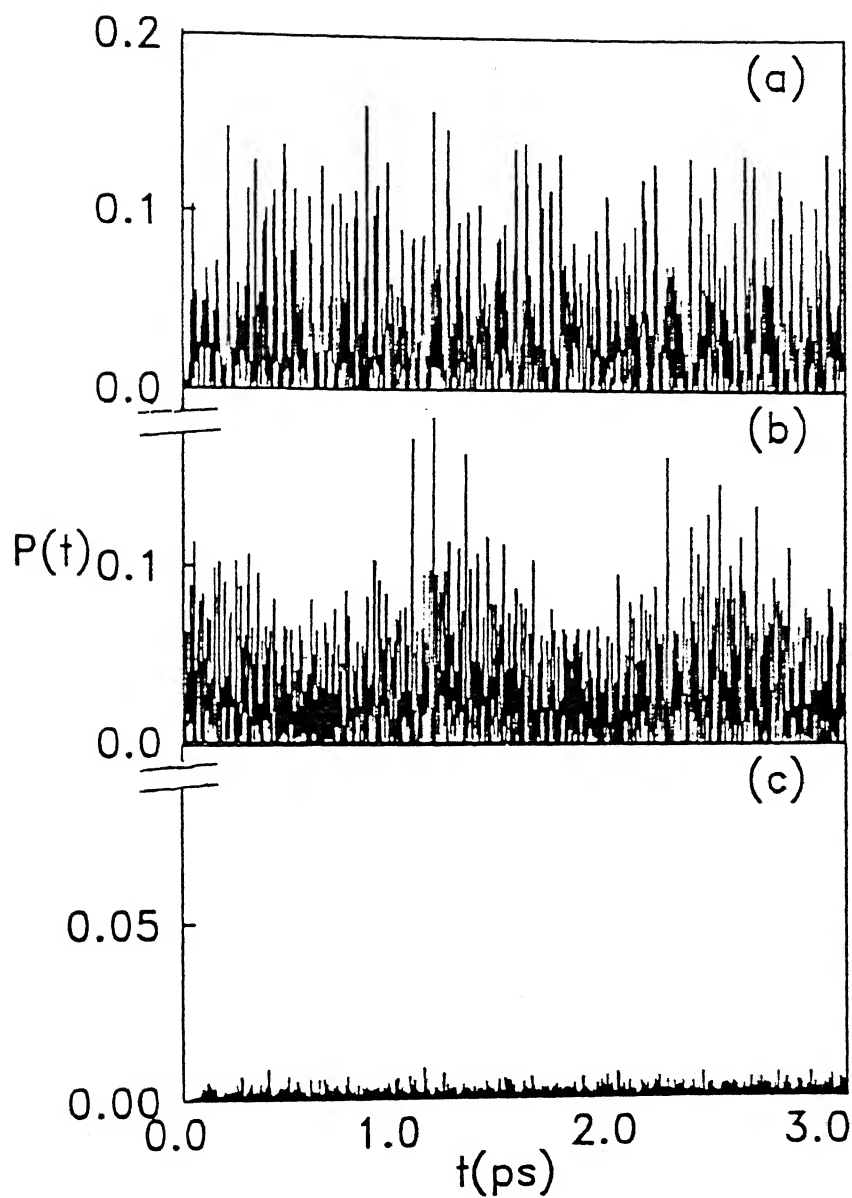
Figure 5.6: The survival probability, $P(t)$, of the wave packets (a), (b) and (c) as a function of time t.

5.4 Discussion and Summary

The signatures of quantum chaos in the scattering dynamics of collinear He,H_2^+ can be seen when the transition state spectra are analysed using commonly employed statistical measures such as the nearest neighbor spacing distribution (Fig. 5.1), the spectral rigidity (Fig. 5.2), and the averaged survival probability (Fig. 5.3). Due to the rather small number of states present in the system, there are large statistical fluctuations, but in all cases it is clear that the system shows level repulsion as well as evidence of being of mixed type, *i.e.* neither regular nor completely irregular. The extent of chaos in the system is estimated to be quite large. By fitting $\langle\langle P(t)\rangle\rangle$ to the RMT, we find that reasonable agreement obtains for $\beta = 0.9$, corresponding to 90% of the states being irregular. This result is not surprising since, as we have discussed earlier, each spectrum originates from a different part of the interaction region of the PES, and the levels are contained within a small section of the phase space. To have an idea of the overall irregularity of the phase space, we did a separate analysis with the whole spectrum obtained by combining the four spectra: $\langle\langle P(t)\rangle\rangle$ for this case is shown in Fig. 5.7(a), and is best fit by $\beta \approx 0.6$, suggesting that approximately 60% of the quantal resonances in R1 are irregular in nature.

In an earlier study, [263, 264] Sathyamurthy and coworkers have investigated the nature and extent of classical chaos in R1. The fractional number of trajectories exhibiting chaotic behavior decreased with increase in energy as shown in Fig. 10 of Ref. [263]. It is not possible to draw a one-to-one correspondence between classical chaos and its signature in the quantum dynamics as the former pertains to a particular energy while the latter involves a distribution of energies.

Complementary results were given in Section 5.3, where we studied the correspondence between the classical trajectory dynamics and quantum wave packet dynamics. It has been shown by Bixon and Jortner [323] that such a correspondence is strictly valid only when a coherent GWP evolves under the action of a harmonic potential. In such situations motion

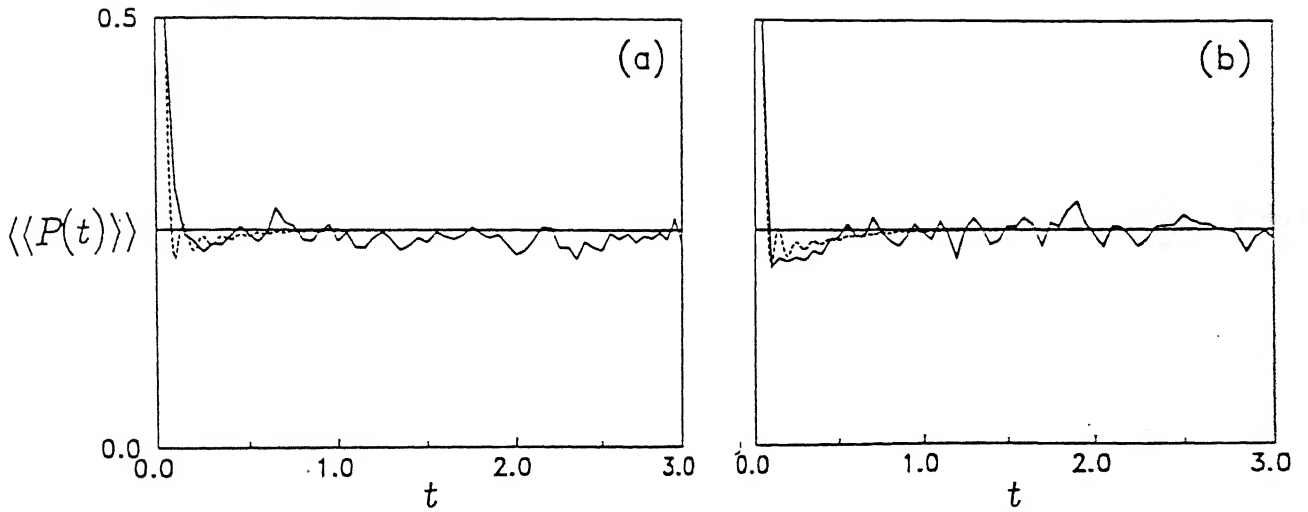Figure 5.7: Variation of survival probability, $\langle\langle P(t)\rangle\rangle$ with time t (a) for the overall spectrum of the phase space, constructed by combining individual spectra, and (b) for the spectrum obtained from the WP (b) illustrated in section 5.3. The RMT $\langle\langle P(t)\rangle\rangle$ values for $\beta = 0.6$ (for (a)) and for $\beta = 0.7$ (for (b)) are superimposed and indicated by the dashed lines.

of the wave packet is described by the first moments $< q >$ and $< p >$ and the center of the wave packet moves along the classical trajectory. However, appearance of terms first order in second moments induces spreading of the wave packet, and due to this the center of the wave packet moves away from the classical trajectory and the correspondence breaks down.

The total volume, $V(t)$, of the phase space the wave packet occupies during its evolution is a quantitative measure of the extent of its spreading. It can be shown that the entropy, S, derived [324] from the partition function varies linearly with $nk_B \ln V$. Therefore, an increase in V gives rise to an increase in S. Our results in Fig. 5.5 show that the entropy associated with the evolution of the wave packet (c) is larger than that for wave packets (b) and (c). Hence, the behavior of the wave packet (c) can be reasonably classified as irregular and that of wave packets (a) and (b) as relatively regular.

The change in the initial state population with time which is termed as the survival probability has been extensively used to check correlation. The semiclassical limit of $P(t)$, as discussed in Section 5.2, is the ensemble averaged value. However, $P(t)$ computed from the wave packet itself contains all the recurrences and shows the following features:

(i) a wave packet initiated at a fixed point corresponding to a stable periodic orbit shows a periodic variation of $P(t)$ with constant amplitude of oscillation which denotes a high degree of correlation;

(ii) for a wave packet initiated at a point corresponding to a quasiperiodic trajectory, $P(t)$ falls sharply below 1.0 and then oscillates with reduced amplitude, signifying moderate correlation;

(iii) for a wave packet initiated at a point corresponding to a chaotic trajectory, $P(t)$ goes to zero sharply as the center of the wave packet moves away due to spreading and shows no correlation.

The behavior of $P(t)$ in Figs. 5.6(a) and 5.6(b) conforms to (ii) above and thus the

corresponding motion can be classified as quasiperiodic, while the behavior in Fig. 5.6(c) conforms to the point (iii) above and hence the corresponding motion is chaotic. The behavior of the power spectrum is complicated in all the cases. However, we find that the power spectrum of wave packets (a) and (b) shows a high degree of regularity and that of (c) a large irregularity arising from the mixing of the different frequency components.

RMT analysis of the power spectra obtained from (a), (b) and (c) does not reveal any distinct difference in the behavior of these spectra in the statistical limit. For example, the ensemble averaged survival probability, $\langle\langle P(t) \rangle\rangle$, computed by RMT gives $\beta = 0.7$ for all of them. $\langle\langle P(t) \rangle\rangle$ generated from the power spectrum of WP (a) (solid line) along with $\langle\langle P(t) \rangle\rangle$ computed by RMT (dashed line) is shown in Fig. 5.7(b). Since the three wave packets differ marginally in terms of their location on the PES and all of them have the same width parameter, the initial energy components present in their basis set are essentially the same. The only difference exists in the weights of the energy components. This difference is reflected in the intensity of the peaks in the spectra. Since the statistical analyses do not depend upon the intensities but on the location of the resonances, all three spectra show similar statistical behavior.

Although the quantum wave packet dynamics reproduces the general classical behavior successfully, quantitative correspondence is lacking. The description can never be complete as the uncertainty principle is at the heart of quantum dynamics and quantum interference effects have no classical analogue. Investigation of the behavior of the wave packet (b) in the classical limit ($\hbar \to 0$), shows that spreading is reduced in this limit and 'scars' in the wave packet coalesce around a point [325]. The power spectrum of $P(t)$ shows peaks at constant spacings and very little mixing of states with different frequencies, verifying that the quantal-classical correspondence becomes pronounced in this limit, as expected.

In summary, we would like to point out that quantal calculations [269, 167, 101] have revealed a large number of resonances for R1 and classical trajectory calculations have

shown a number of trajectories to be irregular [263, 264]. In the present study we have shown, using various measures as NNSD, $\Delta_3(L)$ and $\Sigma^2(L)$ that the quantum dynamics in the system can also be characterized as partly regular and partly irregular, thus establishing a direct link between classical chaos and quantal resonances in this important, prototypical reactive scattering problem.

Chapter 6

Transition State Resonances in Three Dimensional (He,H$_2^+$) Collisions

6.1 Introduction

A number of studies [326] have shown that reactive scattering *resonances* are important in three dimensional collisions. The peaks in the photodetachment spectra obtained by Neumark and coworkers [44-46,109] for a number of heavy-light-heavy (**H-L-H**) systems have been reproduced by the theoretical calculations of Schatz and coworkers [111,112,114-116] . They have been related to the topological features of the corresponding PESs and to the oscillations in the $P_v^R(E)$ curves for the **H + LH** collisions. Kuppermann and coworkers [327] have computed the resonance eigenenergies and lifetimes for the 3D H + H$_2$ ($J = 0, 1$) collisions on the PK2 as well as LSTH PESs. Based on the results of their computation they have anticipated that the 3D resonance energy can be obtained by adding the separable bend energy to the corresponding collinear resonance energy. Recently, Skodje et al [99] have computed the resonance eigenenergies and lifetimes for the 3D H + H$_2$($J = 0$) collisions on the DMBE PES by extending the SQM in three dimensions and found them to be in good agreement with the results of Kuppermann and coworkers [327]. They have reported 33 resonances in 3D [99], in contrast to 13 for the collinear geometry [97, 98] of the system. They have assigned ($\nu_1, \hat{\nu}_2, \nu_3$) quantum numbers to the

eigenfunctions. In addition they have also mentioned that many more resonances exist for the system in 3D, but they could not be assigned clearly because of their complicated nodal pattern and anticipated that the inclusion of the coupling with the higher excited state in the calculation is necessary at higher energies. It also became clear that the collinear resonances exhibit progression along the bending coordinate in three dimensions, and the number is far in excess of that for the collinear geometry for the simplest prototypical exchange reaction.

A large number of narrow resonances have been shown to exist in collinear (He,H_2^+) collisions (chapter 3) and quantum chaos has been inferred (chapter 5). The existence of resonances in 3D He+H_2^+($J = 0$) collisions has been shown by Kress et al [256] and Lepetit and Launay [259] on the MTJS PES. They reported resonances having lifetimes up to ~ 3 ps. Results of Zhang et al [260] and Balakrishnan and Sathyamurthy [265] for 3D $J = 0$ collisions also suggested the existence of numerous resonances on the same PES. Recently, Mandelshtam et al [266] have correlated the quantum mechanical resonances to the classical chaotic scattering through an analysis of the periodic orbits. We have tried to investigate the resonances and their characteristics in 3D He+H_2^+($J = 0$) collisions by extending the SQM in 3D. While the methodology is described in section 6.2, preliminary results are presented in section 6.3 and a succinct summary of our findings follow in section 6.4.

6.2 Methodology

The nuclear Hamiltonian for 3D A+BC ($J = 0$) collisions in mass scaled Jacobi coordinates is given by [225]:

$$
\begin{aligned}
\hat{H} &= \frac{\hat{p}_R^2}{2\mu} + \frac{\hat{p}_r^2}{2\mu} + \frac{\hat{j}^2}{2I} + V(R, r, \gamma) \\
&= -\frac{\hbar^2}{2\mu}\left[\frac{\partial^2}{\partial R^2} + \frac{\partial^2}{\partial r^2}\right] - \frac{\hbar^2}{2I}\frac{1}{\sin\gamma}\frac{\partial}{\partial\gamma}\left(\sin\gamma\frac{\partial}{\partial\gamma}\right) + V(R, r, \gamma)
\end{aligned}
\tag{6.1}
$$

where γ is the angle between $\vec{R}$ and $\vec{r}$. $\gamma = 0$ corresponding to the approach of A to the B end of the BC molecule. μ is the three body reduced mass and $I = \mu(R^2 + r^2)$, is the moment of inertia and $\hat{\mathbf{j}}$ is the angular momentum operator. The associated volume element is $d\tau = \sin\gamma \, dR \, dr \, d\gamma$.

The initial wave function is taken as an even parity GWP, $\Psi(R, r, \gamma, t = 0)$, in terms of the bond coordinates of the triatomic complex ABC:

$$\Psi(R, r, \gamma, t = 0) = N exp\left[-\frac{(r_{AB} - r_{AB}^0)^2}{2\sigma_{AB}^2} - \frac{(r_{BC} - r_{BC}^0)^2}{2\sigma_{BC}^2} - \frac{(\Theta_{ABC} - \Theta_{ABC}^0)^2}{2\sigma_{ABC}^2} \right] \quad (6.2)$$

where N is the normalization constant. The AB and BC internuclear distances r_{AB} and r_{BC} and the bending angle Θ_{ABC} are expressed in terms of (R, r, γ). σ_{AB}, σ_{BC} and σ_{ABC} are the width parameter of the GWP along the respective coordinates.

The TDSE is solved in (R, r, γ) coordinates. The action of the radial and angular kinetic energy operators on the WP is accomplished through the FFT method [66] the DVR method [68,228-230] respectively. The sampling points along the γ coordinate are chosen corresponding to the Gauss-Legendre quadrature points [211]. The grid representation of the initial WP at the point (R_l, r_m, γ_n) is given by:

$$\Phi_{lmn} = \Phi(R_l, r_m, \gamma_n, t = 0) = \sqrt{w_n} \Psi(R_l, r_m, \gamma_n, t = 0) \quad (6.3)$$

where w_n are the Gauss-Legendre weights at γ_n. The temporal evolution of the WP is carried out by the SO method as follows [328]:

$$\begin{aligned}
\Phi_{lmn}(t) &= e^{-i\hat{H}t/\hbar}\Phi_{lmn} \\
&= e^{-i\frac{(\hat{p}_R^2 + \hat{p}_r^2)}{4\mu}t/\hbar} e^{-i\frac{\hat{j}^2}{4I}t/\hbar} \times e^{-iV(R_l, r_m, \gamma_n)t/\hbar} \times \\
&\quad e^{-i\frac{\hat{j}^2}{4I}t/\hbar} e^{-i\frac{(\hat{p}_R^2 + \hat{p}_r^2)}{4\mu}t/\hbar}\Phi_{lmn} + O[(\Delta t)^3]
\end{aligned} \quad (6.4)$$

In numerical calculations this is done as follows :

(i) a 2D forward FFT takes the WP Φ_{lmn} from the (R, r) space to the corresponding (k_R, k_r) space where it is multiplied by the exponential containing the diagonal elements of the kinetic energy operator and then brought back to the (R, r) space through an inverse 2D FFT;

(ii) the results from the above step are then transformed to the angular momentum (j) space (FBR) through the DVR-FBR transformation matrix T_{jn} where the angular kinetic energy operator is diagonal, multiplied by its diagonal values contained in the exponent and brought back to the discrete angle space (DVR) through the inverse transformation matrix $T_{jn}^{\dagger}$;

(iii) since the potential energy operator is diagonal in the discrete space, the result from step (ii) is simply multiplied by the values of the exponential containing the potential $V(R_l, r_m, \gamma_n)$ at the discrete grid points (l, m, n);

(iv) steps (ii) and (i) are repeated on the result.

In practical implementation the time axis is sliced into N steps of length Δt each as mentioned in Sec. 2.4.1, and the entire procedure (i) - (iii) is repeated for each Δt. The DVR-FBR transformation matrix in the Gauss-Legendre quadrature DVR is defined by:

$$\mathbf{T}_{jn} = \sqrt{w_n}\phi_j(\cos\gamma_n) \tag{6.5}$$

where $\phi_j(\cos\gamma)$ are the orthonormal FBR basis functions (normalised Legendre polynomials) which are written in terms of the usual unnormalized Legendre polynomials, $P_j(\cos\gamma)$:

$$\phi_j(\cos\gamma) = \sqrt{\frac{2j+1}{2}}P_j(\cos\gamma) \tag{6.6}$$

The maximum number of angular basis functions used to construct $\mathbf{T}_{jn}$ is equal to $(N_\gamma - 1)$, where N_γ is the number of grid points along γ.

As the WP $\Phi_{lmn}(t)$ at different time steps is computed, the autocrrelation function is also calculated (Eq. (2.115)) and finally Fourier transformed to the energy domain (Eq. (2.116)) to generate the power spectrum. The peaks in the power spectrum are analysed

in the same way as described in chapter 3, to obtain the eigenvalues and the lifetimes of the resonances. The corresponding eigenfunctions are then computed through Eq. (2.122) and analysed to characterize the resonances in terms of $(\nu_1, \hat{\nu}_2, \nu_3)$ quantum numbers.

In order to compute the $He + H_2^+(J = 0)$ resonances on the MTJS PES we constructed a $(128 \times 128 \times 16)$ grid in (R, r, γ) space with the origin at (2.2 a.u., 0.4 a.u., 0.145 rad) and $\Delta R = \Delta r = 0.07$ a.u., $\Delta \gamma \sim 0.19$ rad. The sampling points along γ correspond to the 16 point Gauss-Legendre quadrature. The initial GWP is centered at $(r_{HeH}^0 = 3.20$ a.u., $r_{HH^+}^0 = 5.3$ a.u. , $\Theta_{HeHH^+}^0 = 2.99$ rad) and the width parameters are taken as $\sigma_{HeH} = \sigma_{HH^+} = 0.25$ a.u. and $\sigma_{HeHH^+} = 0.15$ rad. The angular width is chosen such that appreciable bend excitation can occur in the complex HeH_2^+. We set $\Delta t = 0.1616$ fs and the WP is time evolved for a total of 5.29 ps which gives a high enough resolution ($= 7.8 \times 10^{-4}$) in the transition state spectrum. The components of the WP reaching grid edges at a later time are damped out by using the masking function (Eq. (3.13)) which is activated at $R_I = 9.69$ a.u. and $r_I = 7.89$ a.u. and covers 16 % of the grid points in (R, r).

6.3 Results and Discussion

The snapshots of the time evolved WP corresponding to the parameters mentioned in Sec. 6.2 are shown in Fig. 6.1(a-f) in the form of probability density contours superimposed on the potential energy contours in (R, r) plane for a fixed value of $\gamma = 0.145$ rad. Fig. 6.1(a) corresponds to the initial location of the WP. In about 8.08 fs the WP spreads along the asymmetric stretch direction and in another 8.08 fs it develops structures. An analogous feature was found with the WP for the collinear geometry (c.f. Fig. (3.1)). The WP shows a heavy build up of probability density along the ($HeH^+ + H$) channel (Fig.6.1(b)) and the subsequent time evolution (Fig. 6.1(c)) indicates high vibrational excitation of HeH^+ and also of H_2^+. It can be seen from the nodal pattern of this time evolved WP that HeH^+ is excited to the $v' = 5$ and H_2^+ to the $v = 8$ quantum state. In 24.24 fs the WP gets into
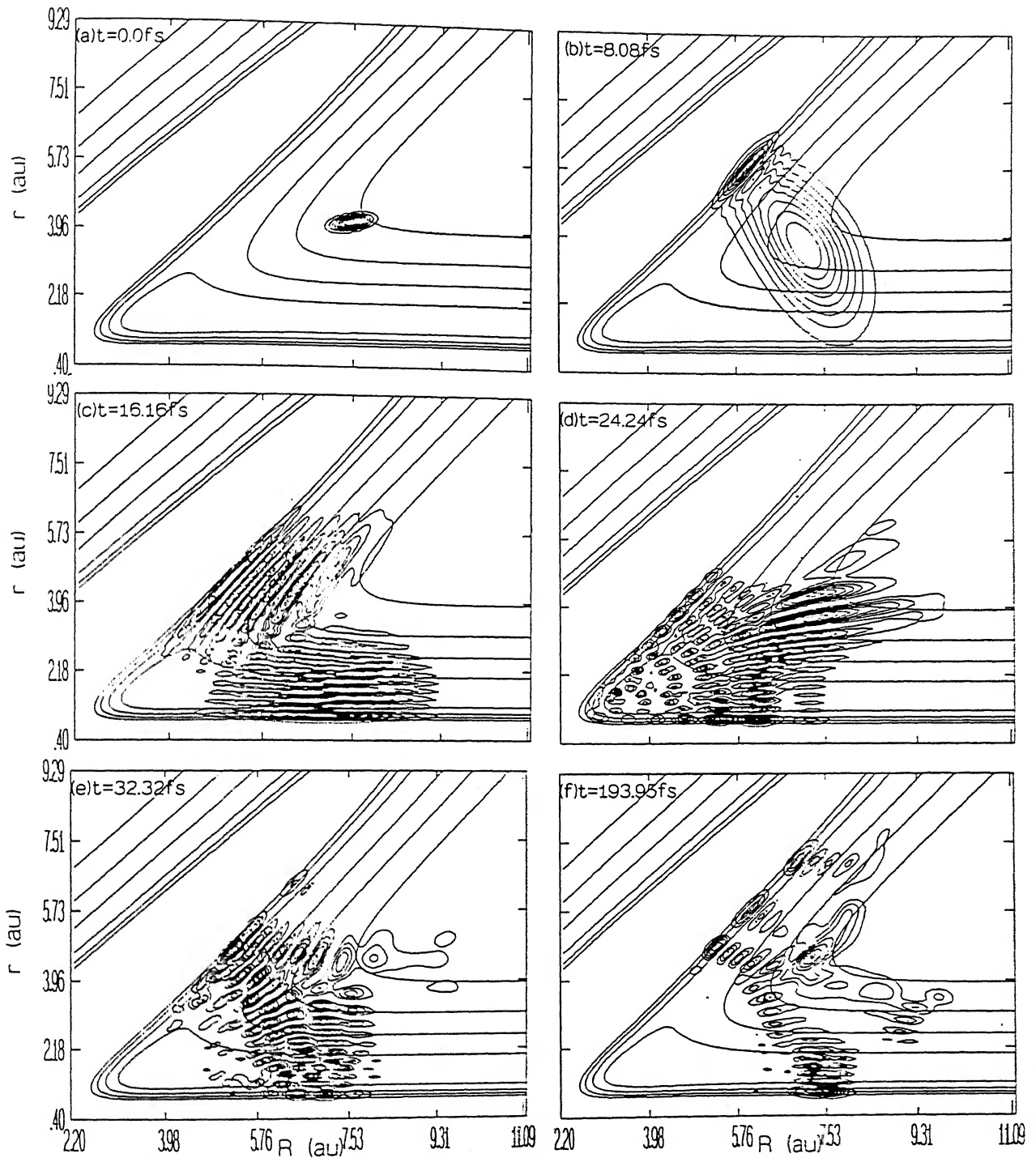
Figure 6.1: Probability density contours of the WP at different times t (indicated inside each box) showing the evolution in (R, r) space for a fixed $\gamma = 0.145$ rad. The norm, $\langle \Psi^* | \Psi \rangle$ of the WP retained on the grid at different times are: 1, 0.99, 0.99, 0.97, 0.94, and 0.20 in (a), (b), (c), (d), (e) and (f) respectively.
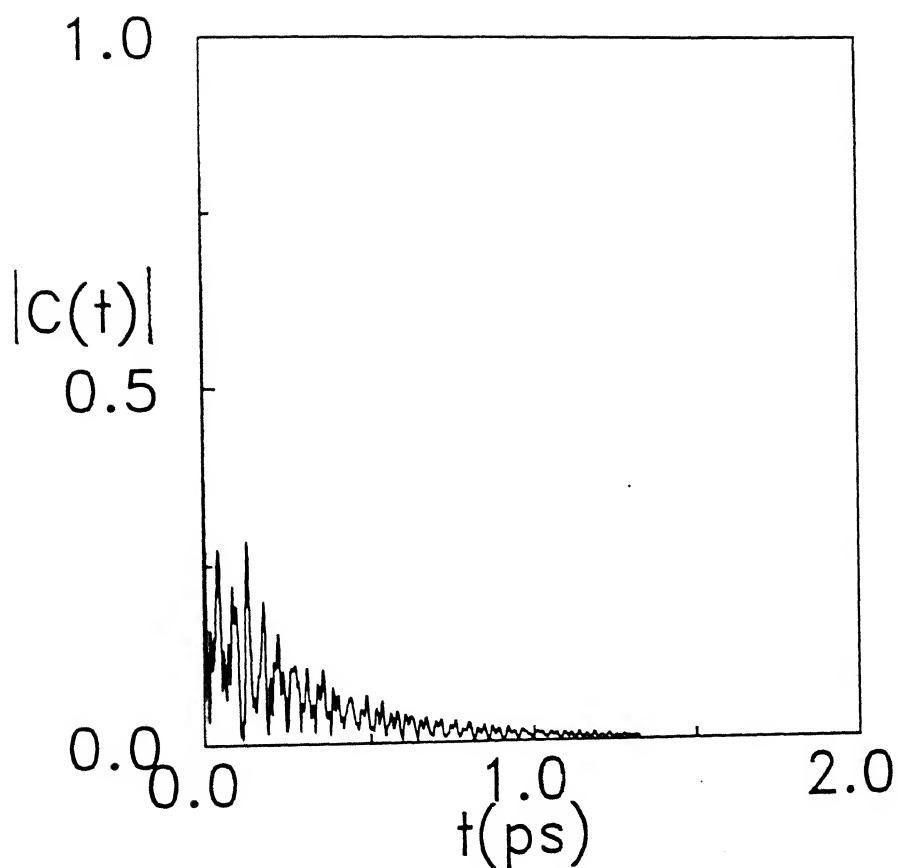
Figure 6.2: Decay of the absolute value of the autocorrelation function $|C(t)|$ for the initial GWP mentioned in the text.
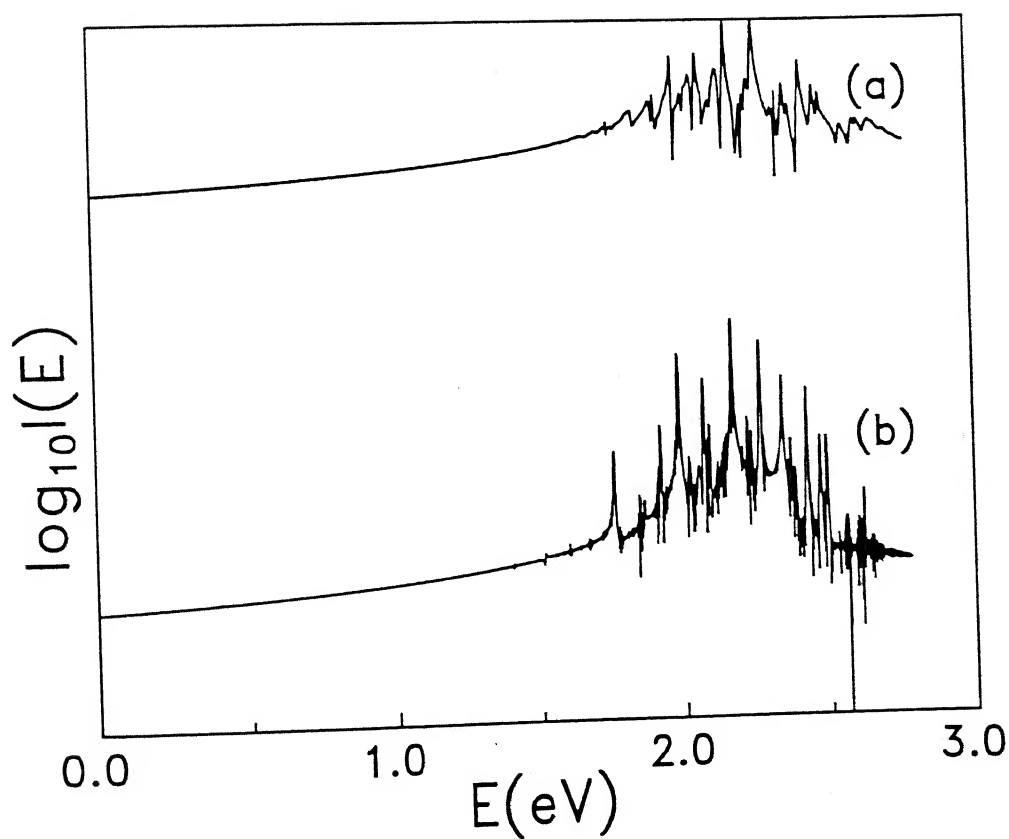
Figure 6.3: Power spectrum in the energy range 0.0-3.0 eV computed by Fourier transforming $C(t)$ of the GWP.

the well of the PES (Fig. 6.1(d)) and it reveals a nodal progression along the asymmetric stretch mode of the HeH_2^+ complex at later times as can be seen in Fig. 6.1(e) and 6.1(f). Since the masking function (Eq. (3.13))is activated at the end of both the channels we do not see any reflection of the WP from grid edges.

The decay of the autocorrelation function (up to 2 ps) is shown in Fig. 6.2. The recurrence pattern is much simpler when compared to the collinear results. The number of recurrences is much less and the amplitude dies off to zero within 1.35 ps. Therefore, it can be concluded that the dynamics of the system is relatively simpler in 3D as was anticipated by Sathyamurthy et al [255] from a study of the nature of the vibrationally adiabatic potential curves for the non-collinear geometries.

The transition state spectrum obtained by Fourier transforming the autocorrelation function is shown in Fig. 6.3. Since the initial WP was centered on a high energy contour of the PES the peaks in the spectrum correspond to the high energy resonances. Fig. 6.3(a) corresponds to the spectrum obtained without using the Hanning window function and 6.4(b) corresponds to the same obtained by using the latter. As can be seen from Fig. 6.3(b) the broad features of Fig. 6.3(a) are resolved into sharp features by the use of the window function. The spacing between the peaks in spectrum 6.3(b) are almost uniform indicating that the corresponding energy levels follow a regular progression. The computation of the resonances at other energies by varying the location of the WP and on a finer grid and a systematic analysis are being pursued.

6.4   Summary and Conclusion

The SQM has been used for investigating resonances in 3D (He, H_2^+) collisions. We have used the FFT method to evaluate the radial derivatives in the Hamiltonian and the Gauss-Legendre DVR for evaluating the angular derivatives. We have obtained preliminary results on a coarse grid for the 3D $He + H_2^+(J = 0)$ collisions which reveal the existence of

resonances. The dynamics of the system appears simpler in three dimensions. A more detailed analysis on a finer grid is presently in progress.

Chapter 7

Summary and Conclusion

Time-dependent quantum mechanical wave packet methods have been used extensively in recent years in investigating problems relating to the area of TS spectroscopy and reactive scattering processes. The TDQM approach provides classical insight into the molecular encounter despite its quantum mechanical origin. Since a real chemical reaction occurs in the time domain this approach offers a direct link with experiment. The development of newer algorithms and faster computing machines has made it possible to study a wide variety of problems in the TDQM frame work. One major advantage of this theory is that a single WP calculation enables the prediction of experimental observables over a range of energy values.

In chapter 1 of the thesis, we have presented an overview of the chronological development of the TDQM methodology. Its application to a variety of problems with a special emphasis on TS spectroscopy and reactive scattering is reviewed. The advantage of the TDQM method over the classical, semi-classical and TIQM methods is discussed.

In chapter 2, the general grid method of solving the time-dependent Schrödinger equation is presented. The representation of the initial WP on a grid and its evolution in space and time are described at length. We present the general collocation or pseudospectral method and its special case when orthogonal basis functions are used, in the context of evaluating $\hat{H}\Psi$. This orthogonal collocation scheme leads to the Fourier method when

plane wave basis functions are used. The use of the fast Fourier transform (FFT) method in order to carry out the $\hat{H}\Psi$ operation has been illustrated. We have also discussed the finite difference (FD) method in this regard and illustrated the superiority of the FFT method over the FD method. The use of the fast Hankel transform (FHT) for evaluation of the action of the radial part of the Laplacian operator in polar coordinates on Ψ is also discussed. Utilising the idea of the orthogonal collocation method, $\hat{H}\Psi$ can also be evaluated locally when a basis set of some classical orthogonal polynomials is used. This results in a set of Gaussian quadrature sampling points in the discrete Hilbert space. A unitary transformation matrix is obtained in this situation which allows one to switch back and forth between the discrete local and non-local spaces. This method is known as the discrete variable representation (DVR) in quantum mechanics. This method is particularly useful in evaluating the action of the angular kinetic energy operator on Ψ where the usual FFT technique ends up with singularity. This DVR method is discussed at length in this chapter.

We have also discussed the various numerical time evolution schemes, viz., the SOD scheme, the SO method, the CP expansion scheme and the SIL method. We have paid special attention to the applicability of these schemes when the negative imaginary potential (NIP) is used to damp out the WP components near the grid edges. Our analysis shows that in presence of a NIP, the SOD scheme is unstable, the SO scheme results in an exponential damping of the WP components near the grid edges, the CP scheme requires the Hamiltonian to be renormalised in order to account for the shift of its eigenvalue spectrum in the complex energy plane and the SIL scheme also results in an exponential damping of the WP components and that the additional complications of the basis vector becoming non-orthogonal can be handled by the Gram-Schmidt orthogonalization scheme.

We have presented the Fourier grid Hamiltonian (FGH) method for computing the bound state eigenvalues and eigenfunctions by utilising the variational method in the

TIQM frame work. The spectral quantization method for computing the bound states as well as the resonance eigenvalues by computing the power spectrum through the Fourier transform of the temporal autocorrelation function of the WP and the eigenfunctions is also described in this chapter. The numerical methods of computation of the vibrational state selected and energy resolved reaction probabilities through a time-energy mapping of the reactive flux of the WP and also the state-to-state reaction probabilities through a time-energy projection are presented. The strategy of computing state-to-state reaction probabilities by computing the S-matrix elements in the Møller operator formalism is also presented.

In chapter 3, we have presented the TS resonances and the dynamics of the collinear

$$\text{He} + \text{H}_2^+ \rightarrow \text{HeH}^+ + \text{H} \quad\quad\quad\quad (R1)$$

reaction and its isotopic variants when one of the two H atoms is replaced by a D on the MTJS PES. We have computed the TS spectrum of all three transients, HeH_2^+, HeHD^+ and HeDH^+ by the spectral quantization method and the reaction probabilities ($P_v^R(E)$) for (He,HD$^+$) and (He,DH$^+$) collisions through a time-energy mapping of the reactive flux of the WP. Interestingly, we have found that the spectra for both HeH_2^+ and HeDH^+ are dominated by a large number of TS resonances compared to that for HeHD^+, for which the threshold resonances seem to dominate. We have computed the eigenfunctions of the resonances and characterized them based on the local and hyperspherical mode description and assigned them appropriate quantum numbers. The analogy of the quantal resonances with the classical resonance periodic orbits is shown for the HeH_2^+ resonances. The life-times of some of the resonances are also reported. The TS spectrum of HeDH$^+$ is found to be densely packed when compared to that of HeH_2^+ and HeHD^+ and the corresponding dynamics is the slowest. The $P_v^R(E)$ values for (He,HD$^+$) show a characteristic staircase-like structure which is related to the threshold resonances and those for (He,DH$^+$) are highly oscillatory, in keeping with a densely packed TS spectrum. The markedly dif-

ferent dynamical behavior of the three systems emphasizes the role of kinematic effects in the system and particularly the complicated dynamics of collinear (He,DH$^+$) collisions suggests the possible existence of "chaos" for which the classical trajectory dynamics would be worth investigating. The results obtained for the reaction (R1) are compared with the available TIQM results.

In chapter 4, the TS resonances and the dynamics of the collinear

$$H^- + H_2 \rightarrow H_2 + H^- \tag{R2}$$

reaction on the SM PES have been reported. This system has shown the existence of a large number of TS resonances when compared to its neutral analog for which the resonances have been shown to be of threshold origin. Although the SM PES is very similar to the LSTH or the DMBE PES for the neutral analog the two systems differ significantly in terms of their dynamical behavior. The $P_v^R(E)$ values computed for reaction (R2) through the time-energy mapping of the reactive flux of the WP are highly oscillatory. We have explained the origin of some of the resonances therein on the basis of the quasibound states supported by the vibrationally adiabatic potentials. The eigenfunctions of the resonances reveal a matted structure at low energies and we have assigned a set of quantum numbers representative of the nodes along the hyperspherical radius (ρ) and angle (ϕ). At higher energies the nodal progression along ρ disappears and results in the hyperspherical modes (progression along ϕ) only. We are presently analysing the classical trajectory dynamics in order to explain the origin of the resonances in the system.

The existence of a large number of narrow TS resonances in collinear (He,H$_2^+$) collisions and its known chaotic behavior in the classical domain inspired us to extract the signature of classical chaos in quantum domain. Although the term "chaos" seems to be well understood in classical mechanics, its meaning and implication in quantum mechanics continues to be the subject of considerable debate. We have examined the short- range and long-range correlations in the eigenvalue spectrum of the TS of the system through a study of

the $P(s)$, and the $\triangle_3(L)$, respectively. The spacing distribution statistics show an intermediate behavior between the Poisson (regular) and the Wigner (irregular) limits. A similar conclusion is drawn from the $\triangle_3(L)$ statistics, which show an intermediate distribution between the Poisson and the Gaussian orthogonal ensemble (GOE) limit. The behavior in the time domain has been examined by computing the ensemble averaged survival probability, $<< P(t) >>$, by Fourier transforming the spectral autocorrelation function followed by averaging over the initial states and the Hamiltonian. $<< P(t) >>$ values when plotted against time t show the existence of the "correlation hole"– a typical quantum chaotic behavior. A quantitative comparison of $<< P(t) >>$ with that obtained from the random matrix theory enables us to conclude that 70% of the phase space exhibits chaotic behavior in collinear (He, H_2^+) collision dynamics. We have also analysed the dynamical evolution of a coherent GWP located initially in different regions of phase space and computed the survival probability, power spectrum and the volume of phase space over which the WP spreads to illustrate the classical-quantal correspondence. The GWP initially centered at a chaotic point of classical phase space resulted in a spreading of the WP over the entire phase space. This leads to a large increase in the statistical entropy during the evolution of the WP. The survival probability values become totally uncorrelated in this chaotic situation. This has been documented in chapter 5 of the thesis.

In chapter 6, we report on a preliminary investigation of the TS resonances in 3D He+$H_2^+(J=0)$ collisions on the MTJS PES. We have extended the SQM in three dimensions to compute the TS spectrum by Fourier transforming the temporal autocorrelation function, $C(t)$, of the initial WP written in terms of bond distances and bond angle. The action of the radial kinetic energy operators are evaluated by the FFT method and the action of the angular kinetic energy operator is evaluated by a 16-point Gauss-Legendre DVR. We have obtained a few high-energy TS resonances of the systems on a $(128 \times 128 \times 16)$ grid in (R, r, γ) coordinates. The dynamics of the system in three dimensions looks simpler

than that in the collinear geometry. The computation of other resonances by varying the location of the initial WP in the interaction region of the PES and their systematic analysis on a finer grid are presently in progress.

Bibliography

[1] H. Eyring and M. Polanyi, Z. Phys. Chem. **B12**, 279 (1931).

[2] D. G. Truhlar (Ed.), Potential Energy Surfaces and Dynamics Calculations, Plenum, New York, 1981.

[3] J. N. Murrell, S. Carter, S. C. Farantos, P. Huxley and A. J. C. Varandas, Molecular Potential Energy Functions, John Wiley, Chichester, 1984.

[4] N. Sathyamurthy, Comput. Phys. Rep. **3**, 1 (1985).

[5] N. Sathyamurthy and T. Joseph, J. Chem. Ed. **61**, 968 (1984).

[6] M. M. Law, J. M. Huston and A. Ernesti (Eds.), Fitting Molecular Potential Energy Surfaces, CCP6, 1993.

[7] W. H. Miller (Ed.), Dynamics of Molecular Collisions, Plenum, New York, 1976.

[8] R. B. Bernstein (Ed.), Atom-Molecule Collision Theory: A Guide for the Experimentalists, Plenum, New York, 1979.

[9] F. A. Gianturco (Ed.), Atomic and Molecular Collision Theory, Plenum, New York, 1982.

[10] J. M. Bowman (Ed.), Molecular Collision Dynamics, Springer-Verlag, Berlin, 1983.

[11] M. Baer (Ed.), The Theory of Chemical Reaction Dynamics, CRC Press, Boca Raton, Florida, Vol. I-IV, 1985.

[12] D. C. Clary (Ed.), The Theory of Chemical Reaction Dynamics, Reidel, Boston, 1986.

[13] R. D. Levine and R. B. Bernstein, Molecular Reaction Dynamics, Oxford Univ. Press, Oxford, 1987.

[14] J. N. Murrell and S. D. Bosanac, Introduction to the Theory of Atomic and Molecular Collisions, John Wiley & Sons, Chichester, 1989.

[15] N. Sathyamurthy (Ed.), Reaction Dynamics: Recent Advances, Narosa, New Delhi, 1991.

[16] A. H. Zewail (Ed.), The Chemical Bond: Structure and Dynamics, Academic Press, New York, 1992.

[17] R. B. Bernstein, R. D. Levine and D. R. Herschbach, J. Phys. Chem. **91**, 5365 (1985).

[18] P. R. Brooks and E. F. Hayes (Eds.), State-to-State Chemistry, ACS Symposium Series, Washington D. C., 1977.

[19] H. J. Loesch and A. Remscheid, J. Chem. Phys. **94**, 4779 (1990); **95**, 8194 (1991).

[20] H. J. Loesch, A. Remscheid, E. Stenzel, F. Stienkemeier and B. Wüstenbecker, IC-PEAC XVII, Brisbane, IOP Publishing, 1992, p. 579.

[21] M. Brouard and J. P. Simons, in: Chemical Dynamics and kinetics of Small Free Radicals, K. Liu and A. L. Wagner (Eds.), World Scientific, Singapore, 1995; M. Brouard, H. M. Lambert, J. Short and J. P. Simons, J. Phys. Chem. **99**, 13571 (1995).

[22] N. E. Shafer, A. J. Orr-Ewing, W. R. Simpson, H. Xu and R. N. Zare, Chem. Phys. Lett. **212**, 155 (1993); R. N. Zare and A. J. Orr-Ewing, in: Ref. 21.

[23] R. B. Bernstein, Chemical Dynamics via Molecular Beam and Laser Techniques, Clarendon Press, Oxford, 1982.

[24] B. Friedrich and D. R. Herschbach, Nature (London) **353**, 412 (1991).

[25] B. Friedrich, D. P. Pullman and D. R. Herschbach, J. Phys. Chem. **95**, 8118 (1991).

[26] B. Friedrich and D. R. Herschbach, Z. Phys. D - Atoms, Molecules and Clusters **18**, 153 (1991); **24**, 25 (1992).

[27] B. Friedrich, D. R. Herschbach, J-M. Rost, H-G. Rubahn, M. Renger and M. Verbeek, J. Chem. Soc. Faraday Trans. **89**(10), 1539 (1993).

[28] P. A. Block, E. J. Bohac and R. E. Miller, Phys. Rev. Lett. **68**, 1303 (1992).

[29] J. M. Rost, J. C. Griffin, B. Friedrich and D. R. Herschbach, Phys. Rev. Lett. **68**, 1299 (1992).

[30] B. Friedrich, H-J. Rubahn and N. Sathyamurthy, Phys. Rev. Lett. **69**, 2487 (1992).

[31] Special issue of J. Phys. Chem. on "Femtosecond Chemistry", **97**(48), 1993.

[32] Special issue of Chem. Phys. on "Photon-Induced Molecular Dynamics", **187** (1-2), 1-225 (1994).

[33] A. H. Zewail, Femtochemistry - Ultrafast Dynamics of the Chemical Bond, World Scientific, Singapore, 1994, Vol. I-II.

[34] J. Manz and L. Wöste (Ed.), Femtosecond Chemistry, VCH, Weinheim, 1995, Vol.I-II.

[35] C. V. Shank, Science **233**, 1276 (1986).

[36] M. J. Rosker, M. Dantus and A. H. Zewail, Science **241**, 1200 (1988).

[37] A. H. Zewail, Science **242**, 1645 (1988).

[38] J. L. Knee and A. H. Zewail, Spectroscopy **3**, 44 (1988).

[39] M. Dantus, R. M. Bowman and A. H. Zewail, Nature **343**, 737 (1990).

[40] A. Mokhtari, P. Cong, J. L. Herek and A. H. Zewail, Nature **348**, 225 (1990).

[41] I. W. M. Smith, Nature **343**, 69 (1990).

[42] L. R. Khundkar and A. H. Zewail, Ann. Rev. Phys. Chem. **41**, 15 (1990).

[43] J. C. Williamson and A. H. Zewail, Proc. Natl. Acad. Sci. USA **88**, 5021 (1991).

[44] R. B. Metz, S. E. Bradforth and D. M. Neumark, Adv. Chem. Phys. **81**, 1 (1992), and references therein.

[45] D. M. Neumark, Acc. Chem. Res. **26**, 33 (1993).

[46] D. E. Manolopoulos, K. Stark, H. -J. Werner, D. W. Arnold, S. E. Bradforth and D. M. Neumark, Science **262**, 1852 (1993).

[47] G. C. Schatz, Science **262**, 1828 (1993).

[48] J. C. Polanyi and A. H. Zewail, Acc. Chem. Res. **28**, 119 (1995).

[49] G. Porter, in: Femtosecond Chemistry, J. Manz and L. Wöste (Ed.), VCH, Weinheim, 1995, pp.3-13.

[50] G. Porter, Proc. R. Soc. London Ser. **A200**, 284 (1950).

[51] G. Porter, Disc. Faraday Soc. **9**, 60 (1950).

[52] M. Karplus, R. N. Porter and R. D. Sharma, J. Chem. Phys. **43**, 3259 (1965).

[53] L. M. Raff and D. L. Thompson, in: Theory of Chemical Reaction Dynamics, M. Baer (Ed.), CRC Press, Boca Raton, Florida, Vol. III, 1985, pp.1-121.

[54] W. H. Miller, Adv. Chem. Phys. **25**, 69 (1974); **30**, 77 (1975).

[55] N. Balakrishnan, C. Kalyanaraman and N. Sathyamurthy, Phys. Rep. (submitted).

[56] E. Schrödinger, Ann. Phys. **79**, 489 (1926).

[57] P. Ehrenfest, Z. Phys. **45**, 455 (1927).

[58] J. Mazur and R. J. Rubin, J. Chem. Phys. **31**, 1395 (1959).

[59] A. Goldberg, H. M. Schey and J. L. Schwartz, Am. J. Phys. **35**, 177 (1967).

[60] E. A. McCullough and R. E. Wyatt, J. Chem. Phys. **51**, 1253 (1969); **54**, 3578, 3592 (1971).

[61] A. Askar and A. S. Cakmak, J. Chem. Phys. **68**, 2794 (1978).

[62] J. Rubin, J. Chem. Phys. **70**, 4811 (1979).

[63] H. F. Harmuth, J. Math. and Phys. **36**, 269 (1957).

[64] J. A. Fleck, Jr., J. R. Morris and M. D. Feit, Appl. Phys. **10**, 129 (1976).

[65] M. D. Feit, J. A. Fleck, Jr., and A. Steiger, J. Comp. Phys. **47**, 412 (1982).

[66] D. Kosloff and R. Kosloff, Comput. Phys. Commun. **30**, 333 (1983); J. Comp. Phys. **52**, 35 (1983).

[67] R. Kosloff and D. Kosloff, J. Chem. Phys. **79**, 1823 (1983).

[68] J. V. Lill, G. A. Parker and J. C. Light, Chem. Phys. Lett. **89**, 483 (1982); J. C. Light, I. P. Hamilton and J. V. Lill, J. Chem. Phys. **82**, 1400 (1985).

[69] H. Tal-Ezer and R. Kosloff, J. Chem. Phys. **81**, 3967 (1984).

[70] R. Bisseling and R. Kosloff, J. Comp. Phys. **59**, 136 (1985).

[71] C. Lanczos, J. Math. Phys. **17**, 123 (1938).

[72] T. J. Park and J. C. Light, J. Chem. Phys. **85**, 5870 (1986) .

[73] F. Quéré and C. Leforestier, J. Chem. Phys. **92**, 247 (1990).

[74] H. Tal-Ezer, R. Kosloff and C. Cerjan, J. Comp. Phys. **100**, 179 (1992).

[75] C. Leforestier, R. Bisseling, C. Cerjan, M. D. Feit, R. Friesner, A. Guldberg, A. Hammerich, G. Jolicard, W. Karrlein, H. -D. Meyer, N. Lipkin, O. Roncero and R. Kosloff, J. Comp. Phys. **94**, 59 (1991).

[76] T. N. Truong, J. J. Tanner, P. Bala, J. A. McCammon, D. J. Kouri, B. Lesyng and D. K. Hoffman, J. Chem. Phys. **96**, 2077 (1992).

[77] D. J. Tannor and S. A. Rice, J. Chem. Phys. **83**, 5013 (1985).

[78] D. J. Tannor, R. Kosloff and S. A. Rice, J. Chem. Phys. **85**, 5805 (1986).

[79] S. Shi, A. Woody and H. Rabitz, J. Chem. Phys. **88**, 6870 (1988).

[80] S. Shi and H. Rabitz, Chem. Phys. **139**, 185 (1989); J. Chem. Phys. **92**, 2927 (1990).

[81] R. Kosloff, S. A. Rice, P. Gaspard, S. H. Tersigni and D. J. Tannor, Chem. Phys. **139**, 201 (1989).

[82] S. H. Tersigni, P. Gaspard and S. A. Rice, J. Chem. Phys. **93**, 1670 (1990).

[83] B. Amstrup, R. J. Carlson, A. Matro and S. A. Rice, J. Phys. Chem. **95**, 8019 (1991).

[84] S. A. Rice, Science **258**, 412 (1992).

[85] C. Kalyanaraman and N. Sathyamurthy, Curr. Sci. **65**, 319 (1993).

[86] P. Brumer and M. Shapiro, Sci. Am. **272**, 34 (1995).

[87] G. Herzberg, Spectra of Diatomic Molecules, Van Nostrand, Princeton, 1950.

[88] H. Lefebvre-Brion and R. W. Field, Perturbations in the Spectra of Diatomic Molecules, Academic Press, Orlando, 1986.

[89] Special issue of Faraday Discuss. Chem. Soc. on: "Dynamics of Molecular Photofragmentation", **82** (1986).

[90] M. N. R. Ashfold and J. E. Baggott, Molecular Photodissociation Dynamics, Royal Society of Chemistry, London, 1987.

[91] R. P. Wayne, Principles and Applications of Photochemistry, Oxford University Press, Oxford, 1988.

[92] E. J. Heller, Acc. Chem. Res. **14**, 368 (1981); in Reference 1.

[93] R. Schinke, Photodissociation Dynamics, Cambridge University Press, Cambridge, 1992.

[94] A. D. Bandrauk (Ed.), Molecules in Laser Fields, Marcel Dekker, Inc. New York, 1993.

[95] G. G. Balint-Kurti and M. M. Law (Eds.), Photodissociation Dynamics, CCP6, Daresbury Laboratory, Daresbury, Warrington, UK, 1994.

[96] C. Kalyanaraman, Ph. D. Thesis, Indian Institute of Technology Kanpur, 1994.

[97] R. Sadeghi and R. T. Skodje, J. Chem. Phys. **98**, 9208 (1993).

[98] R. Sadeghi and R. T. Skodje, J. Chem. Phys. **99**, 5126 (1993).

[99] R. T. Skodje, R. Sadeghi, J. R. Krause and H. Köppel, J. Chem. Phys. **101**, 1725 (1994).

[100] R. Sadeghi and R. T. Skodje, J. Chem. Phys. **102**, 193 (1995).

[101] S. Mahapatra and N. Sathyamurthy, J. Chem. Phys. **102**, 6057 (1995).

[102] S. Mahapatra, N. Sathyamurthy, S. Kumar and F. A. Gianturco, Chem. Phys. Lett. **241**, 223 (1995).

[103] D. G. Truhlar (Ed.), Resonances in Electron-Molecular Scattering, van der Waals Complexes, and Reactive Chemical Dynamics, ACS Symposium Series 263 ACS, Washington, D. C., 1984.

[104] G. C. Schatz, Ann. Rev. Phys. Chem. **39**, 317 (1988).

[105] D. E. Manolopoulos and D. C. Clary, Ann. Rep. Chem. Soc. C, 95 (1989).

[106] W. H. Miller, Ann. Rev. Phys. Chem. **41**, 245 (1990).

[107] R. B. Metz, T. Kitsopoulos, A. Weaver and D. M. Neumark, J. Chem. Phys. **88**, 1463 (1988).

[108] R. B. Metz, A. Weaver, S. E. Bradforth, T. N. Kitsopoulos and D. M. Neumark, J. Phys. Chem. **94**, 1377 (1990)

[109] A. Weaver, R. B. Metz, S. E. Bradforth and D. M. Neumark, J. Phys. Chem. **92**, 5558 (1988); I. M. Waller, T. N. Kitsopoulos and D. M. Neumark, J. Phys. Chem. **94**, 2240 (1990).

[110] E. de Beer, E. H. Kim, D. M. Neumark, R. F. Gunion, and W. C. Lineberger, J. Phys. Chem. **99**, 13627 (1995).

[111] G. C. Schatz, J. Chem. Phys. **90**, 3582 (1989).

[112] G. C. Schatz, J. Chem. Phys. **90**, 4847 (1989); J. Chem. Soc. Faraday Trans. **86**, 1729 (1990).

[113] J. M. Bowman, B. Gazdy and Q. Sun, J. Chem. Soc. Farad. Trans. **86**, 1737 (1990).

[114] G. C. Schatz, D. Sokolovski and J. N. L. Connor, Farad. Discuss. Chem. Soc. **91**, 17 (1991).

[115] G. C. Schatz, D. Sokolovski and J. N. L. Connor, in: Advances in Molecular Vibrations and Collision Dynamics, J. M. Bowman (Ed.), JAI, Greenwich, **2B**, 1-26 (1994).

[116] D. Sokolovski, J. N. L. Connor and G. C. Schatz, Chem. Phys. Lett. **238**, 127 (1995); J. Chem. Phys. **103**, 5979 (1995).

[117] K. C. Kulander, Phys. Rev. A **35**, 445 (1987); K. C. Kulander, K. J. Schafer and J. L. Krause, in: Atoms in Intense Laser Field, Academic Press, 1992, pp. 247-300.

[118] R. Heather and H. Metiu, J. Chem. Phys. **88**, 5496 (1988).

[119] S. O. Williams and D. G. Imre, J. Phys. Chem. **92**, 6636 (1988).

[120] R. H. Bisseling, R. Kosloff and J. Manz, J. Chem. Phys. **83**, 993 (1985).

[121] D. J. Tannor and S. A. Rice, J. Chem. Phys. **83**, 5013 (1985).

[122] H. H. R. Schor, Ber. Bunsenges. Phys. Chem. **89**, 270 (1985).

[123] D. J. Tannor, R. Kosloff and S. A. Rice, J. Chem. Phys. **85**, 5805 (1986).

[124] S. A. Rice, J. Phys. Chem. **90**, 3063 (1986).

[125] (a) T. Joseph and J. Manz, Mol. Phys. **58**, 1149 (1986). (b) T. Joseph, T. -M. Kruel, J. Manz, and I. Rexrodt, Chem. Phys. **113**, 223 (1987); (c) T. Joseph, J. Manz, V. Mohan, and H. -J. Schreier, Ber. Bunsenges. Phys. Chem. **92**, 397 (1988).

[126] B. Hartke, J. Manz and J. Mathis, Chem. Phys. **139**, 123 (1989).

[127] R. Kosloff, S. A. Rice, P. Gaspard, S. Tersigni and D. J. Tannor, Chem. Phys. **139**, 201 (1989).

[128] B. Hartke, E. Kolba, J. Manz and H. H. R. Schor, Ber. Bunsenges. Phys. Chem. **94**, 1312 (1990).

[129] B. Hartke and J. Manz, J. Chem. Phys. **92**, 220 (1990).

[130] B. Amstrup, R. J. Carlson, A. Matro and S. A. Rice, J. Phys. Chem. **95**, 8019 (1991).

[131] S. Chelkowski and A. D. Bandrauk, Chem. Phys. Lett. **186**, 264 (1991).

[132] J. A. Beswick and J. Jortner, Adv. Chem. Phys. **47**, 363 (1981).

[133] J. A. Beswick and N. Halberstadt, Dynamics of Weakly Bound Complexes, Kluwer, Dordrecht, 1993.

[134] S. O. Williams and D. G. Imre, J. Phys. Chem. **92**, 3363 (1988).

[135] R. Heather and H. Metiu, J. Chem. Phys. **90**, 6903 (1989).

[136] (a) B. Hartke, Chem. Phys. Lett. **160**, 538 (1989); (b) M. Ganz, B. Hartke, W. Kiefer, E. Kolba, J. Manz and J. Strumpel, Vibrational Spectroscopy **1**, 119 (1990); (c) B. Hartke, J. Raman Spect. **22**, 131 (1991).

[137] T. Seideman and W. H. Miller, J. Chem. Phys. **95**, 1768 (1991).

[138] M. J. Cohen, N. C. Handy, R. Hernandez, and W. H. Miller, Chem. Phys. Lett. **192**, 407 (1992).

[139] R. Viswanathan, S. Shi, E. Vilallonga and H. Rabitz, J. Chem. Phys. **91**, 2333 (1989).

[140] D. J. Tannor and D. E. Weeks, J. Chem. Phys. **98**, 3884 (1993).

[141] D. E. Weeks and D. J. Tannor, Chem. Phys. Lett. **207**, 301 (1993).

[142] D. J. Tannor and D. E. Weeks, Chem. Phys. Lett. **224**, 451 (1994).

[143] A. Jäckle and H. -D. Meyer, J. Chem. Phys. **102**, 5605 (1995).

[144] S. O. Williams and D. G. Imre, J. Phys. Chem. **92**, 6648 (1988).

[145] W. T. Pollard, S. -Y. Lee and R. A. Mathies, J. Chem. Phys. **92**, 4012 (1990).

[146] (a) H. Metiu and V. Engel, J. Opt. Soc. Am. B**7**, 1709 (1990); (b) H. Metiu, Farad. Disc. Chem. Soc. **91**, 1 (1991); (c) V. Engel and H. Metiu, J. Chem. Phys. **95**, 3444 (1991); (d) R. Bavli, V. Engel and H. Metiu, J. Chem. Phys. **96**, 2600 (1992).

[147] V. Engel and H. Metiu, J. Chem. Phys. **90**, 6116 (1989); **91**, 1596 (1989); **92**, 2317 (1990); **93**, 5693 (1990).

[148] H. Kono and Y. Fujimura, Chem. Phys. Lett. **184**, 497 (1991).

[149] (a) M. Gruebele and A. H. Zewail, Phys. Today **43**, 24 (1990); J. Chem. Phys. **98**, 883 (1993).

[150] A. H. Zewail, Sci. Am. **263**, 40 (1990); J. Phys. Chem. **97**, 12427 (1993).

[151] G. Beddard, Rep. Prog. Phys. **56**, 63 (1993).

[152] B. M. Garraway, S. Stenholm and K. -A. Suominen, Phys. World **6**, 45 (1993).

[153] L. Valko, Phys. Rev. A**47**, 4123 (1993).

[154] C. Leforestier, Chem. Phys. **87**, 241 (1984).

[155] D. Neuhauser and M. Baer, J. Phys. chem. **93**, 2872 (1989).

[156] D. Neuhauser and M. Baer, J. Chem. Phys. **91**, 4651 (1989).

[157] D. Neuhauser and M. Baer, J. Phys. Chem. **94**, 186 (1990).

[158] D. Neuhauser and M. Baer, J. Chem. Phys. **92**, 3419 (1990).

[159] R. S. Judson, D. J. Kouri, D. Neuhauser and M. Baer, Phys. Rev. A **42**, 351 (1990).

[160] D. Neuhauser, M. Baer, R. S. Judson and D. J. Kouri, Chem. Phys. Lett. **169**, 372 (1990).

[161] G. G. Balint-Kurti, R. N. Dixon and C. C. Marston, Farad. Trans. Chem. Soc. **86**, 1741 (1990).

[162] G. G. Balint-Kurti, R. N. Dixon, C. C. Marston and A. J. Mulholland, Comput. Phys. Commun. **63**, 126 (1991).

[163] N. Marković and G. D. Billing, J. Chem. Phys. **97**, 8201 (1992).

[164] D. Neuhauser, M. Baer, R. S. Judson and D. J. Kouri, Comput. Phys. Commun. **63**, 460 (1991).

[165] D. Neuhauser, R. S. Judson, D. J. Kouri, D. E. Adelman, N. E. Shafer, D. A. V. Kliner and R. N. Zare, Science **257**, 519 (1992).

[166] D. H. Zhang and J. Z. H. Zhang, J. Chem. Phys. **99**, 5615 (1993); **100**, 2697 (1994); **101**, 1146 (1994).

[167] N. Balakrishnan and N. Sathyamurthy, Chem. Phys. Lett. **240**, (1995).

[168] G. Jolicard and G. D. Billing, Chem. Phys. **149**, 261 (1991).

[169] R. B. Gerber, R. Kosloff and M. Berman, Comput. Phys. Rep. **5**, 59 (1986).

[170] G. D. Billing, Comput. Phys. Rep. **12**, 385 (1990).

[171] A. T. Yinnon, R. Kosloff and R. B. Gerber, J. Chem. Phys. **88**, 7209 (1988).

[172] R. C. Mowrey, H. F. Bowen and D. J. Kouri, J. Chem. Phys. **86**, 2441 (1987).

[173] B. Jackson and H. Metiu, J. Chem. Phys. **86**, 1026 (1987).

[174] M. R. Hand and S. Holloway, Surf. Sci. **211/212**, 940 (1989); J. Chem. Phys. **91**, 7209 (1989).

[175] R. C. Mowrey and D. J. Kouri, J. Chem. Phys. **86**, 6140 (1990).

[176] D. Lemoine and G. C. Corey, J. Chem. Phys. **92**, 6175 (1990).

[177] D. Halstead and S. Holloway, J. Chem. Phys. **93**, 2859 (1990).

[178] D. Lemoine and G. C. Corey, J. Chem. Phys. **94**, 767 (1991).

[179] S. Holloway, in: Dynamics of Gas-Surface Collisions, M. N. R. Ashfold and C. T. Rettner (Ed.), Royal Soc. Chem., Cambridge, 1991.

[180] H. F. Bowen, D. J. Kouri, R. C. Mowrey, A. T. Yinnon and R. B. Gerber, J. Chem. Phys. **99**, 704 (1993).

[181] G. R. Darling and S. Holloway, Chem. Phys. Lett. **191**, 396 (1992); J. Chem. Phys. **97**, 5182 (1992); Surf. Sci. **304**, L461 (1994); J. Chem. Phys. **101**, 3268 (1994).

[182] G. A. Gates, G. R. Darling and S. Holloway, Chem. Phys. **179**, 199 (1994).

[183] G. A. Gates, G. R. Darling and S. Holloway, J. Chem. Phys. **101**, 6281 (1994).

[184] G. A. Gates and S. Holloway, Surf. Sci. **307**, 132 (1994).

[185] G. Wiesenekker, G. J. Kroes, E. J. Baerends and R. C. Mowrey, J. Chem. Phys. **102**, 3873 (1995).

[186] G. J. Kroes, J. G. Snijders and R. C. Mowrey, J. Chem. Phys. **102**, 5512 (1995).

[187] M. Alagia, N. Balucani, P. Casavecchia, D. Stranges and G. G. Volpi, J. Chem. Soc. Farad. Trans. **91**, 575 (1995).

[188] D. H. Zhang and J. Z. H. Zhang, Chem. Phys. Lett. **232**, 370 (1995); D. H. Zhang, J. Z. H. Zhang, Y. Zhang, D. Wang and Q. Zhang, J. Chem. Phys. **102**, 7400 (1995).

[189] D. Neuhauser, J. Chem. Phys. **100**, 9272 (1994).

[190] N. Balakrishnan and G. D. Billing, J. Chem. Phys. **101**, 2785 (1994); Chem. Phys. Lett. **233**, 145 (1995).

[191] R. Kosloff, J. Phys. Chem. **92**, 2087 (1988).

[192] V. Mohan and N. Sathyamurthy, Comput. Phys. Rep. **7**, 213 (1988).

[193] Thematic issue of Comput. Phys. Commun. on: "Time Dependent Methods for Quantum Dynamics", K. C. Kulander (Ed.), **63**, 1-582 (1991).

[194] J. Broeckhove and L. Lathouwers, Time Dependent Methods for Quantum Dynamics, NATO ASI Ser. B**229**, Plenum Press, New York, 1992.

[195] C. Cerjan (Ed.), Numerical Grid Methods and Their Applications to Schrödinger's Equation, NATO ASI Ser. C**412**, Kluweru Academic Publishers, Dordrecht, The Netherlands, 1993.

[196] R. Kosloff, Ann. Rev. Phys. Chem. **45**, 145 (1994).

[197] D. G. Truhlar, Comput. Phys. Commun. **84**, 78 (1994).

[198] R. Kosloff, "Quantum Molecular Dynamics on Grids" - (preprint)

[199] B. M. Garraway and K-A. Suominen, Rep. Prog. Phys. **58**, 365-419 (1995).

[200] D. Neuhauser and M. Baer, J. Chem. Phys. **90**, 4351 (1989).

[201] D. Neuhauser, M. Baer, R. S. Judson and D. J. Kouri, J. Chem. Phys. **90**, 5882 (1989); D. Neuhauser, M. Baer, and D. J. Kouri, J. Chem. Phys.

[202] R. Kosloff, in: Ref. [195], pp. 175-193.

[203] D. Gottlieb and S. A. Orszag, Numerical Analysis of Spectral Methods: Theory and Applications, SIAM, Philadelphia, 1977.

[204] R. Kosloff, in: Ref. [194], pp. 97-116.

[205] J. W. Cooley and J. W. Tuckey, Math. Comput. **19**, 297 (1965).

[206] H. J. Nussbaumer, Fast Fourier Transform and Convolution Algorithms, Springer Verlag, Berlin, 2nd Ed., 1982.

[207] C. Temperton, J. Comp. Phys. **52**, 1 (1983).

[208] À. Vibok and G. G. Balint-Kurti, J. Chem. Phys. **96**, 7615 (1992).

[209] A. E. Siegman, Opt. Lett. **1**, 13 (1977).

[210] J. D. Talman, J. Comp. Phys. **29**, 35 (1978).

[211] W. H. Press, B. P. Flannery, S. A. Teukolsky and W. T. Vetterling, Numerical Recipes: the art of Scientific Computing, Cambridge University Press, Cambridge, 1989.

[212] D. O. Harris, G. G. Engerholm and W. D. Guinn, J. Chem. Phys. **43**, 151 (1965).

[213] A. S. Dickinson and P. R. Certain, J. Chem. Phys. **49**, 4209 (1968).

[214] B. Shizgal and R. Blackmore, J. Comp. Phys. **55**, 313 (1984); R. Blackmore and B. Shizgal, Phys. Rev. **A31**, 1855 (1985).

[215] G. C. Corey, J. W. Tromp and D. Lemoine, in: Ref. [195], pp. 1-23.

[216] R. M. Whitnell and J. C. Light, J. Chem. Phys. **90**, 1774 (1989).

[217] J. C. Light, R. M. Whitnell, T. J. Park and S. E. Choi, in: Supercomputer Algorithms for Reactivity, Dynamics and Kinetics of Small Molecules, A. Lagana (Ed.), NATO ASI Ser. C **277**, Kluwer Academic Publishers, Dortdrecht, 1989, pp. 187-214.

[218] Z. Bačić and J. C. Light, Ann. Rev. Phys. Chem. **40**, 469 (1989).

[219] D. T. Colbert and W. H. Miller, J. Chem. Phys. **96**, 1982 (1992).

[220] M. J. Bramley, W. H. Green. Jr. and N. C. Handy, Mol. Phys. **73**, 1183 (1991).

[221] J. T. Muckerman, Chem. Phys. Lett. **173**, 200 (1990); F. J. Lin and J. T. Muckerman, Comput. Phys. Commun. **63**, 538 (1991).

[222] D. E. Manolopoulos and R. E. Wyatt, Chem. Phys. Lett. bf 152, 23 (1988); D. E. Manolopoulos, in: Ref. [195], pp. 57-68.

[223] S. Kanfer and M. Shapiro, J. Phys. Chem. **88**, 3964 (1980).

[224] J. Echave and D. C. Clary, Chem. Phys. Lett. **190**, 225 (1992).

[225] J. Tennyson and B. T. Sutcliffe, J. Chem. Phys. **77**, 4061 (1982).

[226] R. N. Dixon, Chem. Phys. Lett. **190**, 430 (1992); J. Chem. Soc. Farad. Trans. **88**, 2575 (1992).

[227] G. G. Balint-Kurti, R. N. Dixon and C. C. Marston, Int. Rev. Phys. Chem. **11**, 317 (1992).

[228] C. Leforestier, J. Chem. Phys. **94**, 6388 (1991).

[229] G. C. Corey and D. Lemoine, J. Chem. Phys. **97**, 4115 (1992).

[230] A. R. Offer and G. G. Balint-Kurti, J. Chem. Phys. **101**, 10416 (1994).

[231] F. Göğtas, G. G. Balint-Kurti and A. R. Offer, - (Preprint).

[232] E. Merzbacher, Quantum Mechanics, John Wiley and Sons, 2nd Ed., 1970.

[233] G. Arfken, Mathematical Methods for Physicists, Academic Press Inc., Prism Books Pvt. Ltd., Bangalore, 1994.

[234] R. C. Mowrey, J. Chem. Phys. **99**, 7049 (1993).

[235] Y. Huang, D. J. Kouri and D. K. Hofmann, Chem. Phys. Lett. **225**, 37 (1994); J. Chem. Phys. **101**, 10493 (1994).

[236] V. A. Mandelshtam and H. S. Taylor, J. Chem. Phys. **103**, 2903 (1995).

[237] D. Neuhauser, J. Chem. Phys. **103**, 8513 (1995).

[238] M. Berman, R. Kosloff and H. Tal-Ezer, J. Phys. A**25**, 1283(1992).

[239] D. J. Tannor, A. Besprozvannaya and C. J. Williams, J. Chem. Phys. **96**, 2998 (1992).

[240] D. Kohen and D. J. Tannor, J. Chem. Phys. **98**, 3168 (1993).

[241] C. C. Marston and G. G. Balint-Kurti, J. Chem. Phys. **91**, 3571 (1989).

[242] M. D. Feit and J. A. Fleck, Jr., J. Chem. Phys. **78**, 301 (1983).

[243] M. D. Feit and J. A. Fleck, Jr. Appl. Opt. **19**, 1154 (1980).

[244] A. D. Bandrauk and H. Shen, Chem. Phys. Lett. **176**, 428 (1991); Can. J. Chem. **70**, 555 (1992); J. Chem. Phys. **99**, 1185 (1993).

[245] S. Mahapatra and N. Sathyamurthy, J. Phys. Chem. (in press).

[246] S. Mahapatra and N. Sathyamurthy, J. Chem. Phys. (submitted).

[247] G. G. Balint-Kurti, F. Göğtas, S. P. Mort, A. R. Offer, A. Lagana and O. Gervasi, J. Chem. Phys. **99**, 9567 (1992).

[248] M. Baer, Adv. Chem. Phys. **49**, 191 (1982).

[249] D. J. Kouri and M. Baer, Chem. Phys. Lett. **24**, 37 (1974).

[250] P. J. Kuntz, Chem. Phys. Lett. **16**, 581(1972).

[251] J. T. Adams, Chem. Phys. Lett. **33**, 275(1975).

[252] F. M. Chapman Jr., and E. F. Hayes, J. Chem. Phys. **62**, 4400(1975); **65**, 1032(1976).

[253] T. Joseph and N. Sathyamurthy, J. Indian Chem. Soc. **62**, 874(1985).

[254] D. R. McLaughlin and D. L. Thompson, J. Chem. Phys. **70**, 2748(1979)

[255] N. Sathyamurthy, M. Baer, and T. Joseph, Chem. Phys. **114**, 73(1987).

[256] J. D. Kress, R. B. Walker, and E. F. Hayes, J. Chem. Phys. **93**, 8085(1990).

[257] G. A. Parker, R. T. Pack, B. J. Archer, and R. B. Walker, Chem. Phys. Lett. **137**, 564(1987); R. T. Pack and G. A. Parker, J. Chem. Phys. **87**, 3888(1987).

[258] T. Joseph and N. Sathyamurthy, J. Chem. Phys. **86**, 704(1987).

[259] B. Lepetit, and J. M. Launay, J. Chem. Phys. **95**, 5159(1991).

[260] J. Z. H. Zhang, D. L. Yeager, and W. H. Miller, Chem. Phys. Lett. **173**, 489(1990).

[261] C. Stroud, N. Sathyamurthy, R. Rangarajan and L. M. Raff, Chem. Phys. Lett. **48**, 350(1977).

[262] N. Balakrishnan, and N. Sathyamurthy, Comp. Phys. Commun. **63**, 209(1991); Chem. Phys. Lett. **201**, 294(1993).

[263] V. Balasubramanian, B. K. Mishra, A. Bahel, S. Kumar and N. Sathyamurthy, J. Chem. Phys. **95**, 4160(1991).

[264] A. Rahaman and N. Sathyamurthy, J. Phys. Chem. **98**, 12481 (1994).

[265] N. Balakrishnan, and N. Sathyamurthy, Proc. Indian Acad. Sci.(Chem. Sci.), **106**, 531(1994).

[266] V. A. Mandelshtam, H. S. Taylor, C. Jung, H. F. Browen, and D. J. Kouri, J. Chem. Phys. **102**, 7988 (1995).

[267] C. C. Marston, J. Chem. Phys. **103**, 8456 (1995).

[268] S. Mahapatra, R. Ramaswamy and N. Sathyamurthy, J. Chem. Phys. (in press).

[269] K. Sakimoto, and K. Onda, Chem. Phys. Lett. **226**, 227 (1994).

[270] M. S. Child, Mol. Phys. **72**, 89(1991).

[271] À. Vibok, and G. G. Balint-Kurti, J. Phys. Chem. **96**, 8712(1992).

[272] T. Joseph, Ph. D. Thesis, Indian Institute of Technology Kanpur, 1983.

[273] I. Burghardt, and P. Gaspard, J. Chem. Phys. **100**, 6395 (1994).

[274] J. Manz, and H. H. R. Schor, Chem. Phys. Lett. **107**, 542 (1984); J. Manz, R. Meyer, E. Pollak, J. Römelt, and H. H. R. Schor, **83**, 333 (1984); J. Manz, Comments At. Mol. Phys., **17**, 91 (1985).

[275] E. Pollak, in: Theory of Chemical Reaction Dynamics, M. Baer (Ed.), CRC Press, Boca Raton, FL, 1985, Vol. III, p.123; J. Phys. Chem. **90**, 3619 (1986).

[276] M. D. Feit and J. A. Fleck, Jr. J. Chem. Phys. **80**, 2578 (1984).

[277] R. S. Friedman and D. G. Truhlar, Chem. Phys. Lett. **183**, 539 (1991).

[278] R. T. Skodje, Ann. Rev. Phys. Chem. **44**, 145 (1993).

[279] D. C. Chatfield, R. S. Friedman, D. G. Truhlar and D. W. Schwenke, Farad. Discuss. Chem. Soc. **91**, 289 (1991).

[280] J. C. Tully and R. K. Preston, J. Chem. Phys. **55**, 562 (1971); M. Berblinger and C. Schlier, J. Chem. Phys. **101**, 4750 (1994) and references therein; L. Wolniewicz and J. Hinze, J. Chem. Phys. **101**, 9817 (1994).

[281] H. H. Michels and J. F. Paulson, in: Potential energy surfaces and dynamics calculations, D. G. Truhlar (Ed.), Plenum Press, New York, 1981, p.535.

[282] M. S. Haq, L. D. Doverspike and R. L. Champion, Phys. Rev. A **27**, 2831 (1983).

[283] M. Zimmer and F. Linder, Chem. Phys. Lett. **195**, 153 (1992); P. Reinig, M. Zimmer and F. Linder, Nucl. Fusion Suppl. **2**, 95 (1992).

[284] U. Hege and F. Linder, Z. Phys. A - Atoms and Nuclei **320** , 95 (1985).

[285] F. A. Gianturco and S. Kumar, J. Chem. Phys. **103**, 2940 (1995); F. A. Gianturco and S. Kumar, J. Phys. Chem. **99**, 15342 (1995).

[286] J. Stärck and W. Meyer, Chem. Phys. **176**, 83 (1993).

[287] A. K. Belyaev, D. T. Colbert, G. C. Groenenboom and W. H. Miller, Chem. Phys. Lett. **209**, 309 (1993).

[288] D. C. Chatfield, R. S. Friedman, D. W. Schwenke and D. G. Truhlar, J. Phys. Chem. **96**, 2414 (1992).

[289] B. Liu, J. Chem. Phys. **58**, 1925 (1973); P. Siegbahn and B. Liu, J. Chem. Phys. **68**, 2457 (1978); D. G. Truhlar and C. J. Horowitz, J. Chem. Phys. **68**, 2466 (1978).

[290] A. Kuppermann, in: Potential Energy Surfaces and Dynamics Calculations, D. G. Truhlar (Ed.), Plenum Press, New York, 1981, p.375.

[291] T. C. Thompson and D. G. Truhlar, Chem. Phys. Lett. **101**, 235 (1983).

[292] R. B. Walker, E. B. Stechel and J. C. Light, J. Chem. Phys. **69**, 1922 (1978).

[293] A. Kuppermann, J. A. Kaye and J. P. Dwyer, Chem. Phys. Lett. **74**, 257 (1980).

[294] A. J. C. Varandas, F. B. Brown, C. A. Mead, D. G. Truhlar, and N. C. Blais, J. Chem. Phys. **86**, 6258 (1987).

[295] R. Ramaswamy, in: Reaction Dynamics: Recent Advances, N. Sathyamurthy (Ed.), Narosa, New Delhi and Springer, Heidelberg, 1991, p. 101.

[296] G. Casati and B. V. Chirikov (Ed.), Quantum Chaos, Cambridge Univ. Press, Cambridge, 1994.

[297] C. E. Porter, Statistical Theories of Spectra : Fluctuations, Academic, New York, 1965.

[298] M. L. Mehta, Random Matrices and Statistical Theory of Energy Levels, Academic, New York, 1965; Random Matrices, 2nd ed., Academic, New York, 1990.

[299] T. A. Brody, J. Flores, J. B. French, P. A. Mello, A. Pandey and S. S. M. Wong, Rev. Mod. Phys. **53**, 385 (1981).

[300] E. B. Stechel and E. J. Heller, Ann. Rev. Phys. Chem. **35**, 563 (1984).

[301] G. Casati (Ed.), Chaotic Behaviour in Quantum Systems: Theory and Applications, Plenum press, New York, 1985, Series B: Physics Vol. 120.

[302] M. C. Gutzwiller, Chaos in Classical and Quantum Mechanics, Springer-Verlag, New York, 1991.

[303] O. Bohigas and M.-J. Giannoni, in: Mathematical and Computational Methods in Nuclear Physics, J. S. Dehesa, J. M. G. Gomez, and A. Polls (Ed.), Lecture Notes in Physics, Vol. 209, Springer Verlag, NY, 1984, P.209.

[304] L. S. Cederbaum, H. Köppel and W. Domcke, Intern. J. Quantum Chem. **15**, 251 (1981); W. Domcke, H. Köppel and L. S. Cederbaum, Mol. Phys. **43**, 851 (1981).

[305] E. Haller, H. Köppel and L. S. Cederbaum, Chem. Phys. Lett. **101**, 215 (1983).

[306] D. M. Leitner, R. S. Berry and R. M. Whitnell, J. Chem. Phys. **91**, 3470 (1989).

[307] B. Eckhardt, Physica D **33**, 89(1988); Phys. Rep. **163**, 205 (1988); B. Eckhardt and P. Cvitanovic, Phys. Rev. Lett. **63**, 823(1989); R. Blümel and U. Smilansky, Phys. Rev. Lett. **60**, 477(1988); **64**, 241(1990); R. Ramaswamy, in: Atomic and Molecular Physics, A. P. Pathak (Ed.), Narosa, New Delhi, 1992, p. 112; K. Someda, R. Ramaswamy and H. Nakamura, J. Chem. Phys. **98**, 1156 (1993).

[308] M. V. Berry and M. Robnik, J. Phys. A **17**, 2413 (1984).

[309] P. Pechukas, Chem. Phys. Lett. **86**, 553 (1982).

[310] J. Wilkie and P. Brumer, Phys. Rev. Lett. **67**, 1185 (1991).

[311] Y. Alhassid and N. Whelan, Phys. Rev. Lett. **70**, 572 (1993).

[312] A. Kudrolli, S. Sridhar, A. Pandey and R. Ramaswamy, Phys. Rev. E **49**, R11 (1994).

[313] J. S. Hutchinson and R. E. Wyatt, Phys. Rev. A **23**, 1567 (1981).

[314] S. S. M. Wong and J. B. French, Nucl. Phys. A **198**, 188 (1972); R. Venkatraman, J. Phys. B **15**, 4293 (1982).

[315] S. Sinha and R. Ramaswamy, Mol. Phys. **67**, 335(1989).

[316] E. P. Wigner, Phys. Rev. **40**, 749 (1932); SIAM Rev. **9**, 1 (1932).

[317] M. V. Berry and M. Tabor, Proc. R. Soc. London Ser. A **356**, 375 (1977).

[318] F. J. Dyson and M. L. Mehta, J. Math. Phys. **4**, 701(1963).

[319] O. Bohigas and M. -J. Gianonni, Ann. Phys. **89**, 393 (1975).

[320] O. Bohigas, M. -J. Giannoni and C. Schmidt, Phys. Rev. Lett. **52**, 1 (1984).

[321] S. Sinha and R. Ramaswamy, J. Phys. B: At. Mol. Opt. Phys. **22**, 2985 (1989).

[322] Y. Alhassid and R. D. Levine, Phys. Rev. A **46**, 4650 (1992).

[323] M. Bixon and J. Jortner, J. Chem. Phys. **77**, 4175(1982).

[324] R. C. Tolman, The Principles of Statistical Mechanics, Dover publications, New York, 1983, p.567.

[325] E. J. Heller, Phys. Rev. Lett. **53**, 1515 (1984).

[326] G. C. Schatz and A. Kuppermann, Phys. Rev. Lett. **35**, 1266 (1975); E. Pollak and M. S. Child, Chem. Phys. **63**, 23 (1981); B. C. Garrett, D. W. Schwenke, R. T. Skodje, D. Thirumalai, T. C. Thompson, and D. G. Truhlar, ACS Symposium Ser. **263**, 375 (1984); M. Zhao, M. Mladenovic, D. G. Truhlar, D. W. Schwenke, O. Sharafeddin, Y. Sun and D. J. Kouri, J. Chem. Phys. **91**, 5302 (1989); W. H. Miller and J. Z. H. Zhang, J. Phys. Chem. **95**, 12 (1991); D. A. Kliner, D. E. Adelman and R. N. Zare, J. Chem. Phys. **94**, 1069 (1991); J. Chang, N. J. Brown, M. D'Mello, R. E. Wyatt and H. Rabitz, J. Chem. Phys. **97**, 6226 (1992).

[327] S. A. Cuccaro, P. G. Hipes and A. Kuppermann, Chem. Phys. Lett. **157**, 440 (1989).

[328] M. R. Hermann and J. A. Fleck, Jr., Phys. Rev. A **38**, 6000 (1988).

Appendix 1

I. Function of an Operator

The eigenvalue equation of $\hat{H}$ is given by:

$$\hat{H}\phi_k = E_k\phi_k \tag{1}$$

If the basis functions (ϕ_k) form a complete orthonormal set then one can write resolution of the identity as

$$1 = \sum_k |\phi_k><\phi_k| \tag{2}$$

and then the spectral resolution will be given by

$$\hat{H} = \sum_k E_k|\phi_k><\phi_k| \tag{3}$$

Therefore any function $f(\hat{H})$ can be expressed as

$$f(\hat{H}) = \sum_k f(E_k)|\phi_k><\phi_k| \tag{4}$$

Hence the evolution operator will be given by

$$\hat{U} = \sum_k e^{-iE_kt/\hbar}|\phi_k><\phi_k| \tag{5}$$

II. The Conservation Laws

II.1. Norm Conservation

The conservation of the norm of the wave packet during time evolution is a direct consequence of the unitarity of the time evolution operator, $\hat{U}\hat{U}^\dagger = \hat{U}^\dagger\hat{U} = 1$, which has the additional requirements that $\hat{H}$ to be Hermitian. This can be illustrated as follows:

$$
\begin{aligned}
\langle\Psi(t)|\Psi(t)\rangle &= \langle\hat{U}\Psi(0)|\hat{U}\Psi(0)\rangle \\
&= \langle\Psi(0)|\hat{U}^\dagger\hat{U}|\Psi(0)\rangle \\
&= \langle\Psi(0)|\Psi(0)\rangle
\end{aligned} \tag{6}
$$

In presence of NIPs $\hat{H}$ becomes complex and loses its Hermitian property. The unitarity of the evolution operator no longer remains valid and hence there will be no norm conservation. What is more important in this situation is, the efficient damping of the WP which reaches the grid boundary:

The TDSE and its complex conjugate in presence of a NIP $[-iV_0]$ can be written as

$$i\hbar\frac{\partial\Psi}{\partial t} = \left[-\frac{\hbar^2}{2m}\nabla^2 + V - iV_0\right]\Psi \tag{7}$$

and

$$-i\hbar\frac{\partial\Psi^*}{\partial t} = \left[-\frac{\hbar^2}{2m}\nabla^2 + V + iV_0\right]\Psi^* \tag{8}$$

Left multiplying Eq. (7) by Ψ^* and Eq. (8) by Ψ and then subtracting one arrives at

$$\frac{\partial < \Psi|\Psi >}{\partial t} = -\frac{2V_0}{\hbar} < \Psi|\Psi > \tag{9}$$

Solution of which results into

$$< \Psi|\Psi >_t = e^{-2V_0 t/\hbar} < \Psi|\Psi >_0 \tag{10}$$

an exponential damping of the norm of the WP.

II.2. Energy Conservation

For a normalised WP the average energy at time t is given by

$$\begin{aligned}\langle E\rangle_t &= \langle\Psi(t)|\hat{H}|\Psi(t)\rangle \\ &= \langle\hat{U}\Psi(0)|\hat{H}|\hat{U}\Psi(0)\rangle \\ &= \langle\Psi(0)|\hat{U}^\dagger\hat{H}\hat{U}|\Psi(0)\rangle\end{aligned} \tag{11}$$

If now Hamiltonian commutes with the evolution operator then $\hat{H}\hat{U} = \hat{U}\hat{H}$, introducing this and with the help of the unitary property of $\hat{U}$ one can finally arrive at

$$\begin{aligned}\langle E\rangle_t &= \langle\Psi(0)|\hat{H}|\Psi(0)\rangle \\ &= \langle E\rangle_0\end{aligned} \tag{12}$$

This remains valid for any form of the Hamiltonian as long as it is time- independent and commutes with the time evolution operator. For time dependent Hamiltonians the evolution operator assumes a complex form and the commutation criterion no longer holds.

II.3. Conservation of the Time Reversal Symmetry

Classical equation of motions are known to be invariant with respect to time reversal, which means *all physical processes goes backward on interchanging the initial and final states of a system and its energy remains conserved.* TDSE is a first order differential equation in time and is a primary physical law. As can be seen below TDSE is also symmetric with respect to time reversal.

The TDSE and its complex conjugate in its differential form can be written as

$$i\hbar \frac{\partial \Psi}{\partial t} = \hat{H}\Psi \tag{13}$$

$$-i\hbar \frac{\partial \Psi^*}{\partial t} = \hat{H}\Psi^* \tag{14}$$

Now, let $\Psi = \Psi(R, t)$ is a solution of the first corresponding to the initial condition $\Psi = \psi_0$ for $t = 0$, then by substituting $t = -t$ in the second one can also have $\Psi'(R, t') = \Psi^*(R, -t)$ corresponding to initial condition $\Psi' = \Psi_0^*$. This symmetry is often called as the principle of microscopic reversibility or detailed balance. The time reversal operator $\hat{t}$ acting on the state function of a system results into its complex conjugate

$$\hat{t}\phi_k = \phi_k^* \tag{15}$$

$\hat{t}$ is antilinear and antiunitary satisfies the equations

$$\hat{t}c\phi_k = c^*\hat{t}\phi_k \tag{16}$$

$$\hat{t}^\dagger t = tt^\dagger = 1 \tag{17}$$

This symmetry operation leaves Hamiltonian unchanged and this symmetry exists as long as the Hamiltonian is real and Hermitian.

Appendix 2

Rotational and Vibrational Excitation of HCl in Small Angle Scattering With He$^+$ at $E_{lab} = 20$-60 eV

I. Introduction

It has been demonstrated in the last several years that proton energy loss spectroscopy could be used to probe the vib-rotational inelasticity of target molecules (see for example, ref.1,2). Recently it has been shown that highly energy resolved He$^+$ could be used as a projectile in place of H$^+$ in such studies[3]. In particular, our recent paper[4] illustrated the nicely resolved structures in the energy loss spectra of He$^+$ scattered in the forward direction due to collisions with HF and also how those structures could be explained in terms of rotational excitation in HF involving a change in rotational quantum number up to $\triangle J = 35$ with no indication of vibrational excitation. The observed propensity for large $\triangle J$ transitions decreased with increasing collision energy, but increased with increase in scattering angle. It was also shown that three dimensional(3D) quasiclassical trajectory (QCT) calculations[5], treating HF as a rigid rotor and using a potential-energy surface (PES) based on the isotropic He$^+$-Ne interaction at short range and ion-dipole (quadrupole) interaction in the long range reproduced all the essential features of the experimental results. In contrast the energy loss spectra of forward scattered He$^+$ in collision with HCl reported in the present paper for E_{lab} in the range 20-60 eV reveal less structures, presumably due to the closer spaced rotational and vibrational levels for HCl (than for HF). While there are considerable large $\triangle J$ transitions, there seem to be accompanying vibrational excitations as well, as was observed by Udseth et al[1] for H$^+$-HCl. In the spirit of our earlier paper[4], we have modelled the He$^+$-HCl interaction at short range based on the isoelectronic He$^+$-Ar[6] and in the long range using ion-dipole (quadrupole) interaction, with the damping functions introduced by Tang and Toennies[7] to

connect the two. We find that treating HCl as a rigid rotor is clearly inadequate to explain the observed experimental results and it becomes necessary to include the vibrational coordinate of HCl in the model.

The experimental details and results are presented in section II and the 3D QCT methodology and results in section III. Summary and conclusion are given in section IV.

II. Experiment

The experimental results were obtained using a crossed beam ion–molecule scattering apparatus described in detail elsewhere[3,8]. Usage of both electrostatic energy selection and analysis of the ions made it possible to achieve an energy resolution of ΔE (FWHM) = 30 meV for a He^+ beam of E_{lab} = 20 eV, for example. To reduce kinematic broadening of the observed spectra the molecular beam was produced by expanding pure HCl gas at room temperature through a nozzle of diameter d = 70 μm with a stagnation pressure of p_0 = 190 mbar. The latter was adjusted to an attenuation of the ion beam of about 30% to avoid multiple collisions. Passing the beam through a skimmer located at 10 mm from the nozzle reduced the angular divergence to less than $\pm 2°$. Thus the overall spread in energy was kept at ΔE = 35 meV. This made it possible to resolve the final rotational states ($J_f > 13$) of HCl in its ground vibrational state (v = 0). The analyser-detector arrangement could be rotated around the axis of the secondary beam for measuring the differential cross section. The angular resolution in the laboratory frame was estimated at $\pm 1°$.

Assuming thermal equilibrium, rotational relaxation during the expansion would result in a rotational temperature $T_{rot} \approx 90$ K for the HCl molecules in the beam. The Boltzmann distribution at that temperature suggests that about 80% of the molecules would be in rotational states $J_i \leq 2$, corresponding to a mean initial rotational energy of about $\bar{E}(J_i) \approx 7.3$ meV. Due to the substantially large rotational constant of HCl ($B_e = 1.31$ meV), however, the higher rotational levels may not relax fast enough to reach thermal equilibrium. This would result in an overpopulation of higher J_i states and thus a broadening of the structures

observed in the experimental spectra.

Energy loss measurements were carried out at $\Theta_{lab} = 0°$ for five different He$^+$ beam energies: $E_{lab} = 20, 25, 30, 40$ and 60 eV. These energies correspond to $E_{c.m.} = 18, -, 27, -,$ and 54 eV respectively. Additional measurements were made at $\Theta_{lab} = 2°$ and 3° at $E_{lab} = 20$ and 30 eV respectively.

It is clear from the energy loss spectrum obtained at different E_{lab} for $\Theta_{lab} = 0°$, shown in Fig.1, that there is substantial vib-rotational energy transfer resulting in $\triangle E$ of as much as 2.4 eV. For v=0, rotational excitation up to J=27 could be identified. It can be seen from the figure that there is a dramatic decrease (by six orders of magnitude) in intensity of the energy loss spectrum, with increase in $\triangle E$. In addition, there seem to be distinct features for large $\triangle E$ for the different E_{lab}.

Results of the energy loss spectra obtained for $E_{lab} = 20$ and 30 eV for $\Theta_{lab} = 2°$ and 3° respectively are included in Fig.2a and 2b, in that order. Perhaps the most important result obtained therein is that the intensity of the energy loss spectrum decreases with increase in Θ_{lab}, over the entire $\triangle E$ range investigated.

III. Theory

III.1. Potential-Energy Surface

The long-range interaction of He$^+$ with HCl was obtained by the well known multipole moment expansion upto fourth order[9]:

$$V(R, r, \gamma) = \frac{\mu(r)P_1(cos\gamma)}{R^2} + \frac{Q(r)P_2(cos\gamma)}{R^3} + [-\frac{\alpha_0(r)}{2R^4} - \frac{\alpha_2(r)P_2(cos\gamma)}{2R^4}] \tag{1}$$

where R is the center-of-mass separation between He$^+$ and HCl, r the internuclear distance of HCl and γ the angle between the HCl bond axis and R with $\gamma = 0°$ representing the approach of He$^+$ at the Cl-end of HCl. P_0 and P_2 are the Legendre polynomials. μ and Q are the dipole and quadrupole moments of HCl while α_0 and α_2 are its isotropic and

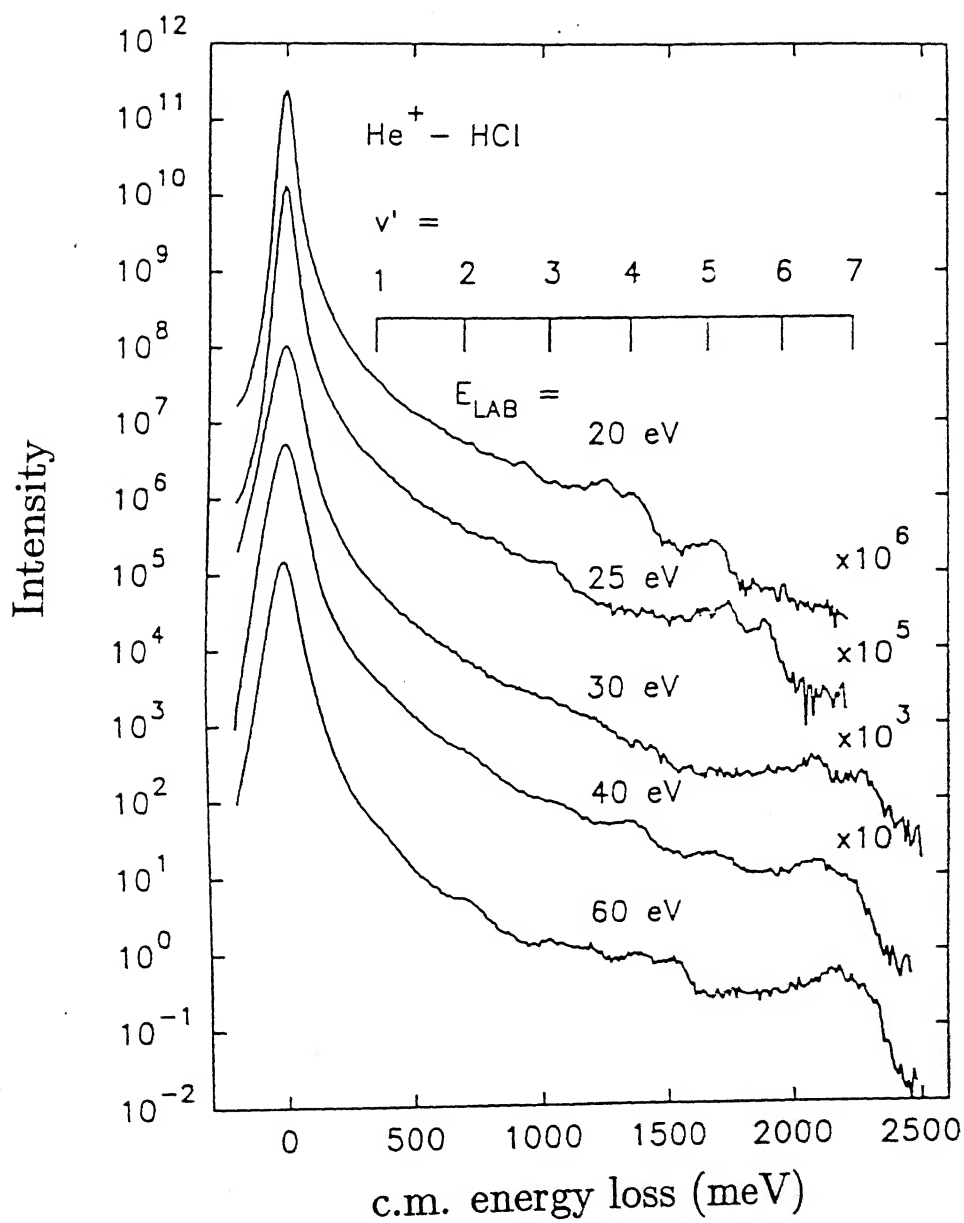Figure 1: Energy loss spectra for He$^+$-HCl(v=0) at E_{lab} =20, 25, 30, 40 and 60 eV and Θ_{lab} = 0°. The vertical lines in the inset indicate the energy loss for the transition to the vibrational state (v') of HCl target.

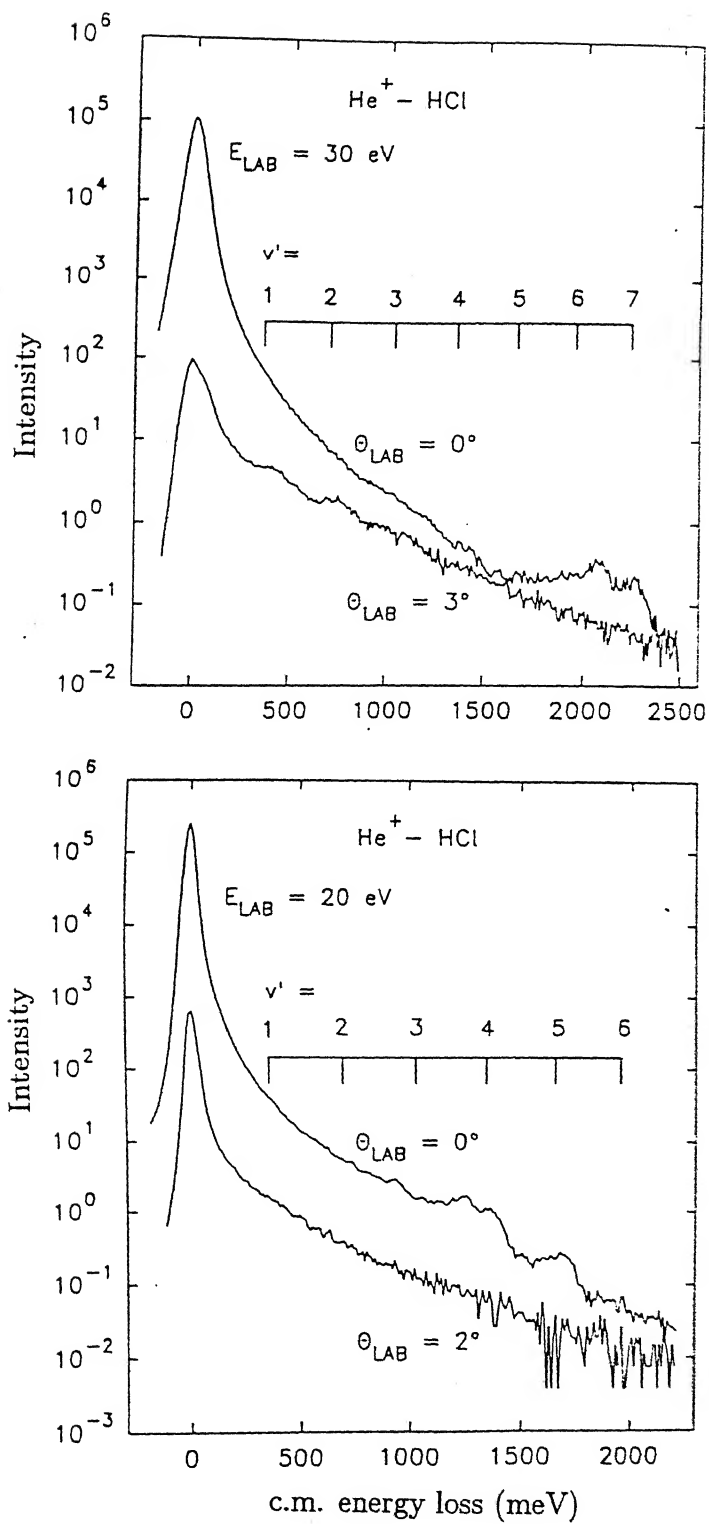Figure 2: Energy loss spectra for He$^+$-HCl(v=0) at (a) $E_{lab} = 20$ eV, $\Theta_{lab} = 0°$ and $2°$ (b) $E_{lab} = 30$ eV, $\Theta_{lab} = 0°$ and $3°$.

anisotropic polarizability values. Contributions due to the polarizability of He$^+$ are negligible in comparison and hence have not been included in the present study.

The *ab initio* calculated data for the variation of μ with r are available in the literature[10] and they can be approximated by a linear relation

$$\mu(r) = ar - b \tag{2}$$

for $1.8 \leq r \leq 3.4$ a.u. as illustrated in Fig.3a. Although the quadrupole moment of HCl is known[11] at r_e, its variation with r is not known. However, dependence of Q on r is known for HF[12] (see Fig.3b). Assuming that the variation of Q with r in the neighbourhood of r_e would be the same for HCl and HF, we write

$$Q(r) = Q(r_e) + c(r - r_e) + d(r - r_e)^2 \tag{3}$$

The *ab initio* values of both parallel $(\alpha_{\parallel})$ and perpendicular $(\alpha_{\perp})$ components of polarizability were reported by Gianturco and Guidotti[13] for HCl at different internuclear distances. The variation of $\alpha_{\parallel}$ and $\alpha_{\perp}$ with r is quadratic in nature. Since α_0 and α_2 are related to $\alpha_{\parallel}$ and $\alpha_{\perp}$ through relations

$$\begin{aligned}
\alpha_0 &= \frac{1}{3}\left[2\alpha_{\parallel} + \alpha_{\perp}\right] \\
\alpha_2 &= \frac{2}{3}\left[\alpha_{\parallel} - \alpha_{\perp}\right]
\end{aligned} \tag{4}$$

we have assumed a similar type of variation with r for α_0 and α_2 (see Fig.3c). Thus

$$\begin{aligned}
\alpha_0 &= a_0 r^2 - b_0 r + c_0 \\
\alpha_2 &= a_2 r^2 - b_2 r + c_2
\end{aligned} \tag{5}$$

All the parameters a, b, $Q(r_e)$, c, d, a_0, b_0, c_0, a_2, b_2, c_2 used in the study are listed in Table 1. The short-range He$^+$ - HCl interaction was taken to be the same as that of the isoelectronic
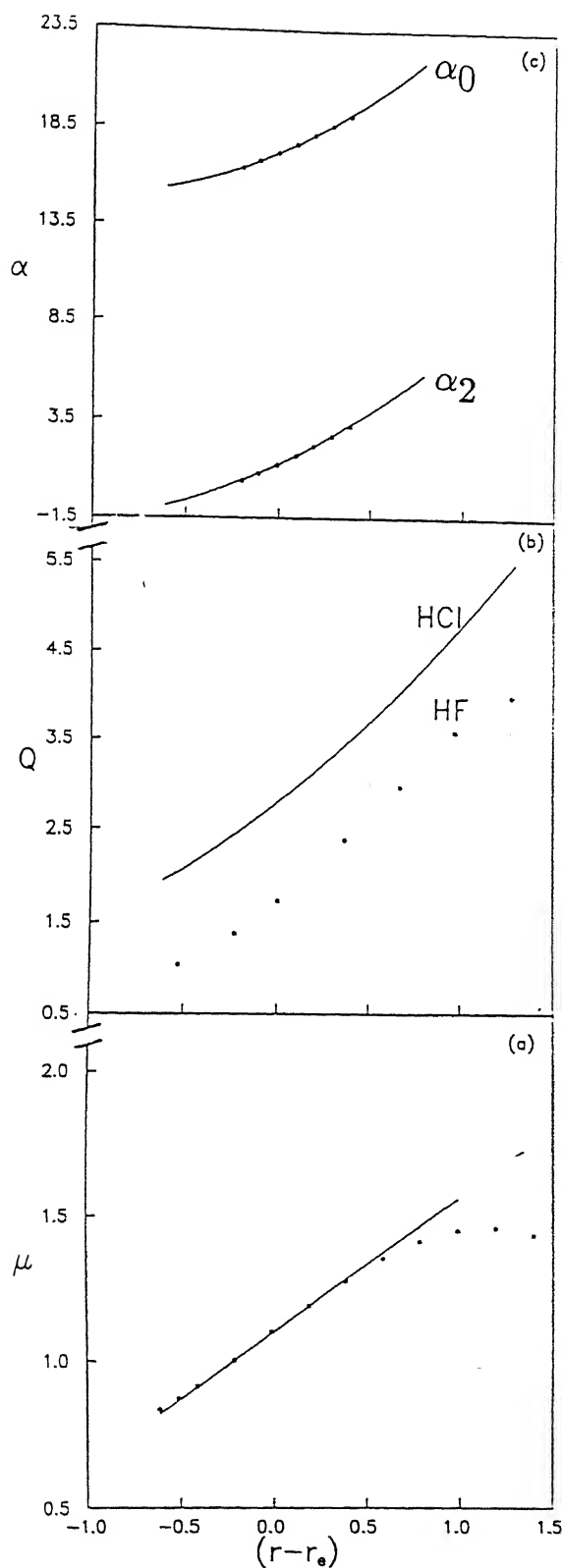
Figure 3: (a) Variation of the dipole moment, μ (in D) of HCl with r-r_e (in a.u.). The points (*) indicate the *ab initio* results of ref.10 and the solid line is the straight line (eq.2) fit to those points for $1.8 \leq r \leq 3.4$ a.u.. (b) Variation of quadrupole moment, Q (in a.u.) of HF with r-r_e(in a.u.) indicated by the points(*). A similar variation is assumed for HCl in the neighbourhood of its equilibrium bond distance and shown by the solid line (eq.3). (c) Variation of isotropic (α_0) and anisotropic (α_2) polarizability (in a.u.) of HCl with r-r_e (in a.u.). The points (*) are the values of the same calculated from the *ab initio* data (ref.13) for the parallel ($\alpha_\parallel$) and perpendicular ($\alpha_\perp$) components of polarizability using eq.4. The solid lines are the quadratic fit to those points (eq.5).

He$^+$ - Ar potential[6] because of the known nearly spherical nature of HCl. The short-range and the long-range potentials were connected smoothly using the damping functions of Tang and Toennies[7]. Representing the intramolecular potential of HCl by a Morse function, the total He$^+$ - HCl interaction is given as

$$V(R. r, \gamma) = Ae^{-\beta R} + D_e \left[1 - e^{-\beta_M (r-r_e)}\right]^2 + \frac{\mu(r)P_1(\cos\gamma)}{R^2}S_2 + \frac{Q(r)P_2(\cos\gamma)}{R^3}S_3$$
$$+ \left[-\frac{\alpha_0(r)}{2R^4} - \frac{\alpha_2(r)P_2(\cos\gamma)}{2R^4}\right]S_4 \tag{6}$$

with

$$S_N = 1 - e^{-\beta R}\sum_{k=0}^{N}\frac{(\beta R)^k}{k!} \tag{7}$$

The parameters A and β and the Morse parameters D$_e$, β_M and r$_e$ for HCl are included in Table 1.

Potential-energy contours for the He$^+$ - HCl interaction for r=r$_e$ of HCl are illustrated in Fig.4. There is a substantial well of depth 0.83 eV at R = 3.86 a.u. and $\gamma = 78°$. Although there are no *ab initio* data available for He$^+$ - HCl interaction we can compare the above with a value of 0.863 eV obtained for He$^+$ - HF at R = 3.72 a.u. and $\gamma = 54°$. These results are consistent with the known *ab initio* results[14] available for H$^+$ - HF which reveal the presence of a deeper well at a shorter R revealing the greater penetrating power of H$^+$ than that of He$^+$.

III.2. The Rigid Rotor Model

Since we could account for much of the energy transfer in He$^+$-HF collisions treating HF as a rigid rotor (RR), we examined first the adequacy of the RR model for HCl-He$^+$ collision also.

The trajectory code for the rigid rotor HCl - He$^+$ collision was based on the algorithm outlined by Pattengill[5]. Fourth order Runge-Kutta method with a stepsize of 0.5387 fs was

a	-4.9504 eV a.u.	-
b	-0.1279 eV a.u.^{2}	-
$Q(r_e)$	75.8 eV a.u.^{3}	[11]
c	45.5392 eV a.u.^{2}	-
d	10.6127 eV a.u.	-
a_0	54.424 eV a.u.^{2}	-
b_0	145.5842 eV a.u.^{3}	-
c_0	505.32684 eV a.u.^{4}	-
a_2	44.8998 eV a.u.^{2}	-
b_2	93.0650 eV a.u.^{3}	-
c_2	-2.6123 eV a.u.^{4}	-
A	462.121 eV	[6]
β	1.7025 a.u.$^{-1}$	[6]
D_e	4.6188 eV	[17]
β_M	0.9886 a.u.$^{-1}$	[17]
r_e	2.4094 a.u.	[17]

Table 1. Potential parameters for He$^+$ - HCl. Units were adjusted to yield energy in eV.
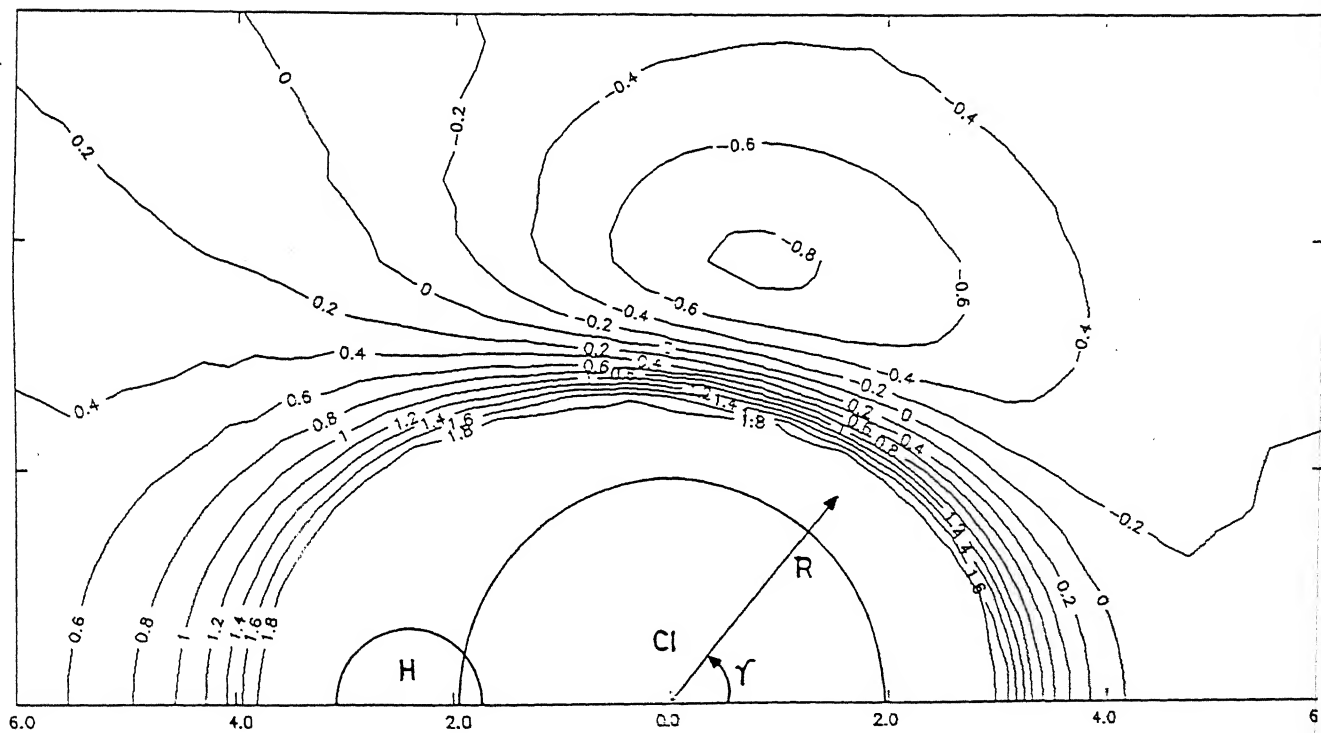
Figure 4: Potential - energy contours (in eV) for He$^+$ interaction with rigid HCl in its equilibrium bond distance. For reference the size of H and Cl are indicated, based on their covalent radii. Distances are in a.u..

used to solve the Hamilton's equations. The HCl molecule was taken to be initially in its ground rotational state ($J_i = 0$). Trajectories were started at R = 35 a.u. where the He^+ - HCl interaction was negligible. The initial value of the center-of-mass relative translational energy (E_{trans}) was fixed at 18, 27, or 54 eV corresponding to E_{lab}= 20, 30 and 60 eV respectively. The initial impact parameter (b) was sampled uniformly as follows:

3.5 (0.1) 9.0 (0.5) 29.0 a.u. at E_{trans}= 18 eV;

3.5 (0.1) 10.0 (0.5) 26.5 a.u. at E_{trans}= 27 eV;

3.4 (0.2) 10.0 (1.0) 23.0 a.u. at E_{trans}= 54 eV.

All other variables were sampled randomly. Typically, 2000 trajectories were run at each value of b. The minimum and the maximum values of b were chosen by examining the final rotational state (J_f) of HCl and the scattering angle $\Theta_{c.m.}$.

In view of the experiments having been carried out for Θ_{lab}= 0° with a resolution of ~ 1°, which corresponds approximately to $\Theta_{c.m.}$= 0°-1°, we were interested mainly in the trajectories leading to $\Theta_{c.m.}$= 0° - 1°. The final rotational state distributions were arrived at by using the standard histogram procedure[5]. However, it must be added that for b $\geq$ 26.5 a.u. at E_{trans}= 27 eV, for example, some of the trajectories led to $0.5 < J_f < 1.0$ indicating that the $0 \rightarrow 1$ rotational transition was classically forbidden[15]. Therefore the collisions were assumed to be elastic at b $\geq$ 26.5 a.u. Similarly the $J_i = 0 \rightarrow J_f = 2$ transition was found to be classically forbidden at b $\geq$ 20.5 a.u. and trajectories with $1.5 \leq J_f < 2.0$ were included under $J_f = 1.0$. A similar procedure was adopted for other J_f values also.

The state-to-state inelastic transition probabilities $P_{J_i \rightarrow J_f}$ were computed as follows:

$$P_{J_i \rightarrow J_f} = \frac{N_{J_i \rightarrow J_f}}{N_{tot}} \tag{8}$$

where $N_{J_i \rightarrow J_f}$ is the number of trajectories resulting in $J_f \pm 0.5$ (vide supra) and N_{tot} the total number of trajectories computed at a particular b. The dependence of $P_{J_i \rightarrow J_f}$ on b for different J_f values is shown in Fig.5, for E_{trans}= 27 eV. As has been observed for other systems
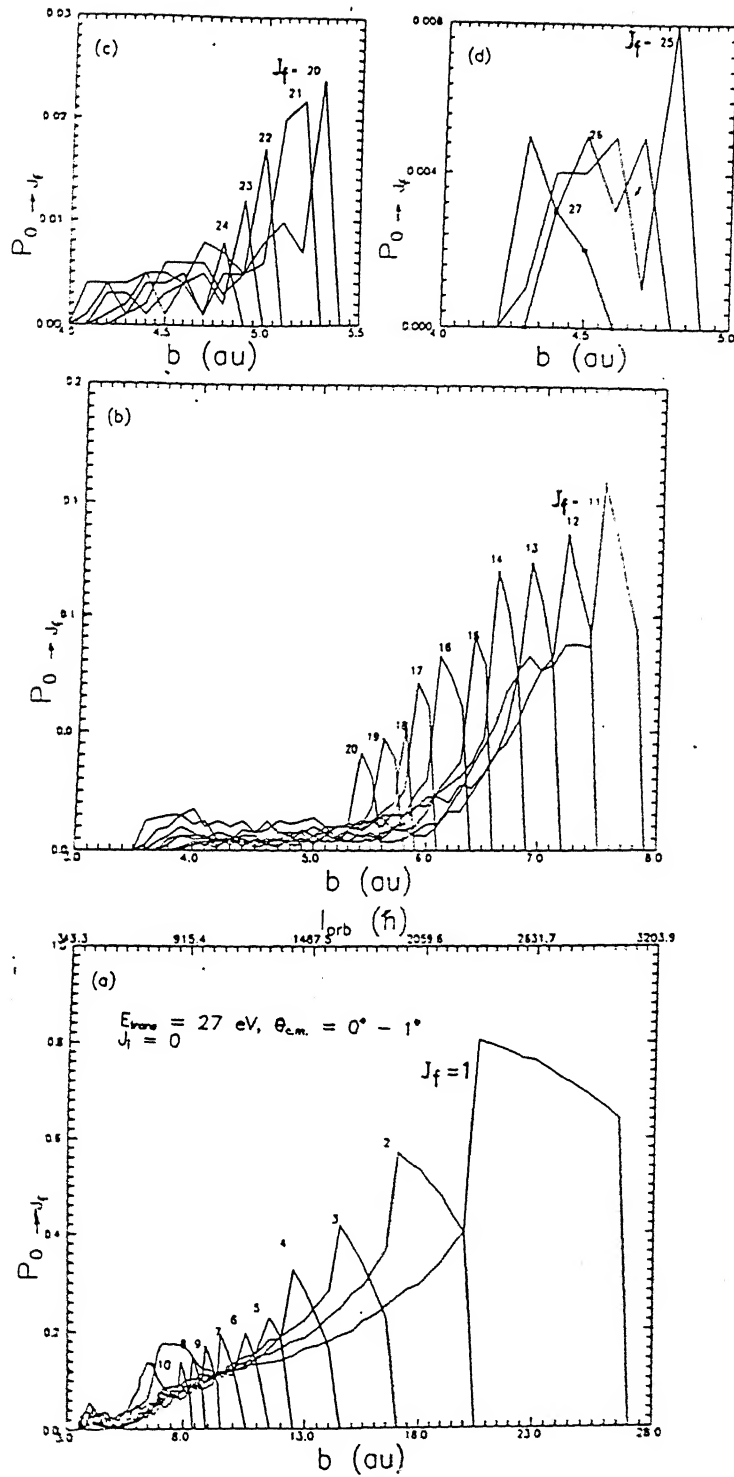
Figure 5: Opacity functions for different J_f, for rigid rotor HCl($J_i=0$)-He$^+$ collisions at E_{trans} = 27 eV for scattering angle $(\Theta_{c.m.})$ in the range 0° - 1°. The orbital angular momentum (l) in units of $\hbar$ are shown in the upper abscissa of Fig.(a) corresponding to the b values in the lower abscissa.

(for example, see ref.4), small $\triangle J$ transitions occur at large b while large $\triangle J$ transitions occur at small b. It is worth emphasizing that the amount of orbital angular momentum (l_{orb} = μ v_{rel} b, where μ is the reduced mass of He$^+$ - HCl and v_{rel} the relative velocity of the collision partners) is two orders of magnitude larger (see Fig.5) than the amount of rotational angular momentum transferred.

The state-to-state differential cross sections for $\Theta_{c.m.}$= 0° - 1° were computed using the relation:

$$\frac{d^2\,\sigma_{J_i \to J_f}\,(\Theta_{c.m.})}{d\,\omega^2} = \frac{1}{sin\Theta_{c.m.}} \sum P_{J_i \to J_f}\,(b, \Theta_{c.m.}) \left| \frac{b\,\triangle b}{\triangle\Theta_{c.m.}} \right| \qquad (9)$$

and the results are plotted as a function of the amount of energy transferred ($\triangle E$) for J_i = 0 at different E_{trans} in Fig.6. The largest energy transferred is about 1500 meV, for E_{trans}= 18 eV, for which the experimental results indicate an energy loss upto 2500 meV. In principle, there could be trajectories resulting in energy loss greater than 1500 meV but they would originate at small b and sample regions in (R,γ) space for which the interaction potential used is of questionable validity. Hence we have not computed such trajectories. Also, our 3D QCT results have already given an intensity variation of five orders of magnitude. Reproduction of larger $\triangle E$ results would require an additional order of magnitude increase in the number of trajectories computed.

A comparison of the simulated energy loss spectra for E_{trans}= 18, 27 and 54 eV with the corresponding experimental results shown in Fig.7 reveals that the agreement between theory and experiment is excellent for $\triangle E$ up to 1500 meV at the lowest E_{trans} used. The range of energy loss for which the agreement between the predicted and the observed spectra is satisfactory, decreases dramatically with increase in E_{trans}.

The maximum value of J_f observed in our trajectory studies also decreases with increasing E_{trans} as can be seen from Fig.6 : 34, 27 and 18 at 18, 27, and 54 eV respectively. This is definitely due to a decrease in the interaction time with increase in E_{trans} and not to the
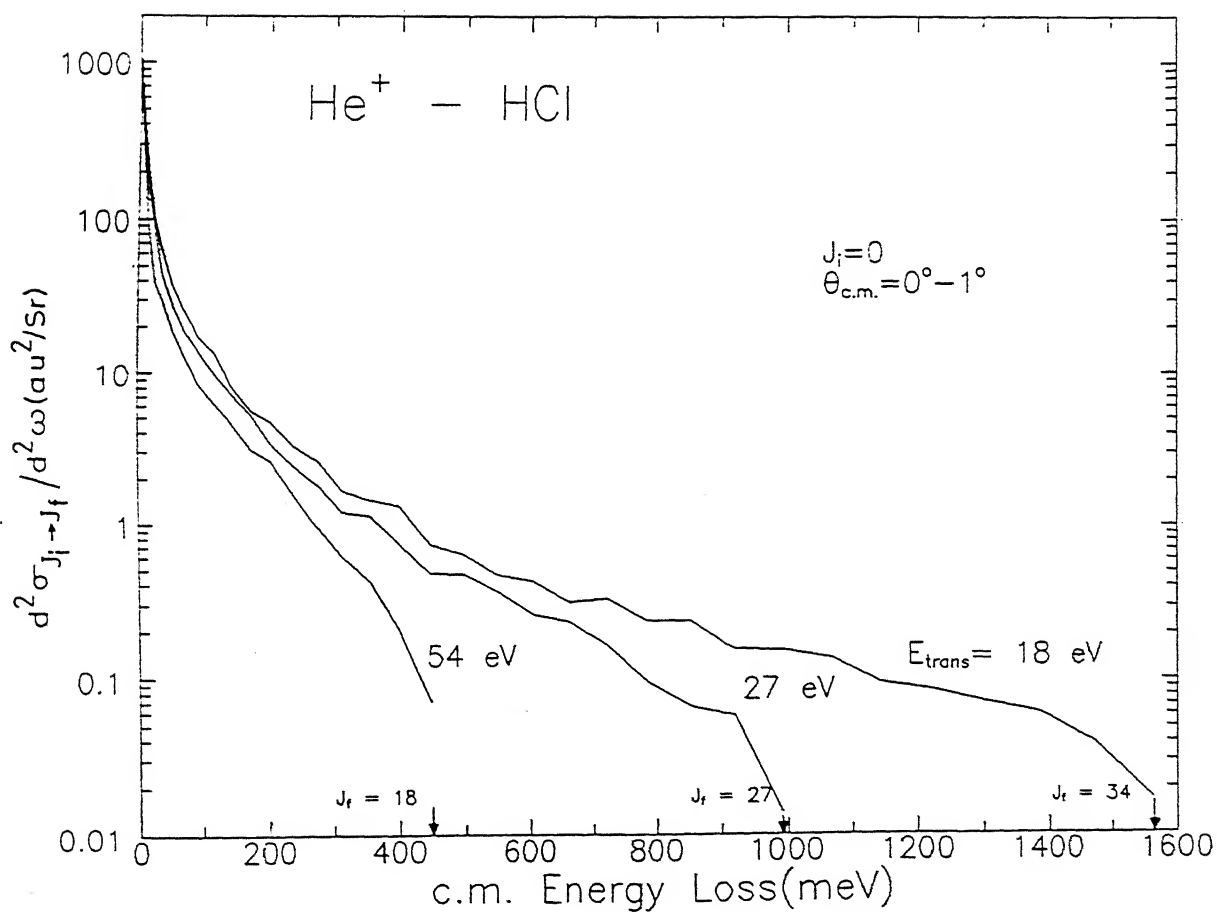
Figure 6: Differential cross sections for scattering in the range $\Theta_{c.m.} = 0° - 1°$, for rigid rotor HCl(J_i=0)-He$^+$ collisions at E_{trans} = 18, 27 and 54 eV.
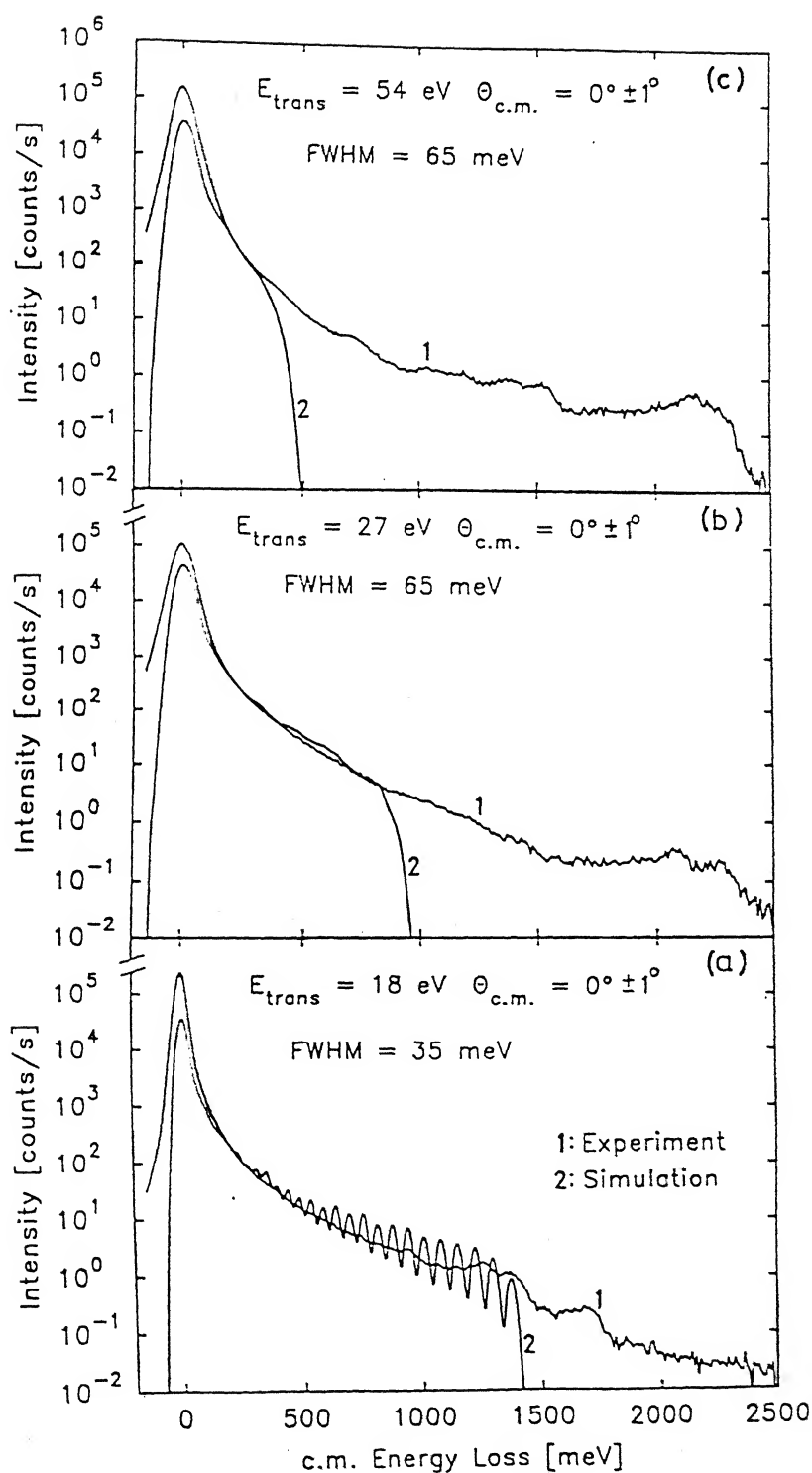
Figure 7: Simulated energy loss spectra compared with the experimental results for rigid rotor HCl(J_i=0)-He$^+$ collision for $\Theta_{c.m.}$ = 0° - 1° at E_{trans} = 18, 27 and 54 eV.

lack of availability of angular momentum in the collisions. Similar results were obtained for He^+ - HF collisions and they were in agreement with experiment.

The dramatically large discrepancy between theory and experiment for HCl-He^+ at large E_{trans} could be due to several factors:

(i) inadequate representation of He^+ - HCl interaction

(ii) use of classical trajectory approach for investigating the dynamics

(iii) neglection of contributions from nonzero J_i states of HCl

(iv) poor energy resolution in He^+ beam and

(v) inadequacy of the rigid rotor model for HCl.

The fact that a classical mechanical treatment using a similar potential (short range mimicking He^+ - Ne and asymptotically accurate long range) led to reasonable agreement between theory and experiment for He^+ - HF suggests that the first two factors are unlikely reasons for the discrepancy. Classical trajectory calculations for $J_i = 1$ and 2 of HCl led to very similar inelastic cross sections as for $J_i = 0$ at $E_{trans}= 18$ eV as illustrated in Fig.8 and this was the case for He^+ - HF as well. The known energy spread (35 - 65 meV) in the He^+ beam is too little to account for a discrepancy in ΔE of the order of 1000 meV. Therefore, it is reasonable to conclude that the rigid rotor model for HCl is not adequate for explaining the large energy transfers at high E_{trans}.

Also it may be pointed out that both the rotational and vibrational constants are smaller for HCl than for HF. This would suggest a larger vibrational excitation cross section in the case of HCl as a target as was found by Udseth et al[1] at lower resolution. This also means that with increasing E_{trans} the vibrational excitation cross section would become larger. This is indeed what is seen in our experiments, cf. the peak at v = 1. The observed peaks in the energy loss spectra coincide with the calculated positions for vibrational transitions of HCl accompanied by rotational energy transfer.

Still there remain some structures in the measured spectra, which cannot be explained
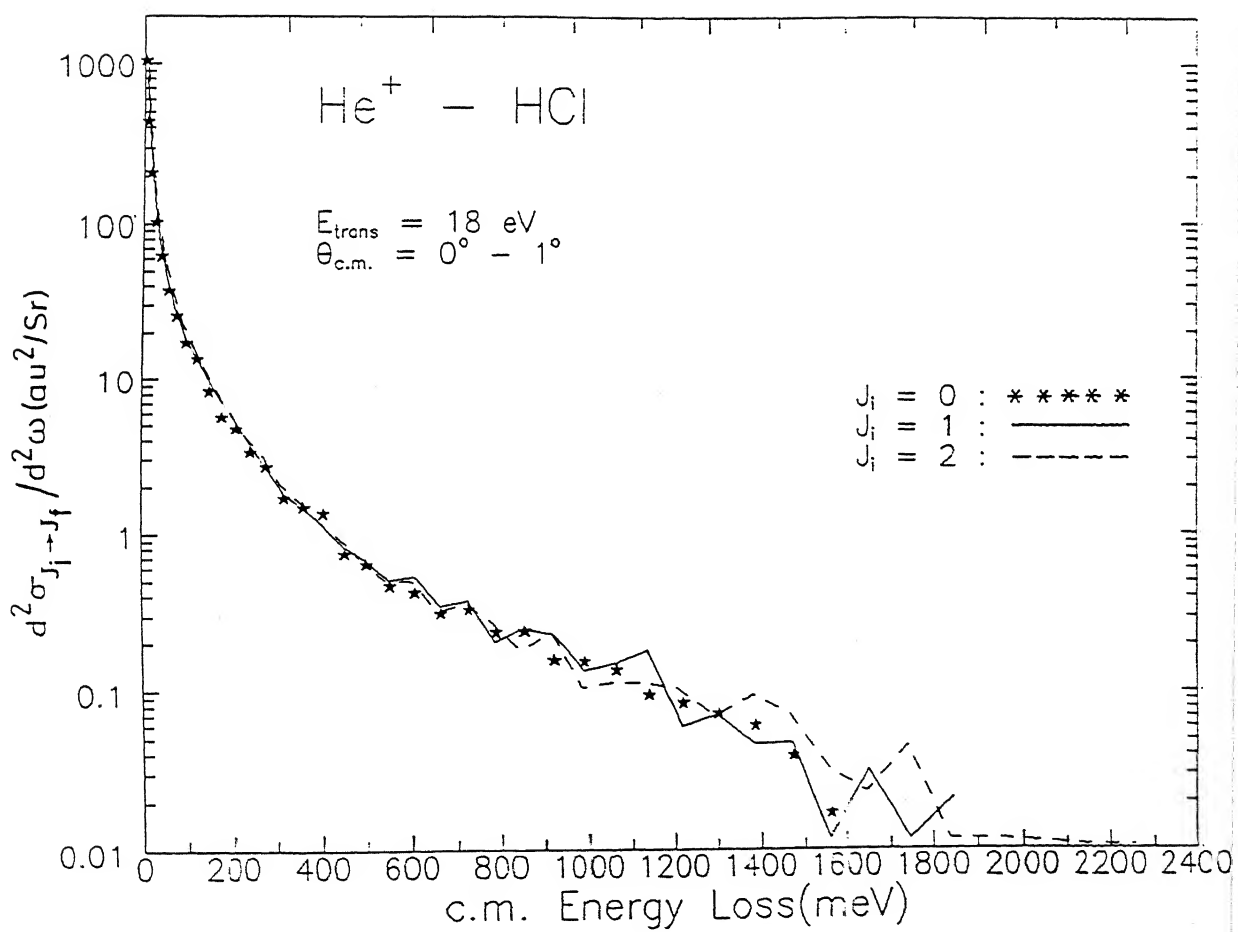
Figure 8: Differential cross sections for scattering in the range $\Theta_{c.m.} = 0° - 1°$, for rigid rotor HCl(J_i=0,1,2)-He$^+$ collisions at $E_{trans} = 18$ eV.

fully at the present level of investigation. These may be due to the excitation of rather high $(J_f > 15)$ rotational states in a given vibrational state v which involve the same amount of energy transfer as the next higher vibrational transition and cannot be resolved. There may also be some combination of v and J_f which are favourably excited in forward scattering. These structures do not appear in spectra recorded under larger $(> 1°)$ scattering angles. Electronic excitation and charge transfer cannot account for these features as they involve energy transfers, greater than 5 eV, not covered by our experiments. Also it may be added that the differences arising from the different rotational and vibrational transitions for the different isotopomers of HCl occuring in nature $(^{35}Cl : {}^{37}Cl = 3:1)$ would hardly account for differences of the order of a few meV, far below the resolution of the recorded spectra.

Therefore it becomes clear that the RR model is inadequate for HCl in explaining the experimental results and it becomes necessary to include the vibrational coordinate of HCl in the simulation.

III.3. The Vibrating Rotor Model

In the vibrating rotor model the initial internuclear distance of HCl was selected randomly using the relation[16]

$$r = r_e - \frac{1}{\beta_M} \ln \left[(-2A) \left[B + \sqrt{B^2 - 4AC} \sin(2\pi\xi) \right]^{-1} \right] \tag{10}$$

where r_e and β_M are the Morse parameters defined above, ξ is a random number varying between 0 and 1 and

The other variables were selected randomly using the standard procedure[5]. The fourth order Runge–Kutta method was used to solve the Hamilton's equations of motion with a step-size of 0.10775 fs. Since the long range part of the potential plays a dominant role in forward scattering we had to start our trajectory at a large R value of 50 a. u., where the interaction potential is practically negligible.

The HCl molecule was initially taken in the $v_i = 0$, $J_i = 0$ state. The initial relative

translational energy was taken to be the same as in the rigid rotor case. The impact parameter was sampled uniformly as follows:

3.4 (0.1) 4.0 (0.2) 29.0 a.u. at E_{trans} = 18 eV;

3.4 (0.1) 4.0 (0.2) 29.0 a.u. at E_{trans} = 27 eV;

3.4 (0.2) 4.0 (0.2) 23.0 a.u. at E_{trans} = 54 eV.

and all the other parameters were sampled randomly as before.

We have analysed the trajectories with the scattering angle $\Theta_{c.m.}$ = 0-1° corresponding to Θ_{lab} = 0° as well as $\Theta_{c.m.}$ = 2-4° corresponding to Θ_{lab} = 3°. The final rotational and vibrational quantum numbers were calculated following the standard histogram procedure[5].

The inelastic transition probabilities were calculated by:

$$P_{v_i,J_i \to v_f,J_f}(b) = \frac{N_{v_i,J_i \to v_f,J_f}}{N_{Tot}} \tag{11}$$

where $N_{v_i,J_i \to v_f,J_f}$ is the number of trajectories originating from an initial (v_i, J_i) state and leading to $(v_f \pm 0.5, J_f \pm 0.5)$. N_{Tot} is the total number of trajectories computed at that particular impact parameter b.

The state-to-state differential cross sections for $\Theta_{c.m.}$ = 0°-1° were computed using the relation:

$$\frac{d^2\, \sigma_{v_i,J_i \to v_f,J_f}\, (\Theta_{c.m.})}{d\, \omega^2} = \frac{1}{sin\Theta_{c.m.}} \sum P_{v_i,J_i \to v_f,J_f}\, (b,\Theta_{c.m.}) \left| \frac{b\, \Delta\, b}{\Delta\Theta_{c.m.}} \right| \tag{12}$$

The results plotted in Fig.9 show that with increase in E_{trans} the amount of energy transferred decreases. For v_f = 0, the extent of rotational energy transferred is approximately the same as obtained from the rigid rotor model. But there is significant energy transferred into v_f = 1 level. The overall energy transferred as obtained from QCT calculations is shown in the form of simulated spectra and compared with the experimental results in Fig.10. The agreement is very good for E_{trans}=18 eV, for $\Delta E \sim$ 1600 meV. The agreement between theory and experiment worsens with increase in E_{trans}. While it is tempting to suggest that the
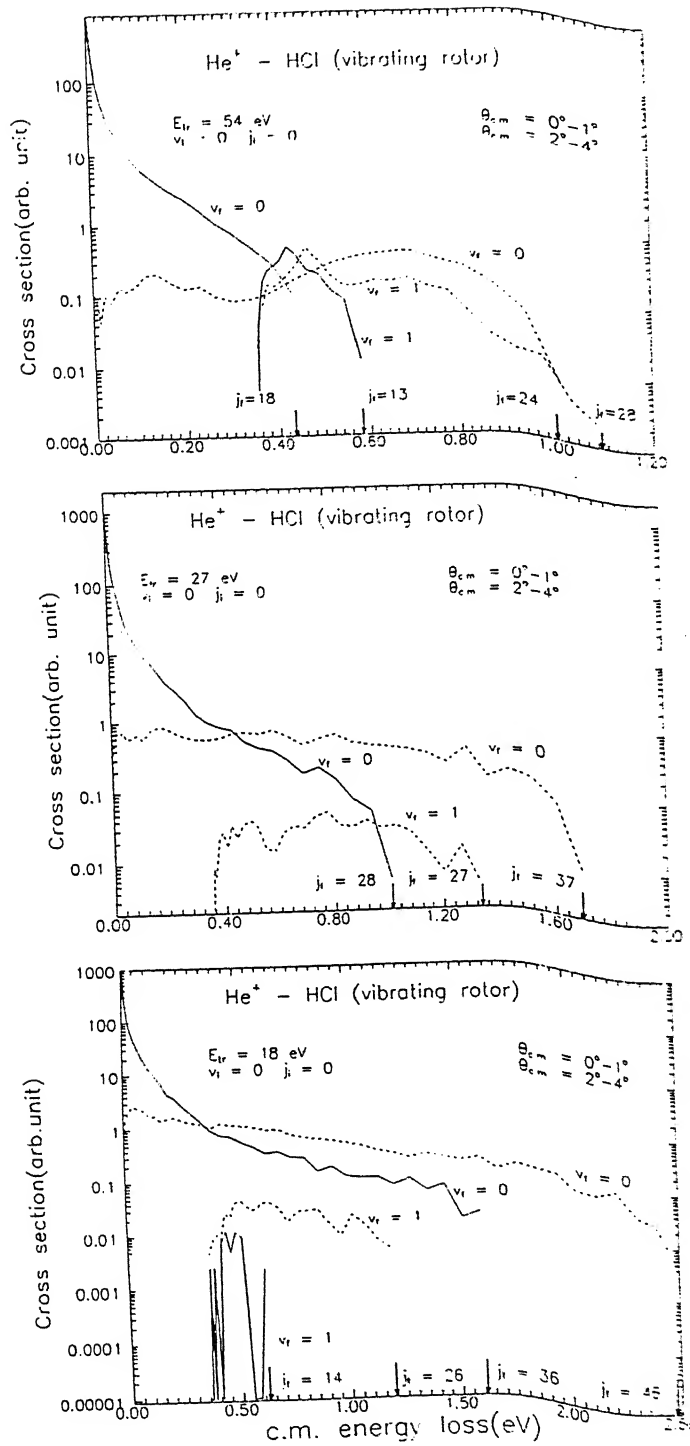
Figure 9: Differential cross sections for the vibrating rotor $HCl(v_i=0,J_i=0)$-He^+ collision for three different E_{trans}, (a) 18 eV (b) 27 eV and (c) 54 eV, for $\Theta_{c.m.}$ =0°-1° (solid lines) and 2°-4° (dashed lines). The maximum rotational excitation (J_f) for different final vibrational levels of $HCl(v_f)$ are indicated by the arrows in the Figure.

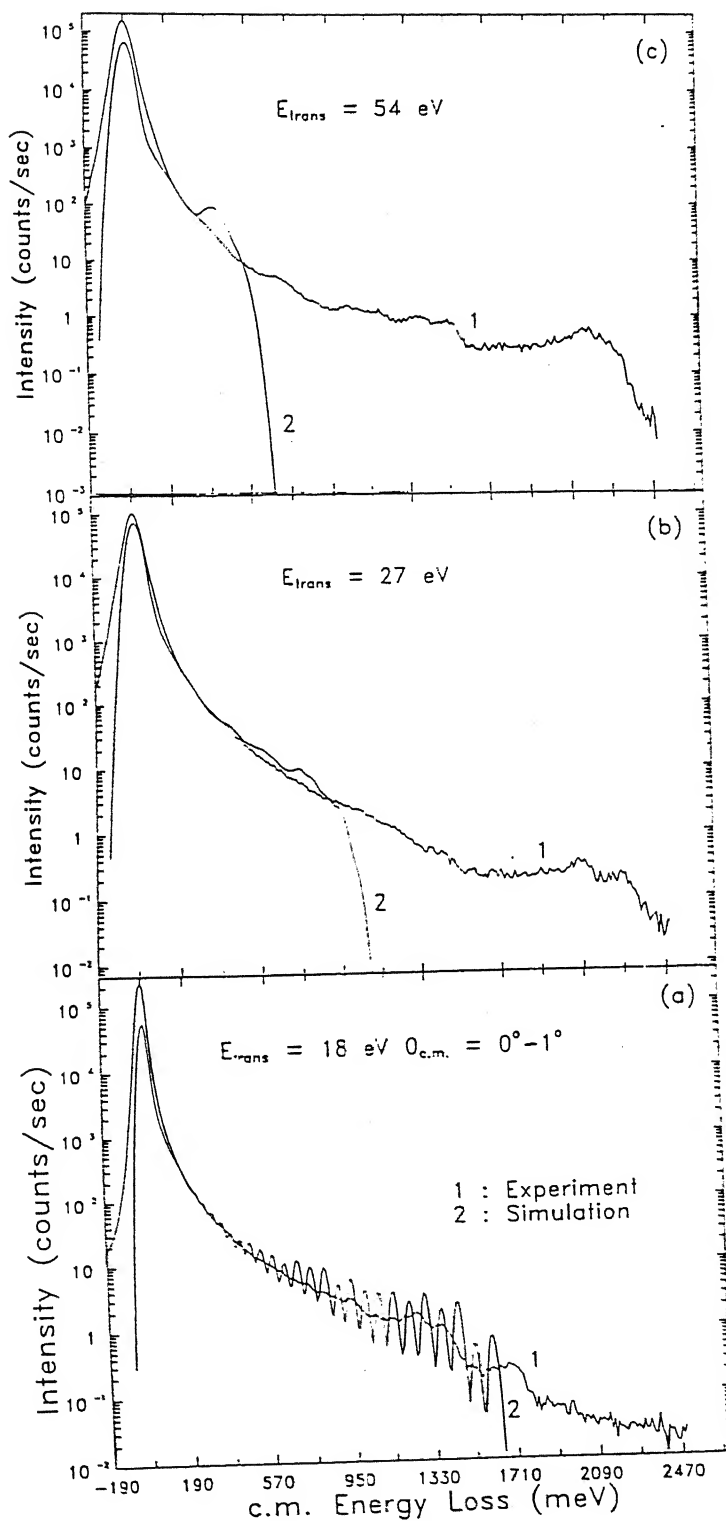Figure 10: Simulated energy loss spectra compared with the experimental results for the vibrating rotor HCl(v_i=0,J_i=0)-He$^+$ collision for $\Theta_{c.m.}$ = 0°-1°.

discrepancy is due to inadequate representation of the potential, we considered the possibility of the range of $\Theta_{c.m.}$ being larger than 1°. That is, we included trajectories with $\Theta_{c.m.} = 0\text{-}2°$ in the simulation. The agreement improves marginally at all energies as shown in Fig.11. We have also computed the energy loss spectra for collisions resulting in $\Theta_{c.m.} = 3 \pm 1°$ and they are in very good agreement with the experimental results as illustrated in Fig.12 for $E_{trans} = 18$ and 27 eV.

The striking discrepancy that persists at higher E_{trans} in all these pictures is that the QCT calculations underestimate the extent of large $\triangle E$ transfer, arising, presumably due to large $\triangle v$ transitions. This could arise, from the fact that the PES used does not satisfactorily depict the r-dependence of the potential at short range. Because of large vibrational level spacings in HF, the rigid rotor model was adequate for HF and the He^+-Ne interaction served as a reasonable representation of the potential at short R, in the case of He^--HF. For He^+-HCl, on the other hand, the inclusion of the r-coordinate becomes essential, but, unfortunately, there is little information available, experimental or theoretical, for the vibrational coupling of the short-range interaction.

IV. Summary and Conclusion

Energy loss spectra obtained for He^+ collisions with HCl at $E_{lab} = 20\text{-}60$ eV for forward scattering of He^+ revealed a dramatic (six order of magnitude) decrease in intensity with increase in $\triangle E$. The spectrum obtained at the lowest E_{trans} (18 eV) could be accounted for, almost quantitatively, for $\triangle E$ up to ~ 1500 meV using 3D QCT calculations treating HCl as a rigid rotor. By including the vibrational coordinate of HCl in the QCT calculation, the agreement improves, till ~ 1700 meV. By allowing a slightly larger (0-2°) margin for the scattering angle, experimental results upto ~ 2000 meV could be reproduced by theory.

With increase in E_{lab}, there is very little variation in the extent of energy transferred, although there seems to be some propensity for large $\triangle v$ transfer. The agreement between theory and experiment is good for small to medium $\triangle E$ even at large E_{trans}. But 3D QCT
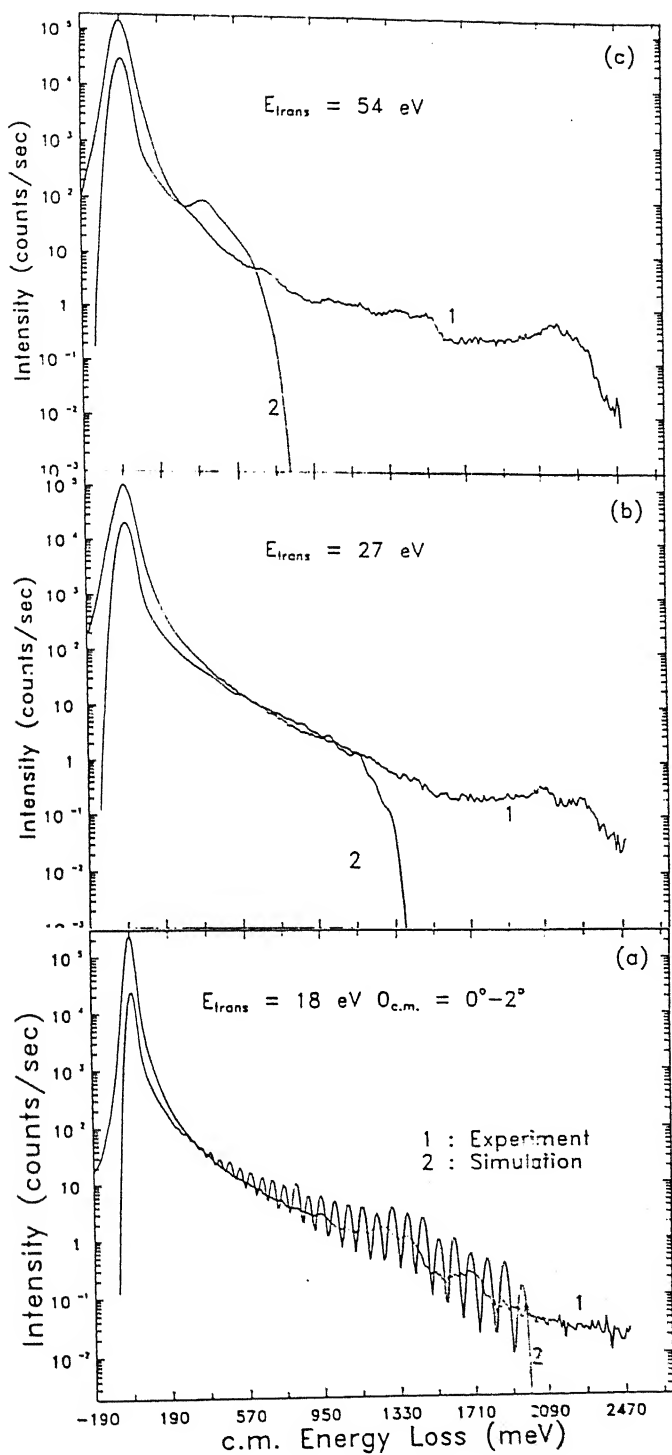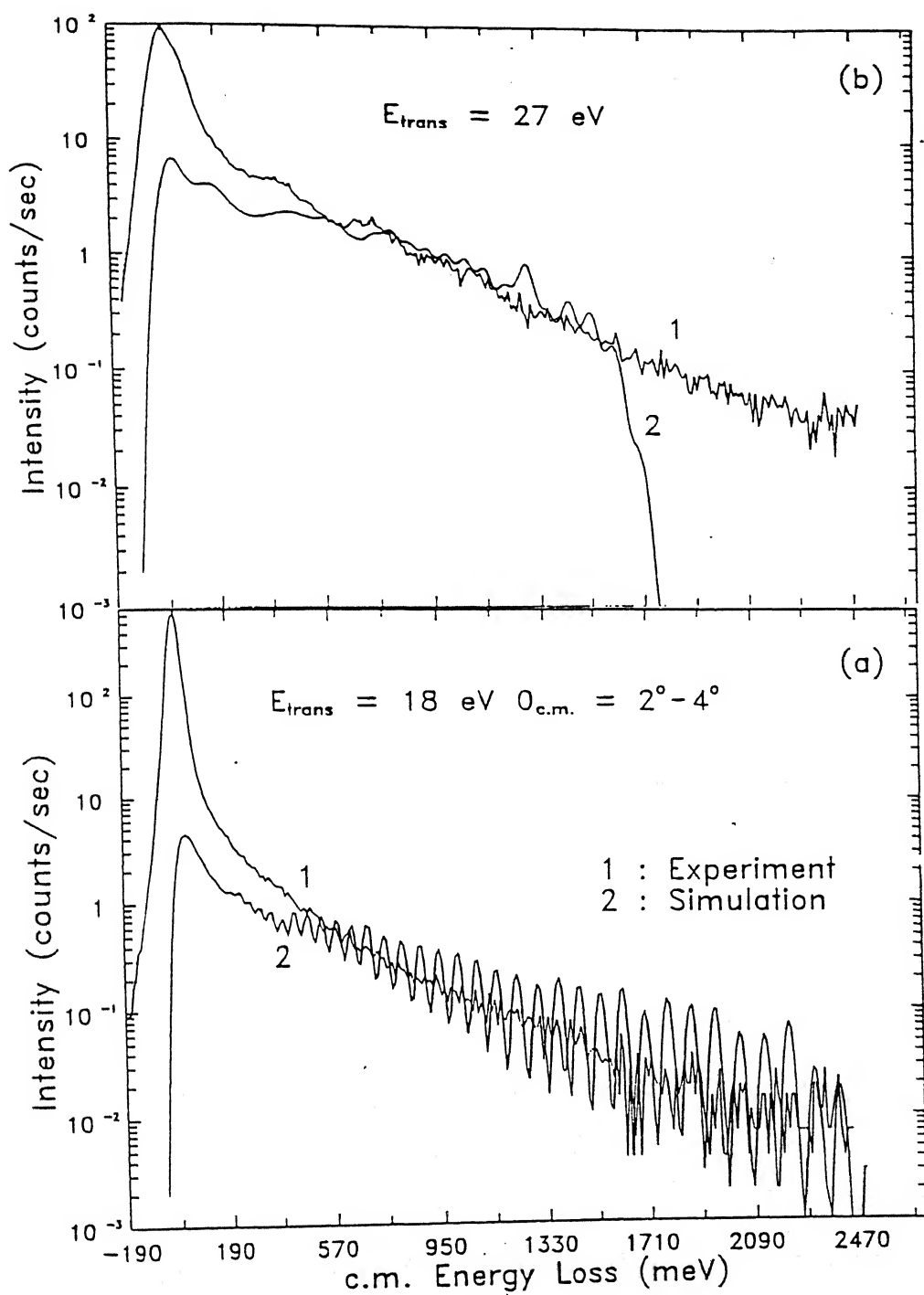
Figure 11: Same as Fig.10 for $\Theta_{c.m.} = 0°\text{-}2°$.

Figure 12: Same as Fig.10 for $\Theta_{c.m.} = 2°-4°$.

calculations fail to reproduce the large ΔE at large E_{trans} , presumably due to inadequate representation of the r-dependence of the potential. Unfortunately there is no experimental or theoretical input available for this aspect of the He$^+$-HCl interaction. Hopefully, *ab initio* calculations might provide insight into the same, in the near future.

References

(1) Udseth, H.; Giese, C. F.; Gentry, W. R. *J. Chem. Phys.* **1974**, 60, 3051.

(2) Niedner-Schatteburg, G.; Toennies, J. P. *Adv. Chem. Phys.* **1992**, LXXXII, 553.

(3) Ruhaltinger, T. *Doctoral Thesis*, Max-Planck-Institut für Strömungsforschung, Göttingen, Germany, 1993.

(4) Ruhaltinger, T.; Sathyamurthy, N.; Toennies, J. P.; Wang, R. G. *J. Chem. Phys.* **1994**, 100, 8877.

(5) Pattengill, M. D. In *Atom - Molecule collision theory: A guide to the experimentalist;* Bernstein, R. B., Ed.; Plenum Press: New York, 1979; p 359.
Truhlar, D. G.; Muckerman, J. T. *ibid.;* p.505.

(6) Radzig, A. A.; Smirnov, B. M. *Reference Data on Atoms, Molecules and Ions;* Springer Verlag: Berlin, 1985.

(7) Tang, K. T.; Toennies, J. P. *J. Chem. Phys.* **1984**, 80, 3726.

(8) Maring, W.; Toennies, J. P.; Wang, R. G.; Levene, H. B. *Chem. Phys. Lett.* **1991**, 184, 262.

(9) Buckingham, A. D. *Adv. Chem. Phys.* **1967**, XII, 107.

(10) Werner, H-J.; Rosmus, P. *J. Chem. Phys.* **1980**, 73, 2319.

(11) Amos, R. D. *Chem. Phys. Lett.* **1982**, 87, 23.

(12) Amos, R. D. *Mol. Phys.* **1978**, 35, 1765.
Gianturco, F. A.; Buonomo, E. -*Private Communication.*

(13) Gianturco, F. A.; Guidotti, C. *J. Phys. B: Atomic and Molecular Physics;* **1978**, 11, L385.

(14) Gianturco, F. A.; Palma, A.; Semprini, E.; Stefani, F.; Diehl, H. P.; Staemmler, V. *Chem. Phys.* **1986**, 107, 293.

(15) Miller, W. H. *Adv. Chem. Phys.* **1974**, 25, 69.

Miller, W. H. *ibid.* **1975**, 30, 77.

(16) Porter, R. N.; Raff, L. M.; Miller, W. H. *J. Chem. Phys.* **1975**, 63, 2214.

(17) Huber, K. P.; Herzberg, G. In *Molecular Spectra and Molecular Structure: IV. Constants of Diatomic Molecules;* Van Nostrand Reinhold Company: New York, 1979, p 282.

Addendum

1. p. 90, second line from the bottom please include ref. 200.

2. Ref. 137 should be read as:

T. Seideman and W. H. Miller, J. Chem. Phys. **96**, 4412 (1992).

3. Ref. 280 should include

Z. Top and M. Baer, Chem. Phys. **25**, 1 (1977).

4. p. 11, Below Eq. (2.14) G should be read as

$$G_{in} = g_n(x_i)$$

5. p. 20, Eq. (2.47) the summation should be read over n.

6. p. 54, Eq. (3.13) is replaced by

$$f(X_i) = \sin\left[\frac{\pi}{2}\frac{(X_{mask} + \Delta X_{mask} - X_i)}{\Delta X_{mask}}\right], \qquad X_i \geq X_{mask}$$

X_{mask} is the point at which the masking function is initiated and $\Delta X_{mask}(= X_{max} - X_{mask})$ is the width over which the function decays from 1 to 0.

7. p. 81, line 5. More recent calculations revealed a slight difference in the bound state energies of HeHD$^+$ and HeDH$^+$. The energy values are -0.1499, -0.0655 eV for the former and -0.1514, -0.0664 eV for the latter.

8. p. 95, five line up from the bottom, "The upper potential" should be read as "The upper bound of the potential".

9. p. 130, line 11, (b) and (c) should be read as (a) and (b).